



**HAL**  
open science

# Generation and control of tactile feedback with longitudinal ultrasonic vibration and human-in-the-Loop analysis

Diana Angélica Torres Guzman

► **To cite this version:**

Diana Angélica Torres Guzman. Generation and control of tactile feedback with longitudinal ultrasonic vibration and human-in-the-Loop analysis. Human-Computer Interaction [cs.HC]. Université de Lille, 2021. English. NNT : 2021LILUN035 . tel-03674797

**HAL Id: tel-03674797**

**<https://theses.hal.science/tel-03674797v1>**

Submitted on 21 May 2022

**HAL** is a multi-disciplinary open access archive for the deposit and dissemination of scientific research documents, whether they are published or not. The documents may come from teaching and research institutions in France or abroad, or from public or private research centers.

L'archive ouverte pluridisciplinaire **HAL**, est destinée au dépôt et à la diffusion de documents scientifiques de niveau recherche, publiés ou non, émanant des établissements d'enseignement et de recherche français ou étrangers, des laboratoires publics ou privés.

THESIS

*In order to obtain the title of*

**Doctor in Electrical Engineering**

---

Presented on the 14/12/2021 by:

**Diana Angélica Torres Guzman**

**“Generation and control of tactile feedback with longitudinal ultrasonic vibration and human-in-the-Loop analysis”**

---

**Doctoral School:**

ENGSYS : Ecole Doctorale des Sciences Pour l'Ingénieur

**Research Unit:**

Laboratoire d'Electrotechnique et d'Electronique de Puissance de Lille (L2EP)

**Supervisors:**

Pr. Betty LEMAIRE-SEMAIL, Université de Lille  
MCF HDR. Frédéric GIRAUD, Université de Lille

**Co-supervisor:**

MCF HDR. Christophe GIRAUD-AUDINE, Arts et Métiers Sciences et Technologies, Lille

**Jury:**

*President* : Pr. Vincent HAYWARD, Sorbonne Université (ISIR) / Actronika SAS, Paris

*Reviewers* : Pr. Christine PRELLE, Université Technologique de Compiègne, MCF HDR. François PIGACHE, ENSEEIHT, Institut National Polytechnique de Toulouse

*Examiners* : Dr. Michaël WIERTLEWSKI, 3mE, TU Delft, Pr. Marie-Ange BUENO, ENSISA, Université de Haute Alsace, Mulhouse

*Invited*: Dr. Matthieu RUPIN, CTO Hap2U

UNIVERSITÉ DE LILLE – FACULTÉ DES SCIENCES ET TECHNOLOGIES

*Thèse en vue de l'obtention du*

Doctorat en Génie Electrique

---

Présentée et soutenue le 14/12/2021 by:

Diana Angélica Torres Guzman

“Génération et Contrôle de retours tactiles par ondes ultrasoniques latérales et analyse human-in-the-Loop ”

---

École Doctorale:

ENGSYS : Ecole Doctorale des Sciences Pour l'Ingénieur

Unité de Recherche:

Laboratoire d'Electrotechnique et d'Electronique de Puissance de Lille (L2EP)

Directeurs de thèse:

Pr. Betty LEMAIRE-SEMAIL, Université de Lille  
MCF HDR. Frédéric GIRAUD, Université de Lille

Co-encadrement:

MCF HDR. Christophe GIRAUD-AUDINE, Arts et Métiers Sciences et Technologies, Lille

Composition du Jury:

*Président :*

Pr. Vincent HAYWARD, Sorbonne Université (ISIR) / Actronika SAS, Paris

*Rapporteurs :*

Pr. Christine PRELLE, Université Technologique de Compiègne

MCF HDR. François PIGACHE, ENSEEIHT, Institut National Polytechnique de Toulouse

*Examineurs:*

Dr. Michaël WIERTLEWSKI, 3mE, TU Delft

Pr. Marie-Ange BUENO, ENSISA, Université de Haute Alsace, Mulhouse

*Invité:*

Dr. Matthieu RUPIN, CTO Hap2U





## *A c k n o w l e d g e m e n t s*

I would like to start by kindly thanking the thesis juries who accepted to read and evaluate our work.

To our team at L2EP laboratory and the Control team. After years of witnessing the efforts and achievements of the incredibly talented people around me, I can only hope that these few lines will suffice to express my awe and gratitude. It has been a fulfilling journey!

A few years ago, after I decided to continue my academic career, I got a phone call. The person that I talked to wanted to know if I was sure of what I was planning to do. I said I had no doubt. And so, after him, one after the other, the brilliant scientists that conform this group have given me something invaluable: their trust. I have since given my best effort to repay this trust with my work.

To my thesis director, Pr. Betty Lemaire-Semail, thank you for being available, for listening, debating and accepting my ideas. Thank you for your expert revisions which greatly improved the quality of this document. In addition to being a director for this thesis, you have been a valuable team mate and a great role model.

My co-director, Dr. Frederic Giraud, whose own ideas served as a seed for many of the contents in this document, thank you for sharing your time and your thoughts. A big thank you also to Dr. Christophe Giraud-Audine, for your trust, and for taking the time for generously sharing your knowledge with me and reviewing my work. Your work has given much value to this document.

Michel Amberg, you made this thesis possible and I am in great debt. Thank you for sharing your unfathomable knowledge with patience and good humor. It is

mostly laughing in front of all this crazy circuitry what I will remember from you. Thank you for your passion and dedication.

I wish to extend my gratitude to the director of the Control team, Prof. Alain Bouscayrol for his presence and good advice.

Of course, I also have the pleasure to thank those brilliant people which I have the luck of finding in my path and the incredible privilege to count amongst my friends. My colleagues at IRCICA, Ehsan, Pierre, G er mie, Yisha, Elis, Detjon, Rabbi, Milad, Rick and also Anis, next to whom, after all the travels, debates and explanations (some of which I understood!), we finally made it through to the end! I am glad we get to keep working together for a while. To my friends at ESPRIT David, Florian and all the others, and my dear friends from master Florentin and Leysmir, I owe you a lot and I hope you know you can count on me!

To my family, loving and supporting us from afar. No amount of distance has kept your embrace, kindness and love to fill me with determination and patience to complete this process. You make me very strong. Of course, this extends to my french family and close ones, for their support, company and great advice. I keep you in my heart (and I'm very glad I completed those 17 points!).

Jeremie, there are no words that suffice to thank those who brought us light when the world looked dark, and then sat and rejoiced together in the light of the good days. This achievement is ours, as we did it all together, for you, for me and for her. Victoria, la magia si existe : lo compruebo cada vez que me haces sonreir.

*“The end of one trip is only the beginning of another. It is necessary to see what has not been seen, to see again what has already been seen, to see in spring what was seen in summer, to see in daytime what was seen at night, with the sun where the rain first fell, to see the green field, the ripe fruit, the stone that changed place, the shadow that was not here. It is necessary to return to the steps that have been taken, to repeat them and to trace new paths alongside them. It is necessary to start the journey all over again. Always.” – J. Saramago*



## *Abstract*

Haptic technology offers users a unique way of interacting with the virtual world, as it allows direct information transfer between the interfaces and the human through the sense of touch. Surface haptic devices use different techniques to achieve friction modulation in order to simulate texture. In the case of ultrasonic surface haptics, this is achieved with the use of piezoelectric ceramics, which, supplied by a sinusoidal alternating voltage, elicit motion on the surface of the device. This motion is transmitted and amplified by the material, at its resonance frequency.

Transverse vibrational modes are commonly used in ultrasonic surface haptic technology. This work evaluates the possibility to use longitudinal vibration as a technological alternative to produce haptic return in ultrasonic devices. Valuable comparisons between transverse and longitudinal modes are performed on a dedicated device, both on the point of view of energetic behavior and stimuli perception quality.

Moreover, in the context of this thesis, we intend to expand the proposed analysis, by integrating the concept of ‘human-in-the-loop’ applied to surface haptics, in order to better evaluate the human interaction, influence and perception of the physical phenomena involved in the creation of surface haptic illusions.

## R é s u m é

La technologie haptique offre aux utilisateurs un moyen unique d'interagir avec les mondes virtuels en permettant le transfert direct d'informations entre les interfaces et l'être humain par le biais du sens du toucher. Les dispositifs haptiques de surface utilisent différentes techniques pour moduler la friction afin de simuler la texture. Dans le cas des surfaces haptiques à ultrasons, on utilise des céramiques piézoélectriques qui, alimentées par une tension alternative sinusoïdale, provoquent un mouvement à la surface du dispositif. Ce mouvement est transmis et amplifié par le matériau, à sa fréquence de résonance.

Les modes vibratoires transversaux sont couramment utilisés dans la technologie haptique des surfaces ultrasoniques. Ce travail évalue la possibilité d'utiliser les vibrations longitudinales comme une alternative technologique pour produire un retour haptique dans les dispositifs à ultrasons. Pour cela, des comparaisons sont effectuées sur les deux familles de modes, à partir d'un dispositif dédié à la fois d'un point de vue performances énergétiques et qualité des stimuli perçus.

De plus, dans le cadre de cette thèse, nous avons proposé d'étendre l'analyse en intégrant le concept de "l'homme dans la boucle" afin de mieux évaluer l'interaction humaine, l'influence et la perception des phénomènes physiques impliqués dans la création d'illusions haptiques de surface.

## G l o s s a r y

$A_c$	- finger-plate contact area
$b$	- Width of a beam
$D_n$	- Modal damping of the $n$ -th mode
DSP	- Digital Signal Processor
$E_e$	- Young Modulus
EMR	- Energetic Macroscopic representation
$errX\%$	- Average relative error of estimation
FE	- Finite element simulation
$f_I$	- Inertial force of a mode
$f_{Lbone}, f_{Nbone}$	- Lateral and normal bone force
$f_{Lmat}, f_{Nmat}$	- lateral and normal forces of the material
$f_{Lsc}, f_{Nsc}$	- lateral and normal force in the stratum corneum
$f_{Lsens}, f_{Nsens}$	- lateral and normal forces at the sensing layer
$f_n$	- Pressure force
$f_{nL}$	- Resonance frequency of the longitudinal mode
$f_{nN}$	- Resonance frequency of the transverse mode
$f_p$	- Motor force from the piezoelectrics
$\underline{f}_p$	- Piezoelectric force (complex)
$F_p$	- Piezoelectric force (Laplace domain)
$F_{pd}, F_{pq}$	- Piezoelectric forces in the rotational reference frame
$f_r$	- Load (or finger) acoustic force
$\underline{f}_r$	- Acoustic finger force (complex)
$F_r$	- Acoustic finger force (Laplace domain)
$\overline{F}_r$	- Mean measurement of acoustic finger force (Laplace)
$F_{rd}, F_{rq}$	- Acoustic finger force in the rotational reference frame
$f_{rL}, f_{rN}$	- Lateral and normal components of the acoustic finger force
$\tilde{F}_{rp}$	- Acoustic finger force estimation for participant 'p'
$f_s$	- Damped-elastic force of a mode
$F_{sd}, F_{sq}$	- Damped-elastic forces in the rotational reference frame
$h$	- Height of a beam

hiL	- Human-in-the-loop
HiL	- Hardware-in-the-loop
$I$	- Quadratic Momentum
$i_m$	- Motional current from the piezoelectrics
$K_n$	- Modal elasticity of the $n$ -th mode
$L$	- Length of a beam
$\mathcal{L}$	- Lagrangian operator
LFU	- Low frequency ultrasound
MCS	- Maximal Control Structure
$M_n$	- Modal mass of the $n$ -th mode
$N_n$	- Electromechanical transformation factor of the $n$ -th mode
PC	- Principal component
PCA	- Principal component analysis
PCR	- Principal component regression
RMSEE	- Root mean square error of estimation
$S$	- Transverse surface of a beam
sc.	- Stratum Corneum
$\mathcal{U}$	- Euler-Bernoulli displacement field
$u_{bone}$	- Bone velocity
$U_d, U_q$	- Velocity coordinates of the device in the rotational dq frame
$u_e$	- velocity of the epidermis
$u_f$	- Finger velocity
$u_{fp}$	- Relative velocity of the finger as seen from the device
$u_{mat}$	- Velocity of the material
$u_p$	- Velocity of the device (plate)
$\underline{u}_p$	- Velocity of the plate (device) complex phasor
$U_{p.ref}$	- Plate velocity reference
$u_{sens}$	- velocity at the sensing layer
$u_{sc}$	- Velocity of the stratum corneum
USHD	- Ultrasonic surface haptic device
$v$	- Input voltage
$\underline{v}$	- Input voltage (complex phasor)
$V_d, V_q$	- Voltage coordinates in the rotational dq frame
$\underline{w}$	- Vibration displacement (complex phasor)
$W$	- Vibration displacement (Laplace)
$W_d, W_q$	- Amplitude coordinates in the rotational dq frame

$w_n, w$	-	Temporal evolution of the vibration displacement of the $n$ -th mode in a modal decomposition
$\dot{w}_n, \dot{w}$	-	Temporal evolution of the vibration velocity of the $n$ -th mode in a modal decomposition
$\ddot{w}_n, \ddot{w}$	-	Temporal evolution of the vibration acceleration of the $n$ -th mode in a modal decomposition
$\beta_l$	-	Wave number of the longitudinal mode
$\beta_n$	-	Wave number of the transverse mode
$\chi$	-	Longitudinal Displacement
$\xi$	-	Damping factor
$\kappa$	-	Potential energy
$\nu$	-	Kinetic energy
$\mu$	-	Friction
$\mu_0, \mu_{max}$	-	Friction of the finger against the surface without vibration
$\mu_d$	-	Dynamic friction
$\Delta\mu$	-	Friction reduction
$\mu_k$	-	at point 'k'
$\mu_{meas}$	-	Measured friction
$\mu'$	-	Relative friction coefficient
$\mu_s$	-	Static friction
$\psi$	-	Transverse displacement
$\varphi_k$	-	Shape of the mode 'k' in a modal decomposition
$\rho$	-	Density
$\sigma_p$	-	$n$ -th PCA coefficient of participant 'p'
$\sigma_{p\_est}$	-	estimation of the 'n-th' PCA coefficient of participant 'p'
$\omega$	-	Angular frequency
$\omega_n$	-	Angular resonance frequency
$\omega_{nL}$	-	Angular resonance frequency of the longitudinal mode
$\omega_{nN}$	-	Angular resonance frequency of the transverse mode



*Table of contents*

<b>Acknowledgements .....</b>	<b>iii</b>
<b>Abstract .....</b>	<b>vi</b>
<b>Résumé.....</b>	<b>vii</b>
<b>Glossary.....</b>	<b>viii</b>
<b>Table of contents.....</b>	<b>xi</b>
<b>General Introduction .....</b>	<b>1</b>
<b>Chapter 1:</b>	
<b>Ultrasonic surface haptic technologies for friction reduction and Human machine interaction .....</b>	<b>4</b>
1.1. Tactile Mechanics.....	5
1.2. Neurophysiology of touch .....	13
1.3. Tactile illusions.....	20
1.4. Overview of haptic technologies.....	21
1.5. Surface Haptics.....	29
1.6. The principle of active lubrication with USHD .....	33
1.7. EMR applied to ‘human-in-the-Loop’ systems .....	35
1.8. Summary .....	38
<b>Chapter 2:</b>	
<b>Design and control of ultrasonic surface haptic devices for longitudinal and transverse mode vibration .....</b>	<b>39</b>
2.1 Pre-design specifications.....	41
2.2 Plate dimensioning and implementation.....	44
2.2.1. Euler-Bernoulli approximation .....	44
2.2.2. Resonance frequencies .....	49
2.2.3. Choice of dimensions and Finite Element simulation.....	50
2.2.4. Implementation and Cartography.....	51
2.3 Dynamic model of one mode in the rotating reference frame dq.....	54
2.3.1 Modal modelling and the orthogonality principle.....	55
2.3.2 EMR of the dynamic modal equation .....	58
2.3.3 Projection in the rotating reference frame dq .....	59
2.4. Vibration amplitude control in the dq frame.....	62
2.4.1 Amplitude control in the dq frame around the resonance..	63
2.4.2 Modal parameter identification .....	65
2.4.3 Closed loop control implementation and testing.....	71
2.5. Conclusion.....	73

<b>Chapter 3:</b>	
<b>Mechanisms of friction reduction in USHDs for longitudinal modes</b>	<b>74</b>
.....	
3.1 Friction reduction mechanisms using transverse modes .....	76
3.2. Friction reduction with longitudinal ultrasonic vibration in one dimension.....	77
3.2.1. Bed of Springs Approximation .....	77
3.2.2. Friction reduction through the ‘Ratchet Mechanism’ on a moving finger .....	78
3.2.3. Friction reduction model validation with experimental data.....	80
3.2.4. Parametric analysis.....	83
3.3. The non-Coulombic model of dynamic friction for longitudinal modes .....	84
3.3.1. Friction variation on a finger pad due to sliding velocity...87	
3.3.2. Friction vs. sliding velocity measurements.....	93
3.3.3. Finger pad Relative Motion and Friction.....	99
3.4. Conclusion.....	104
<b>Chapter 4:</b>	
<b>Performance comparison between longitudinal and transverse modes</b>	<b>106</b>
.....	
4.1. Friction reduction vs. vibration amplitude .....	107
4.1.1. Testing scenarios.....	108
4.1.2. Results .....	111
4.2. Psychophysical Analysis.....	113
4.2.1. Psychophysical measurements at 30 KHz .....	113
4.3. Energy analysis in the mode comparison.....	121
4.3.1. Energy losses in a USHD .....	121
4.3.2. Active power measurements at no load .....	123
4.3.3. Impedance coupling: the effect of pressing with a finger 125	
4.3.4. Amplitude vs. active power function.....	126
4.4. Conclusion.....	127
<b>Chapter 5:</b>	
<b>Fundamental acoustic finger force measurement and its correlation with friction reduction</b>	<b>129</b>
.....	
5.1. Principle of the fundamental acoustic force measurement.....	131
5.1.1. Acoustic finger force at steady state .....	132
5.1.2. Acoustic force estimation in the rotational reference frame.....	133
5.2. Acoustic force measurement and friction correlation: study for transverse modes at a single vibration amplitude.....	137
5.2.1. Experimental setup and measurement protocol .....	137
5.2.2. Results .....	141

5.2.3. PCA of the finger acoustic force measurement .....	144
5.2.4. PCA results for matrix FR.....	147
5.2.5. Coefficient $\sigma_1$ and $F_{rp}$ estimation by PCR.....	149
5.2.6. PCR best predictor selection and results.....	150
5.3 Acoustic Force measurement and friction correlation: Study for longitudinal modes at different vibration amplitudes .....	159
5.3.1. Experimental procedure.....	160
5.3.2. Construction of predictive models .....	163
5.3.3. Tests of the methodology .....	164
5.4. Look-ahead: Towards real time friction control using acoustic finger force observation with longitudinal modes .....	169
5.4.1. Acoustic finger force observation in the rotational reference frame.....	170
5.5. Conclusion.....	174
<b>Chapter 6:</b>	
<b>Human-in-the-Loop analysis for USHD Interaction .....</b>	<b>176</b>
6.1. Skin mechanics and the creation of texture illusions.....	177
6.2. Dynamic model and representation of touch for real and virtual textures .....	180
6.2.1. Dynamic model and representation of touch for real textures .....	180
6.2.2. Dynamic model and representation of touch for virtual objects.....	184
6.3. hiL approach for USHD-human interaction representation .....	185
6.3.1. ‘Human-in-the-Loop’ system components.....	186
6.3.2. EMR of the complete system .....	188
6.4. hiL surface haptic applications .....	189
6.4.1. hiL for introducing standardized perception .....	189
6.5 Conclusions .....	193
<b>Conclusions and Perspectives .....</b>	<b>195</b>
1. Conclusions.....	195
2. Perspectives .....	197
<b>Appendices.....</b>	<b>211</b>
<b>References .....</b>	<b>216</b>



## *General Introduction*

Thanks to new technological advances, it is now possible to imagine touching a virtual object, pushing a virtual button or carrying out a precision task at a distance. It could be conceivable sending a texture via email, commanding automobile functions with our touch or discovering new ways to enjoy art and music. Illusion has been one of the pillars of technological development, and has helped us breach new barriers in perception. From Lumière's cinema to today's virtual reality (VR), illusion plays a central role in our interaction with technology. This is why, including the sense of touch to our devices means a revolution of the human-machine interaction, and may have as many applications as can be imagined. But our sense of touch is complex; it depends on several systems of large organs, and it encompasses an enormous variety of conscious and unconscious interactions of different nature. Haptics is the science of touch. It is therefore in the field of haptics that the present thesis takes place.

Ultrasonic surface haptic devices are designed to simulate tactile sensations, by creating illusions of out of plane textures on flat surfaces (such as tablet screens). This can be achieved by modulating the friction of the surface using ultrasonic vibration.

Ultrasonic tactile feedback devices developed so far, and for which interaction models have been validated, rely on the generation of stationary "out of plane" transverse waves called "Lamb" waves. However, other waveforms exploiting the shearing effect, longitudinal waves, are also able to modify the friction between the finger and the surface subjected to the ultrasonic mechanical deformation. For these specific waveforms, it is necessary to establish a new interaction model, able

to explain the effect of reduction of friction, and to control the vibration of the surface in order to validate and optimize the produced contrast in friction.

The action and perception of the human in this context are very important. Unfortunately, due to the complexity of friction phenomena, the sensory response is different from one user to another, with the same haptic stimulus. For this reason, it is interesting to explore the human in the tactile simulation loop. With this purpose in mind, an initial attempt to develop the concept of "Human-in-the-Loop" in surface haptics is given in this thesis, using the EMR formalism, (Energetic Macroscopic Representation) developed within the L2EP Control team and already commonly applied to HIL (Hardware in the Loop).

This PhD thesis is organized as follows: chapter 1 presents the state of the art and the project positioning. Chapter 2 presents the creation and control of a longitudinal wave surface haptic device. In Chapter 3, the interaction model at the origin of the friction modulation effect with ultrasonic longitudinal vibration is proposed and validated for the case where the exploration occurs in the same axis as the wave motion, as well as the more general case where the exploration occurs in any other direction. In Chapter 4, a series of experiments are conceived to perform a comparative analysis between longitudinal and transverse ultrasonic vibration, in terms of energetic requirements for a given texture intensity. From this study, it is possible to perceive one important problematic in the design of ultrasonic surface haptic devices: the adaptation of the haptic feedback to each user to achieve a standardized perception. Chapter 5 deals with this problematic, by introducing the concept of acoustic finger force and its correlation with the friction reduction phenomenon. Finally, Chapter 6 presents the lessons learned in the previous chapters in a 'Human-in-the-loop' perspective and explores the possible future applications of this type of analysis.

This work has been carried out within the framework of the Mint Project at IRCICA. It takes, therefore, part in the collaborative 'CRIStAL-L2EP-MINT'[1] team, and CNRS GdR TACT[2] group.



## *Chapter 1*

### ULTRASONIC SURFACE HAPTIC TECHNOLOGIES FOR FRICTION REDUCTION AND HUMAN MACHINE INTERACTION

Since the beginning of our lives, the first sense available to us is the sense of touch. It is necessary for human life to thrive, and is essential to our awareness of the world and of our own bodies. Without it, we could not hold and manipulate objects dexterously and securely, and we “would not have a body that belongs to us” [1]. Touch is essential in key tasks associated to human survival, as well as many cognitive functions. For this reason, integrating the tactile modality to technology has innumerable potential applications and proves beneficial in a very wide variety of areas of human knowledge.

Haptic technologies result from this pursuit of bringing tactile sensation to our human-machine interaction. A common way to achieve this is through the creation of texture illusions for virtual object exploration and manipulation. To face this challenge, it is necessary to understand how the tactile sensation arises and how it is interpreted. Understanding the complexity of the interaction of the human-machine interaction from the sense of touch, involves a mechanical and neurophysiological understanding of this sense, and how it can be manipulated for the creation of accurate tactile feedback.

The current chapter deals, therefore, with the question of approaching the sense of touch from a systemic point of view, and the technology that has been developed to do so, focusing primarily in our studied case: the ultrasonic surface haptic devices.

First, we introduce briefly the mechanics and neurophysiology related to touch and texture illusion creation. We then proceed to reflect upon the technological resources that have been developed for this purpose, providing an overview of the



state of the art of haptic technologies. Additionally, we explore the evolution of the concept of ‘human-in-the-loop’ systems for surface haptics and the analytical tools available that can be useful in this analysis. To conclude we present the previous work developed in this area by our team at the L2EP Laboratory.

## **1.1. Tactile Mechanics**

The exploration of the world through our sense of touch takes place with almost every part of our body, from our bones and motor system, to the entirety of our skin. Tactile sensations arise mainly from the scanning of our skin against objects. The mechanic properties of the skin and underlying tissue in the hand have real consequences on texture perception, grip function and motor skills. Hence, the mechanics of this interaction is the source of information that our brain uses to decode the material properties of the world around us. In this section, we present an overview of the mechanics of the finger, the skin and the interactions taking place during the tactile exploration.

### *1.1.1. Anatomy of the finger*

The hand is a motor and sensory organ at the same time. A detail of the anatomy of the fingertip is illustrated in Figure 1.

The region surrounding the hand over the palm and fingers is defined as the ‘volar region’ [2]; it is surrounded by glabrous skin (devoid of hair). Typically, this is the skin that comes in contact with the manipulated objects. It is different in many ways to the skin over the rest of the body, as it has the specific function of manipulation and has a very tight connection to the neural system [1]. Below the skin, the tissues around our skeleton over this area are mostly made of soft, deformable materials.

The fingertip is both very rigid and very flexible. The great rigidity of the finger is conferred by the bone of the third phalanx. This bone is braced to the rest of the

finger and hand by two ligaments above and below the bone [3]. This rigidity is amplified by the nail, a dome of hard keratin, which is connected to the bone by a rigid bond of collagen fibers [2]. This gives the human manipulation capabilities that cover many orders of magnitude from the finest object manipulation to the heaviest load lifting [4].

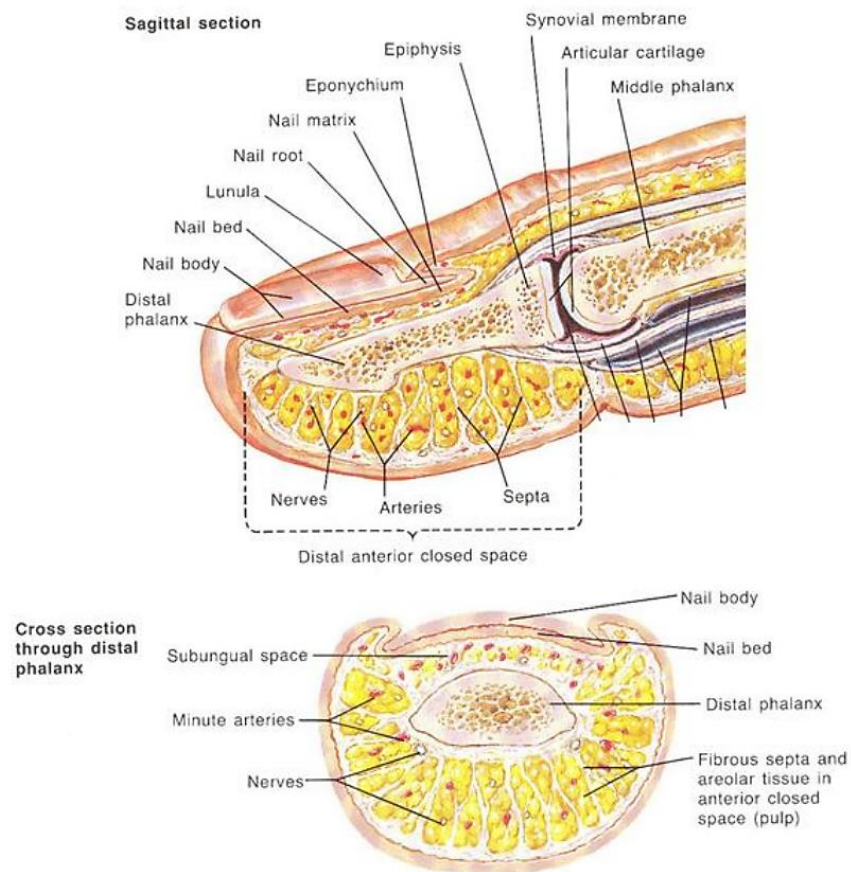


Figure 1. (Above) sagittal cut-away view of human finger. (Below) axial view [5]

The lower side of the fingertip is named the pulp. In contrast to the superior part, it is the flexibility and the viscosity that predominate at the pulp. A layer of fat

surrounds the lower part of the bone of the third phalanx to give it a conformation capacity [6].

Closer to the surface is the subcutaneous cellular tissue. This area contains the blood vessels and a good part of the nerve endings.

The skin is a barrier that protects the inner tissues from infection, dehydration, chemical and mechanical stress. It is composed of a series of layers, each with a specific purpose. The outmost layer of the skin is called epidermis. It is itself composed of a series of layers. The first layer is the '*stratum corneum*' (hereby denominated 'sc.') [7]. It is composed roughly of 10 to 40  $\mu\text{m}$  of overlapped dead epithelial cells without nuclei or organelles (mostly keratin [1]). In the volar region, the sc. is followed by the '*stratum lucidum*', an intermediate layer of dead cells which migrate continuously towards the outside renewing constantly the sc. Further inwards is the '*stratum granulosum*', through which occurs the expulsion of the inner lipid content of the dermis cells that creates a hydrophobic protection layer. Later on, we find the '*stratum spinosum*', which is formed of living cells travelling from the inner to the outer part of the skin. Finally, the '*stratum basale*' contains the outmost sensory receptors of the skin [7]. It is the frontier between the epidermis and the dermis.

The topology of the skin over the volar region, and most specifically the fingertip, observable to the naked eye, is given by the fingerprints, which form regular valleys and mountains of a small size, commonly named friction ridges. The distance between two ridges is of about 300  $\mu\text{m}$ . They are compressible to a certain extent and end in a semi-tubular shape [8]. Since the sc is constantly being renewed, flattened cells pile up on the surface in a disordered manner, forming irregular micro-asperities even within a single fingerprint groove [9]. The functionality and evolutionary reason for the existence of these ridges is still under debate [10]. Even though these ridges probably do not optimize the friction in the grip function, as initially thought [10], it has been shown that they perform several crucial tasks in

the tactile function, such as enhancing tactile sensitivity and humidity regulation to aid contact establishment [11].

It is accepted that each fingerprint is unique. However, some aspects of the friction ridges are recurrent [6]. At the front of the finger, the fingerprint is ridged perpendicular to the finger axis. This changes the mechanical response of the finger depending on the direction of the finger exploration. In [12], it has been shown that the vibrations emitted between a surface and the fingerprints produce a different frequency spectrum depending on the exploration axis. On the other hand, the central area of the skin of the fingertip is composed of convolutions, with concentric circles or spirals and does not favor a particular direction. This is the part that is in contact during grip.

A second aspect of this skin, which makes it unique, is the fact that the human has sweat glands that are permanently releasing moisture to the outmost layers of the skin through the pores to keep the tissues alive. This exudation plays a major role in object manipulation [13], [14]. This is because the sc. is mainly made of keratin: in the presence of water becomes very elastic and has very different mechanical properties than when it is dry [15]. In a few words, moisture is constantly exuded and-re absorbed into the body, so upon contact, water gets trapped between the object's surface and the skin modifying the mechanics locally at the contact point.

### *1.1.2. Finger pad and skin mechanics*

Skin is a non-homogeneous, anisotropic, viscoelastic multi-component material [16]. It exhibits non-linear dynamics over the entire range of frequencies related to the sense of touch [17]. It is very deformable and elastic until a point of maximum deformation (about 2.5mm) and then becomes stiff [18]–[20]. This gives stability to the grip function. The different layers of skin and tissue at the finger and their mutual interaction deeply influence the mechanical behaviour of the finger pad and its response to external stimuli.

A series of experiments were performed [8], [18], [21], [22] to study the behaviour of the finger pad under lateral and normal compressive loadings. Despite the non-isotropic property of the fingertip, in both cases, a loading-unloading hysteresis of the finger's reaction forces to deformation suggested a non-linear viscoelastic behaviour of the finger. This behaviour was observed to be dominated by the mechanical properties of the pulp tissues (ensemble of tissues located on the opposite side of the fingernail on the fingertip), which have a significantly lower stiffness than the epidermis. The parameters of this mechanical response, however, were dependent to the frequency of the presented stimulus.

It has been theorized that the dynamic behaviour of the fingertip can be modeled as a second order oscillator over a large frequency spectrum [23], [24]. As previously mentioned, its behavior is non-linear: mostly elastic in frequencies below 100 Hz, then predominantly viscous. At ultrasonic frequencies ( $\approx 40$  kHz), it was measured that the finger behaves as a mass of  $\approx 0.1$  g in parallel with a damper of  $\approx 20$  N.s/m [17], so the maximum displacement of the skin depends on the velocity of deformation [24]. This is true also at the scale of the ridges. At the speed of interaction for certain fine textures, the ridges can become very stiff. This effect is even more relevant at ultrasonic vibration. Additionally, it was found that in terms of strain the skin has a non-negligible hysteresis [24].

More detailed models [25] propose to represent every layer of the skin with an independent second order mass-spring-damper model. Such representation may be useful in analyzing the details of stimuli propagation through the skin, although they present the difficulty of introducing a larger number of unknowns.

The mechanical impedance is defined as the capacity to counter a given motion. This quantity, noted ' $Z$ ' helps quantifying the energy consumption and phase shift produced by creating a particular motion on a particular body. ' $Z$ ' can be represented in such a way as to separate its active and reactive components. Such a representation has proven useful for a large variety of applications in haptics and

biomechanics, e.g. [26]–[28] , including recent works in surface haptics [17], [29], [30]. This notion is further analyzed in Chapters 3 and 5.

### 1.1.3. Contact and conformation

When the hand comes in contact with an object, it changes its configuration to copy the shape of the object and create a large contact surface [1], as illustrated in Figure 2. The skin needs about 30-60 seconds to fully complete this process [31]. The mechanics of this contact are complex. The contact area evolves non-linearly in function of time and perspiration, so it is a challenge to produce accurate models [8], [31], [32]. Figure 3, for example, presents the image of a finger in contact with a surface during dynamic sliding at different velocities.

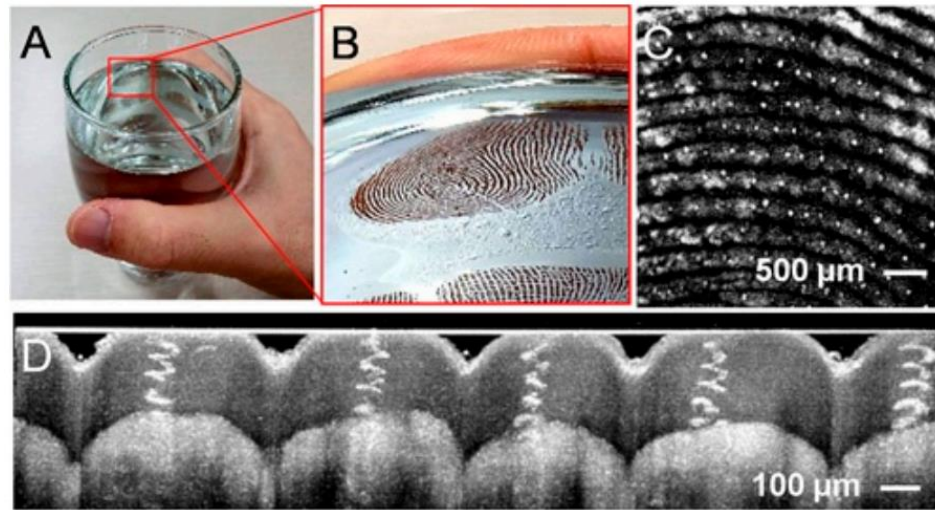


Figure 2. (A–B) Optical images of a finger pad compressed against smooth glass. (B) detail of the fingerprint ridges against the glass (D) Image of a fingerprint showing helical sweat ducts [11]

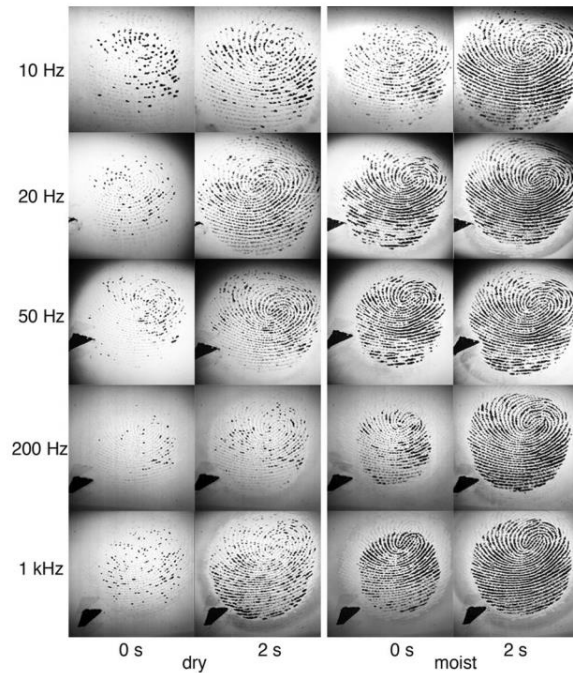


Figure 3. Real contact imaging as a function of tangential loading rate, contact duration, and skin hydration [32]

Additionally, very significant strains can be produced even by very small objects [33], creating contact loss or discontinuity in comparatively large areas of the fingertip. One example is described in [34], where a small hard sphere of about 1-2 mm diameter creates a remarkably large indentation on the glabrous skin of the fingertip, of about 6mm diameter, as can be seen in Figure 4.

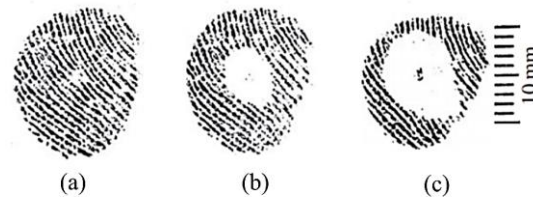


Figure 4. (a) Optical Human fingerprint imaged with the technique described in [33]. (b) Same fingerprint with a 1 mm cylindrical punch indenting the skin by 1 mm. The deformation extends to a 6 mm region as evidenced by the loss of contact with the imaging surface. (c) The region of deformation with an indentation of 2 mm grows to almost 10 mm.

Upon contact, frictional forces develop between the surface of the skin and the object. These frictional forces are crucial in the creation of static grip and sliding contacts [13], [35] and the perception of the object's properties such as material and texture [36]. A more detailed analysis of the contact mechanics and its ensuing frictional response is presented in Chapter 3.

#### *1.1.4. Touch exploratory procedures*

Starting from the hypothesis that a touch exploration is dedicated to the search of privileged haptic information, it has been shown that there are invariants in the procedure used by the human to obtain this information [37], [38]. Four main exploratory procedures have been found for surface touch, these are lateral rub for texture, normal contact for hardness, static contact for temperature and contour tracking for global and exact shape.

Certain procedures are particularly specialized, such as normal contact and lateral rub, since they only sense one property at a time. Others are more global and allow finding two or more properties at the time. This is the case of static contact, for example, which is appropriate for finding temperature, and in a lesser measure, shape. These procedures typically unfold in two stages [37], [38]. First, non-specialized procedures that involve the whole hand are performed. Then, specialized procedures appear (lateral rub and normal contact).

#### *1.1.5. Mechanical response of the finger and hand during lateral rub*

The skin is a distributed sensory medium whose infinitely coupled degrees of freedom are excited in complex ways during tactile interactions [39].

We often think of tactile sensing as a phenomenon which occurs exclusively over a region of the skin that is in close contact with the touched object. Nonetheless, it turns out that active touch can excite non-local, texture-specific sensations and mechanical response on the skin that propagates through the body [40], [41], [42].



Even a much localized input can create vibrations on the finger that cover a large area and propagate along the different tissues of the hand, wrist and arm [43]. In [39], for example, the authors used full-field optical vibrometry to show that vibrations introduced at the fingertip elicit waves in the finger that propagate proximally toward the hand. It was also shown that these waves travel distances that decrease rapidly with frequency.

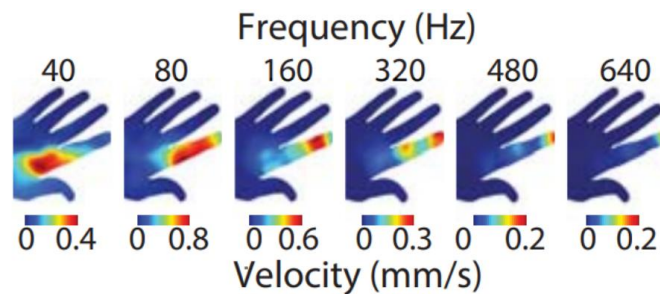


Figure 5. RMS velocity of skin oscillations illustrates the frequency-dependent spatial extent of the wave fields elicited in the skin (shown here for one subject). Low frequencies stimuli excited waves that extended farther in the finger [39].

Both, texture-elicited vibrations and their corresponding sensory responses are highly dependent on exploratory kinematics, such as scanning speed [42]. Nevertheless, even if the movements of the counter-surface are commanded precisely and the digit is immobilized (e.g. a static finger over a moving base containing the haptic surface), the propagation of this vibration cannot be precisely controlled, owing to complex visco-elastic tissue mechanics [34].

## 1.2. Neurophysiology of touch

The human somatosensory system is the system that subserves our sense of touch. Its main purpose is to inform the brain of the mechanical state of the body [1]. In contrast with other senses, this system is not localized on a specific part of our body, but spread throughout, in a complex array of different biological receptors, called ‘mechanoreceptors’.

Touch involves two main modalities: tactile and kinesthetic sensitivities. Tactile sensitivity intervenes in situations of identification or discrimination (the size and shape of objects) and to evaluate phenomena on a small scale (the texture of objects, or their motion in contact with the skin) [44]. The kinesthetic sensitivity or proprioception is a deep sensitivity and refers to a feeling of physical phenomena occurring inside the body, reaching muscles, tendons and bones. It intervenes during the tasks of lifting, large-scale manipulation, and to perceive the position and the movements of the members of the body [44]. To these two main sensitivities must be added the ‘nociception’ for the perception of pain and the thermoception for the perception of temperature. These two modalities must be treated separately because of the high sensitivity of the neurons involved [45] (more selective bandwidth) although there are possible interactions with other subsystems. Surface haptic devices deal mainly with the first modality: tactile sensitivity.

### *1.2.1. Sensory organs and systems*

#### 1.2.1.1. KINESTHETIC TOUCH : MUSCLES, TENDONS AND JOINTS

Skeletal muscles are in great majority organized in agonist– antagonist systems [3]. This means that muscle groups accelerate or prevent movement by contracting and relaxing in alternation and pulling on each other, stiffening the entire biomechanical system [1]. Muscles are connected to the skeleton by tendons which have mechanoreceptors called the Golgi organs [1]. These mechanoreceptors respond to the stress to which they are subjected and report it to the central nervous system, which is thus informed of the effort applied by the muscles needed to reach a static or dynamic equilibrium [1]. The joints include mechanoreceptors as well. They are located in the joint capsule (a type of sleeve made of a dense network of connective tissues wrapping around a joint). These receptors, called Ruffini corpuscles (detailed in section 1.2.1.2), respond to the deformation of the

capsule and appear to play a key role when the joint approaches the end of its useful motion range [46].

#### 1.2.1.2. TACTILE TOUCH: MECHANORECEPTORS IN THE SKIN

The entire surface of the body is covered with skin. Three main types of skin can be distinguished, having very different attributes and functions. These types of skin are mucosal (covers the ‘internal’ surfaces of the body and is in general humid), glabrous (devoid of hair, is the type of skin covering the volar region), and non-glabrous (hairy skin, covering most of the body) [1].

The mechanical displacement of the skin tissues provided by the contact with an external object is sensed by the mechanoreceptors located inside the skin, and transmitted to the brain as spiking electrical potentials through the central nervous system. The mechanoreceptors are very dense on the fingers and palms. As an example, there are about 2000 receptors on one fingertip alone [47].

Four different classes of skin mechanoreceptors are identified [48], [49]. These are the Meissner cells, Merkel cells, Pacinian corpuscles and Ruffini endings. The two first mechanoreceptors are located in the juncture between the epidermis and the dermis, and the other two in the dermis and hypodermis, respectively. These four types of mechanoreceptors, illustrated in Figure 6, are normally grouped in function of the time the receptor takes to respond to a given stimulus, and by the size of their receptive field.

Based on their response time, ranging from a few milliseconds to several seconds, two groups of mechanoreceptors are distinguished: slow adapting (SA) and rapidly/fast adapting (FA). The receptive field is also divided in two main categories, I, for fine receptive fields with detailed limits, and II for larger receptive fields with less detailed borders. A summary of the different mechanoreceptors and their functions is detailed in Table 1 and represented in Figure 6.

Table 1. Generalities of skin mechano-receptors [44], [49]

Mechano-receptor	Adaptation	Receptive fields	Main functions
Meissner Corpuscles	FA I	3-5 millimeters, well delimited	Grip, minimal skin indentations, surface motion and slow vibration
Merkel Disks	SA I	2-3 millimeters, well delimited	Discrimination of shapes (curvature, borders) and coarse textures.
Pacini Corpuscles	FA II	Can cover an entire finger or half the palm. Not well delimited	Discrimination of mobile stimuli, rapid vibrations (200 Hz).
Ruffini Corpuscles	SA II	Can cover an entire finger. Not well delimited	Sensitive to skin persistent stretch produced by finger and body parts (such as joints) motion.

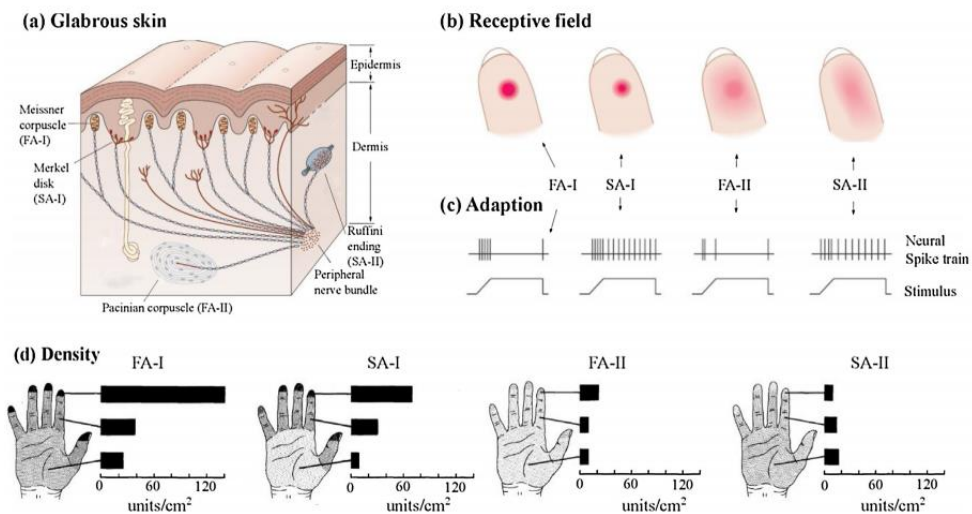


Figure 6. Volar region mechanoreceptors. (a) A cross section of the glabrous skin. (b) The receptive field of each type of mechanoreceptors. (c) The Spike trains of each type of mechanoreceptors in response to a specific stimulus. (d) The density of each type of mechanoreceptors [50].

The Meissner corpuscle (FA I), which innervates the skin densely (about 150 per  $\text{cm}^2$  at the fingertip [49]), plays a fundamental role in touch. In the glabrous skin, it

is located in the superficial regions of the dermis (but connected to the epidermis via a dense network of connective fibers [1]). It is insensitive to static skin deformation, but four times more sensitive to dynamic skin deformation than the SA I [48], [51]. Meissner corpuscles respond to stimuli over their entire receptive field (3-5 mm in diameter), thus producing a poor spatial detail. Of the four afferent types, these are the most effective signaling sudden forces that act on objects, making them essential for the grip function and to manipulate objects with delicacy. It can be said that the main function of the Meissner corpuscles is to signal transient local skin motion. They are insensitive to static force and very low-frequency vibration. If they were not, the response to forces required to grip an object would mask the small signals produced by local microslip [49].

Merkel disks (SA I), also present in large numbers in the fingertip (about 100 per  $\text{cm}^2$  at [49]), have tree-like ramifications (neurite complex) that terminates on 25 – 75 individual receptors. According to [49], they are sensitive to sustained indentation with a slowly adapting discharge that is linearly dependent to indentation depth (from very small indentations of at least 150  $\mu\text{m}$ ). They are very sensitive to points, edges and curvature and have a very high spatial resolution (0.5 mm, which is much smaller than their receptive field of 2-3 mm). Their response to stimulus is independent to the force applied and their spatial resolution is minimally affected by scanning velocities (up to about 80 mm/s). It is at least ten times more sensitive to static than to dynamic stimuli. For these reasons, they are believed to be responsible for form perception [49]. However, according to [1], their functional significance is still unclear. Indeed, there have been a few studies observe that they are responsive to high-frequency vibratory stimulus up to 1500 Hz, like the Pacinian corpuscles [52].

The largest receptor is the Pacini corpuscle (FA II or PC). It is found in the deeper regions of the subcutaneous tissues (several mm) [1]. Its density is moderate, with

approximately 350 per finger and 800 in the palm [49]. Its main tactile function is specific to detecting vibration, responding to 10 nm of motion (applied on the skin) at their maximum sensitivity threshold frequency of about 200 - 250 Hz. Their sensitivity decreases steadily up to about 1000 Hz on the higher frequency threshold and about 10 Hz on the lower [1], corresponding to an intense filtering of about 60 dB/decade [49]. Due to their very high sensitivity, deep location and large receptive fields, Pacinian corpuscles have almost no spatial resolution. They are, however capable of producing a high-fidelity neural image of transient and established vibratory stimuli on the skin, or transmitted to the hand by held objects [49], an important quality to allow ‘embodiment’ of external tools and objects.

The Ruffini corpuscle (SA II) (also present in joints, as explained in 1.2.1.1), has the propensity to associate itself with connective tissues. Recently, it has been suggested that its role in skin-mediated touch is minor, since glabrous skin seems to contain very few of them [1]. Generally speaking, the Ruffini corpuscle is very hard to identify and direct observations are rare [1]. Several studies have shown that these receptors provide mainly kinesthetic and proprioceptive information [1], [49].

Additional slow responding nerve endings are responsible for thermoception. Finally, the nerve endings denominated ‘C fibers’, innervate not only the skin, but also all the inner organs. They are associated with nociception (and tickling) and have a slow response (about 1 m/s). It is doubtful that the information that they provide participates in the conscious perception of objects and surfaces [1].

### *1.2.2. Tactile perception*

Touch sensory abilities on the hands are the most acute at the fingertips. The spatial localization of a point is detectable with a precision of 0,15mm [53] and the spatial resolution between two points is about a millimeter. On a smooth surface, even a texture of 0,06 micron high is detectable [54]. At the vibratory level, the touch

system is sensitive to a maximum frequency of 1 kHz, with an optimum sensitivity at about 200 - 250 Hz, following the threshold dictated by the previously explained mechanoreceptors, as illustrated in Figure 7.

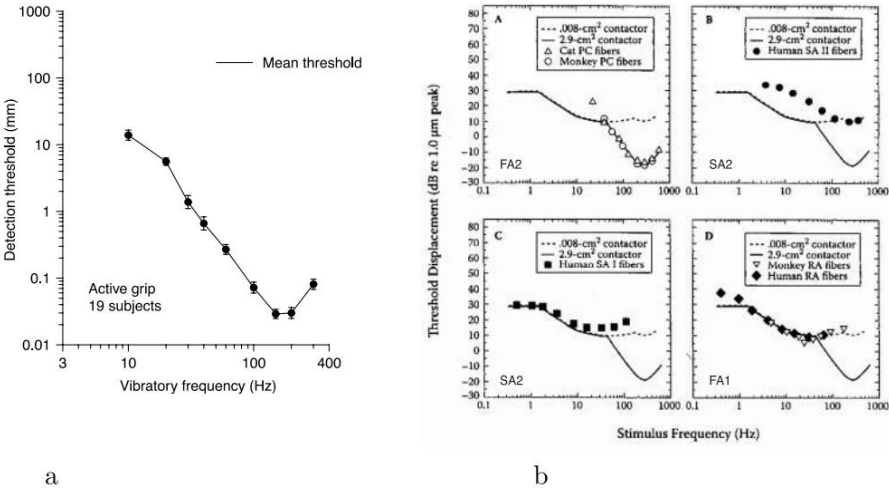


Figure 7. (a) Threshold amplitude detection for vibratory inputs (adapted from [49]). (b) Threshold displacement of the different mechanoreceptors in function of frequency of sinusoidal stimulation (from [55]). [30].

A large amount of research has been dedicated to the study of texture encoding and how it is interpreted by the brain. As explained in 1.1.5, vibration patterns, which are induced on the skin during active exploration are probably at the origin of the tactile sensation.

### 1.2.3. Friction and discriminative touch

Friction is arguably the most important aspect of the haptic function since without it, we could scarcely feel and manipulate objects. Because the finger is a biological, living object, it has properties which often escape our intuition, especially concerning its frictional properties [13].

It was initially believed that the quality of objects was deduced by the human from the perception of the surface topography. However, for ‘smooth’ surfaces (such as glass), it is the friction contrast rather than the topography which is most relevant

in discriminative touch (discriminative touch subserves the perception of pressure, vibration, slip, and texture, all critical in providing haptic information about handled objects and during exploratory procedures [56]). Other cues exist (e.g. temperature), but friction remains key [36].

The quality of the friction function in discriminative touch is linked to the water content of the surface of the finger. Thus, humidity is a fundamental aspect of tactile interaction. This is mostly due to the mechanical characteristics of the sc, given that this part of the skin is mainly composed of keratin, it increments its plasticity and frictional properties in function of the humidity level [11] [14], [15].

### **1.3. Tactile illusions**

As defined in [57], “an illusion is a percept arising from a specific stimulus delivered under specific conditions that gives a different conscious experience when the conditions are changed”. There are many tactile illusions. Some are similar to illusions in other sensing modalities, some are very specific to touch.

Appreciating a sensory illusion requires first-hand experience with the stimulus. While visual and auditory illusions can be rendered using commonly available hardware, haptic illusions are less known and often require dedicated mechanical or electromechanical systems [57]. Nevertheless, they are very interesting for the development of haptic devices, and might also give important insight about the manner by which the brain translates mechanical signals into sensations. They allow to test theoretical models and can have medical applications [57]. For these reasons, it is important to understand the different mechanisms for these tactile illusions: motion of skin, movement of objects, sensations of weight, texture and many more that remain to be discovered. Some texture illusions are related to multimodality of the stimuli, where visual cues may produce pseudo-haptic effects. In [57], a comprehensive list of tactile illusions has been catalogued, excluding, for brevity, the illusions related to awareness of one’s body (such as phantom limb).



These are listed as: object disjunction/conjunction, mislocalization, distance misjudgment, audiotactile interactions (for texture properties such as roughness, crispness, stiffness ...), weight, numerosity, change numbness, temporal ordering, pseudo-haptic effects, shape from distributed cutaneous deformation, geometrical illusions, kinesthetic effects, distal attribution, after-effects and shape effects from force fields.

One illusion, interesting for the application studied in this work, is the texture perception from distributed cutaneous deformation. Under this illusion, perceptual effects that occur when distributed deformation patterns are created on the skin in an orderly and controlled fashion. These skin deformation patterns resemble in some key aspects to those that arise naturally [57], so they can create a robust percept. Surface variations in friction, which is produced by rubbing a finger on surfaces divided into strips made of different materials and/or textures, can create this type of cutaneous deformation. The objective of the haptic devices studied in this work is to be able to create technology that accurately creates and exploits this illusion.

#### **1.4. Overview of haptic technologies**

A haptic interface is a device that allows the user to receive information from a software application or a virtual object through the sense of touch. Because the human interactions with the world are so diverse, so are the haptic technologies that have been historically developed to overtake the task of emulating these interactions. Given this enormous variety, creating an inventory or classification of the different haptic technologies is not a simple task. In [58], the authors propose a classification of the existing haptic devices for virtual reality, based on the ‘paradigm’ or interaction method. According to this work, haptic devices are classified as ‘desktop haptics’ (force feedback for virtual tools), ‘surface haptics’

(hand-screen interaction) and ‘wearable haptics’ (force feedback such as gloves, helmets, shoes, etc).

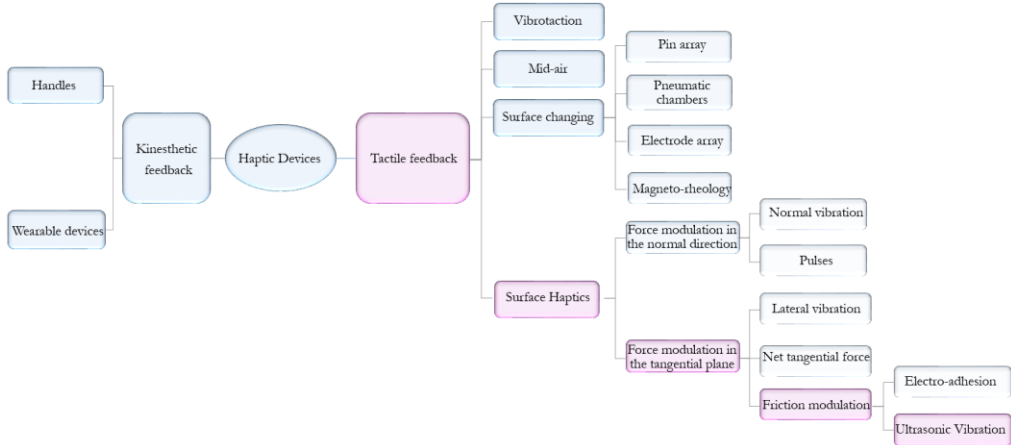


Figure 8. Classification of current haptic devices based on functionality related to the human touch and method used to create haptic response

Later on, [59] adapts this taxonomy, to propose a more global approach to the technological offer, from the point of view of functionality related to the human touch. According to the proposed taxonomy, a first distinction is made between the haptic devices which provide kinesthetic feedback and those which provide tactile feedback (ideally, a realistic simulation would be able to produce both simultaneously. For that purpose, however, different technological devices would be required). The former includes mainly technology providing force feedback and the involvement of muscles, tendons and joints. The second group encompasses the technological solutions which mainly engage the skin mechanoreceptors and tactile sensing.

Finally, a thorough review of surface haptic devices which enable tactile effects on touch surfaces is presented in [60]. This work provides a more detailed classification of surface devices based on their actuation methods and direction of the applied forces (normal or tangential to the tactile surface).

Based on the works by [58]–[60], a surface haptic device taxonomy is proposed in Figure 8 which helps provide a global overview of the existing technologies, with a detailed description of the methodologies employed for tactile feedback using surface haptics. The groups and sub-groups for the case study of this work, i.e. friction modulation surface haptic devices using ultrasonic vibration for tactile feedback, are highlighted in purple in Figure 8.

#### 1.4.1. *Kinesthetic feedback devices*

##### 1.4.1.1. HANDLES

According to the diagram in Figure 8, kinesthetic feedback devices are divided in two large groups (based on [58]). The ‘Desktop’ category proposed in [58] has been replaced by ‘Handles’ in this work, to include non-wearable devices that produce force feedback, which are not necessarily desktop bound.

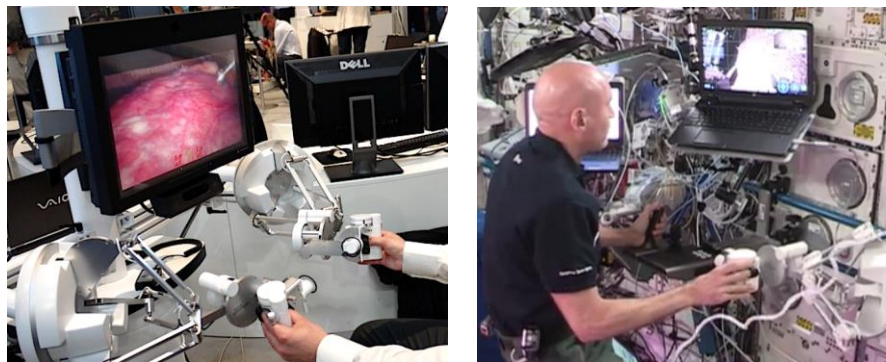


Figure 9. Two examples of applications for kinesthetic feedback ‘handles’. Left: Virtual surgery. Right: maintenance task on airspace equipment [61].

The principle for these ‘handles’ is to allow the user to interact with the virtual environment through a rigid body, that is connected to a mechanism capable of providing motion with two or more degrees of freedom. The handle is meant to represent a virtual tool such as surgical scalpel or a mechanical screwdriver. Two examples are illustrated in Figure 9. A counter-force is transmitted from the handle

to user's hand when the virtual avatar contacts or collides with objects in the virtual environment [58].

Many devices of this type have been developed in recent years, with a significant amount of research directed at developing realistic 6 DoF rendering prototypes and algorithms [62]. Recognized technologies include the Phantom [63] and TouchX series of 3D Systems Inc. [61], the SPIDAR (SPace Interface Device for Artificial Reality) systems [64], the Omega, Sigma, Lambda and Delta series of Force Dimension Inc. [61] (see Figure 9), the Vituose, Scale, Inca and MAT series from Haption [65], Maglev from Butterfly Haptics [66] and the Telerobotics systems developed by Quanser [67], amongst others.

#### 1.4.1.2. FORCE FEEDBACK WEARABLE DEVICES

Wearable devices allow for a greater freedom and larger workspace than most 'handle' devices [68]. Given that these devices are directly worn over and anywhere on the body, their action principle is not limited to kinesthetic feedback. Indeed, wearable haptic technologies can be divided in three categories: force feedback (kinesthetic wearable systems), vibrotactile feedback (included in the Vibrotaction category in Figure 8) and electro-tactile feedback (evoking sensation by passing a current on the skin) [68]. However, the last category has not been fully developed. Common force feedback wearable technologies are mainly of two types: fingertip-mounted and exoskeletons. The complexity, size and weight of fingertip-mounted devices are lower than that of exoskeletons, and they allow providing both tactile and kinesthetic feedbacks. On fingertip-mounted devices, however, only precision grasping can be efficiently simulated, since only the last phalange is reached [68]. One commercial example of these devices is the VRtouch from GotouchVR [69], portrayed in Figure 10.



Figure 10. VRtouch: fingertip mounted device for virtual reality [69]

Haptic gloves are a typical example of exoskeletons, which are widely used in research and in the industry. Different actuation principles can be found in commercial prototypes, although the most common is through a set of wires attached to controlled electric motors. Other types include microfluidic arrays, fiber-enforcement soft actuators and electrostatic attraction amongst others.



Figure 11. A few examples of commercial haptic feedback gloves. In order: CyberGrasp, H-glove, Dexmo, HaptX, Plexus, and VRgluv [58].

There are many examples of commercially available haptic gloves, some of which are illustrated in Figure 11. We can cite: the CyberGrasp from CyberGlove Systems

Inc. [70], the H-glove from Haption [71], Dexmo from DextaRobotics [72], the HaptX glove from HaptX Inc. [73], the Plexus from Plexus Inc. [74], the Sense glove from Senseglove Inc. [75], the Maestro from Contact CI [76], the Senso Glove from Senso Devices Inc. [77], the VR glove by TESLASUIT from VR Electronics Ltd. [78] and the VRgluv from EPFL and ETH Zurich VRgluv [79].

### *1.4.2. Tactile feedback devices*

#### 1.4.2.1. VIBROTACTION

Vibrotactile feedback or mechanical vibration is the most widely used tactile feedback techniques in today's technology [58], given that it can be intuitive, easy to integrate and cost-effective. Many examples can be found in everyday life, such as vibratory notifications in smartphones, console controllers in gaming systems and, as mentioned in 1.4.1, in a wide variety of wearable devices. It is also used, as explained in section 1.5, in different surface haptic technologies.

Vibrotactile rendering seeks to stimulate the tactile perception at the spectrum of maximum cutaneous sensitivity (explained in Figure 7). For doing so, it is necessary to incorporate a vibrotactile actuator. Many technologies of actuators are commercially available. These include: eccentric rotating-mass actuators (ERM), linear resonant actuators (LRA), solenoids, voice coils, audio speakers, rotary electromagnetic actuators or piezoelectric actuators. An example of different actuators used for tactile displays is illustrated in Figure 12. More detailed reviews of the available technology can be found in [80]–[82].

Incorporating the correctly adapted actuator for a specific application in the right location of the device is a primary concern in vibrotactile device design. Important engineering considerations generally include size, shape, cost, availability, robustness, speed of response, input requirements, power consumption, and potential interference with other system components [83].



Figure 12. Sample actuators for vibrotactile displays. S: Five solenoids of varying sizes. VC: A commercial voice coil without bearings. Sp: Two audio speakers. C2: A C2 factor from EAI. Haptuator: A Haptuator from Tactile Labs, Inc. Tactaid: One complete Tactaid from AEC and one opened to show the suspension inside. E: Five shafted/cylindrical eccentric rotating mass motors. P: Three shaftless/pancake eccentric rotating mass motors. A U.S. quarter appears at bottom right for scale [83]

Although mechanical vibration is widely employed, the ability of rendering diversified textures is highly dependent on the quality of the haptic pattern design and the ability of the actuator to reproduce its frequency spectrum, transient and intensity. The complexity of vibrotactile perception and the impedance coupling with the body make it hard to know in advance if the resulting psychophysical response of the implemented prototype is as desired. For this reason, vibrotactile design requires several design iterations including psychophysical tests [83].

#### 1.4.2.2. MID-AIR HAPTICS

Contactless haptic feedback can be achieved using different techniques such as pressurized air jets or air vortex rings. These methods are simple, but have the disadvantage of providing a rough rendering of shape and some lag time. [84]. In contrast, the application of focused ultrasound can provide well-defined tactile feedback including the perception of shapes and borders in three dimensions.

Ultrasonic Mid-Air haptics was first described by Iwamoto in 2008 [85]. It has been commercialized by Ultraleap Ltd [86] since 2013.

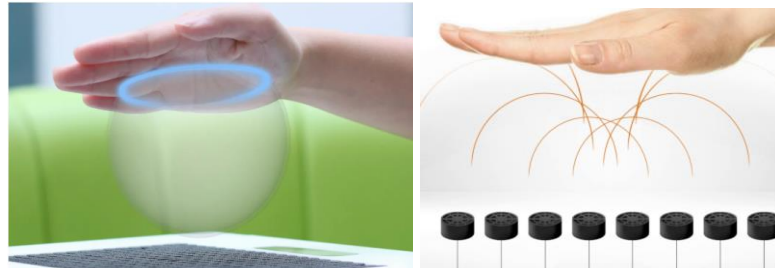


Figure 13. Mid-Air Haptics allows the perception of three-dimensional shapes without contact by directing focused ultrasound to produce shapes on the skin. Left: Example of a sphere simulation [87]. Right: The principle of an ultrasonic phased array. Correctly timed ultrasound waves create acoustic pressure in the focus point [86].

In this technique, a phased array of ultrasonic transducers is used to focus acoustic radiation pressure onto a point in space. The devices used to radiate pressure waves are often called airborne ultrasound tactile displays (AUTD). To create the focalization point, the firing of the transducers needs to be correctly timed and positioned.

When the hand is placed over the focalization point, acoustic radiation force produces small skin deformations. Modulating the focalization point, such that it matches the resonant frequency of the cutaneous mechanoreceptors, causes a perceivable localized tactile sensation [88]. The focal point movement can be controlled fast, and there can be several focal points or shapes [84].

#### 1.4.2.3. SURFACE CHANGING DEVICES

Inspired by Braille display techniques, surface deformation is one of the most intuitive ways to produce tactile sensations. This technique consists in reproducing the tactile properties of an object by simulating its relief. As illustrated in Figure 8, this can be achieved by techniques such as a two-dimensional array composed of pins, air pressured chambers or voice coils, electrode arrays or magneto-rheology.



An example of each of these technologies is illustrated in Figure 14. Amongst the different types of haptic devices, surface changing devices are the ones which allow the most localized tactile stimulation. The resolution of the image or texture, however, is dependent on the density of actuators that can be include in one surface.

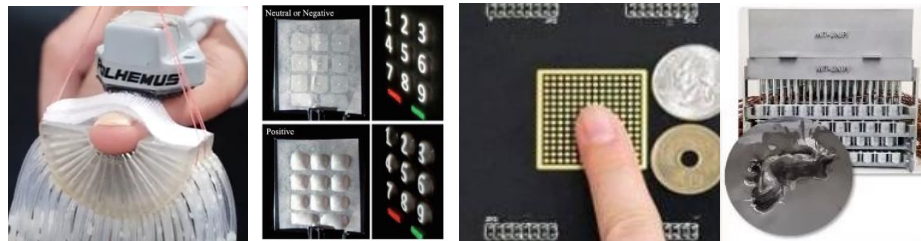


Figure 14. Examples of surface-changing haptic devices. From left to right: Portable pin array [89], Pneumatic chambers [58], electrode arrays [58], magnetorheological fluid [90].

## 1.5. Surface Haptics

This work is focused on surface haptic devices. The goal of surface haptics is to generate tactile effects on touch surfaces such as mobile phones, tablets, information displays, home appliances or inside car' s boards. From the technological point of view, the goal of surface haptics is to display tactile feedback to the users by modulating the interaction forces between the finger and the touched surface [60].

### 1.5.1. Force modulation

As represented in Figure 8, force modulation in surface devices can be done in the 'normal' direction (perpendicular to the surface), or the 'lateral' direction (parallel to the surface). Vibrotaction, as explained in 1.4.2.1, is one of the most widely used technologies in surface haptics. However, more advanced techniques can be used to create more elaborate sensations on the fingertip.

Creating localized stimulation in surface devices is a subject that has attracted the attention of researchers and developers, for applications such as the creation of multi-touch screens or the localized button-click sensation. Normal vibration can be used to create localized sensations on a screen, with the help of piezoelectric actuators. Three main techniques are described in the literature to achieve this target: phase shifted acoustic pulses, time reversal technique and multimodal superposition [59], [91].

Analogously to the technique explained in section 1.4.2.2, the objective of these techniques is to create a focalization point by firing an array of actuators at specific times. In [92], the authors applied the same principle on a solid and transparent surface, actuated via electromagnetic actuators, placed on its periphery.

It is possible to improve the precision of the localized stimulation by using the time reversal technique [93]. To calculate the input from each actuator, the piezoelectric actuators are first used as sensors, to record the mechanical effect of applying a localized force pulse (tapping) on the device. The acoustic wave propagates and reflects on the boundaries. Then, the electrical signals on each transducer are recorded. The time inversion of these electrical signals allows to reproduce the initial deformation at the respective locations.

Finally, multimodal decomposition can be used to create localized sensations. By analogy to a Fourier series decomposition, the desired deformation can be projected onto the orthogonal basis of the structure, in order to obtain the contribution coefficients of each mode, allowing to approximate the initial shape by re-composition of the modes [59].

### *1.5.2. Tangential force modulation using friction variation*

Friction modulation haptic surfaces utilize techniques to achieve friction modulation in order to simulate texture. As explained in previous sections, creating differences in friction affects the forces moving along the finger pad, which influence the nature of the vibrations generated by the relative motion of the skin,

thus creating the sensation of a differentiated texture [13]. For doing so, two techniques are typically used: electro-adhesion [94]–[96] and ultrasonic vibration. These techniques may be utilized together with the same purpose [97], [98].

#### 1.5.2.1. FRICTION MODULATION DEVICES BASED ON ELECTRO-ADHESION

This technique utilizes a conductive plate covered with an insulator and supplied with high voltage, in order to produce a temporal electrical polarization of the finger pad, creating a ‘capacitive’ effect. The resulting attractive force results in an increased friction between the display and the sc. Its working principle is depicted in Figure 15.

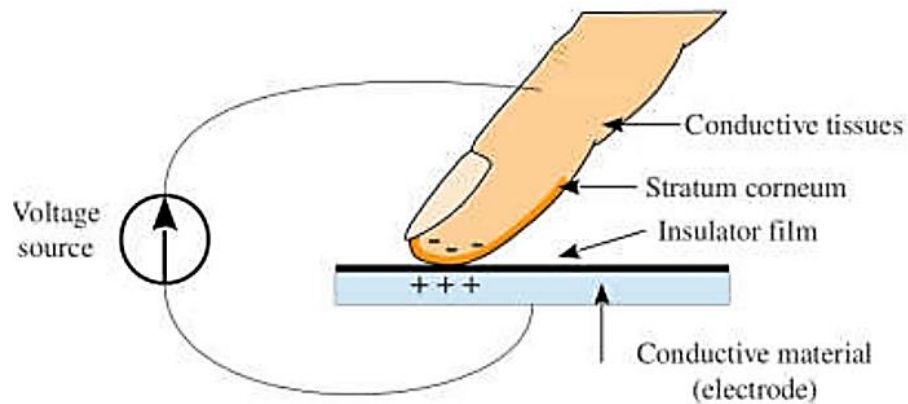


Figure 15. Working principle of electro-adhesion [30]

The principle has been known since the fifties [99], but has gained interest with the recent development of haptic technologies. Different devices have been designed based on electro-vibration. A few examples may be cited, such as TeslaTouch [100], 3D rendering texture by Disney research [101], commercial products such as Tanvas™ [102], and research prototypes such as in [103].

#### 1.5.2.2. ULTRASONIC SURFACE HAPTIC DEVICES (USHD)

To achieve friction modulation, ultrasonic vibration may also be used. An ultrasonic wave is, by definition, a mechanical wave whose frequency is not audible by the human ear. The frequency range of these waves starts from 20 kHz. Like in the case of sound, these mechanical waves propagate on different solid materials such as aluminum or glass. When a surface is submitted to ultrasonic vibration, its friction is reduced. To generate ultrasonic vibration on a touch surface, piezoelectric actuators are typically glued on a plate's surface and actuated by sinusoidal voltage signals at the resonance frequency of the plate.

The first use of ultrasonic vibration on the human finger against a surface is attributed to Watanabe and Fukui [104]. In this experiment, high frequency actuators made a surface vibrate with an amplitude of up to 2  $\mu\text{m}$  with a frequency of a few tens of kilohertz. A sandpaper was attached on the active surface of the device. When this vibration exceeded a frequency of 20 kilohertz, a sensation of softness was perceived on the sandpaper. The authors noted that the effect is increased with increasing vibration amplitude.

Since then, different ultrasonic surface haptic devices have been proposed and developed. Together with the L2EP's StimTac [105] project (see Figure 16), the 'T-Pad' project [106] from Northwestern University was one of the first proposals. This prototype was based on a small circular piezoelectric ceramic. Developing from this idea, the principle was implemented in the TPad Fire<sup>TM</sup> which included an LCD screen. Other examples include the work of Wiertlewski [107], Winter [108], or products such as the XploreTouch<sup>TM</sup> from Hap2U<sup>TM</sup>, which also includes visual-tactile co-simulation.

For many of these devices, the presence of the finger has an influence on the vibration of the plates [109]. This influence may affect the perception of friction

modulation from one user to another. For this reason, a closed-loop control of the vibration amplitude was introduced, and implemented. This closed-loop control implementation is thoroughly explained in [110].



Figure 16. Evolution of the Stimtac prototype: 1D configuration, 2D feedback, 2D input and feedback (2008), compact USB prototype (2010) [30] and transparent prototype (2015) [111].

Even though the phenomenon of friction reduction with ultrasonic vibration has been thoroughly explored for several ‘out of plane’ vibration modes (including transverse mode vibration [25], [38], [97], [104], [112]–[118], travelling waves [119], surface acoustic waves [120], [121] and transverse combined with longitudinal vibration modes [122], [123]), the effect and parametric dependence of the interaction mechanism through which friction is reduced with purely lateral vibration is seldom explored, thus perhaps underestimated or even neglected. We may cite a few studies about that: in [124], a combination of electro-adhesion and lateral vibration is studied for a haptic device. In [35], the authors propose a simplified finger model in order to explore the effects of this lateral motion on the grip function.

## 1.6. The principle of active lubrication with USHD

As explained in previous sections, submitting a volume to ultrasonic vibration causes a reduction of its surface’s friction. This ‘active lubrication’ effect has been widely studied for transverse vibration. Nonetheless, the actual interaction between the fingertip and the vibrating surface at ultrasonic frequencies is not yet completely

clear. There is, therefore, not a definitive explanation for the friction reduction effect that occurs from this interaction. Two theories are offered in the literature as an explanation. These are the squeeze-film [38], [112], [125]–[127] and the intermittent contact theories [25], [114], [115] (see Appendix 1 for more detail).

#### *1.6.1. Squeeze-film*

The principle behind this theory relies on the generation of a thin film of air in the contact region between the plate and the finger pad by the high speed compression-decompression cycle of the air. In [128]–[130], the authors characterize this phenomenon between a vibrating plate and a free one. With a finger pad, the film of air induced due to the ultrasonic vibration creates an acoustic levitation of the skin, thus reducing the friction between the finger and the plate. The solution proposed by [44] is recalled in Appendix 1.

#### *1.6.2. Intermittent contact*

The squeeze film theory is one of the most widely accepted hypothesis to explain the active lubrication effect. However, as it has been observed in [113], the measured friction reduction between a finger pad and a flat surface subjected to ultrasonic vibration does not behave as predicted by the squeeze film effect only. For this reason, an alternative explanation is produced, which correlates with experimentally observed data. The ‘intermittent contact’ theory proposes an interaction mechanism in which, at certain vibration amplitudes, a regime is established where the finger loses and regains periodically contact with the vibrating plate, thus effectively reducing the amount of lateral force employed to slide over its surface. The proposed mechanism emphasizes the dependence of this effect on the vibration amplitude and frequency, and on certain finger parameters. Indeed, in addition to the vibration of the plate, the mechanical properties of the skin are a determinant factor when calculating the amount of friction modulation

[116]–[118], [131]. It is possible to calculate the friction force based on this theory, by proposing a model for the lateral impedance of the finger. A simplified solution, assuming that the dynamic friction of the finger is Coulombic, is proposed in [115].

### *1.6.3. Combined effect for friction reduction for transverse wave ultrasonic vibration*

A few studies[132] have observed that both intermittent contact and squeeze film effects contributed to active lubrication with transverse vibration. However, it is not yet clear to what extent each mechanism participates on this effect, because of the complexity of isolating the contribution of one and the other under atmospheric pressure conditions.

In [133], it has been observed that the contact oscillates with the plate, out of phase by an angle dependent on the coefficient of the finger damping. Furthermore, the amplitude of the finger oscillation decreases as the amplitude of the plate oscillation increases [127]. The combination of these observations suggests that the intermittent contact of the skin is not directly on the glass plate but on the air film that composes the squeeze-film.

## **1.7. EMR applied to ‘human-in-the-Loop’ systems**

### *1.7.1. Energetic Macroscopic representation (EMR)*

EMR is a graphical formalism for the synthetic representation of multidisciplinary energy systems [134], which has been developed at the L2EP laboratory in the University of Lille, France. It has been used since the year 2000 to analyze and study many different applications. The EMR is a functional description of an energy system. It respects the action and reaction principle as well as the integral causality of the studied system, which makes it possible to deduce a control

structure in a systematic way. More information on EMR and its elements is provided in Appendix 2 and the EMR website [135].

### 1.7.2. *Energetic Macroscopic representation (EMR) for 'Hardware-in-the-Loop' (HiL) analysis*

The properties of this formalism make it particularly helpful when performing real time analysis and simulations such as 'Hardware-in-the-loop' (HiL)[136] [137]. Indeed, EMR has already been used successfully to organize HiL simulations [138]. HiL helps developers test different designs of systems in real life conditions before manufacturing and building costly prototypes. This involves replacing the power system with models in order to define and tune the control algorithm. Hardware-in-the-loop simulation is used for validation tests of real-time embedded systems before implementation on actual processes. In this technique, simulation software is used to check the performance of the system and its control. The process model and the control are both studied in the same simulation environment. The actual process is then replaced by a process model or an equivalent hardware [139]. The simulation environment and the hardware are connected through an interface. Strict requirements are imposed to this interface in order to successfully carry out the testing. It needs to be "as transparent as possible", that is: correctly interpret and transform the energy information and dimensions, be able to respond with real time constraints, and respect dynamic interactions, i.e. the causality effect.

Such a methodology has been used in aeronautics for a long time [140]. Even though a lot of HiL simulations are dedicated to assess controller boards e.g. [141], traction applications are nowadays more and more developed using this methodology before the final implementation [142]–[144]. Sustainable transportation applications are largely assessed at the L2EP [138], [145]. HiL simulations of wind energy conversion system have also been developed [146].



A parallel between the methods explained in the HiL bibliography and the interaction with human systems may be imagined. For this reason, a similar logic is applied in the ‘human-in-the-loop’ analysis. Moreover, given that EMR has proven useful to represent such complex interface dynamics, it is also considered to be a valid tool to develop this concept.

### *1.7.3. ‘Human-in-the-loop systems’ (hiL)*

Human-in-the-loop systems (hereby referred to as hiL) are composed of two main categories of sub-systems: technical systems (which may be engineered, designed and controlled), and biological systems (the human, which cannot be engineered and is difficult to model and measure). These two kinds of systems differ from their nature: their fundamental organization, complexity and behavior. Thus, hiL analysis deals with the difficulty of coupling and integrating these two in a behaviorally coherent way [147]. Human modelling may be understood as a scientific way to consider a person’s characteristics and their coupling with their environment. This task needs an approach that enables to question the representativeness and validity of used models and related concepts. Thus, a new conceptual framework that questions the nature of the interaction between the human and technology as an integrated biological, anatomical, and physiological process, has to be developed [148].

Equivalently to HiL systems, the interface used to integrate the human and the technological elements in the system must seem as transparent as possible to the subject’s perception. This interface is, therefore, subject to strict time and safety constraints. For example, any control architecture hypothesized for human sensory control must accommodate the delays in feedback signals in order to fit the natural neurological responses.

#### *1.7.4. Human-in-the-loop' concept applied to surface haptics*

Research on haptics has repeatedly led to pose the question of human modelling [26], [116], [118], [149], interaction analysis [35], [38], [108], [112], [115], [127], perception [150], [151], and the integration of these two elements into the system control [152]–[154]. In surface haptics, this may be interesting for purposes of tactile sensation rendering standardization or equalization [155].

An approach to developing this analysis from an 'hiL' approach has been performed during the PhD. Thesis of T. Zheng [156] at the L2EP, and serves as a precedent for the current work. In this thesis, the EMR formalism applied to the hiL approach, helped to understand the coupling of the kinesthetic and tactile feedbacks performed at the level of the interface as well as at the human perception level.

### **1.8. Summary**

In this chapter, we summarized the main aspects of the contact between the finger and a surface during tactile exploration. Based on these considerations, the importance of friction modulation for the creation of tactile illusions is explained. A state of the art of the different haptic devices has been presented, with an emphasis on ultrasonic surface haptic devices for friction modulation.

The principle of friction modulation using transverse vibration, through a combination of the squeeze film and intermittent contact effects, is explained.

Finally, the concept of human-in-the-loop for surface haptics is introduced, including previous research on this subject. For that aim, an analytical tool, EMR, is presented as a means to perform future analysis on this subject.

## *Chapter 2*

### DESIGN AND CONTROL OF ULTRASONIC SURFACE HAPTIC DEVICES FOR LONGITUDINAL AND TRANSVERSE MODE VIBRATION

Surface haptic devices for texture discrimination utilize techniques to achieve friction modulation, since differences in friction may create different texture perceptions [13]. For doing so, ultrasonic vibration may be used. In this technique, a solid volume, which will serve as the haptic interface, is made to vibrate at ultrasonic frequencies using piezoelectric ceramics as actuators. The amount of friction reduction is dependent primarily on the speed of vibration. Achieving friction attenuation using vibrations in the low frequency ultrasound spectrum (LFU: from 20 to about 100 kHz) requires the vibration amplitude of the structure to achieve a few micrometers or more. In order to optimize the amount of actuators and energy necessary to achieve such displacement on a complete structure, the volume is generally excited at its resonance frequency.

There are several ways in which the material could be deformed, so different types of vibration are possible. In this work, we distinguish two types: the term "transverse vibration" is used to denote the deformation due to flexural strains, which produce an "out-of-plane" vibration. On the other hand, the term "longitudinal vibration" is used to denominate the deformation due to extension-compression strains, which produce an 'in-plane' vibration. In order to validate the potential of longitudinal vibration in the creation of friction-based surface haptic devices and to provide some design clues to future developers, we propose a comparative study of the performance of longitudinal vs. transverse vibration in ultrasonic surface haptic devices (USHD).

The objective of this chapter is to detail the design and creation of a USHD capable of producing both types of vibration at very close frequencies. Producing both modes on the same device helps creating a ‘fairer’ tribological and energetic comparison basis for the two modes, eliminating some bias since the material, geometry, the amount and placement of piezoelectric ceramics and the voltage source are the same. Equally, the selected resonance frequency has an energetic and tribological effect on the performance of the USHD. Accordingly, specifying ‘close’ resonance frequencies is essential in having a comparison of these two technological alternatives.

The methodology followed for the design and control of this device is equally applicable for producing any USHD, with the advantage of including amplitude closed-loop control. Firstly, in section 2.1, a pre-design and specifications phase is explained. In this first step, the objectives and constraints of the design are laid-out. An initial outline of the geometry of the device and placement of the piezoelectric ceramics is proposed, taking into account factors such as practicality, ergonomics, ease of implementation (including avoiding common difficulties such as crosstalk interference of the actuators and sensors), energetic performance and resonance frequency constraints. Once this first step is completed, the dimensions of the device which follow the pre-defined specifications are found analytically in section 2.2, using the principles of vibrational mechanics. A finite element simulation of the resulting structure helps confirming and refining the analytical design results. It also helps to provide information of the additional expected vibrational modes around the resonance of the desired operating ones, and provide clues on how to avoid them. Following the finite element simulation, the resulting design is implemented for testing. A laser cartography determined whether the desired specifications are achieved.

In order to accurately modulate the friction reduction with the implemented device, the vibration amplitude must be controlled. For doing so, it is necessary to find a model which serves to explain the dynamic behaviour of the structure. This

dynamic behaviour, which is found in 2.3, is typically governed by spatio-temporal partially differential equations, which produce models that are unsuitably complex for dynamic analysis and control. Modal analysis, on the other hand, can be used to decouple the spatio-temporal problem into two sub-problems and treat them independently [91] : the modal analysis and the modal projection. Analogously to a Taylor series, the modal decomposition allows expressing any given material deformation, as the addition of a number of time-based differential equations, each representing one of the modes of the plate that has specific amplitude, dynamic parameters, frequency and a unique deformation shape [157]. Using modal projection, each selected mode can be characterized as a second-order spring-mass-damper lumped parameter system. As a consequence, a simple electromechanical transformation serves to represent dynamically the effect of the piezoelectric actuators.

The modal parameters, as well as the electromechanical transformation factor for the selected modes are experimentally identified by measuring the structure's response to a specific excitation. Finally, in section 2.4, a simplified control scheme as in [110] proposes to work in a virtual rotating reference frame, which can be performed by modulation-demodulation techniques.

## **2.1 Pre-design specifications**

Our objective is to design a USHD to evaluate the performance of longitudinal vibration compared to transverse vibration modes. In order to perform an accurate comparison of the two modes, we defined a set of design specifications. The first requirement for the device was to excite both modes independently at close vibration frequencies, without any mutual interference. Secondly, it was required that the motion source (electrical supply + actuators) of both modes be the same. Moreover, as a previous study [158] provided preliminary comparison results for vibration frequencies around 30 kHz, we decided to work at a higher frequency to extend the comparison range. The resonance frequency of 60 kHz was chosen,

expecting an improvement in friction reduction performance of the devices [114]. Finally, the device was required to allow a clean flat exploration length of over 3 cm to allow tribological and psychophysical measurements. Finally, the wavelength of each mode was meant to allow a ‘uniform’ exploration along the desired surface. This means for the longitudinal mode, that half a wavelength should be larger than the exploration surface, and for the transverse mode that half a wavelength should be smaller than 1 cm, a dimension which allows a good homogeneity at the perceptual level [159].

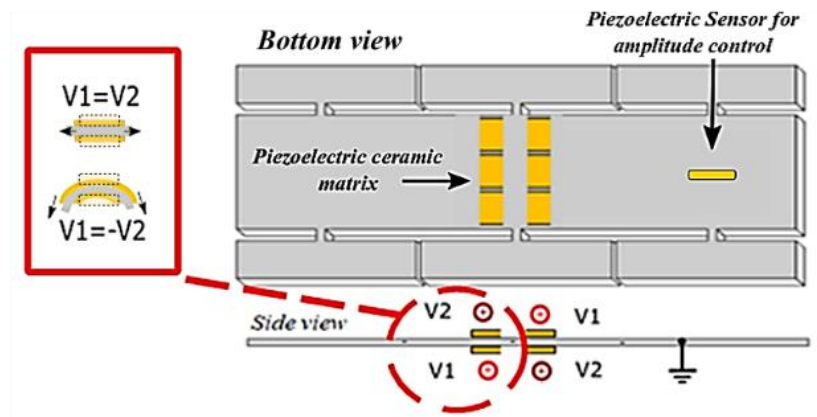


Figure 17. Top and side view of the plate design and setup to perform mode comparison on the same surface haptic device. The design includes 12 piezoelectric ceramics as source of motion and one as sensor for both modes.

The final designed structure is illustrated in Figure 17. The structure consists of an aluminum plate with a matrix of 12 piezoelectric ceramics (6 on each side) glued to the center of the device on the top and bottom sides, and a separate one glued on the bottom surface to serve as motion sensor. The resonator (aluminum plate) is attached to an immobile aluminum section through a series of isthmuses situated approximately at the vibrational nodes of both modes. A damp-proof polymeric sheet is glued to the aluminum beam on both sides of the actuator matrix on the top facet of the device.

To excite each mode selectively, the matrix of piezoelectric ceramics is placed and connected to follow the same basic principles as proposed in [158]; the deformation induced on the plate is the result of opposite surface tensions induced in both sides of the plate by the piezoelectric ceramics.

The ‘top’ and ‘bottom’ side actuators are connected to two independent voltage sources ( $V_1$  and  $V_2$  on Figure 17), with the common ground connected to the conductive plate. The ceramics bend creating a surface stress on the aluminum plate. When  $V_1 = V_2$ , an extension is produced simultaneously on both sides of the aluminum plate, leading to the longitudinal mode. When  $V_1 = -V_2$ , one surface is stretched, while the other compressed, ‘bending’ the material, thus producing the transverse mode.

The geometry and placement of the motor ceramics were designed to obtain a symmetrical deformation for both modes with respect to the center of the plate. Additionally, we sought to minimize the ceramics’ interference with the plate’s deformation. For the transverse modes, for example, this meant that the length of the ceramics should be shorter than half a waveform length of the mode. It was, however, not sought to optimize the coupling of the ceramic placement and the mode deformation, as it would be hard to comply for both modes at the same time. A sensing ceramic was necessary to perform wave amplitude closed-loop control. The placement and geometry of the sensing ceramic were designed specifically to maximize the sensitivity to the deformation of both modes, with a single sensor, while minimizing the interference with the deformation of the mode, as recommended in [160]. In practical terms, this meant that the sensing ceramic was required to be ‘small’ and placed simultaneously along a maximum of vibration for the transverse mode and on a vibrational node for the longitudinal mode. Moreover, in order to avoid sensing errors due to crosstalk interference, it was recommended to place the sensing ceramic away from the actuators.

## 2.2 Plate dimensioning and implementation

In order to follow the established specifications, we proposed an analytical approach to the plate's dimensioning, based on a simplified mechanical model of vibration in solid bodies. Thanks to this analysis, we were able to find an expression for the resonance frequency of both modes in terms of the plate's dimensions. The dimensions which helped minimizing the difference between the resonance frequencies of the two modes were calculated. The final design was chosen in function of the wavelength of the modes which could be produced around 60 kHz. A finite element analysis was then performed on the resulting geometry, to verify and deduce the final design. Following the finite element simulation, the resulting prototype is implemented for testing. A laser cartography helped to determine whether the desired specifications were achieved.

### 2.2.1. Euler-Bernoulli approximation

To find an analytical expression for the resonance frequency of each mode (longitudinal and transverse) in function of the plate's dimensions, we considered that it was possible to approximate the behavior of the proposed structure of the resonator (Figure 18) to that of a uniform solid beam. Given that we planned to work around 60 kHz, it was possible to perform this analysis using the Euler-Bernoulli beam approximation [161], [162].

Following this model, on the  $x, y, z$  space, we consider a parallelepipedic elastic body, continuous and isotropic, cut in a rectilinear shape, with dimensions  $L, b, h$ , for length, width and height, as illustrated in Figure 18. This volume  $\Omega = bhL$  has a transverse surface  $S = bh$ , with  $L \gg b$  and  $L \gg h$ . The mechanical properties of Young Modulus, quadratic momentum and volumetric density of the material, are represented by  $E_e, I$  and  $\rho$  respectively. Under external forces, the beam changes shape. Due to this deformation, the particles in the beam are displaced. We define  $\chi$  as the longitudinal displacement and  $\psi$  as the transverse displacement.



According to the Euler-Bernoulli theorem, the displacement field in the  $zx$  plane,  $\mathcal{U}$  can be expressed as (1). [162] The kinetic and potential energies  $\boldsymbol{\kappa}$  and  $\boldsymbol{\nu}$  can be expressed as (2) and (3) respectively. The origin is placed at the middle of the structure. The mid-plane is represented in gray in Figure 18.

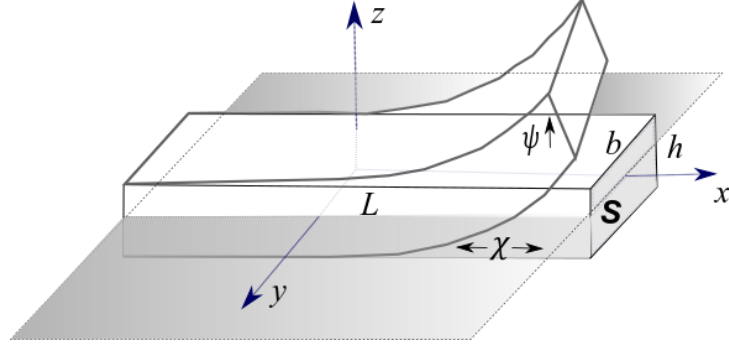


Figure 18. Euler-Bernoulli beam.  $\chi$  and  $\psi$  are the out and in plane displacements with respect to the mid-plane (in gray).

$$\mathcal{U} = \begin{bmatrix} \chi - z \frac{\partial \psi}{\partial x} \\ \psi \end{bmatrix} \quad (1)$$

$$\boldsymbol{\kappa} = \frac{1}{2} \int_{\Omega} \left[ \rho \left( \frac{d\chi}{dt} - z \frac{d}{dt} \left( \frac{\partial \psi}{\partial x} \right) \right)^2 + \rho \left( \frac{d\psi}{dt} \right)^2 \right] d\Omega \quad (2)$$

$$\boldsymbol{\nu} = \frac{1}{2} \int_{\Omega} E_e \left( \frac{\partial \chi}{\partial x} - z \frac{\partial^2 \psi}{\partial x^2} \right)^2 d\Omega \quad (3)$$

We can write (2) and (3) as (4) and (5).

$$\begin{aligned} \boldsymbol{\kappa} = \frac{1}{2} \int_{-L/2}^{L/2} \int_{-b/2}^{b/2} \int_{-h/2}^{h/2} & \left[ \rho \left( \frac{d\chi}{dt} \right)^2 - 2\rho z \frac{d\chi}{dt} \left( \frac{d}{dt} \left( \frac{\partial \psi}{\partial x} \right) \right) + \rho z^2 \left( \frac{d}{dt} \left( \frac{\partial \psi}{\partial x} \right) \right)^2 \right. \\ & \left. + \rho \left( \frac{d\psi}{dt} \right)^2 \right] dx dy dz \end{aligned} \quad (4)$$

$$\mathbf{v} = \frac{1}{2} \int_{-L/2}^{L/2} \int_{-b/2}^{b/2} \int_{-h/2}^{h/2} \left[ E_e \left( \frac{\partial \chi}{\partial x} \right)^2 - 2E_e z \frac{\partial^2 \psi}{\partial x^2} \left( \frac{\partial \chi}{\partial x} \right) + E_e z^2 \left( \frac{\partial^2 \psi}{\partial x^2} \right)^2 \right] dx dy dz \quad (5)$$

Since  $\int_{-h/2}^{h/2} z dz = 0$  and defining surface  $S = \int_{-b/2}^{b/2} \int_{-h/2}^{h/2} dy dz$ , and rotational inertia  $J = \rho I = \rho \int_{-b/2}^{b/2} \int_{-h/2}^{h/2} z^2 dy dz = \rho S \left[ \frac{z^3}{3} \right]_{-h/2}^{h/2}$ , we can conclude that  $\rho I = \rho S \frac{h^3}{12}$ . If we use these definitions to integrate (4) and (5) with respect to  $y$  and  $z$ , we obtain (6) and (7).

$$\boldsymbol{\kappa} = \frac{1}{2} \int_{-L/2}^{L/2} \left[ \rho S \left( \frac{d\chi}{dt} \right)^2 + \rho I \left( \frac{d}{dt} \left( \frac{\partial \psi}{\partial x} \right) \right)^2 + \rho S \left( \frac{d\psi}{dt} \right)^2 \right] dx \quad (6)$$

$$\mathbf{v} = \frac{1}{2} \int_{-L/2}^{L/2} \left[ E_e S \left( \frac{\partial \chi}{\partial x} \right)^2 + E_e I \left( \frac{\partial^2 \psi}{\partial x^2} \right)^2 \right] dx \quad (7)$$

With these kinetic and potential energy definitions, we may define the Lagrangian, as a function of velocities and displacement fields as  $\mathcal{L} = \boldsymbol{\kappa} - \mathbf{v}$ . We define the action as  $A = \int_{t_1}^{t_2} \mathcal{L} dt$ . A variation of the Lagrangian can be defined as  $\delta \mathcal{L}$  and so  $\delta A = \int_{t_1}^{t_2} \delta \mathcal{L} dt$ , with  $\delta A(t_1) = \delta A(t_2) = 0$  [163].

The least action principle (LAP) states that for a variation of the Lagrangian  $\delta \mathcal{L}$ ,  $\int_{t_1}^{t_2} \delta \mathcal{L} dt = \int_{t_1}^{t_2} (\delta \boldsymbol{\kappa} - \delta \mathbf{v}) dt = 0$  such that  $\delta \mathcal{L} = 0$  at  $t_1$  and  $t_2$ . The expression for  $\delta \boldsymbol{\kappa}$  and  $\delta \mathbf{v}$  are given in (8) and (9).

$$\delta \boldsymbol{\kappa} = \int_{-L/2}^{L/2} \left[ \rho S \frac{d\chi}{dt} \delta \left( \frac{d\chi}{dt} \right) + \rho I \frac{d}{dt} \left( \frac{\partial \psi}{\partial x} \right) \delta \left( \frac{d}{dt} \left( \frac{\partial \psi}{\partial x} \right) \right) + \rho S \frac{d\psi}{dt} \delta \left( \frac{d\psi}{dt} \right) \right] dx \quad (8)$$

$$\delta \mathbf{v} = \int_{-L/2}^{L/2} \left[ E_e S \frac{\partial \chi}{\partial x} \delta \left( \frac{\partial \chi}{\partial x} \right) + E_e I \frac{\partial^2 \psi^2}{\partial x^2} \delta \left( \frac{\partial^2 \psi^2}{\partial x^2} \right) \right] dx \quad (9)$$

Applying the least action principle using (8) and (9) produces (10).

$$\int_{t_1}^{t_2} \delta \tilde{\mathcal{L}} dt = \int_{t_1}^{t_2} \left( \int_{-L/2}^{L/2} \left[ \rho S \frac{d\chi}{dt} \delta \left( \frac{d\chi}{dt} \right) + \rho I \frac{d}{dt} \left( \frac{\partial \psi}{\partial x} \right) \delta \left( \frac{d}{dt} \left( \frac{\partial \psi}{\partial x} \right) \right) + \rho S \frac{d\psi}{dt} \delta \left( \frac{d\psi}{dt} \right) \right] dx - \int_{-L/2}^{L/2} \left[ E_e S \frac{\partial \chi}{\partial x} \delta \left( \frac{\partial \chi}{\partial x} \right) + E_e I \frac{\partial^2 \psi^2}{\partial x^2} \delta \left( \frac{\partial^2 \psi^2}{\partial x^2} \right) \right] dx \right) dt = 0 \quad (10)$$

The first spatial integral in (10) corresponds to  $\int_{t_1}^{t_2} \delta \mathbf{\kappa} dt$ . If we integrate the differential terms once according to time we obtain (11). The second spatial integral corresponds to  $\int_{t_1}^{t_2} \delta \mathbf{v} dt$  if we integrate the differential terms once according to  $x$ , we obtain (12). Putting the two together gives us (13).

$$\int_{t_1}^{t_2} \delta \mathbf{\kappa} dt = \int_{t_1}^{t_2} \left( \int_{-L/2}^{L/2} \left[ \rho S \frac{d^2 \chi}{dt^2} \delta \chi + \rho I \frac{\partial}{\partial x} \left( \frac{d^2 \psi}{dt^2} \right) \delta \psi + \rho S \frac{d^2 \psi}{dt^2} \delta \psi \right] dx \right) dt \quad (11)$$

$$- \int_{t_1}^{t_2} \delta \mathbf{v} dt = - \int_{t_1}^{t_2} \left( \left[ E_e S \frac{\partial \chi}{\partial x} \delta \chi + E_e I \frac{\partial^2 \psi}{\partial x^2} \delta \frac{\partial \psi}{\partial x} \right]_{-L/2}^{L/2} + \left[ E_e I \frac{\partial^3 \psi}{\partial x^3} \delta \psi \right]_{-L/2}^{L/2} \right) dt \quad (12)$$

$$\begin{aligned} \int_{t_1}^{t_2} \delta \tilde{\mathcal{L}} dt &= \int_{t_1}^{t_2} \left( \int_{-L/2}^{L/2} \left[ \rho S \frac{d^2 \chi}{dt^2} + E_e S \chi \right] \delta \chi dx - \left[ E_e S \frac{\partial \chi}{\partial x} \delta \chi \right]_{-L/2}^{L/2} \right) dt + \\ &\int_{t_1}^{t_2} \left( \int_{-L/2}^{L/2} \left[ \rho I \frac{\partial}{\partial x} \left( \frac{d^2 \psi}{dt^2} \right) + \rho S \frac{d^2 \psi}{dt^2} + E_e I \frac{\partial^4 \psi}{\partial x^4} \right] \delta \psi dx - \right. \\ &\left. \left[ E_e I \frac{\partial^3 \psi}{\partial x^3} \delta \left( \frac{\partial \psi}{\partial x} \right) \right]_{-L/2}^{L/2} - \left[ E_e I \frac{\partial^3 \psi}{\partial x^3} \delta \psi \right]_{-L/2}^{L/2} \right) dt = 0 \end{aligned} \quad (13)$$

Equation (13) must hold for any variation  $\delta\chi$  and  $\delta\psi$ , which is possible only if all the factors accompanying these variations are zero. We can observe from this result that the deformation fields  $\chi$  and  $\psi$  are decoupled, so we can deduce the equilibrium equations and the boundary conditions for each mode independently. The highlighted part of the second time integral gives us the factors relevant to the out of plane variations, giving  $\rho I \frac{\partial}{\partial x} \left( \frac{d^2\psi}{dt^2} \right) + \rho S \frac{d^2\psi}{dt^2} + E_e I \frac{\partial^4\psi}{\partial x^4} = 0$ . We examine the first factor, related to the inertial effect  $\rho I \frac{\partial}{\partial x} \left( \frac{d^2\psi}{dt^2} \right)$ . Firstly, we note that for a thin beam  $L \gg h$ , the ratio between rotational inertia  $\rho I$  and surface  $S$  is very small  $\frac{\rho I}{S} = \frac{h^2}{12}$ . Under periodic excitation in a free-free regime, at certain frequencies, a sinusoidal stationary vibration is induced on the plate. In this case we can find an expression for factor  $\frac{\partial}{\partial x} \left( \frac{d^2\psi}{dt^2} \right)$ , which can also be written  $\frac{d^2}{dt^2} \left( \frac{\partial\psi}{\partial x} \right)$ . For this type of periodic sinusoidal deformation, with vibration amplitude  $\hat{\psi}$ , angular frequency  $\omega$ , and wavelength  $\lambda$ , the transverse deformation can be written as  $\psi(x, t) \approx \hat{\psi} \sin \left( \frac{2\pi}{\lambda} x - \omega t \right)$ . At  $x = 0$ ,  $\frac{\partial\psi}{\partial x} \approx \hat{\psi} \frac{2\pi}{\lambda} \cos(-\omega t)$  and therefore  $\frac{d^2}{dt^2} \left( \frac{\partial\psi}{\partial x} \right) \approx -\hat{\psi} \frac{2\pi}{\lambda} \omega^2 \cos(-\omega t) = -\hat{\psi} \frac{2\pi}{\lambda} \omega^2$  at  $t = 0$ . It can be observed that we can only neglect factor  $\rho I \frac{\partial}{\partial x} \left( \frac{d^2\psi}{dt^2} \right)$  because we made the hypothesis that  $h$  was very small and  $\omega$  is specified within the tens of kHz. This way we get the wave equation (14) for the transverse deformation. Similarly, we can deduce equation (15) for the longitudinal mode from the first two factors of the first time integral in (13).

$$\rho S \frac{d^2\psi}{dt^2} + E_e I \frac{\partial^4\psi}{\partial x^4} = 0 \quad (14)$$

$$E_e S \frac{\partial^2\chi}{\partial x^2} - \rho S \frac{\partial^2\chi}{\partial t^2} = 0 \quad (15)$$

### 2.2.2. Resonance frequencies

#### 2.2.2.1 LONGITUDINAL MODES

In the case of the longitudinal modes, the conditions for resonance to solve (15) can be written as  $\frac{E_e}{\rho} \beta_l^2 = \omega_n^2$ . The term  $\beta_l$  represents the wave number of the longitudinal mode and  $\omega_n$  the resonance. Free-free kinematic boundary conditions imply that  $\frac{\partial \chi(x)}{\partial x} = 0$  at the limits  $x = 0$  and  $x = L$ . Applying these, we can find  $\beta_l = k_L \pi / L$ , with  $k_L \in \mathbb{N}$ . Each value of  $k_L$  defines one resonance frequency. With this result, it is possible to calculate the resonance frequency  $f_{nL}$  of the beam as in (16). The angular resonance frequency of the longitudinal mode is represented by  $\omega_{nL}$ .

$$f_{nL} = \left(\frac{1}{2\pi}\right) \omega_{nL} = \left(\frac{1}{2\pi}\right) \frac{k_L \pi}{L} \sqrt{\frac{E_e}{\rho}} \quad (16)$$

#### 2.2.2.2 TRANSVERSE MODES

The resonance frequency of the transverse modes  $f_{nN}$  can be found by solving (14), using the free-free regime boundary conditions as explained in [161], [162] (moment  $E_e I \frac{\partial^2 \psi}{\partial x^2} = 0$ , and shear force  $-E_e I \frac{\partial^3 \psi}{\partial x^3} = 0$ ). The solution is expressed in (17), with the wave number of each transverse mode  $k_N$  described by  $\beta_n \approx (2k_N + 1) \frac{\pi}{2}$ , given  $k_N > 3$ .

$$f_{nN} = \left(\frac{1}{2\pi}\right) \omega_{nN} = \left(\frac{1}{2\pi}\right) \left(\frac{\beta_n}{L}\right)^2 h \sqrt{\frac{E_e}{12\rho}} \quad (17)$$

In order to design a geometry which achieves ‘close’ frequencies, we may write  $f_{nL} \approx f_{nN}$ . Doing this we obtain (18) for  $k_N > 3$ . We cognize from the resulting equation that the dimensions which would provide similar transverse and longitudinal mode frequencies are independent from the material from which the device is made.

$$k_L \approx \frac{\pi h}{8\sqrt{3}L} (2k_N + 1)^2 \quad (18)$$

### 2.2.3. Choice of dimensions and Finite Element simulation

For this specific device, the ‘height’ dimension  $h$  was defined by the thickness of the available material, which in our case was 1.94 mm. The length of the plate  $L$ , and the harmonic numbers  $k_N$  and  $k_L$  were selected in consequence.

Given the geometry of the plate, and the desired exploration area, a mode  $k_L = 3$  was selected for the longitudinal mode. It was expected that this deformation shape allowed placing one vibrational mode at each isthmus of the geometry. Then, the transverse mode  $k_N$  which produced the closest resonance without interference was deduced. At about 60 kHz, the plate length chosen was of about 128 mm, with  $k_N = 14$ . From (18) it is possible to deduce that the side  $b$  does not influence the resonance frequencies, as long as the ‘beam’ hypothesis is maintained (i.e.  $L \gg b$ ). For this reason, we chose a dimension  $b$  which allowed exploring the device in many directions, while still remaining comparatively small with respect to the length  $L$ . The selected dimensions of the resonator for simulation were, therefore, 128 mm x 30mm x 1.94mm, and the ceramics had a magnitude of 5 mm x 9mm x 0.3mm. These dimensions produced  $f_{nL} = 57.4\text{kHz}$  and  $f_{nN} = 55.3\text{kHz}$  according to (16) and (17), which we believed, was close enough to produce comparable results, while avoiding mutual interference.

A finite element simulation for the selected dimensions is performed around 60 kHz using Salome-Meca from Code\_Aster [164]. The algorithm included the geometry and material of the piezo-ceramics. The results are depicted in Figure 19. The modes obtained in the finite element simulation are measured at about 56.5 kHz for the longitudinal mode and 54.5 kHz for the transverse mode. Each mode can be excited and measured independently. The difference between the results from the simulation and the equations are explained by the many

differences between the device and the Euler-Bernoulli beam, such as the inclusion of the isthmus and immobile aluminum sections attached to the plate, and the inclusion of the ceramics in the simulation model.

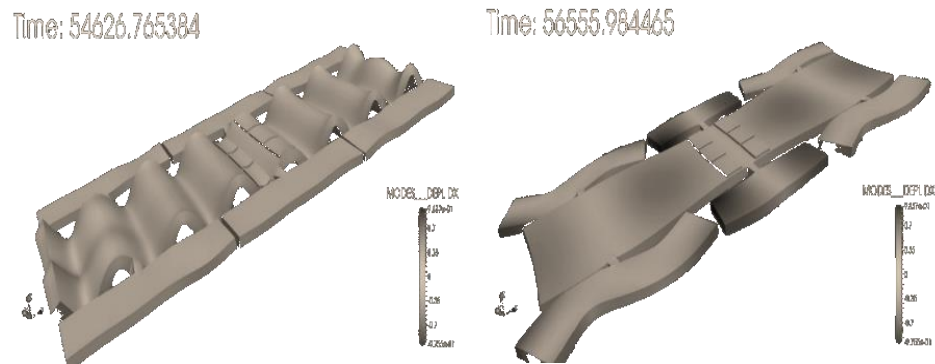


Figure 19. Finite element simulation of the modes of the plate with the selected dimensions including the piezoelectric ceramics. On the left, the transverse mode with  $k_N = 14$  appears in the simulation at around 54,5 kHz. On the right, the longitudinal mode with  $k_L = 3$  appears at about 56.5 kHz. There are no resonant modes between the two.

#### 2.2.4. Implementation and Cartography

The device implementation is performed as shown in Figure 20. The structure is supported with a hard and light polymeric base glued to the immobile aluminum section that is attached to the plate through a series of isthmus.

The support is designed to allow the necessary cabling to be connected without interfering with the vibration of the device. A smooth damp-proof polymeric cover is glued to the upper surface of the device because this material allows achieving good tribological conditions. Over it, an orange rectangle highlights a portion of one facet of the device. This framed 30 mm x 55 mm surface represents the area scanned for creating the cartography of both modes. From the simulation presented in

Figure 19, we cognize that both modes are symmetrical with respect to the center of the plate, so scanning the selected portion of the surface is sufficient to understand the behaviour of both facets of the structure.

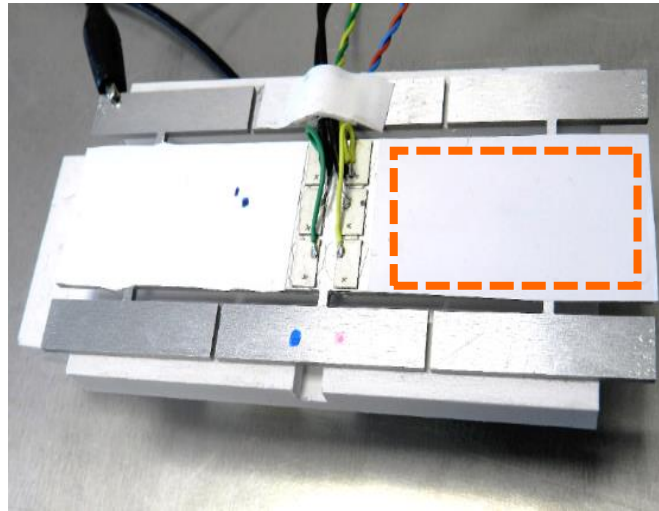


Figure 20. Implementation of the device designed for the comparison of transverse vs. longitudinal modes around 60 kHz. The device consists of an aluminum plate with 13 piezoelectric ceramics and a damp-proof polymeric cover glued to its surface. The framed section is the area which is cartographed and used for haptic return.

The frequencies of the modes are found thanks to a frequency sweep performed on the mounted device. They are measured at about 58 kHz for the longitudinal mode and 56 kHz for the transverse mode. Each mode can be excited and measured independently.

The setup for measuring the longitudinal and the transverse motion is illustrated in Figure 21. The measurements were performed with the help of the Polytec OFV-5000 modular vibrometer base with Polytec OFV-505 sensor head. The ultrasonic surface haptic device was placed on a programmable moving base that located a selected matrix of points of the surface under the laser beam. Each point was measured twice, with the laser vibrometer placed at two different positions ( $+45^\circ$  and  $-45^\circ$  parallel to the  $x$  axis).



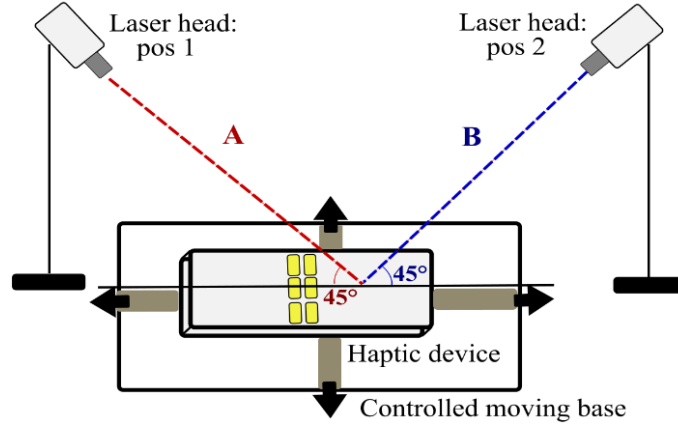


Figure 21. Setup for performing the cartography measurement of the longitudinal and the transverse modes.

$$w_A = w_N \sin(45^\circ) + w_L \cos(45^\circ) = \frac{\sqrt{2}}{2} w_N + \frac{\sqrt{2}}{2} w_L \quad (19)$$

$$w_B = w_N \sin(-45^\circ) + w_L \cos(-45^\circ) = \frac{-\sqrt{2}}{2} w_N + \frac{\sqrt{2}}{2} w_L \quad (20)$$

$$w_N = \frac{w_A - w_B}{\sqrt{2}} \quad (21)$$

$$w_L = \frac{w_A + w_B}{\sqrt{2}} \quad (22)$$

The two beams reaching the measurement point (A and B in Figure 21) produced two vibration amplitude measurements, noted  $w_A$  and  $w_B$  in (19) and (20), respectively. These raw data were used to deduce the magnitude of the transverse ( $w_N$ ) and the longitudinal ( $w_L$ ) displacement, by the difference and addition of each value, respectively, as described in (21) and (22).

The results for the transverse and longitudinal motion measurement of the two modes are illustrated in Figure 22. The measurements confirm that there are no parasitic modes around the resonance of the desired modes. We obtained, therefore, an almost pure longitudinal motion for the longitudinal mode (less than 5% of transverse motion), as well as an almost purely transverse motion for the transverse mode (less than 2% of longitudinal motion). We confirmed that this

design allows an exploration area through a length of over 3 cm between two nodes of the longitudinal mode.

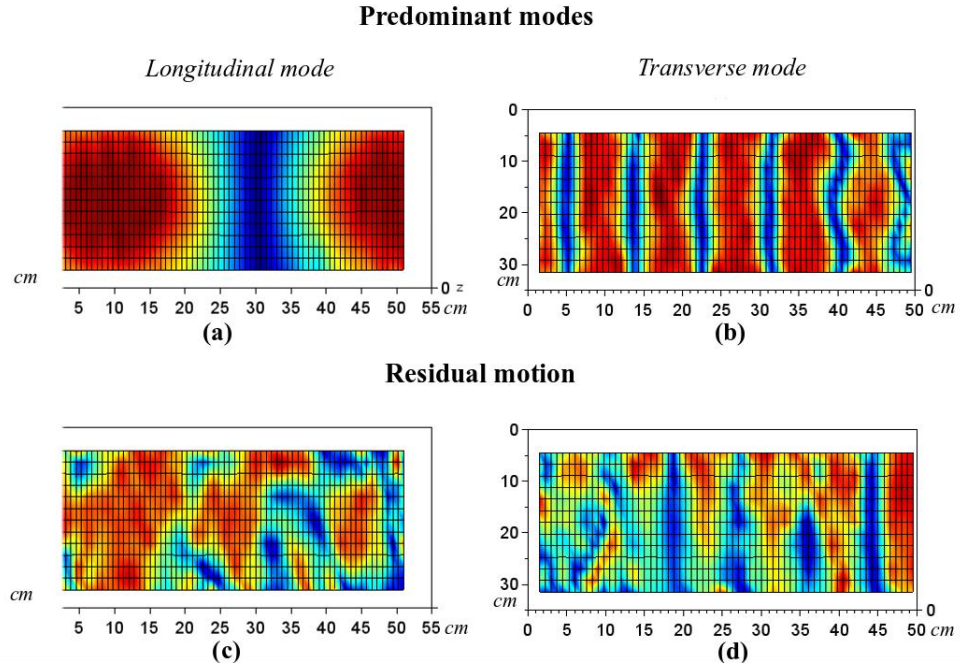


Figure 22. Cartography of one facet of the plate (highlighted in Figure 20) at resonance for transverse and longitudinal feeding conditions. (a) Longitudinal vibration amplitude at longitudinal mode conditions: 58 kHz, ( $V1=V2$ ). Red corresponds to a maximum vibration amplitude of  $\sim 0.5 \mu\text{mp-p}$ , dark blue  $0 \mu\text{mp-p}$ . (b) Transverse vibration amplitude at transverse mode feeding conditions: 56 kHz, ( $V1=-V2$ ). Red corresponds to a maximum  $0.1 \mu\text{mp-p}$ , dark blue  $0 \mu\text{mp-p}$ . (c) Transverse vibration amplitude at longitudinal mode feeding conditions. Red corresponds to a maximum of  $0.005 \mu\text{mp-p}$ , dark blue to  $0 \mu\text{mp-p}$ . (d) Longitudinal vibration amplitude at transverse mode feeding conditions: Red corresponds to a maximum of  $0.01 \mu\text{mp-p}$ , dark blue  $0 \mu\text{mp-p}$ .

### 2.3 Dynamic model of one mode in the rotating reference frame dq

For both vibrating modes, in order to achieve an accurate friction reduction despite the external effects (such as the finger pressure), it is necessary to perform a regulation of the vibration amplitude. Measuring and controlling the vibration amplitude in closed-loop requires a simplified dynamic model of the system. In

order to create and identify the dynamic behavior and parameters of the USHD, we exploit the modal decomposition method based on the orthogonality property of eigenmodes and finally derive the dynamic equation governing each mode [91], [157], [165].

### 2.3.1 Modal modelling and the orthogonality principle

A deformation at a point  $\mathbf{x}$  of the structure in any direction  $\chi$  or  $\psi$  can be denominated  $\mathbf{d}(\mathbf{x}, t)$ . In modal theory, this spatio-temporal behaviour can be described with an infinite series of the products of spatial eigenvectors (mode shapes  $\varphi_k(\mathbf{x})$ , which describe the spatial deformation) multiplied by temporal coefficients ( $w_k(t)$ , that represents the temporal behaviour) as described by (23), with every  $k$  corresponding to each mode of the plate. Each one of these  $k$  modes is orthogonal to the others, and together, they form a  $k$ -dimensional sub-space.

$$\mathbf{d}(\mathbf{x}, t) = \sum_{k=1}^{\infty} \varphi_k(\mathbf{x}) w_k(t) \quad (23)$$

In the case of longitudinal forced vibrations, the wave equation (15) is modified, and the external force from the piezoelectric ceramics  $p(\mathbf{x}, t)$  is included. This results in (24). When this equation is expressed in the modal base, we obtain (25).

$$p(\mathbf{x}, t) = E_e S \frac{\partial^2 \chi}{\partial x^2} - \rho S \frac{\partial^2 \chi}{\partial t^2} \quad (24)$$

$$p(\mathbf{x}, t) = \sum_{k=1}^{\infty} E_e S \frac{\partial^2 \varphi_k(\mathbf{x})}{\partial x^2} w_k(t) - \sum_{k=1}^{\infty} \rho S \varphi_k(\mathbf{x}) \frac{d^2 w_k(t)}{dt^2} \quad (25)$$

Because the modes are orthogonal in the  $k$ -dimensional base, by the orthogonality principle, the integrals of the projections  $\int_{-L/2}^{L/2} \rho S \varphi_i(\mathbf{x}) \cdot \varphi_j(\mathbf{x}) dx = 0$  for

every  $i \neq j$  and they are equal to the modal mass  $M_n$  for  $i = j$ . If we project the  $n^{th}$  mode on the modal base, we get (26).

$$\begin{aligned} \int_{-L/2}^{L/2} p(x, t) \varphi_n(x) dx \\ = \sum_{k=1}^{\infty} \int_{-L/2}^{L/2} E_e S \frac{\partial^2 \varphi_k(x)}{\partial x^2} \varphi_n(x) w_k(t) dx \\ - \sum_{k=1}^{\infty} \int_{-L/2}^{L/2} \rho S \varphi_k(x) \frac{d^2 w_k(t)}{dt^2} \varphi_n(x) dx \end{aligned} \quad (26)$$

Using the orthogonality principle, we can deduce (27) from the second factor on the right of the equation. Integrating the first factor gives us (28).

$$\sum_{k=1}^{\infty} \frac{d^2 w_k(t)}{dt^2} \int_{-L/2}^{L/2} \rho S \varphi_k(x) \varphi_n(x) dx = \frac{d^2 w_n(t)}{dt^2} \int_{-L/2}^{L/2} \rho S \varphi_n^2(x) dx \quad (27)$$

$$\begin{aligned} \sum_{k=1}^{\infty} \int_{-L/2}^{L/2} E_e S \frac{\partial^2 \varphi_k(x)}{\partial x^2} \varphi_n(x) w_k(t) dx \\ = -w_n(t) \int_{-L/2}^{L/2} E_e S \frac{\partial \varphi_n(x)}{\partial x} \frac{\partial \varphi_k(x)}{\partial x} dx \\ + w_n(t) \left[ E_e S \frac{\partial \varphi_k(x)}{\partial x} \varphi_n(x) \right]_{-L/2}^{L/2} \end{aligned} \quad (28)$$

The last factor of the right side of (28), contains, as we know from 2.2.1, the expression for the boundary conditions for the force. The modal elasticity  $K_n$  may be introduced as in equation (30) and, as we know already, the modal mass in (29).

$$M_n = \int_{-L/2}^{L/2} \rho S \varphi_n^2(x) dx \quad (29)$$

$$K_n = \int_{-L/2}^{L/2} E_e S \frac{\partial^2 \varphi_n(x)}{\partial x^2} dx \quad (30)$$

Replacing (29) and (30) in (27) and (28) respectively, (26) can be written as (31), with  $f_p(x, t) = \int_{-L/2}^{L/2} p(x, t) \varphi_n(x) dx + [F(x = L/2) \varphi_n(x = L/2)] - [F(x = -L/2) \varphi_n(x = -L/2)]$  being the piezoelectric force associated to the  $n^{th}$  mode, including the force constraints  $F(x = L/2)$  and  $F(x = -L/2)$  at the edges of the plate. For simplicity, we use  $\dot{w}_n(t)$  to denote the first time derivative of  $w_n(t)$  and  $\ddot{w}_n(t)$  for the second time derivative. This same reasoning is applicable to the deformation  $\psi$  for transverse modes, as has been shown in [166] (see Appendix 3). For this reason (31) is applicable to all modes of the plate, independently of the direction of the deformation.

$$f_p(t) = M_n \ddot{w}_n(t) + K_n w_n(t) \quad (31)$$

In reality, all systems lose energy, so (26) can be modified to include a modal dampening factor  $D_n$ , so  $\int_{-L/2}^{L/2} p(x, t) \varphi_n(x) dx + [F(L) \varphi_n(L)] - [F(0) \varphi_n(0)] = f_p(t) - D_n \dot{w}_n(t)$ . Moreover, the modal force of the piezoelectrics can be represented as a simple linear electro-mechanical transformation, such that  $f_p(t) = N_n v(t)$ , with  $N_n$  equal to the electromechanical transformation constant for the piezoelectrics for the  $n^{th}$  mode, and  $v(t)$  equal to the input voltage [167], [168]. The final result is the modal dynamic model of the piezoelectric-plate system (32).

$$N_n v(t) = M_n \ddot{w}_n(t) + D_n \dot{w}_n(t) + K_n w_n(t) \quad (32)$$

The open loop system can be represented in the frequency domain as in Figure 23, if we consider that capital letters  $V$  and  $W$  represent the Laplace transform of

pulsating signals  $v(t)$  and  $w_n(t)$ , respectively and writing  $N, M, D$  and  $K$  for  $N_n, M_n, D_n$  and  $K_n$  respectively.

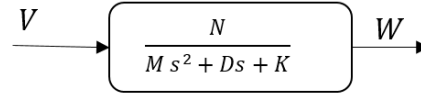


Figure 23. Transfer function of a single mode

### 2.3.2 EMR of the dynamic modal equation

In order to follow the causality principle in EMR [134], it is useful to express the system in its integral form [169]. We may define the inertial force  $f_I = M\dot{w}$  and the damped-elastic force  $f_s = D\dot{w}(t) + Kw(t)$ . This way, the system may be represented with equations (33) and (34).

$$\dot{w}(t) = \frac{1}{M} \int f_I(t) dt \quad (33)$$

$$f_I = f_p - f_s \quad (34)$$

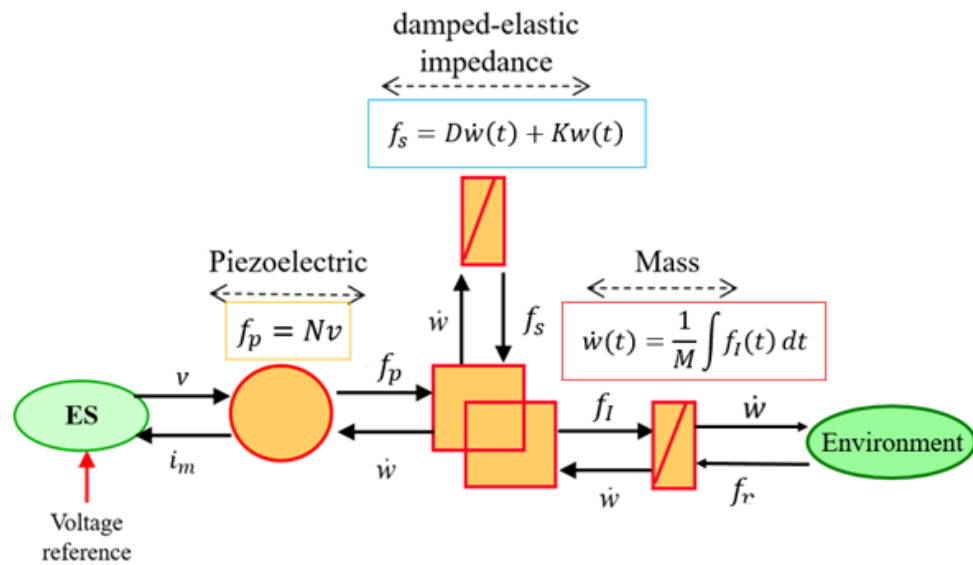


Figure 24. Energetic Macroscopic Representation (EMR) of the vibrating plate modal behavior

Given that the electrical source  $v(t)$  is an input, it can be established from equation (33) that  $\dot{w}(t)$  is an output.  $i_m$  is the motional current on the piezoelectric matrix. The electrical source 'ES' corresponds to a voltage source, where the effect of the internal capacitance of the piezoelectric matrix is included [168]. The force applied by the environment or load,  $f_r$  is assumed to be an external disturbance and therefore not considered in the controller synthesis.

### 2.3.3 Projection in the rotating reference frame dq

Relation (32) provides the dynamic behaviour of any mode of the plate. However, using this equation to perform vibration control presents a series of practical challenges, given that  $v(t)$  is a sinusoidal signal with a very high frequency (generally between 25kHz and 100kHz). Acquiring enough data to correctly discretize this type of systems and control them in both amplitude and phase, would require a very significant processing power (which is incompatible with portable devices). In order to address this issue, [110] proposes a direct control in a virtual rotating reference frame which can be performed by modulation/demodulation techniques. At steady state, this type of control deals with constant references, which can easily be handled by standard PI controllers. The actual voltages are then obtained by modulating their output with a high frequency signal corresponding to the resonance of the mode. For doing this, we introduce the demodulation process in the rotating reference frame, also called dq frame (d and q stand for 'direct' and 'quadrature', making a parallel between the proposed modulated vibration amplitude control and vector control in electrical engineering). This representation is illustrated in Figure 25.

$$\underline{v}(t) = (V_d + jV_q)e^{j\omega t} \quad (35)$$

$$\underline{w}(t) = (W_d + jW_q)e^{j\omega t} \quad (36)$$

Assuming that  $v(t)$  is a sinusoidal function in steady state, it can be represented by the use of complex phasors, as in (35)-(36), where  $\underline{v}(t)$  is the complex phasor of  $v(t)$ , and  $\underline{w}(t)$  is the complex phasor of  $w(t)$ . The signals  $V_d$  and  $W_d$  correspond to the magnitude of the projection of  $\underline{v}(t)$  and  $\underline{w}(t)$  in the  $d$  axis, respectively; and correspondingly,  $V_q$  and  $W_q$  the projections of  $\underline{v}(t)$  and  $\underline{w}(t)$  in the  $q$  axis.

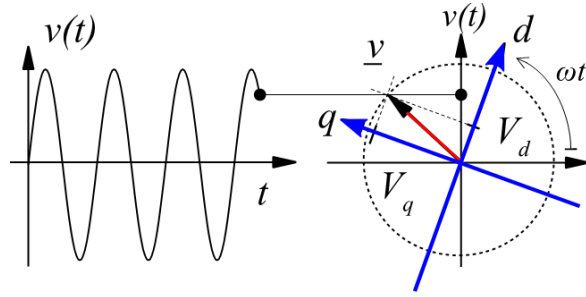


Figure 25. Projection of  $v(t)$  in the rotating reference frame dq at a frequency  $\omega$   
[170]

It may be noticed that the signals  $\underline{v}(t)$  and  $\underline{w}(t)$  have high frequency dynamics, since they are multiplied by  $e^{j\omega t}$ , whereas the signals  $V_d$ ,  $V_q$ ,  $W_d$  and  $W_q$  have slower dynamics in comparison and therefore, they may be considered as a ‘modulation envelope’. Replacing (35) and (36) in (32), leads to (37) for the real part of the equation projected into axis d and (38) for the imaginary part, projected into axis q.

$$NV_d = M\ddot{W}_d + D\dot{W}_d + (K - M\omega^2)W_d - \omega(2M\dot{W}_q + DW_q) \quad (37)$$

$$NV_q = M\ddot{W}_q + D\dot{W}_q + (K - M\omega^2)W_q + \omega(2M\dot{W}_d + DW_d) \quad (38)$$



Because the dynamic of the vibration is very fast compared to the evolution of the reference (envelope) in steady state, it is possible to assume that  $|\ddot{W}_d| \ll \omega^2 |W_d|$  and respectively  $|\ddot{W}_q| \ll \omega^2 |W_q|$ . Moreover, it can also be deduced from this hypothesis that  $\frac{D}{K}|W_d| \ll |W_d|$  and  $\frac{D}{K}|W_q| \ll |W_q|$ . This way, we obtain (39) and (40) as the dynamic equation of the two axes d and q [171]. The system projected onto the dq frame as described by (39) and (40).

$$NV_d = (K - M\omega^2)W_d - \omega(2M\dot{W}_q + DW_q) \quad (39)$$

$$NV_q = (K - M\omega^2)W_q + \omega(2M\dot{W}_d + DW_d) \quad (40)$$

As previously stated, the variable associated with energy is the velocity, not the displacement. Consequently, for using EMR, equations (39) and (40) should be expressed in terms of velocity and not in terms of amplitude. For this reason, we may calculate  $\underline{\dot{w}}(t) = (-\omega W_q + j\omega W_d + \dot{W}_d + j\dot{W}_q)e^{j\omega t}$ . Following the development proposed in [171], we can propose a new velocity variable  $\underline{\dot{w}}(t) = \underline{u}(t) = (U_d + jU_q)e^{j\omega t}$ . We can thus find that equations (39) and (40) can be written as in (41) and (42).

$$NV_d = 2M\dot{U}_d + DU_d - \left(\frac{K}{\omega} - M\omega\right)U_q \quad (41)$$

$$NV_q = 2M\dot{U}_q + DU_q + \left(\frac{K}{\omega} - M\omega\right)U_d \quad (42)$$

We can define the piezoelectric force of each axis in terms of the axe voltages, respectively as  $F_{pd} = NV_d$  and  $F_{pq} = NV_q$ . A complex phasor can also be applied to the external force acting on the plate (environment), which can in turn be expressed as  $\underline{f}_r(t) = (F_{rd} + jF_{rq})e^{j\omega t}$ .

Finally, the reactive force of the plate, produced by an inertial-elastic impedance can be expressed for each axis as  $F_{Sd} = F_{pd} - F_{rd}$  and  $F_{Sq} = F_{pq} - F_{rq}$ . The



### 2.4.1 Amplitude control in the dq frame around the resonance

The MCS (maximal control structure) of the coupled system can be derived from inverting the EMR in Figure 26, thus obtaining the structure depicted in Figure 27. There is, however, significant difficulty in controlling coupled axes. It is possible, however to simplify this task, by making sure to always operate the USHD at frequencies close to the resonance of the mode. At resonance, we can express  $\omega \approx \omega_n = \sqrt{\frac{K}{M}}$  and therefore  $\delta\omega \approx 0$ . By this relation, it is possible to decouple the d and q axes, because when the coupling factor is negligible, (39) and (40) can be simplified to (43) and (44), and equivalently, (41) and (42) can be written as (45) and (46). It is worth noting that a different approach is required if the USHD is operated further from the resonance, and the coupling factor  $\delta\omega = (K - M\omega^2)$  becomes significant. An example of such approach is discussed in [173].

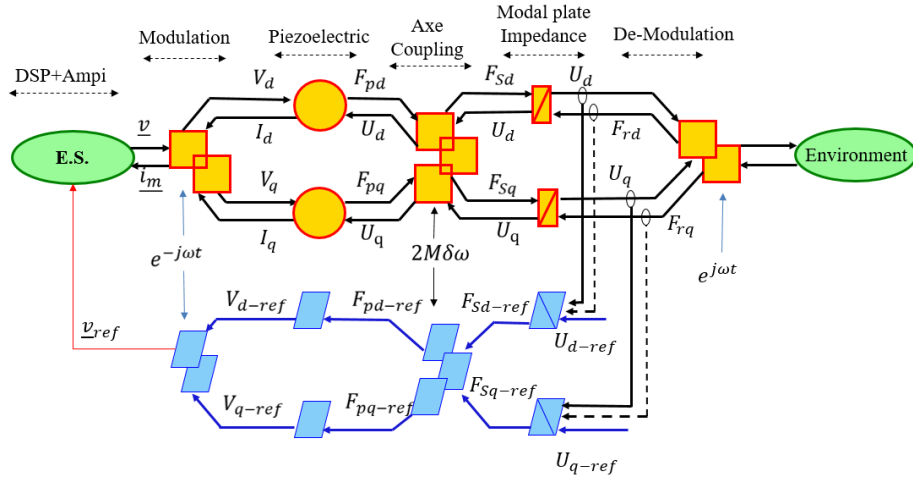


Figure 27. MCS of the equivalent coupled system for a single mode in the dq frame

$$W_d = \left(\frac{1}{\omega}\right) \frac{NV_q/D}{2M/D s + 1} \quad (43)$$



### 2.4.2 Modal parameter identification

In 2.4.1 we have found a control scheme for the equivalent decoupled system in the rotating reference frame around the resonance. However, the modal parameters  $N$ ,  $M$ ,  $D$  and  $K$  are different and unique for each mode, and so, in order to compute the controller coefficients, the modal parameters have to be identified for both longitudinal and transverse modes. These modal parameters can be found experimentally as described in [168], [172]. This method is applied to the longitudinal and transverse modes found in Section 2.2.

The method consists of two separate experiments, both performed on the longitudinal and transverse modes, one for finding the electromechanical transformation factor  $N$ , which is explained in section 2.4.2.1 and one for finding the modal plate parameters, which is explained in 2.4.2.2.

For performing these experiments, the setup shown in Figure 29 is used. For this setup, the piezoelectric sensor is calibrated to measure the longitudinal and transverse mode displacement, with the help of the Polytec OFV-50000 modular vibrometer base with Polytec OFV-505 sensor head and the PicoScope 3406D PC Oscilloscope.

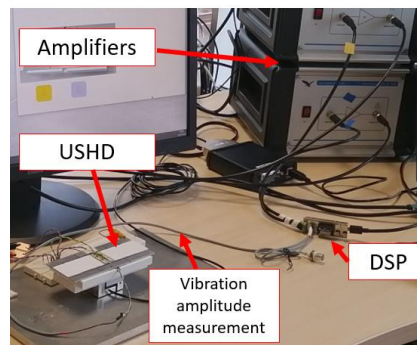


Figure 29. Setup for modal parameter identification

The piezoelectric sensor is connected to a Digital Signal Processor (DSP) STM427 from ST Microelectronics. The DSP is able to provide a voltage reference and

modulate the voltage measurements from the amplitude sensor in the dq frame. The DSP provides two separate outputs for voltages V1 and V2 (see 2.2.4), which are connected to two external power amplifiers (WMA-300 from Falco Systems) with outputs ranging up to  $150 V_{p-p}$ . For the first experiment a current probe is connected to the output of the power amplifiers.

2.4.2.1. ELECTROMECHANICAL TRANSFORMATION FACTOR  $N$

Calculating the modal parameters using measurements for a frequency sweep around the resonance requires first knowing the value of the electromechanical transformation factor  $N$  for the specific mode. For finding this, we use the Mason model [167] to characterize the piezoelectric ceramics, as explained in [168]. The model is depicted in Figure 30.  $R_0$  and  $C_0$  represent the dielectric resistance and the blocking capacitance;  $i_m$  is the motional current. The electromechanical transformation factor  $N$  is represented by the transformer ratio in the equivalent circuit.

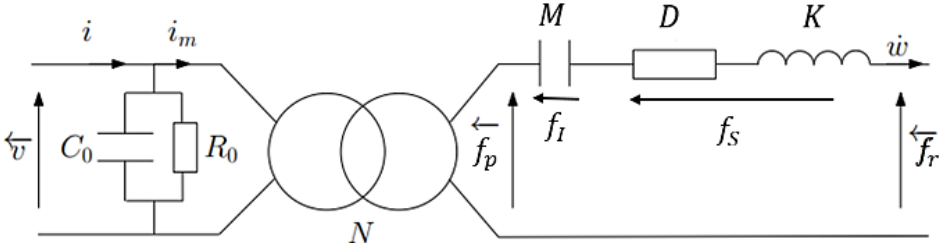


Figure 30. Mason’s Electromechanical equivalent circuit of the piezoelectric ceramic in vicinity of the resonance [168]

$$i = C_0 \frac{dv}{dt} + R_0 v + i_m \tag{47}$$

A nodal analysis of the electrical (left) part of the circuit gives us (47). For simplicity, we neglect the current going through  $R_0$  and consider the capacitance  $C_0$  as saturated, thus  $C_0 \frac{dv}{dt} = 0$  and  $i = i_m$ . Finally, the transformer ratio can be

identified by measuring the ratio between  $i_m$  and the vibration velocity  $\dot{w}$  at resonance (48). The magnitude of  $i_m$  and  $\dot{w}$  at the resonance are measured at different voltage levels for both modes using the setup described in Figure 29. The electromechanical transformation factor  $N$  for both modes is then calculated from these measurements.

$$N = \frac{|i_m|}{|\dot{w}|} \quad (48)$$

#### 2.4.2.2. MODAL PARAMETERS M, K D

For determining the modal parameters, the magnitude of the displacement  $w$  is measured for a frequency sweep around the resonance ( $\pm 1$  kHz), using a fixed voltage  $V_d$  of about  $20 V_{p-p}$  for the transverse mode, and about  $40 V_{p-p}$  for the longitudinal mode. For generating the voltage references and the measurements in the dq frame, a DSP is used, as shown in Figure 29.

Because the measurements take place along a large spectrum of frequencies, we consider that the model is best described by equations (39) and (40) in the dq frame, which include the coupling factor. In steady state, we may assume that the time derivation of variables  $W_d$  and  $W_q$  is equal to 0. Moreover, we choose to align the d axis of the rotating frame to the input voltage, so  $V_d$  is constant and  $V_q = 0$ . Taking these simplifications into account (39) and (40) are expressed as (49) and (50).

$$NV_d = (K - M\omega^2)W_d - \omega(DW_q) \quad (49)$$

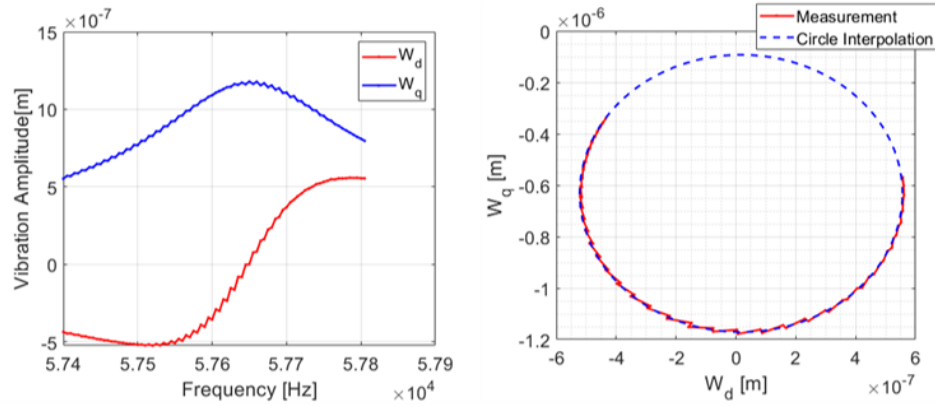
$$0 = (K - M\omega^2)W_q + \omega(DW_d) \quad (50)$$

From (50) we get that  $\frac{(K-M\omega^2)}{D\omega} = \frac{-W_d}{W_q}$ . Replacing this in (49) gives the relation  $\frac{NV_d}{D\omega} = -\frac{W_d^2}{W_q} - W_q$ . This equation can also be written as (51), which is the

equation of a circle in the complex plane  $W_d, W_q$  with center in  $\left(0, \frac{-NV_d}{2D\omega}\right)$  and radius in  $\frac{NV_d}{2D\omega}$ . This circle equation is used to calculate the modal parameters of the longitudinal and transverse modes.

$$W_d^2 + \left(W_q + \frac{NV_d}{2D\omega}\right)^2 = \left(\frac{NV_d}{2D\omega}\right)^2 \quad (51)$$

### Longitudinal mode frequency sweep



### Transverse mode frequency sweep

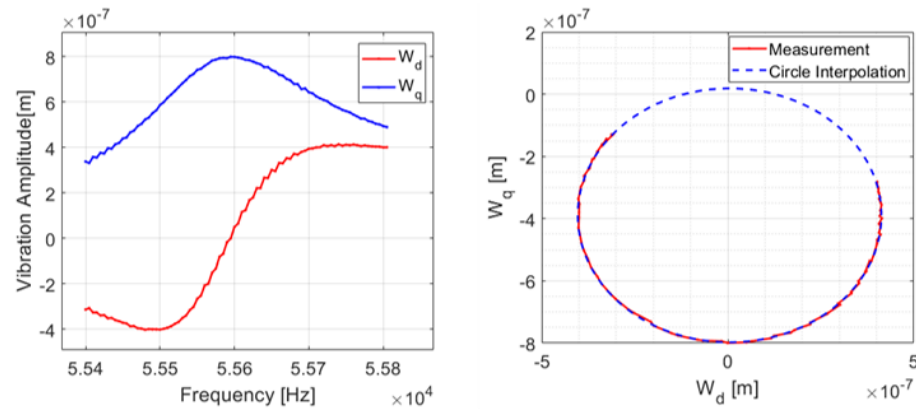


Figure 31.  $W_d$  and  $W_q$  measurements for a frequency sweep (Bandwidth  $f_{rL} \pm 200$  Hz and  $f_{rN} \pm 200$  Hz) at constant voltage  $V_d$  and  $V_q = 0$  for the transverse and longitudinal modes of the USHD implemented in 2.2. Left: Amplitude vs. Frequency. Right: Amplitudes in the complex plane.



The vibration amplitude vs. frequency measurements for the sweep are performed for the longitudinal and transverse modes using the setup described in Figure 29. The results in the frequency and in the complex plane are plotted in Figure 31. A detailed illustration on how the modal parameters are inferred from the circular interpolation of the measurements of the frequency sweep in the complex plane is shown in Figure 32. In the figure, we can see that the radius of the interpolated circle corresponds to  $\frac{NV_d}{2D\omega}$  as explained in (51).

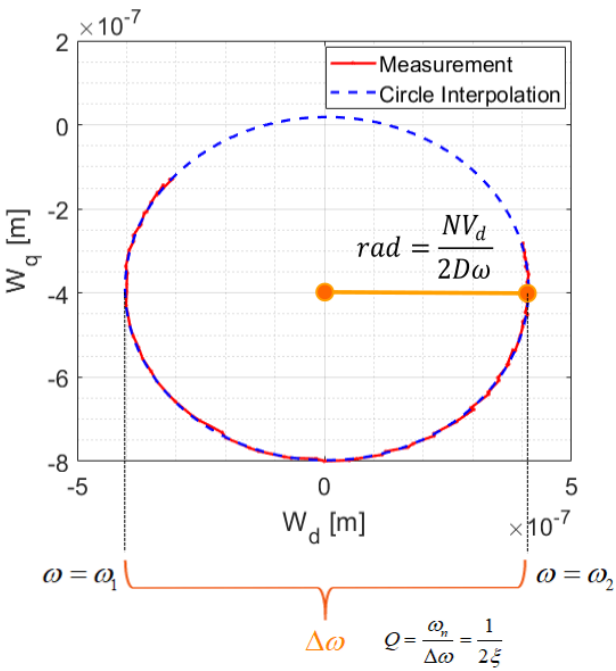


Figure 32. Mode parameter identification from the frequency sweep magnitudes  $W_d$  and  $W_q$  plotted in the complex plane.

With this reference frame, at the resonance  $\omega_n$ ,  $W_d = 0$ ,  $W_q = \frac{-NV_d}{D\omega_n}$ . If we replace these values in (50), we obtain (53). At the limit frequencies of the spectrum  $\omega_1$  and  $\omega_2$ ,  $W_d = W_q = \frac{-NV_d}{2D\omega_1}$  and  $W_d = -W_q = \frac{NV_d}{2D\omega_2}$  respectively. Replacing  $W_d$ ,  $W_q$  and  $\omega_1$  in (50) gives us (54). With  $\omega_2$  we get (55). Adding equations (54) and

(55), we obtain (56), from which we may deduce  $\Delta\omega$ , as in (57). Finally, the parameters for each mode are calculated using (52), (53) and (57).

$$rad = \frac{NV_d}{2D\omega} \quad (52)$$

$$\omega_n^2 = \frac{K}{M} \quad (53)$$

$$0 = (K - M\omega_1^2) \left( \frac{NV_d}{2D\omega_1} \right) + \omega_1 D \left( \frac{NV_d}{2D\omega_1} \right) \quad (54)$$

$$0 = (K - M\omega_2^2) \left( \frac{-NV_d}{2D\omega_2} \right) + \omega_2 D \left( \frac{NV_d}{2D\omega_2} \right) \quad (55)$$

$$0 = M(\omega_2^2 - \omega_1^2) + D(\omega_2 + \omega_1) \quad (56)$$

$$\Delta\omega = \omega_1 - \omega_2 = \frac{D}{M} \quad (57)$$

**Table 2. Modal parameters identified for the longitudinal and transverse modes [174]**

Parameter	Mode	Symbol	Value
Electro-mechanical transformation factor	Longitudinal	$N_{L,3}$	0.0773 N/V
Modal Mass	Longitudinal	$M_{L,3}$	15.4 g
Modal Dampening	Longitudinal	$D_{L,3}$	27 N s/m
Modal Elasticity	Longitudinal	$K_{L,3}$	2017 MPa
Electro-mechanical transformation factor	Transverse	$N_{N,14}$	0.3 N/V
Modal Mass	Transverse	$M_{N,14}$	13.8 g
Modal Dampening	Transverse	$D_{N,14}$	22.1 N s/m
Modal Elasticity	Transverse	$K_{N,14}$	1678 MPa

The results for the final obtained parameters for both modes are shown in Table 2. The sub-indexes  $L, k_L$  and  $N, k_N$  mean that the identified parameters correspond to either the longitudinal or the transverse mode, respectively, for the chosen harmonic number of each mode.

### 2.4.3 Closed loop control implementation and testing

Using the parameters found in Table 2, it is possible to calculate and implement the closed-loop controller for each axis, as explained in 2.4.1. Taking into account the decoupled model proposed in this chapter, we consider that a PI controller is sufficient for the objective of maintaining a desired vibration amplitude reference envelope, with a response time rapid enough, so the transitory is transparent for USHD tactile applications. Thus, a closed loop amplitude control is implemented for longitudinal and transverse modes using one PI controller for each axis. The tuning is identical. The design allows a response time  $\tau = 1.1\text{ms}$  for both modes. The damping factor in closed loop is chosen  $\xi = 1$ , so there is no overshoot, and the steady state error is 0.

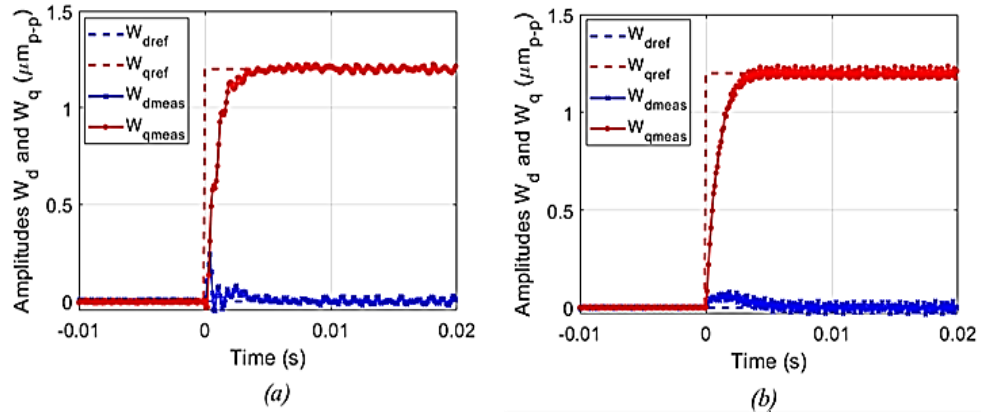


Figure 33. Measured values  $W_{dmeas}$  and  $W_{qmeas}$  step response for (a) transverse and (b) longitudinal modes around the resonance with no load.

To test the implemented controller at no load, we impose a step reference from the DSP at a given time  $t = 0$ . We chose a reference for  $W_{dref}$  equal to 0, since we have established (48) that at no load the reference frame provided  $W_d = 0$  with  $V_q = 0$  at the resonance, and  $W_{qref}$  equal to  $1.2 \mu\text{m}_{p-p}$ . The results of the test are plotted in Figure 33. In this figure, we can observe for both modes, the

reference values next to the measured values  $W_{dmeas}$  and  $W_{qmeas}$  for a time of 0.01s before and 0.02s after the step. We can see that the specifications for the controller in terms of response time and overshoot are correctly achieved. Finally, we verify the controller response in the presence of an external load. For doing so, we impose a step reference at no load, as previously, and then after a few seconds, a finger is placed on the plate, with a pressure of about 0.5N. The results of vibration amplitude and controller voltage are plotted in Figure 34. In the figure, we can observe that the presence of the finger does not affect the value of the vibration amplitude. As we can see in the controller voltages, the dynamic of the finger pressing is slow in comparison to the controller response time, so the controller is able to adapt the output and there is no visible disturbance.

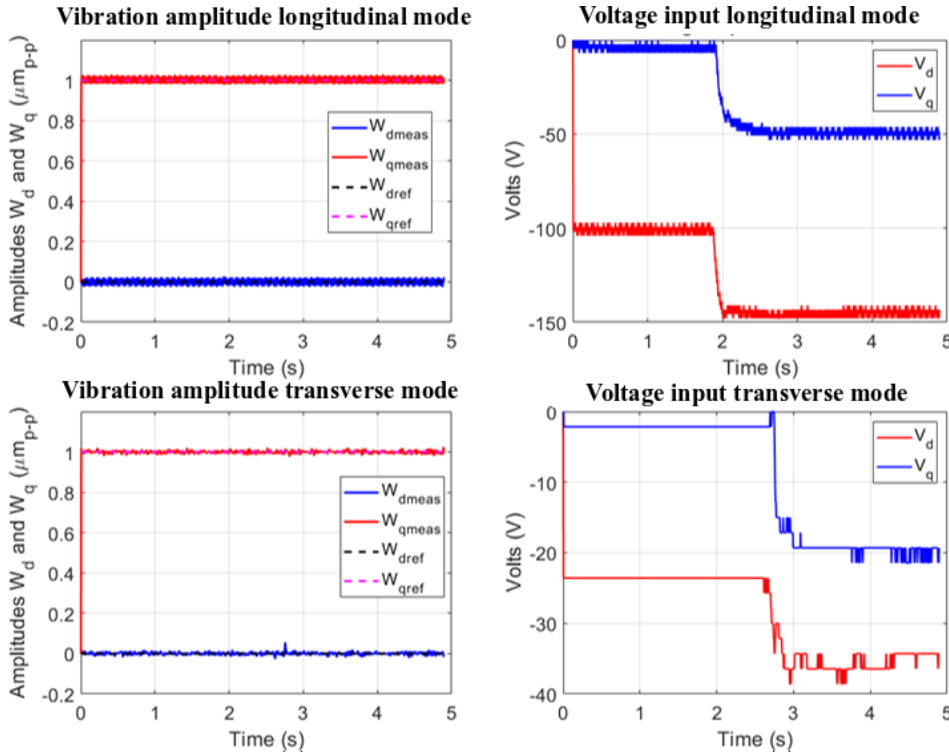


Figure 34. (Left) Measured values  $W_{dmeas}$  and  $W_{qmeas}$  step response for transverse and longitudinal modes over 5 seconds. (Right) Controller voltages  $V_d$  and  $V_q$  throughout the same period of time. A finger is placed on the plate after about 2s for the longitudinal mode, and almost 3s for the transverse mode.

## 2.5. Conclusion

This chapter deals with the design and control of a surface haptic device based on ultrasonic vibration (USHD), aimed at comparing transverse and longitudinal vibration modes. This USHD consists of an aluminum plate with a set of 12 motors and 1 sensor piezoelectric ceramics glued to its surface.

With the built device, we are able to excite independently one longitudinal and one transverse mode at close resonance frequencies of about 60 kHz. The cartography of the device confirmed that the modes are pure and there is no parasitic motion. Thanks to modal analysis and the orthogonality property, we were able to deduce a simplified dynamic model of the plate. This model was then projected in the rotational reference frame, so a model for control could be obtained. The parameters for each mode were then identified experimentally.

Using the dynamic equation in the rotational reference frame, a decoupled model of the plate at resonance was deduced. Based on this decoupled model, we were able to design and implement a simplified control scheme, using two PI controllers. The results show that we were able to achieve closed loop control of both modes on the plate, with a response time  $\tau = 1.1$  ms, no overshoot, and the steady state error of 0. We have proven that the controller performs well in the presence of an external load such as a finger pressing on the surface of the device without being affected by this disturbance.

In the upcoming chapters we will discuss the mechanisms by which longitudinal and transverse vibrations reduce the friction on the surface of the USHDs. These analysis will help us evaluate the performance of both modes, to determine whether longitudinal vibration is a plausible technological alternative to transverse vibration for ultrasonic haptic applications.

MECHANISMS OF FRICTION REDUCTION IN USHDs FOR  
LONGITUDINAL MODES

Creating a realistic texture illusion using a USHD would ideally require the device to be able to emulate enough properties of the biomechanical interaction of the skin with the simulated material to modify the subject's perception (at any speed, force and direction the user decides to explore). Given the large difficulty of replicating all the different mechanical interactions of the skin against a material, the illusion is constructed simply by creating differences in friction during exploratory touch. Doing this affects the forces applied to the moving finger pad, which influences the nature of the vibrations generated by the relative motion of the skin. This skin motion creates the sensation of a differentiated texture [13]. According to [150], the perception intensity of a texture illusion depends on the amount of friction contrast  $\frac{\Delta\mu}{\mu_0}$  felt during active exploration, with  $\mu_0$  being the friction of the finger against the surface without vibration and  $\Delta\mu = \mu_0 - \mu_{meas}$  the amount of variation of this friction achievable by a given vibration amplitude ( $\mu_{meas}$  is the measurement of friction coefficient at a given vibration amplitude). For producing this friction contrast, the USHD relies on a phenomenon usually referred to as "active lubrication". Through this phenomenon, the friction coefficient of the surface is reduced in the presence of ultrasonic vibration, thus creating a sensation of 'smoothness' [13]. Larger vibration amplitudes are related to a more pronounced friction modulation effect. Consequently, it could be understood that a model of a surface is in fact a spatial arrangement of friction coefficient variations in function of the finger position.

Analyzing the mechanisms by which friction is reduced on both longitudinal and transverse modes can help identifying and understanding the relevant parameters affecting this effect and consequently address the design challenges related to the shortcomings of each technique used.

The phenomenon of friction reduction with ultrasonic vibration has been thoroughly explored with transverse vibration modes, as discussed in Chapter 1 and it is briefly recalled in section 3.1. However, the interaction mechanisms through which friction is reduced with purely longitudinal vibration are seldom explored, thus perhaps underestimated or even neglected. A few examples where this technique is addressed include [124], where a combination of electro-adhesion and longitudinal vibration is studied for a haptic device. In [35], a simplified first order finger model, denominated ‘Bed of Springs’, is proposed in order to explore the effects of this longitudinal motion on the grip function. In this publication, the friction reduction is explained by the ‘Ratchet mechanism’ i.e., the passage from ‘sticking’ to ‘slipping’ states in the stationary grip and the periodical shifting of forces that occur as a product of the vibration. This mechanism is recalled, adapted and evaluated experimentally in [158] for explaining the friction reduction effect using ultrasonic vibration with a finger sliding in the direction of the wave propagation. This development is explained in section 3.2.

However, friction reduction for longitudinal vibration is a subject that requires a deeper assessment. While the semi-Coulombic ‘Ratchet mechanism’ explained in [158] has proven sufficient to justify friction modulation in one dimension along the wave propagation direction, it is not equipped to detail the change in friction when the finger slides in another direction over the surface of a longitudinal USHD. For those cases, we propose that the friction is attenuated mainly due to the increase of the relative exploration velocities that takes place when the device vibrates. To test this theory, a set of measurements at different finger exploration

velocities and directions is made using the device designed in Chapter II. These measurements are used to propose and evaluate a non-Coulombic adhesion model based on experimental results. This approach is developed in section 3.3.

### **3.1 Friction reduction mechanisms using transverse modes**

As detailed in Chapter 1, two main theories are offered in the literature as an explanation to the friction reduction using transversal modes. The first one is the ‘squeeze film’ effect [38], [104], [112], [126], [127]. The principle behind this theory relies on the generation of a thin film of air in the contact region between the USHD and the finger pad by the high speed compression-decompression cycle of the air, which, in turn, creates an acoustic levitation of the skin, thus reducing the friction between the finger and the surface. Alternatively, the ‘intermittent contact’ theory, as illustrated by [25], [35], [114], [115], proposes an interaction mechanism in which, from certain vibration amplitudes, the finger loses and regains periodically contact with the vibrating device, thus effectively reducing the amount of lateral force employed to slide over its surface.

It is accepted that both of the proposed mechanisms contribute to friction modulation on surface ultrasonic devices [132]. However, isolating the contribution of one and the other under atmospheric pressure conditions is highly complex and it is impossible to know exactly in what proportion each mechanism acts [132].

Nevertheless, a set of experiments seem to indicate that the contact between the finger and the USHD oscillates along with the device’s vibration, but out of phase by an angle dependent on the dynamic damping of the finger [175]. Furthermore, it appears that the average distance between the finger ridges and the haptic surface increases with vibration [132]. The combination of these observations suggests that the intermittent contact of the skin is not directly on the surface of the USHD but on the air film that composes the squeeze-film [132].



Finally, in addition to the device's vibration characteristics (amplitude and frequency), the mechanical properties of the probing object are a determinant factor when calculating the amount of friction modulation [116]–[118], [131]. This dependence and the relation to the finger's biomechanics are explored in the upcoming chapters.

### 3.2. Friction reduction with longitudinal ultrasonic vibration in one dimension

#### 3.2.1. Bed of Springs Approximation

In this model, the finger is modelled as two adjacent springs, with constants  $k_{nf}$  and  $k_{lf}$  representing the normal and lateral elasticity of sc. at ultrasonic frequencies respectively.

Table 3. Parameters of the simplified finger model

Parameter	Simulation values		
	Equation	Symbol	Value
Young Modulus sc	-	$E_e$	1 – 100 MPa
Poisson Modulus	-	$\nu_f$	0.4
Shear Modulus sc	$G_{ef} = \frac{E_{ef}}{2(1 + \nu_f)}$	$G_{ef}$	1.43x106 Pa
Height of fingerprint ridges	-	$h_{ef}$	150 $\mu\text{m}$
Elastic constant for finger deformation	experimental data	$k$	138.1 x10 <sup>-6</sup>
Normal force applied on the device	-	$f_n$	0.5 N
Lateral force applied on the device	-	$f_l$	-
Contact area (Herzian)	$A_c = kF_n^{2/3}$	$A_c$	8.7x10 <sup>-5</sup> m <sup>2</sup>
Normal spring elasticity	$k_{nf} = \frac{2E_{ef}A_c}{h_{ef}}$	$k_{nf}$	4.64 x10 <sup>6</sup> Nm
Lateral spring elasticity	$k_{lf} = \frac{G_{ef}A_c}{h_{ef}}$	$k_{lf}$	2.07x10 <sup>6</sup> Nm

It is believed [30] that, at ultrasonic vibration frequencies, the sc is the main part of the finger which is concerned with the interaction.

The parameters used for the calculations are based on [115] and adjusted for this work. They are detailed in Table 3. For the analysis presented in section 3.2.2., it is assumed that the lateral spring is equally deformable in every direction over the surface.

### 3.2.2. Friction reduction through the 'Ratchet Mechanism' on a moving finger

In a longitudinal vibration mode, it is assumed that the compression of the normal spring is constant, so the finger is continuously in contact with the device, producing a global pressure force  $f_n$ . The deformation of the lateral spring, on the other hand, depends on the relative velocity between the finger pad and the explored surface (plate). For this initial analysis, it is also assumed that the finger slides in the axe of the longitudinal wave propagation, so the motion can be defined along a single axe. The velocity of the longitudinal deformation at a point on the plate can thus be described as in (58), with  $u_p(t)$  representing the instantaneous velocity of vibration, ' $W$ ' the peak amplitude,  $\omega$  the angular frequency and  $t$  the time (the angle of vibration is  $\theta = \omega t$ ). We consider that the finger moves with a constant velocity  $u_f(t)$ . Hence, the relative velocity of the finger viewed from the device  $u_{fp}(t)$  can be expressed as in (59) (positive velocities are defined to be in the same direction as the finger displacement).

$$u_p = \omega W \cos(\omega t) \quad (58)$$

$$u_{fp} = u_f(t) - \omega W \cos(\omega t) \quad (59)$$

With a relative velocity such as the one described in (59), the interaction of the device and the finger can be described as a state machine with three states: 'stick', 'slip' and 'drag' ('drag' is a representation of the 'slip' state, but in the opposite direction. It is useful to separate them for the analysis). The state machine is

described in Figure 35. Whenever  $u_{fp} = 0$ , the finger enters in ‘stick’ state. In this state, the lateral force applied by the sc on the plate,  $f_l$ , is dictated by the elongation of the lateral spring, denoted  $\Delta x$  and its elastic constant  $k_{lf}$  (exemplified in Table 3). The sign of  $f_l$  denotes the direction of the deformation of the lateral spring (positive friction is referenced opposite to the direction of the finger motion). Once the machine has entered in ‘stick’, it stays in this state until the spring reaches a maximum deformation in either direction ( $\Delta x_{max}$  or  $\Delta x_{min}$ ), that is, when the force exerted by the spring surpasses the static friction coefficient  $\mu_s$ , multiplied by  $f_n$ :  $k_{lf}\Delta x_{max} = f_n\mu_s$  and  $\Delta x_{min} = -\Delta x_{max}$ .  $f_l = f_n\mu_d$

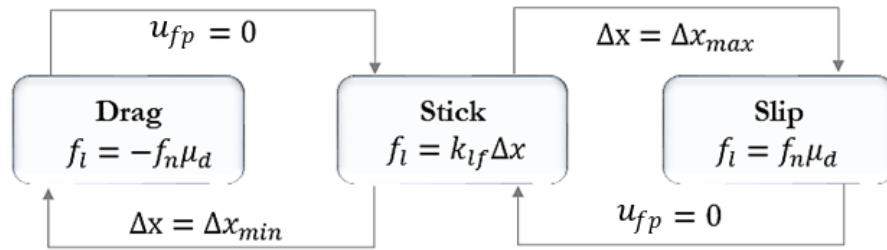


Figure 35. State machine describing the finger-device interaction according to the “ratchet mechanism”

If the deformation is in the direction of the finger displacement, the next state is ‘drag’. If not, it is ‘slip’. In any of these two states, the lateral force is considered Coulombic, thus, equal to  $f_n\mu_d$ . This interaction is simulated and shown in Figure 36.

Finally, the lateral force felt by the finger is equal to the absolute value of the average of the lateral forces over a complete period of vibration.

As the amplitude  $W$  or frequency  $\omega$  increase, so does the magnitude of the speed of the plate, according to (58). Increasing plate velocity relative to  $u_f$  has the effect of making  $u_{fp}$  more centered in zero and in consequence, the average lateral force over a period will be reduced.

### Longitudinal wave interaction according to the ratchet mechanism

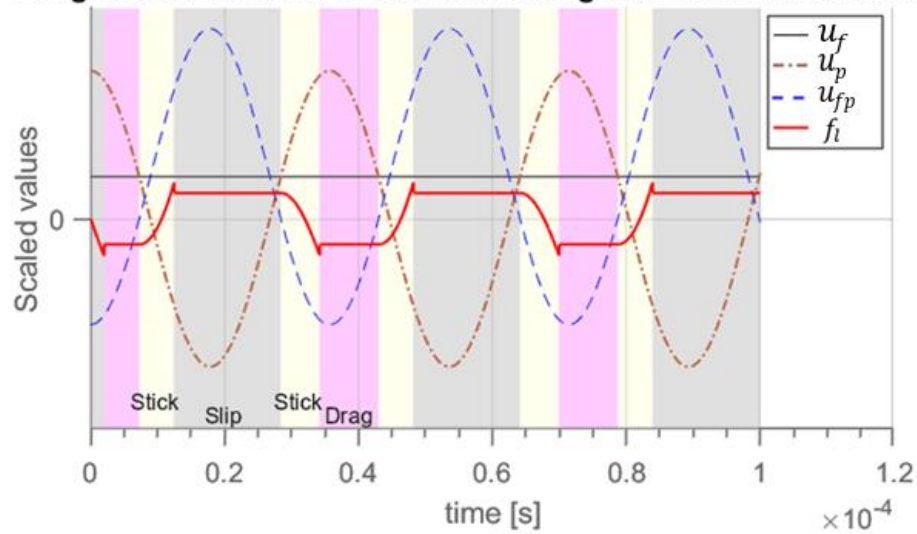


Figure 36. Longitudinal wave interaction model depicting states stick, slip and drag. Lateral force  $f_l$  is presented together with the plate velocity  $u_p$ , the finger velocity  $u_f$  and the relative velocity of the finger seen from the plate  $u_{fp}$ , over a number of periods measured from an arbitrary time.

#### 3.2.3. Friction reduction model validation with experimental data

The proposed friction modulation model is validated with the 30 kHz longitudinal ultrasonic device created as explained in Appendix 4. The longitudinal wave device is mounted on a tribometer as depicted in Figure 37. The utilized probe is composed of a rigid polymeric material covered in plaster.

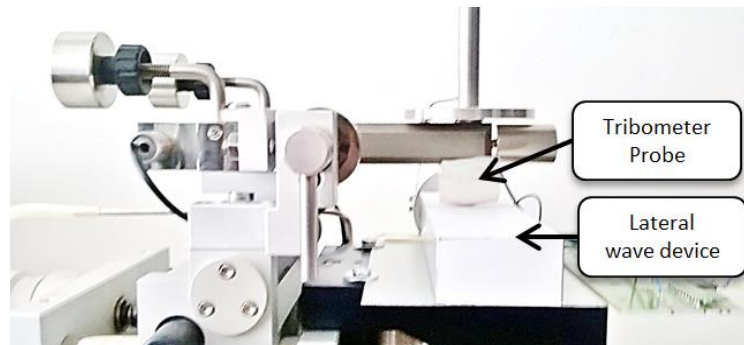


Figure 37. Longitudinal vibration device mounted on a tribometer to perform tests on friction reduction at different vibration amplitudes

A series of tests is performed at various exploration speeds (30, 60, 90 and 120 mm/s) with three normal forces (0.5N, 1N and 1.5N). These exploration speeds and normal forces are imposed on the tribometer probe against the vibrating beam. The probe is made to perform a reciprocating lateral motion through a distance of about 6cm, passing along the maximum of longitudinal vibration.

The relative friction coefficient is related to the friction contrast by the equation  $\mu' = 1 - \Delta\mu/\mu_0$ . It is calculated from the tribological measurements as in equations (4) to (6). The measured friction  $\mu_{meas} = \mu_k$  at each point 'k', represents a measurement at a given probe velocity and vibration amplitude, and  $k = 0$  is the no vibration point. The relative friction coefficient at every amplitude and velocity in the tested range is plotted in Figure 38, for three different normal force values.

$$\mu_k = f_{l_k} / f_{n_k} \quad (4)$$

$$\mu_0 = f_{l_0} / f_{n_0} \quad (5)$$

$$\mu'_k = \mu_k / \mu_0 \quad (6)$$

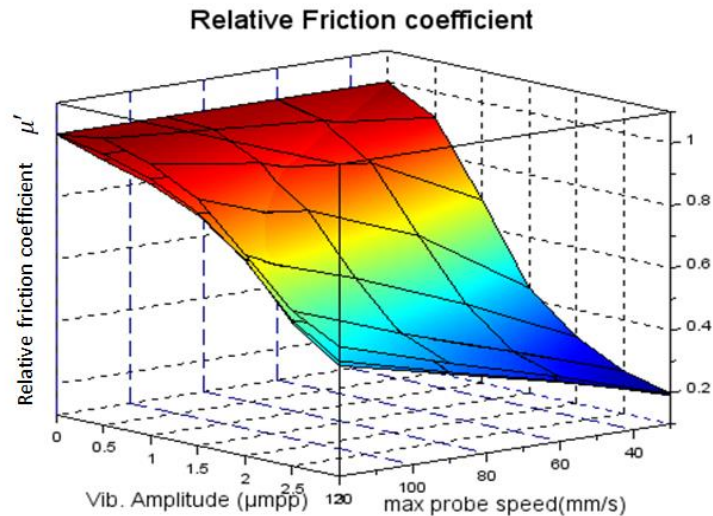


Figure 38. Relative friction coefficient in function of probe speed and vibration amplitude for three normal force tests

Based on the obtained results, it may be noticed that, as expected, the friction modulation increases with the amplitude of vibration. Additionally, it can be observed that variations of the applied normal force do not influence significantly the modulation results. On the other hand, an important inverse dependence is found between friction coefficient modulation and finger exploration speed. This means that, as the probe goes faster, the effect of ultrasonic longitudinal vibration in friction reduction is diminished, because the vibration speed is smaller in comparison to the speed of the probe. This emphasizes once again the influence of the relative speed.

An example of tribometric results against model estimations is depicted in Figure 39. The properties of the probe are estimated in order to fit the model to the results. When confronted with the measurements, the model is able to provide curves with similar tendencies and values (with a margin of error of about +/- 0.1, related to the simplicity of the model and assumptions made).

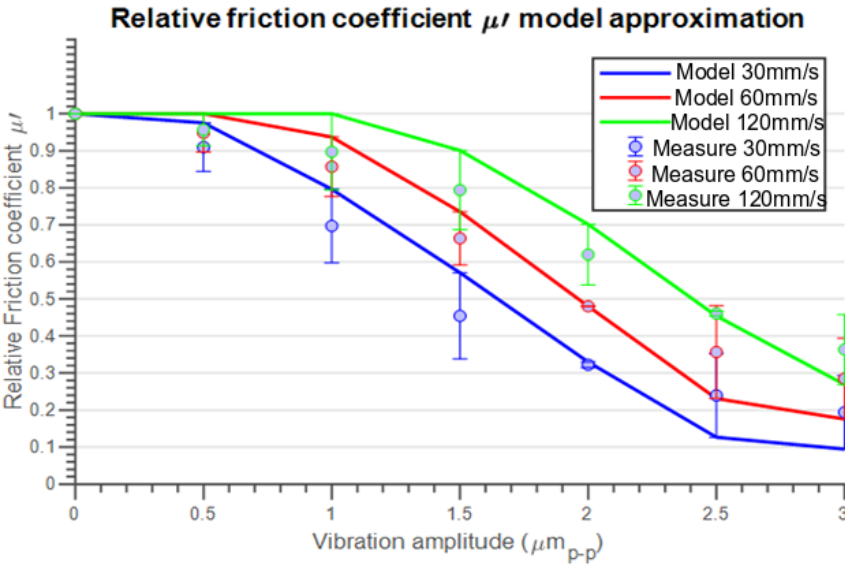


Figure 39. Relative friction coefficient at constant  $f_n = 1.5N$  and varying exploration speeds (30, 60, 120mm/s) vs. model results (continuous lines).  $E_{ef} = 10MPa$ ,  $\mu_s = 1$  and  $\mu_d = 0.9$ .

### *3.2.4. Parametric analysis*

From the results obtained in the previous sections, it can be noticed that a set of parameters of exploration are more relevant in terms of friction modulation with longitudinal modes than others. These main parameters are the velocity of exploration and the vibration frequency (i.e. the relative velocity between the probe and the plate), plus the mechanical properties of the probe. One interesting result, is that the normal force does not seem to have an important impact on the relative friction contrast created at a given vibration amplitude, which is why it is not relevant in the presented analysis. In the following sub-sections, we detail the impact of the selected exploration parameters in the friction modulation with longitudinal modes.

#### 3.2.4.1. RELATIVE VELOCITY

For transverse modes, it has been proven [115] that an increase of the exploration velocity reduces the amount of achievable friction contrast at a given vibration amplitude. This is also the case in longitudinal modes [158]. Similarly, it has been observed [114], [115] that the friction contrast is increased at higher vibration frequencies for both transverse and longitudinal modes. The two observations lead to the same inference, that in transverse and longitudinal modes, the friction reduction is dependent on the relative velocity between the probe or finger and the vibrating plate. In short, the faster the plate moves with regards to the probe, the more present is the friction reduction phenomenon.

An explanation for this result in transverse modes is given in [115], using an intermittent contact model with a mass-spring system representing the stratum corneum. With this model it is shown that a reduced relative velocity leads to a shortening of the finger elastic loading time in the no-contact (fly) state, increasing the pre-contact residual deformation of the finger, thus provoking its surface to spend more time ‘sliding’ over the surface than deforming. As a result, the mean

friction over a vibration period is increased. In the case of longitudinal modes, it can be deduced from a simple spring-slider model [35] that, as the speed of the finger is increased, the relative velocity between this finger and the plate is reduced consequently. As explained in section 3.2.3 (and furthermore in 3.3), this leads to a reduced friction contrast.

#### 3.2.4.3. PROBE ELASTICITY

As observed in previous studies [115], [116], [118], [131], [158], [176], the phenomenon of active lubrication for both modes is highly depending on the physical characteristics of the probing object. From [158] it can be observed that the stiffness of the probe tends to favor longitudinal modes over transverse modes and vice-versa. This will be further addressed in Chapter 4.

### **3.3. The non-Coulombic model of dynamic friction for longitudinal modes**

The ratchet mechanism approach, explained in the previous sections, appears appropriate to explain and simulate the mechanical interaction between the finger and the vibrating surface when the finger movement coincides with the axis of the longitudinal wave propagation. However, an amount of friction reduction is also noticed when the finger moves in other directions over the surface. This phenomenon is not explainable by the proposed approach and thus, alternative explanations need to be explored, going deeper in the contact physics. This paragraph aims at proposing an additional interaction model, which may serve to explain the friction modulation using longitudinal vibration, irrespectively of the direction of exploration.

For a USHD, the friction modulation that is experienced arising from lateral ultrasonic vibration, could be explained by a few simultaneous effects. Friction is the result of the energy dissipated per unit sliding distance in a sub-surface region of the order of 100 nm (interfacial mechanism) or in much deeper regions



(deformation mechanism). In the case of skin, it has been shown that the friction is dominated by the interfacial mechanism [177] for which the frictional force is given by the product of the interfacial shear strength and the contact area; this is known as the adhesion mechanism since this shear strength depends on the intermittent formation and rupture of intermolecular bonds such as the van der Waals bonds. In the dry state, the skin exhibits glassy behaviour and the shear strength increases gradually with sliding velocity. However, in a persistent contact with an impermeable surface such as glass, a finger pad becomes plasticized by occlusion of the secreted moisture by the sweat such that there is a transition to the rubbery state, which corresponds to the experimental conditions applied in the current work.

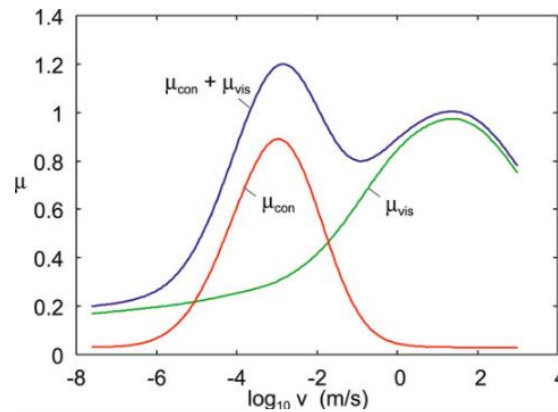


Figure 40. The contribution to the friction coefficient from viscoelastic deformations ( $\mu_{vis}$  in the figure) and from the adhesion over the area of real contact ( $\mu_{con}$  in the figure) as function of sliding speed in a typical case at room temperature (Schematic) [178].

As exemplified in [178], and illustrated in Figure 40, the friction as the function of velocity for a rubber sliding on a rough track shows, in general, two peaks. One occurs at high sliding velocities and it has been mainly attributed to a viscoelastic contribution, and the other, occurring in general at much lower velocities, that corresponds to those studied here, is considered attributable to the adhesion mechanism [179]. This may be explained as following: the energy

dissipation involves the stochastic pinning and depinning of surface polymeric molecules to the counter surface by a stress aided thermally activated process that depends on the surface exploration velocity [13], [177], [180]. At low velocities, there is sufficient time for the molecules to stretch within the critical depinning time. As the velocity increases, the molecular extension increases and, hence, so does the frictional force. However, at higher velocities, the rate of breakage of bonds is greater than their formation, which causes the friction to decrease with increasing velocity. Additionally, if a finger pad behaves as an elastomer, the strength of adhesion generally increases with the time of contact, due to slow molecular rearrangements that occur at the interface and increase the bond strength [181].

The real contact area  $A_c$  is also an important factor which affects the dynamic friction at different exploration speeds. Assuming constant ridge contact, a Herizian model would allow considering that the evolution of the contact area at the fully occluded state increases with the normal force with a power  $m=2/3$ . In reality, however, the contact corresponding to a finger pad and a plate is not Herizian. The evolution of the contact area is therefore a complex mechanism that depends on many factors such as the loading [8], the geometry of the finger and ridges [182], the dwell time of the contact [31], [183], the onset of occlusion [13], [31] and the contact deformation due to the velocity and direction of exploration [182].

So, in addition to the ratchet mechanism, friction reduction due to longitudinal vibration can also be explained by the variation in shear strength because of an augmented relative velocity of the finger against the plate and a reduction in the real contact area.

In this section we propose to develop a dynamic friction model based on practical measurements using a USHD, which takes into account the variation of the most relevant parameters related to friction in function of velocity, assuming that

additional factors such as loading force, finger inclination and exploration direction are controlled and constant throughout the tests.

Under these conditions, we assume that while sliding, the friction forces could be represented by the extension of a spring, with variable elastic coefficient depending on velocity. The elastic coefficient dependence with the velocity function is built based on experimental results, which are supposed to reflect the added effect of shear strength and contact area variation.

Based on the explained assumptions, a series of experiments is proposed to explore the friction reduction model due to longitudinal ultrasonic vibration. Section 3.3.1 briefly explains the effect of exploration speed on the shear strength and contact area in sliding finger contacts. In section 3.3.2, we propose an experiment to measure the change of friction at different speeds for a finger pad in the case without vibration. The measurements are fitted to the model obtained in 3.3.1. In section 3.3.3, a series of measurements is made to obtain the mean friction reduction at different speeds and vibration amplitudes, in two different exploration directions. In section 3.3.4, simulations aim to describe the 2-dimensional relative velocities and relative trajectories of the finger against the plate when it is vibrating. The empirical model fitted in section 3.3.2 is then used to evaluate whether the friction attenuation with a longitudinal ultrasonic vibration can be explained by the changes in finger relative velocity  $u_{fp}$  during exploration.

### *3.3.1. Friction variation on a finger pad due to sliding velocity*

#### 3.3.1.1. TIME-CONSTRAINED SHEAR STRENGTH

The sliding velocity range that is most relevant to tactile exploration is about 10–200 mm/s [13]. Within this sliding velocity range, it is possible to find a dynamic friction peak related to adhesion [179], such as the one exemplified in Figure 40.0. Provided that a finger pad is sufficiently moist, particularly due to occlusion of moisture secreted from the sweat pores in the finger print ridges, it has been

shown [177] that the friction may be described by molecular theories that have been developed for elastomers [180], [184]. In such cases, the friction arises from the intermittent extension and rupture of monomer chains between the elastomer and the surface. We assume the van der Waals forces cause the adhesion of the polymers to the surface, so we can define a critical rupture stretch  $S^*$ , a rupture energy  $\varphi^*$  and a rupture length  $a^* = r^*/Rf$ , where  $r^*$  is the elongation of the chain and  $Rf$  is equal to the Flory ratio [180]. The effect of every link is independent, so the resulting force is the addition of all individual forces [180].

### 3.3.1.2. STATIC FINGER ANALYSIS

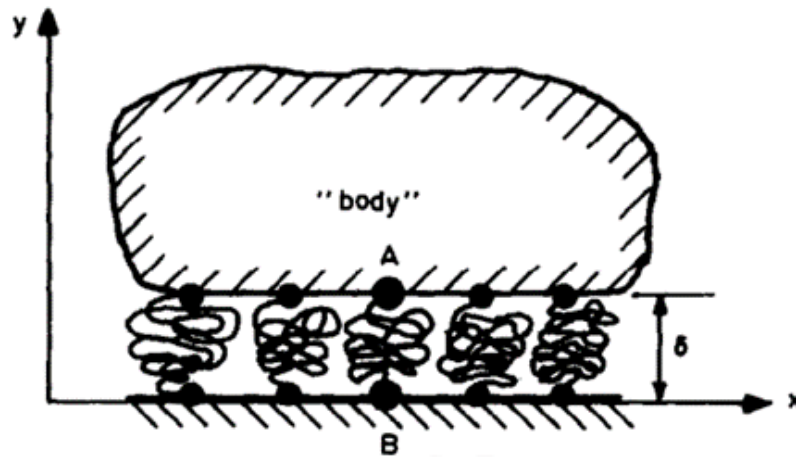


Figure 41. Sketch of the contact region between the elastomer body and the surface. A and B are the terminal points of the linking chain [180].

When the finger is static, the contact can be visualized as exemplified in Figure 41. The distance between the tethered ends of the link is  $\delta$ , so the mean stretch force of a single polymer chain is defined by  $\langle S \rangle_{ob} = B\varphi' \delta / Rf$ , with  $B$  equal to the Boltzmann constant [180].

The polymer chain, which we assume attached at  $t = 0$ , receives a constant influx of thermal energy from the surface, the environment and the body. Since this input is completely random, the probability  $\mathcal{P}(t)$  that exactly  $\nu$  excitations (thermal energy input to a single chain) with an energy exceeding a certain value  $U$  excite the linking chain during time  $t$  is given by the Poisson distribution  $\mathcal{P}_\nu = \frac{(t/\tau_0)^\nu}{\nu!} e^{-(t/\tau_0)}$ . At a standard temperature  $T$ , we may write  $\tau_0 = \tau^* e^{\frac{\nu}{BT}}$  with  $\tau^*$  being a time constant proportional to  $Rf^3$  [177]. At this temperature  $T$ , the probability of a linking chain to survive the period  $(0, t)$  is  $\langle \mathcal{P} \rangle_{ob} = e^{-(t/\tau_0)}$ , so the probability of a linking chain to break during the same period is  $\langle \mathcal{P} \rangle_o = 1 - e^{-(t/\tau_0)}$ . We can therefore express the probability density for thermal breakdown as in (60) [180].

$$p_{bf} = \frac{d\langle \mathcal{P} \rangle_o}{dt} = \frac{1}{\tau_0} e^{-(t/\tau_0)} \quad (60)$$

The quantity  $p_{bf}$  is in fact the transition probability from a bounded to a free state. In consequence, the mean time for which a polymer chain stays in contact with the surface  $\langle t \rangle_{ob}$  is defined in (61), so we can infer that  $\tau_0$  is the lifetime of the polymer linking chain when the finger is not moving [180].

$$\langle t \rangle_{ob} = \int_0^\infty t p_{bf}(t) dt = \tau_0 \quad (61)$$

Similarly, if the linking chain is hovering in close proximity to the counter-surface, we can express  $p_{fb}$  as the probability density of capture of the chain by the surface at instant  $t$ , and we can write for the hovering time  $\langle t \rangle_f = \int_0^\infty t p_{fb}(t) dt = \tau$  (where  $p_{fb}$  is the probability of transition from a free to a bounded state and  $\tau$  is therefore defined as the ‘fundamental relaxation time’ [180]). To make the linking chains detach, the excitation energy  $U$  must be conveyed to all chain segments simultaneously, which is a very rare event. From

these considerations, it is inferred that  $\tau_0$  should be identical with the fundamental relaxation time  $\tau$  when the finger is not moving.

Since we assumed that all polymer linking chains are identical, the mean number of the linked chains per unit area is given by (62), where  $N_0$  represents all the linking chains over a unit area.

$$\widehat{N}_o = N_0 \frac{\langle t \rangle_{ob}}{\langle t \rangle_{ob} + \langle t \rangle_f} = N_0 \frac{\tau_0}{\tau_0 + \tau} \quad (62)$$

Finally, the vertical force (over the  $z$  axis, out of plane) formed due to the linked polymer chains of a static finger can be expressed as the mean stress of a single chain, multiplied by the mean number of linked chains per unit area (63) [180].

$$f_z = \widehat{N}_o \langle S \rangle_{ob} = N_0 \frac{\tau_0}{\tau_0 + \tau} \left( \frac{B\varphi'\delta}{Rf} \right) \quad (63)$$

### 3.3.1.3. DYNAMIC FINGER ANALYSIS

We assume that the finger begins to slide over the surface with a velocity  $u_f$  in the lateral  $x$  axis. A chain is attached at  $t = 0$  over a random point  $A'$  on the elastomer, to which we assign the  $x, y, z$  coordinates  $(0, 0, \delta)$ . At time  $t$ , it has slid to point  $A = (u_f t, 0, \delta)$ , as exemplified in Figure 42, and we may write  $S(t) = \frac{B\varphi'r}{Rf}$  with  $r(t) = \sqrt{\delta^2 + u_f^2 t^2}$ .

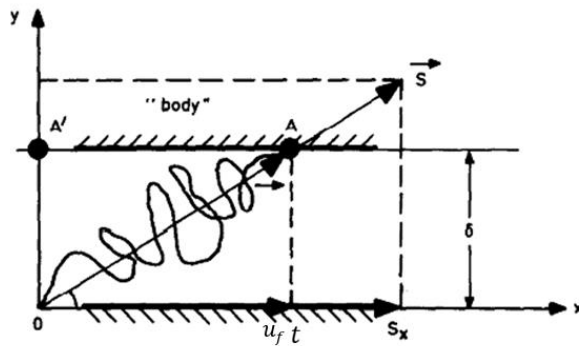


Figure 42. Sketch of the polymeric linking chain stretching from points  $A'$  to  $A$ .  $S$  is the vector of the tension force in the linking chain [180].

This yields that at a higher sliding velocity, the stretch  $S$  caused by the elongation of the linking chain is greater and thus, the associated activation energy for rupture is reduced and the lifetime of the bonds is also reduced. It is possible to define, therefore, a pinned time constant  $\tau_p$ , as a function of contact time and sliding velocity as described in (64) [180].

$$\tau_p(u_f, t) = \tau_0 e^{-\left(\frac{S(t)}{BT}\right)} \quad (64)$$

For the case that the activation energy for the depinning of a chain is constant, the mean lifetime for survival of pinned chains  $\langle t \rangle_p$  can be expressed as (65), where the ‘break off length’  $a^* = r^*/Rf$  can be defined as in 3.3.1.1 [177].

$$\langle t \rangle_p = \tau_p \left( 1 - e^{-\left(\frac{a^*}{u_f \tau_p}\right)} \right) \quad (65)$$

The new amount of pinned molecular chains  $N_p$ , given in (66) is therefore smaller than the number when there is no sliding  $\hat{N}_o$  given by (62), since  $\langle t \rangle_p < \langle t \rangle_{ob}$ .

$$N_p = N_0 \frac{\langle t \rangle_p}{\langle t \rangle_p + \langle t \rangle_f} \quad (66)$$

The model developed for describing the dependence of dynamic friction on sliding velocity was extended to account for the viscous retardation [180]. An expression for the equilibrium value of the coefficient of friction,  $\mu_E$ , was derived and found to be consistent with data measured for the finger pad [177]. In this latter work, the expression was written as in (67), where  $q = \tau_0/\tau_p$  and  $u_f^* = u_f/u_{f_0}$  such that  $u_{f_0}$  corresponds to the critical velocity at which stress-aided depinning becomes significant.

$$\mu_E = 2\mu^+(q + 1) \left\{ \frac{u_f^* [1 - e^{-1/u_f^*}] - e^{-1/u_f^*}}{1 + q - e^{-1/u_f^*}} \right\} \quad (67)$$

The parameter  $\mu^+$  corresponds to the maximum value of the friction coefficient  $\mu$  with respect to the sliding velocity and normal force  $f_n$ , and is given by (68).

$$\mu^+ = \frac{N_0 B T a^*}{2(1 + q R_F^2) f_n} \quad (68)$$

#### 3.3.1.4. DWELL TIME, VELOCITY AND FRICTION

It is easy to deduce that the result of (68) is dependent on the available number of linking chains per unit area  $N_0$ . During the derivation in section 3.3.1.1, we have assumed that this is a constant value. In reality, however, the availability of linking chains is dependent on the contact area  $A_c(t)$ , which, in the case of smooth, impermeable surfaces such as glass, increases very slowly as a function of the dwell time. In [31], this temporal evolution of the contact area against glass is described with a first order kinetics equation,  $A_0$  and  $A_\infty$  correspond to  $A_c$  at  $t = 0$  and  $t \rightarrow \infty$ , respectively and  $\lambda$  is a characteristic time constant (69).

$$A_c(t) = A_\infty + (A_0 - A_\infty) e^{-\left(\frac{t}{\lambda}\right)} \quad (69)$$

In practice, it is difficult to produce ranges for these values, since there is a very large variability between the different studies on different subjects and materials [31]. Additionally, (69) does not take into account the deformation at the contact area between the finger and a flat surface during the onset of tangential sliding movements in the different directions (proximal, distal, radial and ulnar, which vary in different amounts at different values of normal force and tangential speeds [182]. According to this last study, the contact area was more or less inversely proportional to velocity  $u_f$ , and more or less symmetrical in the radial-ulnar direction.

#### 3.3.1.5. FRICTION FUNCTION APPROXIMATION

Considering the various effects that influence the velocity dependent friction function of a finger pad against an impermeable, hard and smooth surface such as



glass, it is difficult to produce a completely analytical model. We propose therefore a simplified adaptation of (67), modifying  $\mu^+$  to be  $\mu^*(u_f)$ , a friction factor dependent on speed, described by a second order kinetics equation (71).

$$\mu_E = 2\mu^*(q + 1) \left\{ \frac{u_f^* [1 - e^{-1/u_f^*}] - e^{-1/u_f^*}}{1 + q - e^{-1/u_f^*}} \right\} \quad (70)$$

$$\mu^*(V) = \mu_{t \rightarrow 0} + (\mu_{t \rightarrow \infty} - \mu_{t \rightarrow 0}) e^{-(u_f^2/k_V)} \quad (71)$$

We could therefore find limit values for  $\mu^*$ , which would account for the friction variation dependence on exploration speed, such as junction area increase, stretch increase of the individual linking chains, and real contact area deformation, as in (71), with a pinning constant  $k_V$ . This model can be fitted to average experimental data, in order to obtain the values  $\mu_{t \rightarrow \infty}$ ,  $\mu_{t \rightarrow 0}$ ,  $k_V$ , together with  $q$  and  $v_{f_0}$ . We assume for these measurements that they are obtained at almost constant normal forces  $f_n$  after a period  $t$ , which is sufficient for processes such as occlusion to take place.

### 3.3.2. Friction vs. sliding velocity measurements

#### 3.3.2.1. FORCE MEASUREMENTS WITHOUT VIBRATION AND FRICTION MODEL FIT

The surface haptic device developed in Chapter II is used for data collection. The device is placed over the moving base of a tribometer, as depicted in Figure 43. Below the device, a three-axial force sensor (GSV-4USB from ME-Meßsysteme) is installed to record the normal and friction forces. Next to the setup, a base is installed for the hand and finger, so that they may be properly positioned over the surface of the device.

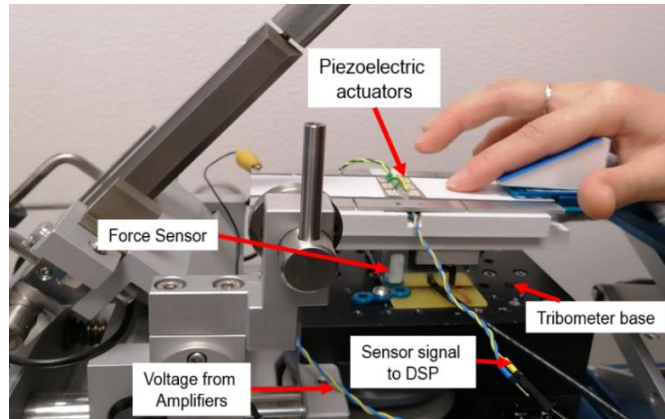


Figure 43. Haptic device placed over three-axial force sensor and tribometer base

In the initial phase of the experiment, a participant is asked to clean and dry his (her) finger, and to position it on top of the upper surface, as shown in Figure 43. A visual interface allows the participant to maintain an appropriate normal force on the device of about 0.5N. The base of the tribometer is programmed to perform several reciprocating motions below the static finger, while the information is recovered with the three-axial force sensor.

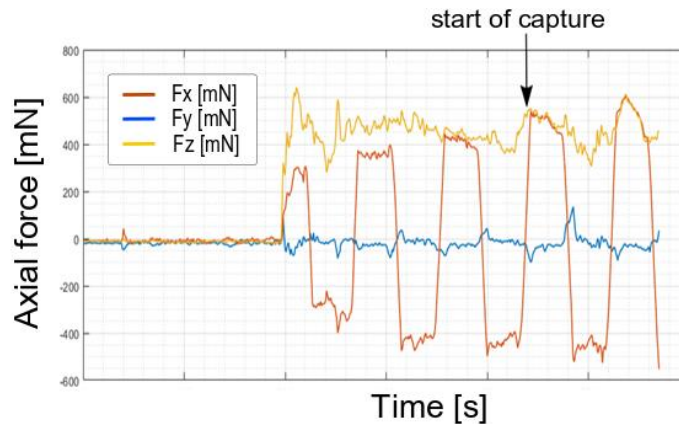


Figure 44. Force measurement for axes  $x$  (red),  $y$  (blue),  $z$  (yellow) in [mN]. The arrow represents the start of data acquisition.

The force signals from the  $x$ ,  $y$ ,  $z$  axes are acquired as shown in Figure 44. After the finger is positioned on the plate, six to eight reciprocating motions were applied

before beginning the data acquisition. The coefficient of friction was calculated by dividing the force measurement on the  $x$  axis by the force in the  $z$  axis.

Friction measurements were obtained in the range of 20 mm/s to 140 mm/s in increments of 20 mm/s. The mean friction at each velocity was recorded. Measurements were then repeated for a group of eight participants aged between 18 and 60 years. All participants gave informed consent. The investigation conformed to the principles of the Declaration of Helsinki and experiments were performed in accordance with relevant guidelines and regulations.

The friction measurements without vibration for eight participants and the mean of the complete set are shown in Figure 45.

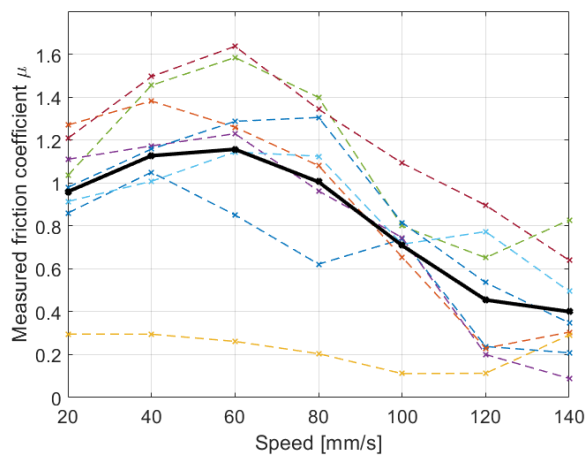


Figure 45. Friction coefficient measurement with no vibration for eight participants (dotted lines) and the mean of the complete set (solid black). The mean value at each speed is calculated from the measurements of all participants depicted in the figure.

As expected, a dynamic friction peak is found around 20 to 60 mm/s, followed by a steady reduction up until 140 mm/s. From 120 mm/s, some participants show a continuity or even an increase of the dynamic friction. . Finally, one of the seven participants appears to have a coefficient of friction significantly smaller than the others, and thus this friction variation is also less significant in scale. This particular case may be explained by a drier skin.

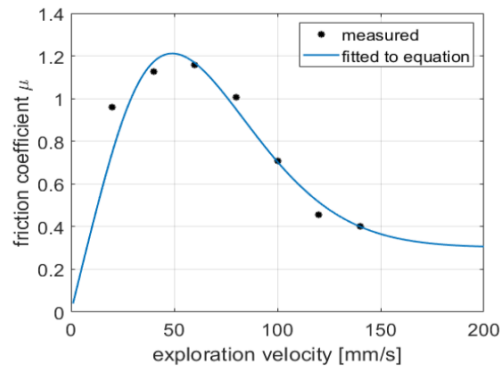


Figure 46. Mean friction coefficient vs. speed data measurements fitted to model in (72)

The mean values of friction are fitted to (70), as can be seen in Figure 46, with  $\mu_{t \rightarrow \infty} = 1.86$ ,  $\mu_{t \rightarrow 0} = 0.156$ ,  $k_V = 0.0048 \text{ m}^2/\text{s}^2$ ,  $q = 0.0177$  and  $u_{f_0} = 68 \text{ mm/s}$ .

### 3.3.2.2. FORCE MEASUREMENT WITH ULTRASONIC VIBRATION ACCORDING TO EXPLORATION DIRECTION

A two-dimensional view of the exploration surface over the  $xy$  plane is recalled in Figure 47.

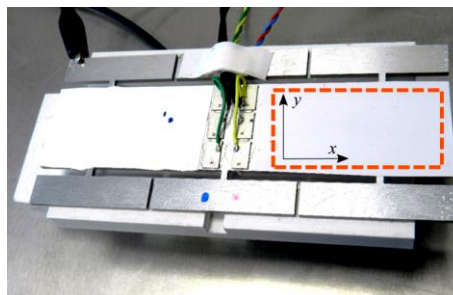


Figure 47.  $xy$  coordinate system over the exploration surface of the USHD, as defined in Chapter 2.

It is assumed that  $x$  represents the direction of the longitudinal wave propagation. Using the procedure described in section 3.3.2.1, the friction measurements were

made with all participants at the same velocities as for the previous experiment. This time, a longitudinal closed loop vibration of about 58 kHz at six different vibration amplitudes of 0, 0.8, 1, 1.2, 1.4 and 1.6  $\mu\text{m}_{\text{p-p}}$  is imposed on the device. The measurements are taken as the finger explores along the  $x$  axis and then again exploring along the  $y$  axis (the finger moves always in the radial-ulnar direction, but the plate changes orientation). The results are recorded separately. Figure 48 shows two plots of the mean of the measurements in both directions at the different exploration speeds and vibration amplitudes. A friction attenuation in both directions is perceived in the measurements, (although it seems slightly greater in the  $x$  direction).

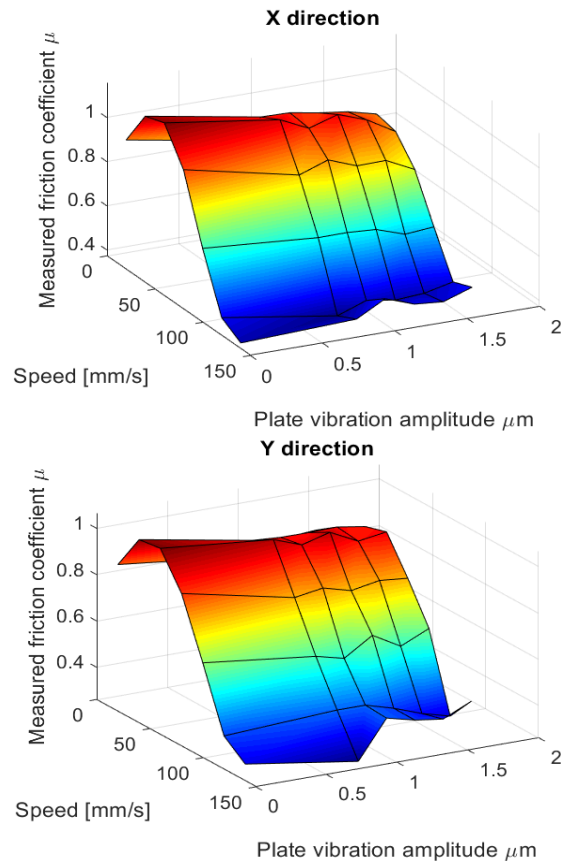


Figure 48. Mean friction measurements for exploration in the  $x$  and  $y$  directions, in function of speed and vibration amplitude with  $f_n=0.5\text{N}$

In

Figure 49 we present the detail of the mean measurements along the  $x$  and the  $y$  axes without vibration, and with a vibration of  $1.6 \mu\text{m}_{\text{p-p}}$ . The mean friction in the  $x$  direction appears a little higher than the mean friction measured in the  $y$  direction (in part due to measurement error margins). Nevertheless, we observe that the friction attenuation effect is similar in both cases. It is more important at lower velocities, below about  $90 \text{ mm/s}$ . From this result, it can also be observed that, even though a little smaller, the friction attenuation is possible when the finger moves along the  $y$  axis, as well as it does along the  $x$  axis. The reason for this, as will be explained in the next section, is that the vibration increases the average relative sliding velocity, causing the friction to reduce through the mechanisms explained in section 3.3.1.

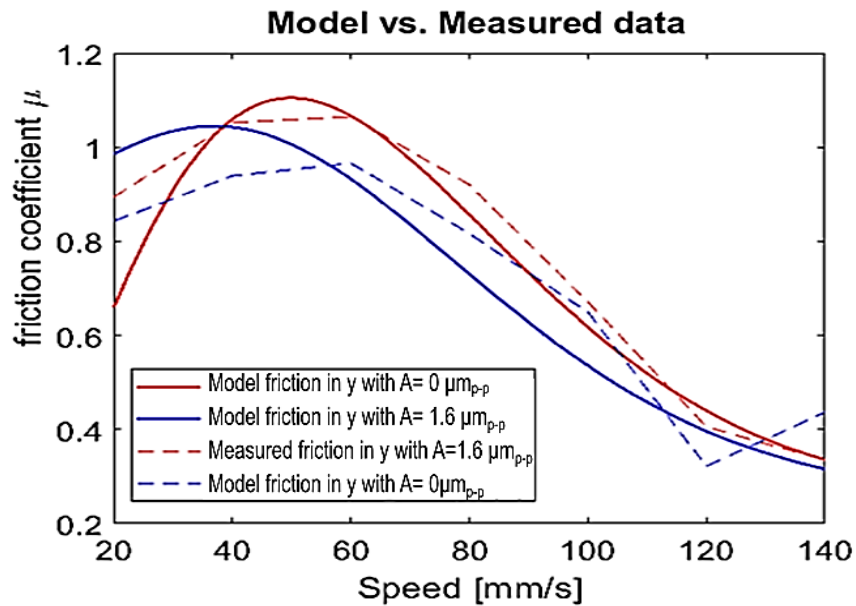


Figure 49. Mean friction measurements with and without vibration at different finger speeds for the  $x$  and  $y$  exploration direction with  $F_n=0.5\text{N}$ . To change the direction, the device is repositioned on the base.

### 3.3.3. Finger pad Relative Motion and Friction

#### 3.3.3.1. RATCHET MECHANISM WITH NON-COULOMBIC DYNAMIC FRICTION ON A PLANE

As explained in 3.3.1, when the skin slides over the flat surface of the haptic device, it experiences a frictional force that depends on the speed of exploration. When a lateral vibration is imposed on the device, the relative speed of the finger pad over the surface is modified. As a consequence of this motion, the skin of the stratum corneum (sc) is expected to be deformed and then to slide over the surface. To calculate the reactive force produced from this interaction, a simplified polar spring-slider model is proposed. This model visualizes the skin as a dampened spring deformable in any direction over the  $xy$  plane.

In a similar way as in section 3.2, the interaction can be visualized as a state machine with two different states, ‘stick’ and ‘slide’ (‘drag’ is incorporated in the ‘slide’ state). When sticking, the deformation of the dampened spring produces a radial force  $f_{rad}$  in the direction of the motion. If we add a dampening factor, this force is equal to  $f_{rad} = K_{rf}r_f + D_{rf}\dot{r}_f$ , with  $r_f$  representing the radial elongation of the spring  $K_{rf}$ ,  $\dot{r}_f$  the velocity of this elongation and parameters  $K_{rf}$  and  $D_{rf}$  equal to the radial elasticity and dampening of the sc respectively (similar to  $k_{lf}$  in section 3.2, but in the polar coordinate system and an added dampening factor. We assume for this model that these parameters are the same in every direction).

The ‘stick’ state is induced only when  $\dot{r}_f = 0$  and corresponds to a no-slip boundary condition. During this state, the skin remains stuck to the surface of the plate. The relative motion of the skin against the plate stretches the sc until the absolute value of the radial force is larger than the static friction coefficient multiplied by the pressing force  $f_n$ , i.e.  $|f_{rad}| > \mu_s f_n$ . Subsequently, the skin is in ‘slide’ state, and the friction force depends on  $f_n$  and the dynamic friction coefficient  $\mu_d$  as explained in section 3.3.1.

We will see that whenever the finger is not sliding along the  $x$  axis (i.e. in the direction of the ultrasonic wave propagation), it will mainly stay in the sliding mode.

3.3.3.2. RELATIVE RADIAL VELOCITY AND TRAJECTORY: EXAMPLE

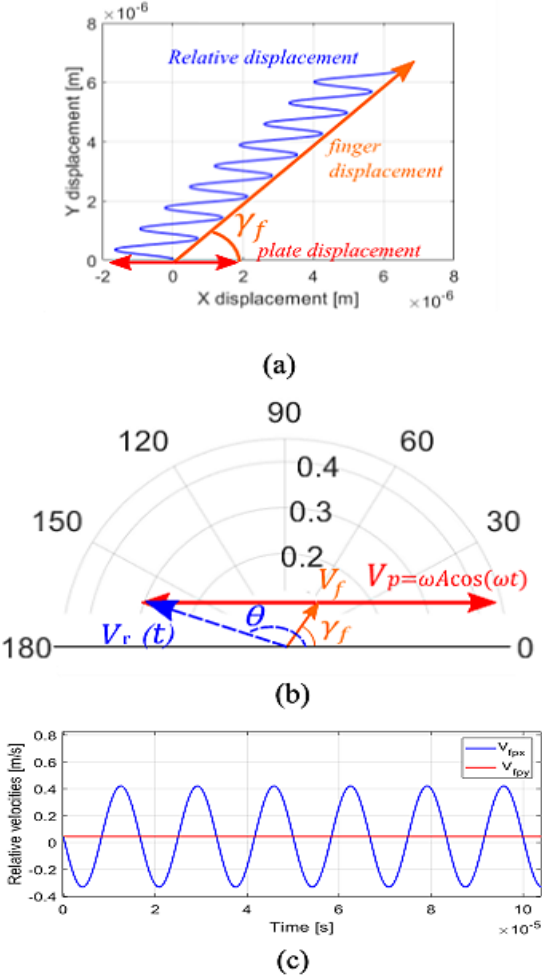


Figure 50. Motion of the finger with and without ultrasonic vibration. (a) Displacement of the finger relative to the plate in a cartesian coordinate system. The trajectory of the finger (orange) and the plate motion (red) are represented for the theoretical example:  $\gamma_f(t) = \pi/3$ ,  $V_f(t) = 60\text{mm/s}$ ,  $A = 1 \mu\text{m}_{p-p}$  and  $2\pi\omega = 60 \text{ kHz}$ . The xy plane corresponds to the surface of one facet of the haptic device. (b) Representation of the velocities in the polar coordinate system. The velocity of the finger (orange) is added to the plate velocity (red), which depends on time, producing  $V_r(t)$  and angle  $\theta(t)$ . (c) Relative velocities  $V_{fpx}$  and  $V_{fpy}$  in function of time.



To calculate  $u_{fp}$  during active exploration over the  $xy$  plane, we assume that the finger is moving with a velocity of magnitude  $v_f(t)$  and angle  $\gamma_f(t)$ , as illustrated in Figure 50.

The plate is simultaneously vibrating along the  $x$  axis following a motion described by  $w = A \sin \omega t$  and therefore a speed of  $u_p = \dot{w} = \omega A \cos(\omega t)$ , with  $A$  equal to the peak-to-peak vibration amplitude (typically within the range of a few micrometers) and  $\omega$  being the applied angular vibration frequency. The relative velocity of the finger viewed from the vibrating plate  $u_{fp}$  is described by (72).

$$\begin{aligned} u_{fpx}(t) &= u_f(t) \cos(\gamma_f(t)) - \omega A \cos(\omega t) \\ u_{fpy}(t) &= u_f(t) \sin(\gamma_f(t)) \end{aligned} \quad (72)$$

From the velocities described in the Cartesian coordinate system in (72), it is possible to calculate the relative velocity  $u_{fp}$  in the polar coordinates, which we term  $u_r(t)$ , the relative angle in the polar coordinates,  $\theta(t)$  and the angle variation  $\dot{\theta}$ . Fig. 13(b) represents an example of this transformation in the case when  $u_f(t)$  and  $\gamma_f(t)$  are constant and larger than 0 and the plate is vibrating along the  $x$  axis. In this example  $\gamma_f(t) = \pi/3$ ,  $u_f(t) = 60\text{mm/s}$ ,  $A = 1 \mu\text{m}_{p-p}$  and  $2\pi\omega = 58 \text{ kHz}$ .

It can be noted that only when  $\gamma_f(t) = k\pi$  (i.e.  $\theta = k\pi$ ) (with  $k = 0,1,2,3, \dots$ ) can the motion of the plate have the same angle and direction than the motion of the finger. In other words, if the finger is not moving along the  $x$  axis, it will never pass by the ‘drag’ state. Moreover, once the finger has been set in motion,  $u_r(t) \neq 0$  at all times unless the finger moves along the  $x$  axis. Specifically, this means that unless the finger is static or  $\gamma_f(t) = k\pi$  (the special cases analyzed in [35], [158]), the finger will remain in the ‘sliding’ state, and the friction will mainly depend on the velocity  $u_r(t)$ . We can therefore note that when the finger slides completely

parallel to the wave propagation direction is an exception to the more general case, which is the exploration in any other direction.

### 3.3.3.3. FRICTION REDUCTION USING THE PROPOSED MODEL: EVALUATION OF THE CASE $\gamma_f(t) = \pm\pi/2$

From the example in the previous section, we may deduce that whenever  $A \neq 0$ , the mean value of the finger velocity  $\bar{u}_f$  over a given time is smaller than the mean magnitude of the relative velocity  $|\bar{u}_r|$ . In other words, the vibration of the surface increases the relative sliding velocity of the finger over the plate. This velocity increase produces a variation in the dynamic friction coefficient according to (70)-(71).

To compare the theoretical against the actual friction reduction when the finger moves with an angle  $\gamma_f(t) \neq 0$ , we take the case measured in section 3.3.2 in the  $y$  direction. The friction is calculated using (70)-(71) for a finger exploring the plate at different constant speed  $v_f$  along the  $y$  axis  $\gamma_f(t) = \pm\pi/2$ , without any vibration.

The process is then repeated in the case of a vibration of  $A=1.6 \mu\text{m}_{\text{p-p}}$ . This time, the velocity-dependent friction coefficient  $\mu_E$  is calculated for the relative velocity  $v_r$  at every sampling point. The lateral force can be deduced from  $f_l = \mu_E f_n$  (at constant  $f_n = 0.5\text{N}$ ). The mean lateral force  $\bar{f}_l$  will be equal to the mean of the force calculation over a time period. Finally, the friction coefficient with vibration is equal to the mean lateral force divided by  $f_n$ .

The simulation results are presented in Figure 51, along with the measured values. In this figure it can be perceived that, even though there is a considerable error in the low velocity range, the effect of the vibration on friction is correctly described by the model that was obtained by data fitting in section 3.3.2.

We calculated that the mean error of the model against the measured data without vibration is of about 5.5%. With vibration it is higher of about 11.2%.

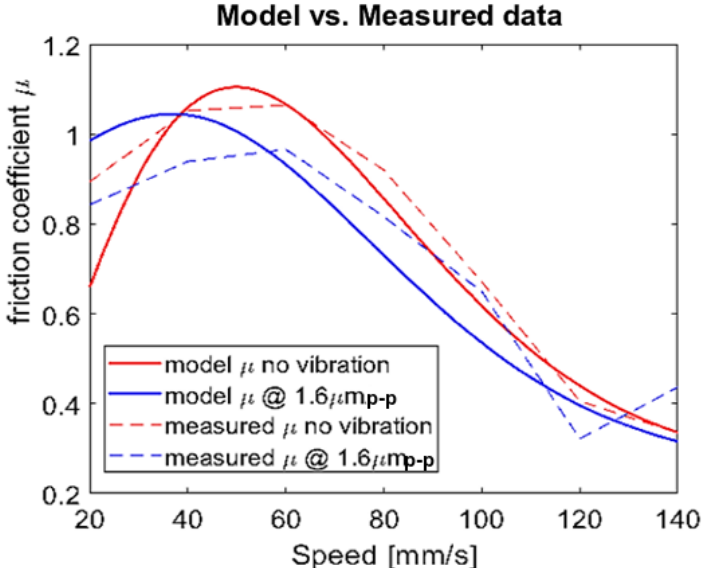


Figure 51. Fitted model vs. measured data for friction reduction using longitudinal ultrasonic vibration, with the finger exploring at  $\gamma_f(t) = \pm\pi/2$  and a vibration amplitude of  $1.6\mu m_{p-p}$ .

*3.3.4. Considerations on the non-Coulombic friction model and the Ratchet mechanism*

Through the relative motion analysis, we consider that the particular case of sliding parallel to the propagation of the longitudinal wave (explored in section 3.2), is an exception to the more general case of the exploration at various angles in any direction in the 2D plane. In this general case (the one explored in 3.3), we can observe that once the finger enters the ‘slide’ state and it remains there, until the user either stops the exploratory motion or changes direction. Consequently, it is logical to assume that the friction attenuation phenomenon when  $\gamma_f(t) = k\pi$  is

mostly explained by the non-Coulombic, velocity dependence of the dynamic friction coefficient.

In the special case of exploring along the  $x$  axis, however, the skin of the sc undergoes the three different states ‘stick’, ‘slip’ and ‘drag’, as explained in 3.2. The forces experienced by the finger while deforming are largely dependent on finger parameters such as finger elasticity and damping. This makes an integrated friction reduction model creation more complex, since it is difficult to understand how much each effect (ratchet mechanism vs. non-Coulombic friction model) influences the friction reduction. It is therefore an interesting subject to study in future research.

The simplified model described in the current work is useful in order to establish key principles which could help formulate models that are more complete. However, the comparison with measured data shows a margin of error for the friction estimations at lower speeds, and thus the model needs to be better fitted in this case. Different additional mechanisms may take place at lower and higher velocities, which have not yet been integrated. Future works can therefore focus in these mechanisms

### **3.4. Conclusion**

This chapter deals with the analysis of the mechanisms by which friction is reduced, in the specific case of longitudinal ultrasonic vibration. Initially, the friction reduction mechanism and parametric analyses are explained with the help of a simplified first-order model.

A tribological experiment helped to prove that a haptic interaction with a surface using friction modulation can be achieved with the use of purely longitudinal waves. The lubrication effect increases with the increase of vibration amplitude. It is also observed that increasing frequency improves the friction modulation effect at a given amplitude, and that the finger exploration speed decreases significantly

the active lubrication effect. This is because the instantaneous vibration speeds need to be comparable to the finger speeds for the relative velocity to produce the 'Ratchet' effect, where the direction of the plate motion 'pushes' the finger during exploration. Finally, it was possible to deduce that the mechanical properties of the probing object were an influencing factor on the amount of friction reduction.

This simplified model, however, fails to explain why friction is reduced when the finger explores in different directions along the plate. For this reason, we introduce a non-Coulombic friction model of the interaction, which is dependent on the relative velocity in two dimensions between the finger and the plate, in the ranges of finger velocity and vibration amplitudes relevant to active touch and the longitudinal USHD. Comparison to experimental data allows observing that, although the model seems well fitted to describe the friction attenuation for the speeds relative to active touch in any exploration direction, it is less fitted for lower velocities. Finally, the proposed model helps to validate the parametric analysis proposed following the ratchet mechanism model development.

Now that we have established that longitudinal vibration is capable of producing friction reduction on surfaces, it is interesting to evaluate whether these modes can be considered as a technological alternative for the design and implementation of USHDs. For doing this, the upcoming chapter presents a series of experiments that are focused on answering this question.

## *Chapter 4*

### PERFORMANCE COMPARISON BETWEEN LONGITUDINAL AND TRANSVERSE MODES

Examining whether longitudinal vibration is a suitable technological alternative to transverse vibration in USHDs, begs to inquire on the question of performance, how it is defined and how it is measured in the context of surface haptics. In this context, we could argue that the final objective is to be able to produce perceivable texture illusions, while minimizing the material and energetic resources required.

In the previous chapters it was explained that the perception of texture depends on the amount of friction reduction, which is a function of the vibration amplitude of the USHD; a physical quantity that can be controlled in closed loop. One could note, however, that an advantage in perception intensity for a given vibration amplitude does not necessarily mean that the performance of one mode is superior to the other. A more significant comparison base could be proposed in terms of energy consumption. As explained in [174], the energetic performance could be considered a determinant factor in the mode choice for haptic devices. Indeed, if the USHD is to be used with a battery, a better energetic performance may help increasing autonomy and reducing battery capacity specifications.

To perform this performance comparison between longitudinal and transverse modes in terms of energy, we propose to evaluate the active power necessary to create a specific perceived friction contrast, on an average person, during active exploration, for both modes. For doing so, the problem is approached in three steps.

The first section is focused on tribology. Using amplitude-controlled USHDs at two different resonance frequencies of 60Hz and 30 kHz, we compare the

vibration amplitude of the two modes vs. friction measurements and perform a parametric analysis.

In the second section, the tribological measurements are confronted with perception measurements, thanks to a set of psychophysical experiments, resulting on a comparative relation of texture perception vs. vibration amplitude.

Finally, an energetic analysis is performed in section 3, where we measure the active power necessary for each mode on the USHD to achieve a set of specific vibration amplitudes with and without a finger pressing on the device. These values are confronted with the amplitude vs. perception relation obtained previously, which will help determining which mode presents a performance advantage, and hopefully provide design clues for future developments.

#### **4.1. Friction reduction vs. vibration amplitude**

In Chapter 3, we explored the different mechanisms by which friction is reduced in USHDs. Based on the presented theories, a parametric analysis was suggested. From this analysis, it was concluded that, aside from the vibration amplitude, three other factors determined the amount of modulation possible using ultrasonic vibration. These factors were identified as the velocity of exploration, the resonance frequency of the selected mode (together being the relative velocity between the surface and the finger) and the mechanical properties of the probe (e.g. elasticity and damping). We believe these parameters are also determinant in the tribological comparison of the longitudinal against the transverse mode. Nevertheless, it has not yet been defined by what extent the performance of each mode is affected by each one of these parameters.

In order to verify these questions, a series of friction measurements is carried out in three separate experiments designed to perform the comparison of each parameter against a base case scenario.

#### 4.1.1. Testing scenarios

The different tests explained in this section aim at comparing the performance of transverse and longitudinal modes in USHDs, while analyzing the impact that the different parameters have on them. Since the pressing force is not one of the evaluated parameters, it is considered constant and kept at 0.5N throughout all tests.

##### 4.1.1.1. USHD USED FOR TESTING

Along with the two vibrational modes, USHDs with two resonance frequencies are required to carry out the complete set of parametric tests. These are 60 kHz and 30 kHz. The design and control of the 60 kHz device is thoroughly described in Chapter 2. With this device it is possible to produce and control one transverse and one longitudinal mode independently on a single test surface of about 3 cm long.

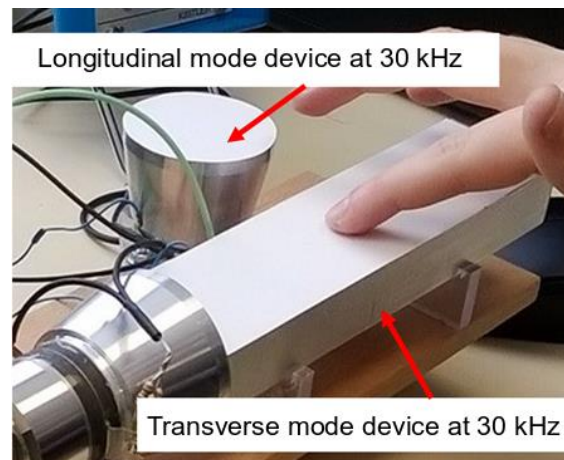


Figure 52. 30 kHz Transverse and longitudinal USHDs used for tribological and psychophysical measurements

For testing the 30 kHz resonance frequency, on the other hand, two separate devices are built. The longitudinal mode device, explained in detail in Appendix 4, consists of a Langevin Transducer (Fujicera ref. FBL28502HA), attached to the side of an aluminum beam, as depicted in Figure 52. The beam is covered with



the same damp-proof polymeric material as the one used for the 60 kHz device. For the transverse modes, we performed tribological measurements on the same model of Langevin Transducer (Fujicera ref. FBL28502HA), placed vertically and covered with the same surface material as the other two devices.

#### 4.1.1.2. BASE CASE SCENARIO

The base case scenario consists of a series of vibration amplitude vs. friction tests performed with a precision tribometer at 30 mm/s, using a hard polymeric semi-spherical probe covered in plaster on the 60 kHz USHD, as illustrated in Figure 53 (b). Concerning the physical properties of the probe, it is considered that they are substantially different to the ones related to the human finger (higher rigidity, lower damping).

The tribometer probe is controlled from an external computer. It is made to perform several reciprocating motions over the surface and the mean friction is measured when the probe slides over the surface of the USHD along the  $x$  axis. A series of amplitudes between 0 and  $1.6 \mu\text{m}_{p-p}$  is tested and the friction coefficient is calculated from the forces recorded.

#### 4.1.1.3. FIRST SCENARIO: PROBE EXPLORATION VELOCITY ANALYSIS

The objective of the first experiment is to illustrate the effect of increasing exploration speed in USHD using longitudinal and transverse modes. For this purpose, the same setup as the base case scenario is used. With this setup, a second set of measurements is performed: the tribometer probe is programmed to slide over the surface at 60mm/s, which is the double of the speed used in the base case scenario.

The results for the relative friction coefficient  $\mu' = \mu_{meas}/\mu_0 = 1 - \Delta\mu/\mu_0$  are measured for both modes at different vibration amplitudes. The results are plotted in Figure 54(a).

#### 4.1.1.4. SECOND SCENARIO: VIBRATION FREQUENCY ANALYSIS

In this experiment, we compare the performance of both modes at different resonance frequencies. For doing this, the base case scenario is compared to measurements performed with the same conditions but on the 30 kHz devices. The results for  $\mu'$  measurements at 30 kHz and 60 kHz are plotted in Figure 54(b).

#### 4.1.1.4. THIRD SCENARIO: MECHANICAL PROPERTIES OF THE PROBE

To test the effect of changing the mechanical properties of the testing object, the tribometer measurements of the base scenario are compared to a series of measurements taken during active exploration with a human finger. A single participant is used as a representative reference of the human finger.

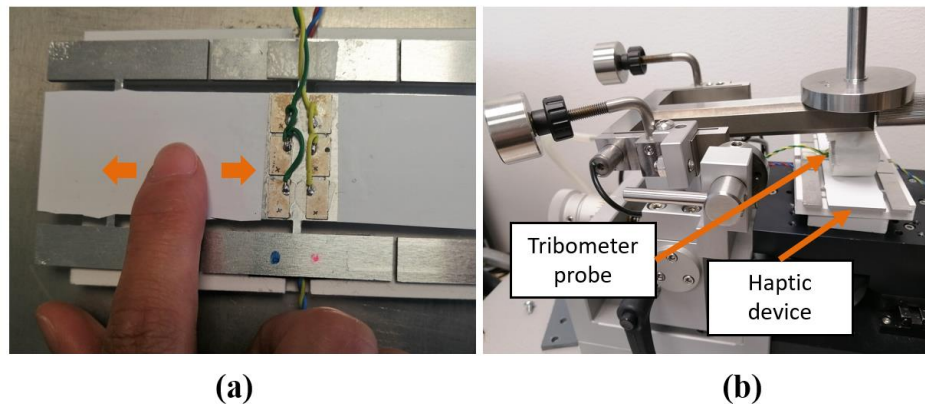


Figure 53. Two methods used for friction measurements with a tribometer probe and a human finger. (a) Top view of the active exploration of the surface: the participant performed several reciprocating motions at constant vibration amplitude, focusing on the exploration velocity and pressure, guided by visual aids. The friction measurements were performed by a three-axial force sensor attached to the base of the device. (b) Longitudinal view of the surface haptic device mounted on a tribometer, which performed and recorded the friction measurements. The tribometer's semi-spherical hard polymer probe was covered in plaster.

The measurements are performed during 'active' exploration, i.e. allowing the participant to control the force, speed and inclination of the finger motion.

For performing the measurements, the participant is requested to slide his/her finger, performing reciprocating motions over the surface of the 60 kHz USHD surface, along the  $x$  axis, as illustrated in Figure 53(a). In order to acquire the lateral and normal force measurements, the device is mounted on a three-axial force sensor (GSV-4USB from ME-Meßsysteme).

The participant is requested to maintain, within reasonably possible, a constant exploration speed, finger angle and pressure force throughout the measurements. To aid the participant, a visual interface has been programmed with the help of OpenSesame graphic interphase software [185]. The visual interface guides the user's probing velocity and force with a moving arrow on the screen, which indicates a motion of 30 mm/s and it turns green when the pressing force is within a defined threshold of  $\pm 0.1\text{N}$  around 0.5N. The results for  $\mu'$  using the participant's finger against the base case scenario are plotted in Figure 54(c).

#### 4.1.2. Results

For examining the results it is useful to remember that the objective of the ultrasonic vibration is to maximize the friction contrast at a given vibration amplitude. Given that  $\mu' = 1 - \Delta\mu/\mu$ , a good performance, in terms of vibration amplitude, is understood as the smallest value of  $\mu'$  at a given vibration amplitude.

##### 4.1.2.1. BASE CASE SCENARIO

The results show that it is possible to obtain friction modulation using either the transverse or the longitudinal mode with the parameters tested on the base scenario. However, a much higher friction reduction is observed using the longitudinal mode, which can produce a  $\mu'$  as low as about 0.35, as compared to about 0.8 for transverse modes.

4.1.2.2. PARAMETRIC ANALYSIS

Concerning the exploration velocity, the measurements show a similar effect on both modes. As predicted by the interaction models, Figure 54(a) shows that an increase in velocity has a negative effect on the performance of the devices. It appears that in the ranges explored, both modes are affected by about the same amount.

In terms of resonance frequency, it can be observed in Figure 54(b) that both modes perform better at higher frequencies, with a higher improvement for the longitudinal mode within the tested vibration amplitudes.

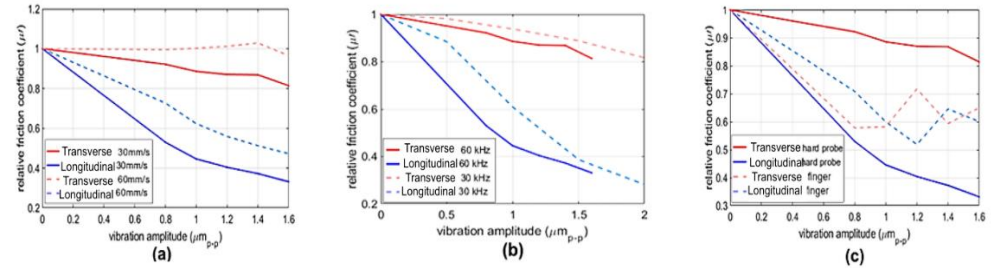


Figure 54. Tribology measurements of the relative friction coefficient at different vibration amplitudes for the two modes: Longitudinal (blue and light blue) and transverse (red and light red) (a) Exploration speed effect: in solid lines the measurements at 30 mm/s. In lighter dashed lines the measurements at 60 mm/s. (b) Frequency effect: In solid lines the measurements at 60 kHz. In lighter dashed lines, the measurements at 30 kHz. (c) Probe impedance effect: In solid lines the measurements with a stiff probe. In lighter dashed lines, the measurements with a finger.

Extrapolating from the results obtained for exploration velocity and frequency, it is possible to conclude that irrespectively of the mode, the relative velocity of the probe against the vibration velocity of the plate is a key parameter for the friction attenuation due to ultrasonic vibration. The higher the vibration velocity is with respect to the finger, the better the results are. This is consistent with the model predictions explained in [114] for transverse modes and in Chapter 3 for longitudinal modes. For this reason, it is recommended to increase this velocity

difference as much as possible. This can be achieved by working at higher resonant frequencies.

Finally, the decrease in probe stiffness and increase in damping produced by the use of a finger, has a significant effect in the performance of both modes. The transverse mode performs significantly better with the finger than with the probe and inversely, the longitudinal mode significantly better with the probe than with the finger.

## **4.2. Psychophysical Analysis**

Thanks to a psychophysical analysis, it is possible to compare the perception intensity of friction contrast for both modes, for a set of vibration amplitudes, using the 30 kHz and the 60 kHz ultrasonic surface haptic devices.

The experiment carried out with the 30 kHz device, which is detailed in 4.2.1, is performed in open loop (the vibration amplitude is not controlled, so the finger attenuates the vibration). However, the vibration attenuation due to the finger is taken into account, as an adjustment is made by the user, and the vibration amplitude is recorded when the finger is on the device.

The 60 kHz device is used to perform two different psychophysical tests, in closed loop, using a different comparison protocol as the one described in 4.2.1. The protocol is described in 4.2.2. Each of the psychophysical tests is performed with the participant performing reciprocating motions along a different axis on the surface of the device ( $xy$  coordinate system detailed in Figure 47); i.e. once along the  $x$  axis, and once along the  $y$  axis

### *4.2.1. Psychophysical measurements at 30 KHz*

#### 4.2.1.1. SETUP AND Protocol

For the 30 kHz experiment, the devices presented in Appendix 4, and illustrated on Figure 52 are used to perform an ‘adjustment’ type psychophysical comparison between longitudinal and transverse modes. Both devices are

mounted on a common base, and a normal force sensor is integrated below. The force sensor is calibrated to measure only the added force of the exploring finger. For all tests, the transverse force and speed of exploration are controlled by the tested participants, with the help of a force sensor and a metronome, respectively. For each test, a sinusoidal modulated signal at 10 Hz is fed to the Langevin transducers at different modulation amplitudes. As explained in previous sections, larger modulation amplitudes are expected to produce a higher friction ‘contrast’ between the maximum and minimum values of the envelope. Increased contrast in friction is assumed to produce a more perceivable or ‘stronger’ sensation. The envelope modulation and real time vibration amplitude measurements can be respectively imposed and acquired via two network-interconnected computers (master and users’ console), through a visual interface programmed for this application. The complete setup is shown in Figure 55.

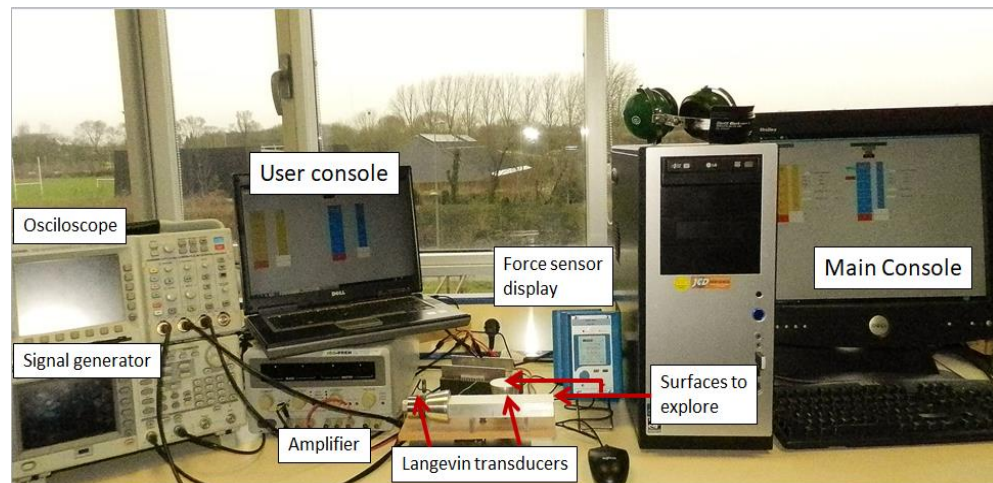


Figure 55. Setup for the ‘adjusting’ psychophysical experiment at 30 kHz

A group of 12 participants, male and female, between the ages of twenty to forty years old, are requested to participate in the experiment. Participants’ fingers are cleaned at the beginning of the experiment, and all participants are asked to wipe

their fingers between each test. Throughout the trials, all participants are requested to wear sound-proof headsets.

For the adjustment protocol, each user is given the supervised control of the users' console, which tunes the modulation amplitude of both modes. The transverse mode device is set to a given amplitude level. Then, the amplitude of vibration of the longitudinal mode device is set by the user in order to find "the same feeling" on both surfaces, when applying a similar normal force, at the same exploration speed and finger inclination. The user can adjust the level as much as he/she desires until a sensitive equivalent is found. Once the adjustment is done, the amplitude measurement values are recorded when the finger is on the device (in open loop, the vibration amplitudes are affected by the presence of the finger).

This process is repeated for each amplitude level, tuning the transverse mode device at  $1 \mu\text{m}_{\text{p-p}}$ ,  $1.5 \mu\text{m}_{\text{p-p}}$ ,  $2 \mu\text{m}_{\text{p-p}}$ ,  $2.5 \mu\text{m}_{\text{p-p}}$  and  $3 \mu\text{m}_{\text{p-p}}$ .

#### 4.2.1.2. AMPLITUDE COMPARISON RESULTS AND ANALYSIS

The results of this experiment are plotted in Figure 56. The line  $x=y$  represents the points where theoretically, vibration is perceived at the same level for the same vibration amplitude in the two modes. Any point placed above (or to the left) of this line would mean that vibration in the transverse mode produces a more intense sensation than the longitudinal mode for a given vibration amplitude.

It can be observed that between the amplitudes of  $0.3 - 2.5 \mu\text{m}_{\text{p-p}}$ , over 90% of the points are located on the upper side of the equivalence line, which proves a more intense perception of the friction modulation effect for the transverse mode for this operating conditions. It can be seen however, that at higher and lower vibration amplitudes, this tendency seems to reverse.

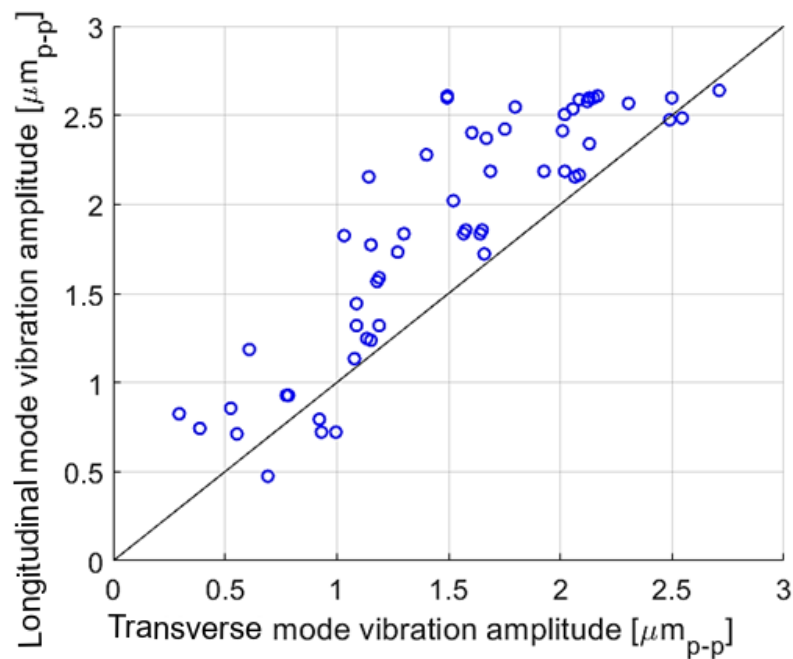


Figure 56. Psychophysical results for Transverse vs. Longitudinal vibration comparison with a bare finger during active exploration with exploration velocities around 30 mm/s. The points represent the vibration amplitudes for longitudinal and transverse modes which produce the same sensation when presented to a vibration modulated by a 10 Hz sinusoid..

#### 4.2.2. Psychophysical measurements at 60 KHz

Accounting to the results obtained with the 30kHz devices, and especially the tendency at higher amplitude, it becomes interesting to evaluate both modes at higher frequencies. For this reason, we evaluated the perception intensity of friction contrast for a set of vibration amplitudes with the 60 kHz USHD.

Without questioning the already obtained results at 30 kHz, the experimental protocol has been improved for the new tests at 60 kHz. This new protocol is detailed in this section. In particular, we chose a 'staircase' protocol, which we believed was more adapted than the adjustment method previously implemented.



#### 4.2.2.1. SETUP AND PROTOCOL

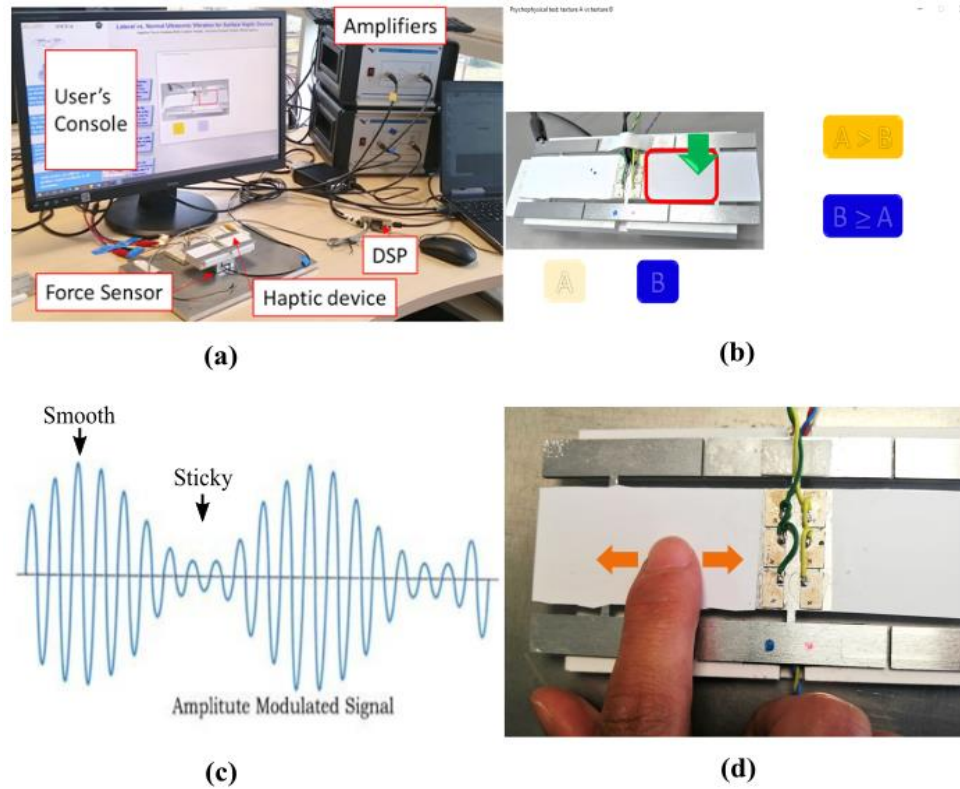


Figure 57. Setup for comparative psychophysical experiments. (a) Complete setup with all its parts. The user interacts only with the haptic device and the user's console. (b) View of the user's console with visual guides for force (arrow color) and velocity (arrow speed) of exploration. The user's console also allows the participant to change the mode (A or B) by clicking the corresponding virtual button and answer which is the mode that provides the strongest sensation, by clicking the virtual answer buttons ( $A > B$  or  $B \geq A$ ). The answers are used to perform a staircase type of comparative test. (c) Shape of the amplitude modulated vibration signal presented on the device. The amplitude of the envelope represents each tested vibration level, the frequency of the envelope is low to produce a texture. (d) View of the active exploration of the surface: the participant performs several reciprocating motions as the signal is presented, focusing on the intensity of the tactual feedback of the modulated vibration.

To perform the psychophysical tests at 60kHz, the setup shown in Figure 57 is used. Before the tests, the participants were requested to clean and dry their hands. Data were collected from thirteen healthy volunteers aged between 18 and 50 (6 females). All participants gave written informed consent. The research conformed

to the principles of the Declaration of Helsinki and experiments were performed in accordance with relevant guidelines and regulations.

. The participants conducted a series of trials. In each trial, two textures (A and B) were presented. Each texture consisted of a closed loop ultrasonic vibration, modulated by a 10 Hz sinusoid that went from a value of 0  $\mu\text{m-p}$  to a tested amplitude, as illustrated in Figure 57(c). One texture was generated with transverse vibration and the other with longitudinal vibration.

For each texture, the participants were asked to slide their finger over the surface of the ultrasonic surface haptic device along the  $x$  axis in the radial-ulnar direction, focusing on the perceptual intensity the texture provided. They were then requested to control their pressure force to be around 0.5N, and longitudinal speed close to 30 mm/s with the help of visual guides presented on the user's console. They were later told to decide which of the two textures produced a more 'intense' or clear sensation.

The participants were able to feel both textures as many times as needed to make a choice, but they were not informed which texture corresponded to which mode. It is important to note that the longitudinal mode did not provide a uniform sensation over a complete facet of the ultrasonic surface haptic device, since the nodes were too large and thus perceivable. For this reason, we reduced the exploration area to cover only the 2-3 cm closer to the piezoelectric ceramics.

The amplitudes of the modulating signal were presented following a comparative one-up - one-down staircase test, such as the one explained in [186], where the reference was one fixed transverse mode modulating amplitude and the variable was the longitudinal mode modulating amplitude, which was meant to converge to the amplitude which produced an equivalent sensation in the transverse mode after a number of steps.

Each test was repeated for a series of reference transverse mode amplitudes ranging from 0.8  $\mu\text{m-p}$  to 1.6  $\mu\text{m-p}$ , with steps of 0.2  $\mu\text{m-p}$  from one reference to the next. The tested levels were pseudo-randomized to prevent learning curve effects.

Finally, a normality distribution test is performed on the obtained data to verify that a representative sample had been measured, such as in [186].

4.2.2.2. AMPLITUDE COMPARISON RESULTS IN THE X DIRECTION

The results are presented as a boxplot in Figure 58. The line ( $x=y$ ) is presented for comparison.

The results of this psychophysical test favor slightly the longitudinal mode over the transverse mode at 60 kHz, especially at higher amplitudes. It is, however, possible to appreciate that the variance of the perception measurements at one reference is sometimes larger than the reference step.

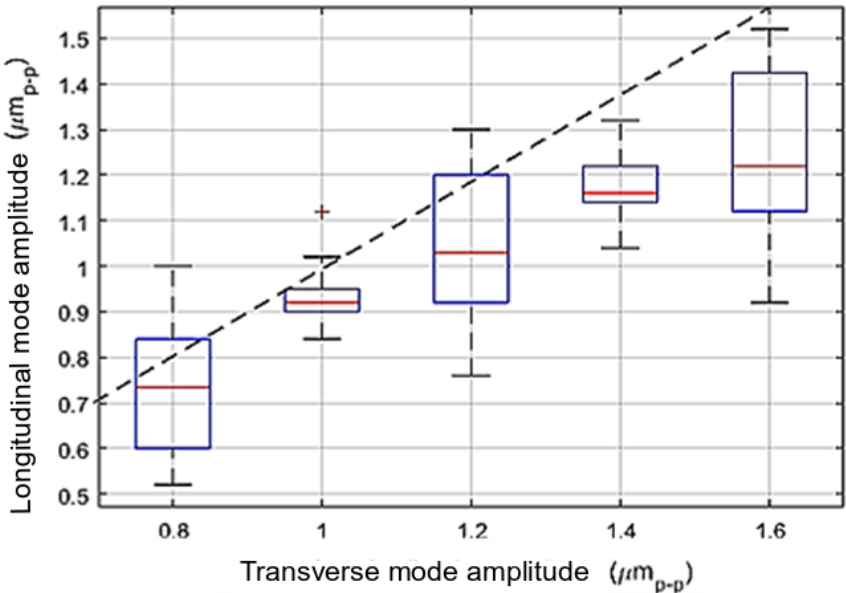


Figure 58. Box plot of the psychophysical test results of the comparison between transverse and longitudinal modes at about 60 kHz resonance frequency with a finger with exploration velocities around 30 mm/s. The boxes represent the vibration amplitudes for longitudinal and transverse modes which produce, in average, the same sensation when presented modulated by a 10 Hz sinusoid.

#### 4.2.2.3. PSYCHOPHYSICAL MEASUREMENTS AT 60 KHZ IN THE Y DIRECTION

To evaluate the effect of the exploration direction on the haptic feedback and the performance of the modes, the psychophysical experiment explained in section 4.2.2.1 is repeated for the same participant group in the  $y$  direction. The participants were instructed to explore the USHD at a point where there was a maximum of both modes, and the finger still explores in the radial-ulnar direction. The boxplot representing the psychophysical results in the  $y$  direction are plotted in Figure 59.

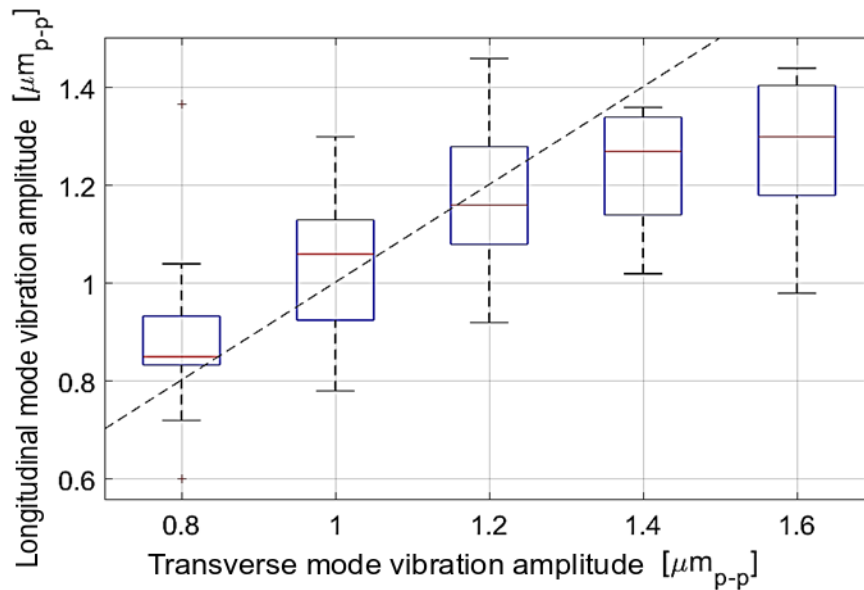


Figure 59. Box plot of the psychophysical test results of the comparison between transverse and longitudinal modes at about 60 kHz resonance frequency with a finger with exploration velocities around 30 mm/s exploring in the  $y$  direction. The boxes represent the vibration amplitudes for longitudinal and transverse modes which produce, in average, the same sensation when presented modulated by a 10 Hz sinusoid.

The results are very similar to those obtained for the  $x$  direction in Figure 58. This time, however, there is a slight improvement of the transverse mode in comparison

to the longitudinal mode, as was predicted by the tribological measurements in Chapter 3.

Attention must be made when analyzing the results of the boxplots in the  $x$  and  $y$  directions. A bias could be introduced by the protocol at the higher values of  $1.4 \mu\text{m}_{\text{p-p}}$  and  $1.6 \mu\text{m}_{\text{p-p}}$ , since  $1.6 \mu\text{m}_{\text{p-p}}$  is the technical limit of the plate amplitude with the setup available. If we consider this bias in the analysis, we could still appreciate that both modes produce, in average, a very similar perception intensity in terms of amplitude, with a slight advantage on the longitudinal modes, with the conditions tested.

### **4.3. Energy analysis in the mode comparison**

The previous sections focused on the comparison of the performance in terms of amplitude vs. relative friction coefficient and amplitude vs. perception of friction contrast for the two modes. In both comparisons, it has been observed that for a finger exploring an ultrasonic surface haptic device vibrating at 60 kHz, longitudinal and transverse modes show a more or less equivalent performance in terms of vibration amplitude, with a slight advantage of the longitudinal mode in the psychophysical tests. This does not necessarily mean that their performance is equivalent in terms of energy consumption. As explained in [174] the energetic performance could be a determinant factor in the mode choice for haptic devices. Indeed, if the ultrasonic surface haptic device is to be used with a battery, for example, a better energetic performance may help increasing autonomy or reducing battery capacity specifications.

#### *4.3.1. Energy losses in a USHD*

The energy consumption in an ultrasonic surface haptic device can be explained by two separate mechanisms: mechanical power losses and electric power losses [187]–[189]. The mechanical power losses are produced when the acoustic energy

of the ultrasonic surface haptic device (including the resonator, the piezo ceramics and the glue) is dissipated due to internal material interactions, interactions with external forces and the surrounding environment. The electrical power losses, on the other hand, come from the hysteresis losses in dielectric and the hysteresis cycle in the piezoelectric coupling (hereby referred to as ‘piezoelectric’ losses) [187], [188], [190].

It is mostly agreed [187], [189]–[192] that the losses on the dielectric are negligible with regards to the mechanical and piezoelectric power losses in this type of ultrasonic surface haptic device. This is partly because we are working with hard ceramics, where dielectric losses are less significant [190]. Additionally, it can be observed that the proportion of material in the aluminum resonator is very large when compared to the amount of material in the piezoelectric actuators, rendering its associated dielectric losses less important in comparison.

The piezoelectric power losses, which may be significant, are related to the shape, mechanical and electrical properties and placement of the piezo-ceramics [189]. In [188], complex parameters are included in the dynamic equation of the piezo-ceramics to obtain an analytical model for the piezoelectric losses. However, in general, it can be assumed that for any given mode and plate shape, a geometry and placement of piezoelectric ceramics may be found, which maximizes the coupling with the mode [160], [193]. By doing this, the voltage requirements can be reduced, together with the piezoelectric losses. As explained in section 2.1, this type of optimization is hard to comply for both modes on the same device. For this reason, it was not carried out in the current study.

In [192] it is concluded that the chosen vibrational mode has an effect on the material’s damping. In consequence, the minimization of the damping is a technique that has been used for energy optimization in previous studies. In [191], [192] for example, the thickness of the resonator is reduced in order to minimize the damping, thus optimizing the energetic consumption of the device. However, internal dissipation is not the only factor to consider in terms of energy

optimization. Indeed, the interaction with external forces (produced by air and finger) could be determinant for improving the efficiency of the ultrasonic surface haptic device [192].

For the reasons exposed, this study focuses on highlighting the influence of the finger mechanical impedance on the losses for both modes. For doing this, we performed two series of power measurements on the device. First, at no load, and then when there is a finger present.

4.3.2. Active power measurements at no load

To evaluate the active power requirements on the ultrasonic surface haptic device at no load, a series of measurements is made. In order to measure the active power consumption, a Fluke Norma 4000 power analyzer was connected to the motor ceramics. A frequency sweep was made at about +/-1 kHz around the resonance at three different voltage levels. The voltages were set for each mode to produce a vibration amplitude of around 0.8 μmp-p, 0.6 μmp-p and 0.3 μmp-p at resonance.

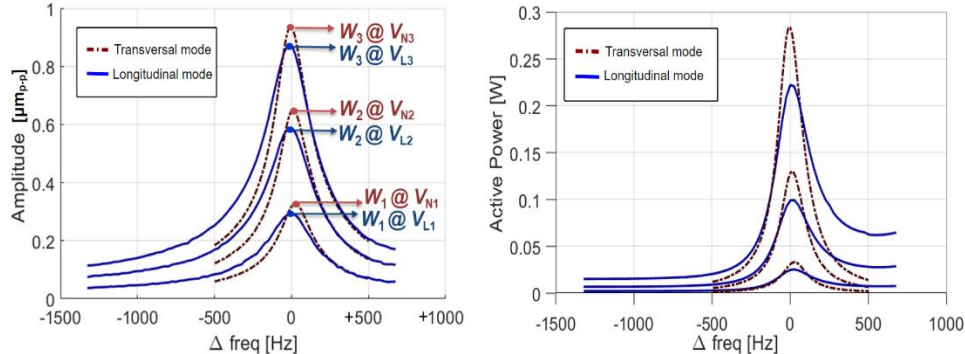


Figure 60. Vibration amplitude and active power measurements for transverse and longitudinal modes for three frequency sweeps at given voltages around the resonance of each mode.  $V_{Lk}$  and  $V_{Nk}$  represent the voltage needed to achieve vibration amplitudes  $W_k$ , with  $k = 1,2,3$ .

The vibration amplitude was recorded together with the total active power measurements for each frequency. The measurements were performed three times

at the same voltage levels at no load, and the mean of the three sweeps was recorded. The results for amplitude and active power measurements at no load condition around the resonance are presented in Figure 60.

The quality factor  $Q$  which is inversely proportional to the internal losses of the device, is affected by both dissipation and electric/mechanical energy storage elements. It may be observed from Figure 60 that  $Q$  is slightly higher for the transverse mode than for the longitudinal one. We can confirm similar results from the parameters identified in Table 2 of Chapter 2. With  $Q_n = K_n/\omega_n D_n$ , we obtain  $Q_N = 216.9$ ,  $Q_L = 206.4$ .

Additionally, the electromechanical conversion factor of the transverse mode  $N_N = 0.3 \text{ N/V}$  is about 3.8 times higher than the one for the longitudinal mode  $N_L = 0.0773 \text{ N/V}$ , even though we used the same motor piezo-ceramics for both modes. This difference may be related to the positioning and size of the piezo-ceramics with regards to the obtained mode shapes. In this case, it appears that the positioning of the ceramics provides a better electromechanical coupling with the modal shape of the transverse mode. Consequently, the voltage needed to achieve a given vibration amplitude (in Figure 60,  $V_{Lk}$  and  $V_{Nk}$ ) is over three times higher for the longitudinal mode than for the transverse mode ( $V_{Lk} \approx 3V_{Nk}$  for  $k = 1,2,3$ ). This voltage may perhaps produce additional conversion losses. However, if we observe the active power measurements, it can be concluded that, even though the longitudinal mode has a lower quality factor and requires higher voltages to reach a given vibration amplitude than the transverse mode, it also requires slightly less active power.

Overall, it can be observed that at no load, both modes show a similar energetic performance, with a slight advantage on the longitudinal mode, even though it requires higher voltage levels. The difference can be explained by the acoustic losses to the environment, which are higher for the transverse modes.



### 4.3.3. Impedance coupling: the effect of pressing with a finger

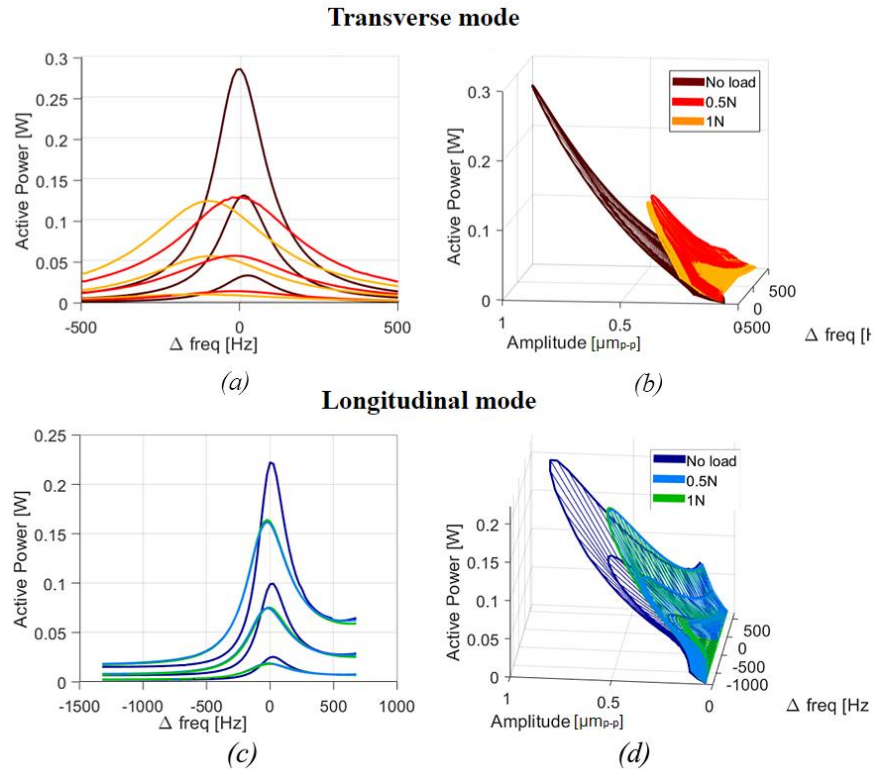


Figure 61. Active power for a frequency sweep for transverse and longitudinal modes, for three constant voltage levels. The images present the measurements at no load vs. the measurements with a finger pressing the surface of the ultrasonic surface haptic device at constant pressures of 0.5N and 1N. Figures (a) and (c) represent active power vs. frequency shift. Figures (b) and (d) represent the surface formed by the measurements of active power vs. vibration amplitude around the resonance of each mode.

The measurements taken in 4.3.2 were repeated with a static finger pressing over a vibration maximum with a normal force of 0.5N, and again with a finger pressing at 1N. The amplitudes and active power measurements were recorded over the three sweeps for each mode and plotted in Figure 61.

On the left, the figure shows the active power measurements at no load, compared to those with a finger on, at two different pressure forces of 0.5N and 1N. On the right, the surfaces show the relationship between the vibration amplitude and the

active power consumption over a range of frequencies around the resonance of each mode. A 'steeper' curve represents a worse performance than a flatter one.

Three results can be observed:

1- Attenuation: the amplitude is attenuated by over 54% by the presence of the finger with the transverse mode and only about 32% for the longitudinal mode (the measurements are performed in open loop).

2- Quality factor: the quality factor of the transverse mode is significantly reduced by the presence of the finger. An effect much less present in the longitudinal mode.

3- - Pressure force dependency: increasing the finger pressure from 0.5 to 1N has little to no effect on the frequency response of the longitudinal mode. However, the same pressure tends to shift the spectrum of the transverse modes towards lower frequencies.

#### *4.3.4. Amplitude vs. active power function*

A final set of measurements was taken in open loop, which served to characterize the relationship between active power and vibration amplitude for each mode, considering the cases where there is no load, and when a finger is pressing with different forces. For the case where the finger is present, new measurements were taken at higher amplitudes, and the active power measurements at the resonance were recorded.

With these measurements, it was possible to create a second order polynomial interpolation which produced a power/amplitude function for each mode at the different loads.

These relations are represented in Figure 62. In the figure, it can be observed that, while the consumption at no load is similar for both modes, the load presented by the finger increases significantly the value of the power function vs. amplitude for the transverse mode more than for the longitudinal mode. In other words, we may

interpret that the finger acoustic impedance is smaller for the longitudinal mode. This effect will cause a higher wave attenuation with the transverse mode, and thus a better performance (less active power losses) with longitudinal mode.

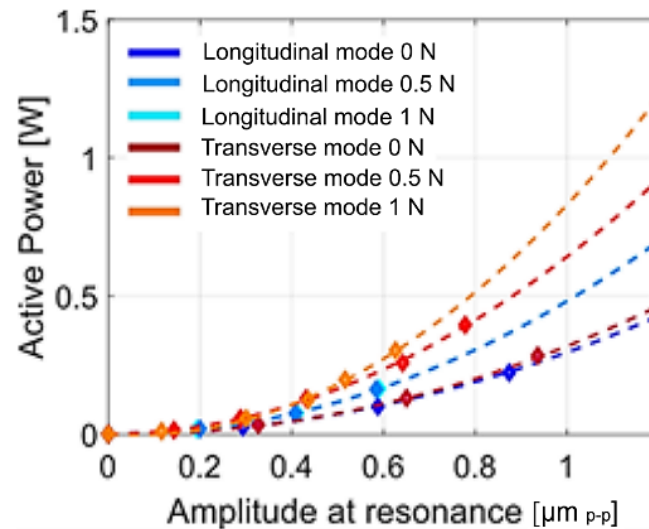


Figure 62. Active Power vs. Amplitude relation for the data measured at resonance. The quadratic fit of the longitudinal power measurements at loads of 0.5 N and 1 N are superposed

This result helps confirming that the interaction mechanism with the finger is one of the decisive factors when considering energy performances of the ultrasonic surface haptic device.

#### 4.4. Conclusion

In the current chapter we presented a series of tests designed to analyze the comparison between the longitudinal and transverse modes, with the purpose of determining whether longitudinal vibration may be a suitable alternative to transverse vibration in USHDs. The comparison has been carried out in terms of energy requirements for producing a specific perception intensity. For

obtaining this value, we performed measurements of friction, contrast perception and active power losses.

In terms of friction reduction, a set of chosen relevant parameters are analyzed. These are the resonance frequency of the mode, the velocity of exploration and the mechanic characteristics of the probing element. In the case of the ‘typical’ operation conditions, i.e. a finger exploring at mean exploration velocity of 30mm/s over a surface vibrating around 60 kHz, with a pressing force of 0.5N, both modes produce similar performance results.

The perception of friction contrast at different amplitudes was assessed with a group of participants thanks to a set of psychophysical comparative tests at different frequencies and exploration directions. The results show that at 30 kHz, there exists a definite advantage for the transverse mode at lower vibration amplitudes. This result is, however reversed at higher amplitudes and frequencies. Finally, the energetic assessment helped to conclude that the main factor affecting the active power losses on a surface haptic device dealt with the energy dissipation due to the presence of a finger. Because of the nature of the contact mechanics, the lateral acoustic impedance of the finger is smaller than the normal acoustic impedance. For this reason, longitudinal modes have the potential to be more energy-efficient and therefore more performant than transverse modes.

The upcoming chapter explores the question of the impact that the probing finger has on the perception of friction contrast, and proposes alternatives to address this issue.

## *Chapter 5*

### FUNDAMENTAL ACOUSTIC FINGER FORCE MEASUREMENT AND ITS CORRELATION WITH FRICTION REDUCTION

Thanks to the device designed in Chapter 2 and tested in Chapters 3 and 4, it was possible to verify that longitudinal vibration is indeed a technological alternative for the creation of USHD. However, in the tests performed in Chapters 3 and 4, it was also possible to observe a common issue present on both longitudinal and transverse mode USHD, which raises the question of viability and robustness of ultrasonic devices. It concerns the problem of tactile perception standardization. In a nutshell, the different mechanical properties of the skin amongst different users may produce non-homogeneous haptic return at a given vibration amplitude from one person to another [117], [132]. Creating a more uniform perception of friction modulation throughout the population is desirable, since this would help to improve the construction and rendering of texture models for USHDs. In order to achieve this objective, a more comprehensive view of the system needs to be envisaged, where the human is considered as a part of the system and not external to it. The work performed in this chapter is, therefore, a step towards the ‘human-in-the-loop’ concept and how it can be applied to surface haptics. The methods presented in this chapter could either be used to calibrate a USHD reference [170], or for future developments in real time friction control, or to deduce mechanical properties of the measured skin. .

Finger bio-mechanics may be used to predict the behavior of friction forces during tactile surface exploration. In [175], it was established that the damping of the sc (outmost layer of the epidermis) at ultrasonic frequencies greatly affects the subject’s susceptibility to ultrasonic friction modulation. Therefore, it is

conceivable that certain finger mechanical properties are correlated to textural perception. In [150] it is shown that the perceptual intensity of the tactile stimuli is a function of the friction contrast. In [194], this perception intensity is described in function of several parameters related to the mechanics of the surface contact.

It may be therefore assumed that, in order to obtain a homogeneous perceptual intensity of a tactile stimulus, the vibration amplitude should be adapted to each user in order to obtain the desired friction in real time. An attempt at implementing this type of control has been performed in [195] using a real time friction sensor integrated in the tactile feedback surface. However, in this setup, the feedback signal was noisy and difficult to use in a closed loop control. In [196] a novel force sensor is proposed to reduce the noise ratio and provide an accurate friction correction in closed loop.

An alternative approach, which wouldn't require specified material, may be the adaptation of the amplitude reference according to a given set of parameters. Some of these parameters, such as exploration speed and pressing force, are easily measurable with the available sensors, while others, such as the biomechanical properties of the finger, may change significantly from one user to another and are harder to measure. In [118], the measured acoustic impedance of the skin pressing against the plate is correlated to the perception of a simulated key-click, since this parameter is directly correlated to the biomechanical properties of the finger pad. Therefore, the authors propose to use this measurement as a monitoring tool to produce a calibrated stimulation adapted to the skin of the user's finger.

In this chapter, a similar objective is targeted: to adapt the vibration amplitude so the friction modulation can be adjusted for all users. We propose to approach this problem by following the methodology explained in [132] and [170] for transverse modes and adapt it to longitudinal modes. Finally, a solution is proposed to apply this approach in real-time for friction control.

In section 5.1, we explain the principle and method by which the acoustic finger force is estimated from the voltage measurements of the plate operating in

vibration amplitude closed-loop control. The complete study for one vibration amplitude using a transverse mode device at about 25 kHz is presented in section 5.2. Section 5.3 presents the longitudinal mode study for several vibration amplitudes with the 60 kHz longitudinal USHD. Finally, section 5.4 presents the explanation and preliminary work on real time friction correction using the observation of the acoustic finger force, and the results for the longitudinal mode study.

### 5.1. Principle of the fundamental acoustic force measurement

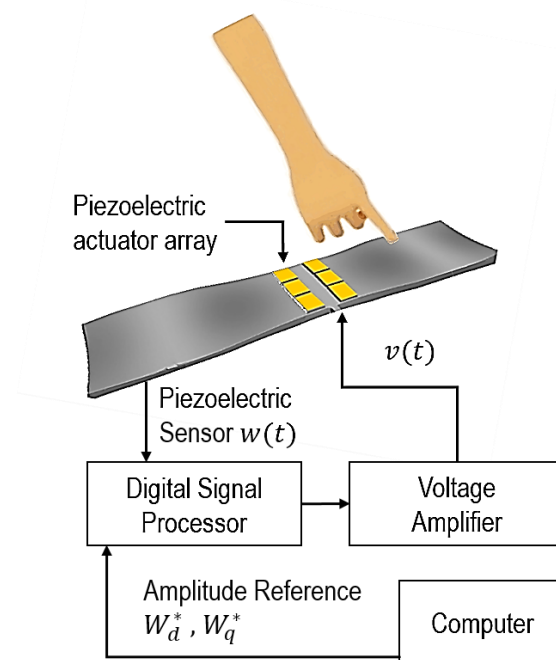


Figure 63. Experimental set-up for the acoustic finger force measurement

The system for performing the acoustic finger force measurement is illustrated in Figure 63. . The figure represents the USHD described in Chapter 2, composed of an aluminum plate, which vibrates in a longitudinal or transverse mode, thanks to a piezoelectric transducer array fed with a sinusoidal voltage  $v(t)$ . As illustrated in the figure, a static finger presses the surface at the point of maximum displacement

of the mode. On the bottom side of the plate, a piezoelectric sensor is glued to the surface. The signal of the vibration amplitude sensor  $w(t)$  is controlled using the closed-loop control implemented in Chapter 2.

### 5.1.1. Acoustic finger force at steady state

The supply voltage in steady state can be used to estimate the acoustic finger force. To do this, we refer to the simplified model of the USHD explained in Chapter 2. Assuming a single predominant mode, the force equation of the device with a mechanical load pressing against its surface domain is given by (73), where  $F_r$  is the acoustic finger force,  $F_p$  the piezoelectric force,  $W$  represents the vibration amplitude and  $M$ ,  $K$  and  $D$  are the modal parameters of the plate (see Chapter 2).

$$F_p - F_r = MWs^2 + DWs + KW \quad (73)$$

The device is designed to work at the resonance frequency of the mode  $\omega_n$ , with  $\omega_n = \sqrt{K/M}$ . We can thus state for the Laplace variable that  $s = j\omega_n$ . In steady state, this leads to the simplified plate model (74) at no load. When a load is present,  $F_r$  is included and (74) becomes (75) [176] (underlined variables represent a complex value) [176]. We have established in Chapter 2 that the piezoelectric force was defined by  $F_p = NV$ , where  $N$  represents the electromechanical transformation factor of the mode and  $V$  the peak to peak input voltage.

$$N\underline{V}_{no-load} = jD\omega_n\underline{W} = \underline{F}_p \quad (74)$$

$$N\underline{V}_{load} = jD\omega_n\underline{W} + \underline{F}_r = \underline{F}_p \quad (75)$$

$$\underline{F}_r = N(\underline{V}_{load} - \underline{V}_{no-load}) \quad (76)$$

The amplitude and phase of  $\underline{W}$  are controlled in closed-loop. As a result, the voltage  $v(t)$  is adapted, so that  $\underline{F}_p$  can compensate for the attenuation of the vibration amplitude produced by the finger when there is contact.  $\underline{F}_r$  is then



deduced from (74) and (75), by measuring the voltage difference with and without a load, as described in (76).

### 5.1.2. Acoustic force estimation in the rotational reference frame

Assuming that  $v(t)$  is a sinusoidal function, it can be projected into the rotational reference frame by the use of complex phasors, as explained in Chapter 2. The resulting variable  $\underline{v}(t) = (V_d + jV_q)e^{j\omega t}$ , is the complex phasor of  $v(t)$ .

$V_d$  and  $V_q$  are the coordinates of  $\underline{v}$  in the d-q frame. In the same way, the complex coordinates  $F_{rd}$  and  $F_{rq}$  can be calculated from the acoustic force  $\underline{F}_r$  that is estimated from equation (76).

As explained in Chapter 2, the plate is controlled in such a way that  $W_q = 0$ , leading to  $\underline{W} = W_d$ . This way, (75) leads to two new equations (77), after projecting on axis  $d$  and  $q$ . These equations will be used to deduce the acoustic force in the scenarios explained in the following sections.

$$F_{rd} = NV_d \quad , \quad F_{rq} = NV_q - D\omega W_d \quad (77)$$

#### 5.1.2.1. TRANSVERSE MODE INTERACTION SCENARIOS

In order to explain how  $\underline{F}_r$  is calculated in the rotational reference frame, and give some clues to predict the behavior of these forces over an amplitude sweep at constant frequency, we present the three possible scenarios of interaction and their corresponding  $\underline{F}_r$  calculation for transverse modes: a calibration scenario when there is no contact, a low-amplitude vibration scenario, where the contact between the plate and the skin is not lost, and a high-amplitude vibration scenario, where intermittent contact is established.

##### *A. Scenario 1: calibration*

In the first example, we consider a no-load condition (the probing finger is absent), leading to  $\underline{F}_r = 0$ . Then, the equation (77) yields:

$$V_d = 0 \quad V_q = \frac{D}{N} \omega_n W_d \quad (78)$$

A ‘no-load’ characteristic curve can thus be deduced, where  $W_q = 0$  and  $W_d$  increases linearly with the increase of  $V_q$ , with a slope of  $\frac{D}{N} \omega_n$ . This procedure is applicable for the transverse as well as longitudinal modes and is needed in order to use equation (74).

*B. Scenario 2: permanent contact, linear acoustic impedance*

This scenario occurs at low vibration amplitudes. In this case, the finger is assumed to be constantly in contact with the vibrating plate, inducing a forced out of plane sinusoidal displacement. Due to the fact that ultrasonic vibration has a short penetration on the skin tissues, it is assumed that the interaction takes place mainly with the sc. (stratum corneum) [30]. If we consider a typical sc. model [175] that includes the internal damping of the skin on the presence of normal deformation (denoted by  $D_{fn}$ ) and its vibrating mass  $M_{fn}$ , then, using Newton’s second law in the time domain yields  $f_r = D_{fn}\dot{w} + M_{fn}\ddot{w}$ , leading to the complex components for the acoustic force (79).

$$F_{rd} = -M_{fn}\omega_n^2 W_d \quad F_{rq} = D_{fn}\omega_n W_d \quad (79)$$

These forces are split on the complex axis: the  $d$  axis contains the inertial force while the  $q$  axis contains the damping force. It can be inferred that, since the phase of the force is assumed to be constant, the ratio between  $F_{rd}$  and  $F_{rq}$  is constant and the total force follows a straight line in the d-q frame as the amplitude increases.

*C. Scenario 3: idealized bouncing*

At higher vibration amplitudes, the contact between the finger and the vibrating surface is assumed to be an intermittent one, induced by an ideal elastic shock. When the contact is intermittent,  $f_r$  is supposed to consist of pulses at the

frequency of the vibration, as illustrated in Figure 64, and with a phase shift named  $\Phi$  [115], [127], [175].

Each time the skin bounces on the plate, the force  $f_r$  increases before returning to zero when the skin is detached from the plate. For illustrative purposes, we consider a perfect bounce of the skin: the contact time equals zero, and the contact force is infinite when the plate touches the finger. Therefore, we write  $f_r$  as a Dirac comb distribution with  $f_r = f_0 \sum_{n=-\infty}^{\infty} \delta\left(t - \frac{2\pi n - \Phi}{\omega}\right)$ .

We require the model to have a mean value equal to  $f_n$  which is the mean force applied by the finger. Considering the complex coefficients of the Fourier series of a Dirac comb, this results in  $\underline{c}_0 = f_n$  and  $\underline{c}_n = f_n e^{-jn\Phi}$ , with  $\underline{f}_r = \underline{c}_0 + \sum_{n=1}^{\infty} \underline{c}_n e^{jn\omega t} + \underline{c}_n^* e^{-jn\omega t}$ .

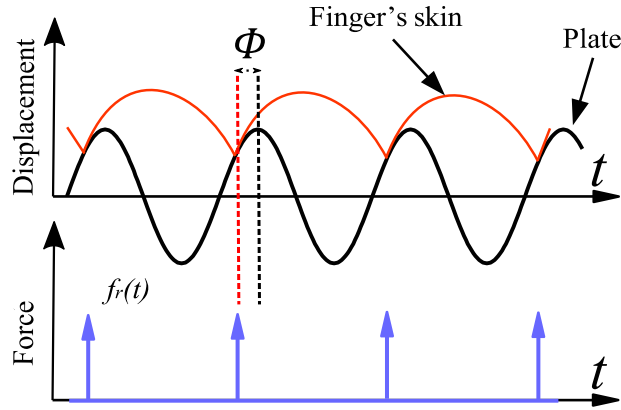


Figure 64. Evolution of  $f_r$  in case of an ideal intermittent contact. Angle  $\Phi$  represents the phase between the displacement peak and the force peak.

It can be inferred that in the limit case, the estimated acoustic force no longer directly reflects the mechanical properties of the finger. Instead, the response is related to the contact occurrence and its phase in reference to the plate vibration, called  $\Phi$ . Moreover, the mean value of this theoretical force over a number of periods is  $|f_r| = 2f_n$ .

Over an amplitude sweep, scenarios 2 and 3 probably occur consecutively [115], [127]. That is, for lower vibration amplitudes, the finger remains in contact with

the plate, and the forces in the dq frame are defined by (79). At a given vibration amplitude, hereby defined as the 'breakpoint', intermittent contact starts. The value of  $\underline{F}_r$  derived from the measurements thus continues to increase tending towards the saturation value of  $2f_n$ .

We expect this kind of evolution of  $|F_r|$  throughout our tests: an initial linear section, followed by a non-linear increase limited by the saturation.

Finally, it is important to note that this scenario is modelled without the inclusion of the effects of the air gap produced by the squeeze film. As explained in [132], this mechanism may lead to additional perceived load, and the finger to bounce on the air and not the on the plate from time to time.

#### 5.1.2.2. LONGITUDINAL MODE INTERACTION SCENARIOS

The approach used to predict the interaction scenarios of the transverse mode in 5.1.2.1, can also be used to predict the behaviour of  $\underline{F}_r$  for an amplitude sweep at the resonance frequency of a longitudinal mode. Nevertheless, excepting the calibration scenario (where only the modal parameters are changed), the interaction mechanisms with longitudinal vibration are very different from the ones presented for transverse vibration. In particular, we part from the hypothesis that the finger is constantly in contact with the plate.

Considering the mechanisms detailed in Chapter 3, two longitudinal interaction scenarios are considered additionally to the calibration: one at low vibration amplitude, where the sc. is deformed but it does not slide, and one at higher amplitude, where the skin slides.

##### *A. Scenario 1: the skin is deformed but it does not slide*

Given that the experiment is performed over a static finger, at very small vibration amplitudes, we may assume that the s.c. does not 'slide' over the device, but is only deformed by the vibration. In this case, we can neglect the skin mass and consider only the damping and stiffness coefficients,  $D_{fl}$  and  $K_{fl}$ , respectively. When the

skin is deformed in the lateral direction, we may write  $f_r = K_{fl}w + D_{fl}\dot{w}$ . This skin model leads to two new equations in the  $dq$  frame (80), considering the closed loop amplitude control strategy mentioned previously ( $W_q=0$ ). In this case, it is possible to expect an increasing linear relation between the magnitude of  $\underline{F}_r$  and  $W_d$ , with the slope of the curve being proportional to the lateral elasticity and dampening of the sc. at ultrasonic frequencies.

$$F_{rd} = K_{fl}W_d \quad , \quad F_{rq} = D_{fl}\omega_n W_d \quad (80)$$

### B. Scenario 2: the skin is deformed and it slides

As the vibration amplitude increases, the tissues of the s.c. may reach maximum extension, and the lateral force added by the vibrating plate may surpass the static friction force. In this case, the surface will slide under the finger. As a result,  $\underline{F}_r$  is proportional to the pressing force  $f_n$  multiplied by the dynamic friction coefficient  $\mu_d$ , which is a function of the relative sliding velocity, as explained in Chapter 3.

## 5.2. Acoustic force measurement and friction correlation: study for transverse modes at a single vibration amplitude

### 5.2.1. Experimental setup and measurement protocol

The transverse mode study was initially performed in [176] with an aluminum beam designed to create a gutter-shaped transverse mode with a resonance frequency of about 25 kHz. The beam design and the experimental setup are briefly described in this section.

#### 5.2.1.1 MATERIAL

The transverse mode haptic device consists of an aluminum beam (18 mm x 119 mm x 2 mm), with four piezoelectric ceramics (14 mm x 6 mm x 0.5 mm) attached

to the lower surface of the beam to produce the vibration. One of them was used as a vibration amplitude sensor. The placement of the actuators and sensor is designed to be well coupled with the vibration mode, without changing the mode shape.

The geometry of the beam, size and position of the piezoelectric ceramics were designed and simulated with a FE (finite element) analysis [164] in order to obtain a pre-defined transverse wave vibration mode at the plate's resonance frequency. We obtained a resonant frequency of 24870 Hz. The placement of the piezoelectric ceramics and FE simulation result is depicted in Figure 65(b).

The setup for this experiment is shown in Figure 66(a). The upper surface of the device is covered with a hydrophobic surface, and sustained by a structure equipped with a 6-dimensional force sensor (ATI Nano 43). An analog Standard Volume Indicator (UV meter) gives a visual feedback of the pressing force. The vibration amplitude sensor is calibrated with a laser vibrometer measurement at the center of the plate, where the maximum displacement occurs for the selected mode.

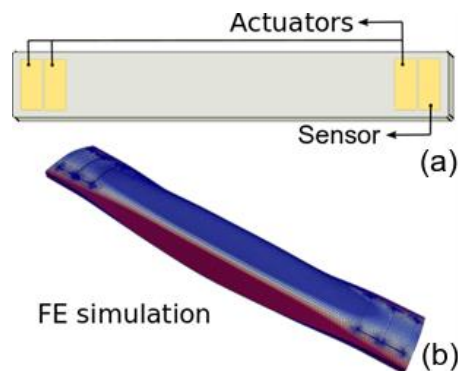


Figure 65. (a) Design of the ultrasonic vibrating plate with the placement of the piezoelectric ceramics, 3 serving as actuators and one as sensor. (b) FE simulation [164] result of the plate and piezoelectric ceramics at the chosen vibration mode.

A closed loop control of the vibration amplitude of the beam was achieved thanks to the use of a Digital Signal Processor (STM32F4 from ST Microelectronics). The

acoustic forces are calculated online, and sent to a main computer through a serial connection for data collection. The vibration control was achieved at 10 kHz. An external power amplifier (HSA 4051 from NF, Japan) amplified the controller's output up to 300 V peak-peak.

In order to implement the controller, the electromechanical transformation parameter  $N$  of the plate-ceramics setup was identified using the methodology described in Chapter 2. Its value is  $N = 0.02 \text{ NV}^{-1}$ . The no-load test measurement was used to identify  $D=0.2848 \text{ Nsm}^{-1}$ , from (10), with an amplitude sweep  $W_d$  varying back and forth from 0 to  $2 \mu\text{m}_{\text{p-p}}$  (with 20 steps of  $0.1 \mu\text{m}_{\text{p-p}}$ ),  $V_d = 0$  and  $V_q = 12 \times 10^6 W_d$ .

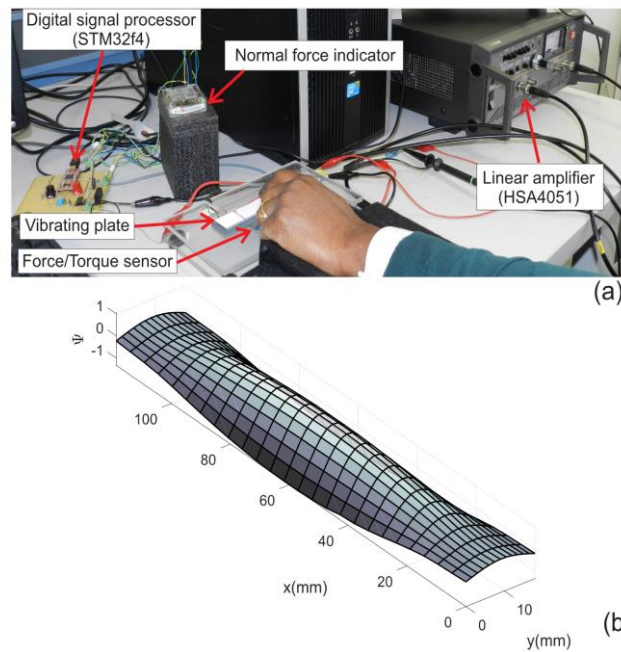


Figure 66. The experimental setup; (a) is the general view and (b) represents the cartography of the measured vibration amplitude, depicting the mode shape.

#### 5.2.1.2. EXPERIMENTAL PROCEDURE

Twelve healthy people aged from 22 to 60 participated in the experiments. They were asked to thoroughly wash and dry their hands before the tests. All participants

gave written informed consent. The research conformed to the principles of the Declaration of Helsinki and all experiments were performed in accordance with relevant guidelines and regulations.

Two experiments were designed; one to obtain the acoustic finger force measurement and another to obtain the friction coefficient reduction. In the first experiment, the participants placed their static finger on the middle of the plate, with the finger in contact at an angle of  $45^\circ$  with respect to the plate's plane, pressing with a normal force of 0.5 N.

At the beginning of the test, an initial calibration step in the no-load condition was performed as explained in scenario 1 of section 5.1.2.1. Then, the finger is placed on the plate and the test begins.

During the experiment, the vibration amplitude  $W_d$  was imposed in closed loop control, just as for the no-load condition, i.e.  $W_d$  varying back and forth from 0 to  $2 \mu\text{m}_{\text{p-p}}$  (with 20 steps of  $0.1 \mu\text{m}_{\text{p-p}}$ ). The cycle was repeated five times. The components  $F_{rd}$  and  $F_{rq}$  were calculated at the end of each step from the measured voltage, from equations (76) and (77). Finally, the result of the five cycles was averaged, obtaining the mean of the acoustic force measurements  $\bar{F}_{rd}$  and  $\bar{F}_{rq}$  and their mean acoustic force magnitude calculation  $\bar{F}_r$  (the average of the magnitude calculation for the five cycles).

In the second experiment, the participants slid their finger in reciprocating motions along the x axis. They were asked to maintain their fingers pressed at an inclination of  $45^\circ$  (with regards to the plate's plane) and a pressing force of 0.4 - 0.5 N.

A metronome was used to control the finger's speed at  $70 \text{ mms}^{-1}$ . It emitted a periodic click at 1bps, which served as a cue for the participants to move their finger between two marked lines on the plate. At each trial, the sinusoidal vibration amplitude applied to the plate was modulated by a low frequency square signal varying from 0.1 to  $2 \mu\text{m}_{\text{p-p}}$ , and the normal and tangential forces were recorded at a sampling rate of 100 Hz.



The second experiment was performed right after the first. This allowed to reduce the variation of experimental conditions of the skin and the device, and to benefit from the training the participant's had to maintain the finger inclination and pressing force. Throughout the tests, we observed that the participants were able to maintain an almost constant pressing force (with standard deviation  $SD = 0.07$  N over all participants).

### 5.2.2. Results

#### 5.2.2.1. RESULTS FROM EXPERIMENT 1

The mean measured forces,  $\bar{F}_{rd}$  and  $\bar{F}_{rq}$  and their mean acoustic force magnitude  $\bar{F}_r$  are depicted for all participants in Figure 67.

We notice that the evolution and maximal values of the obtained  $\bar{F}_r$  and components  $\bar{F}_{rd}$  and  $\bar{F}_{rq}$  differ from one participant to another, due to the different mechanical properties of their skin.

Based on the analysis illustrated in section 5.1, for an applied pressure of about 0.5 N, we expected a linearly increasing  $\bar{F}_r$  which stops at a given 'breakpoint'. From this point, a second increasing curve would start and continue, reaching a saturation at about 1 N ( $2f_n$ ). However, the actual measurements exhibit a difference from this expected behavior for most participants. Some, such as participants 1-2, and 8-12, provide a measurement up to two times higher than the expected 1 N. Others, such as 4, 6 and 7 seem to reach a lower inflection point (or 'breakpoint'), at about 0.5 N, but steadily increase from there. This result may lead to the conclusion that the intermittent contact models used for the examples are perhaps lacking a few elements to describe the full complexity of the contact between the finger and the plate.

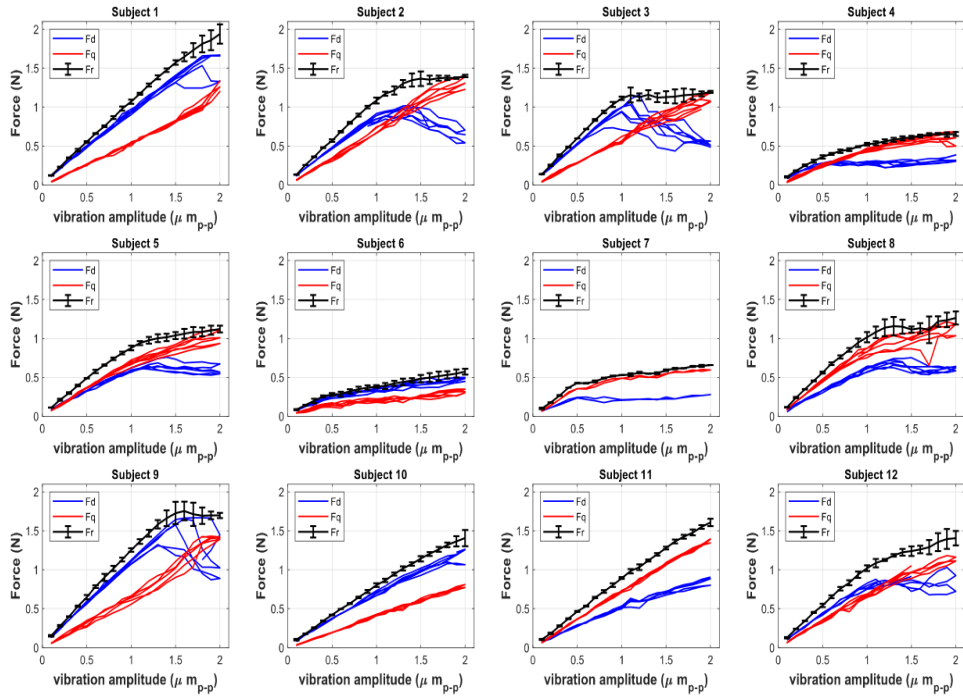


Figure 67. Measured force values  $F_{rd}$  (blue),  $F_{rq}$  (red) and the average force magnitude  $\bar{F}_r$  (black), as a function of amplitude  $w$  for each participant

A possible explanation for this difference may be related to the non-consideration of the existing column of air between the finger and the plate when there is contact loss, as explained by the squeeze film theory. An alternative explanation regards the frequency spectrum of the finger reaction force. For example, if some harmonics of  $f_r$  are produced, as they appear at frequencies other than the resonance, they are neglected in our calculation. In that case, the fundamental acoustic force component may take higher values than expected in order to compensate for these harmonics and maintain a mean of  $f_n$  as expected.

#### 5.2.2.2. RESULTS FROM EXPERIMENT 2

The second experiment helped to obtain a measurement of the friction of the finger against the plate for every participant, with and without vibration.

Figure 68 depicts a typical friction measurement. A positive friction coefficient, denoted  $\mu$ , is obtained when the finger is sliding from left to right, while a negative  $\mu$  is obtained in the reverse direction. The modulation of  $\mu$  is due to the variation of the vibrating amplitude  $W$  with a low frequency square signal while sliding.

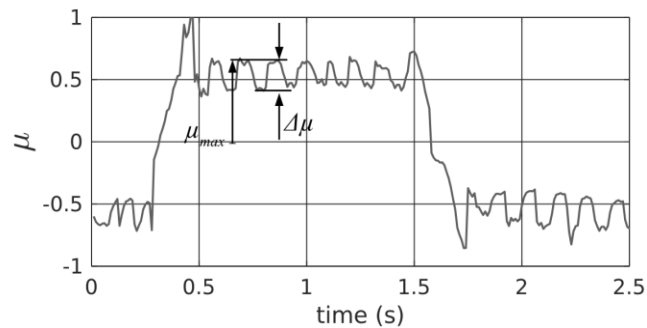


Figure 68. Typical friction coefficient measurements when a participant slides their finger over a haptic device where a temporal grating is imposed.  $\mu_{max}$  and  $\Delta\mu$  represent the maximum friction coefficient and its variation, respectively

To characterize this friction modulation, the lateral and normal force measurements are collected and averaged over 6 periods of reciprocating motion (considering either the positive or negative coefficients), so irregularities and other disturbances may be filtered out. Subsequently, the maximum of  $\mu$ , named  $\mu_{max}$  and the friction reduction denoted  $\Delta\mu$  are computed from the force measurements. The obtained values for all participants are represented in the bar graph in Figure 69. The data indicate that the friction coefficient may be very different from one participant to another, with differences ranging up to 0.6 N/m. Some measurements, such as the ones from participants 3 -7, have a low  $\mu_{max}$  (below 0.5). It can be verified from Figure 67 that these participants also have a low value of maximal acoustic finger force (less than 1.5 N). Participants of the other group (1-2, 8-12) have a high level of friction (above 0.5) and a minimum saturation force of 1.5 N. Therefore, it seems reasonable to consider an existing correlation between the acoustic force measurement and the friction of the finger against the

plate. Although it may seem less evident from the measurements presented in Figure 69, this correlation may also exist for  $\Delta\mu$ .

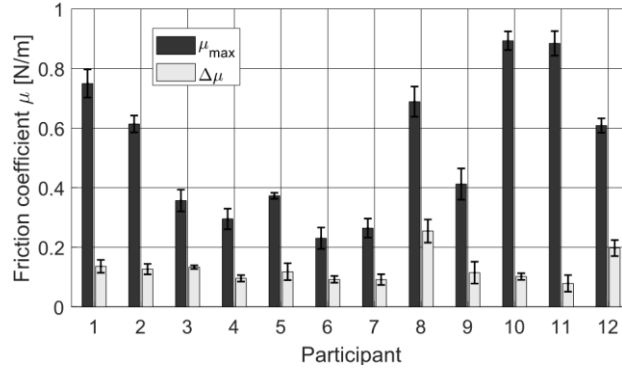


Figure 69. Maximum of friction  $\mu_{\max}$  and  $\Delta\mu$  for each participant

### 5.2.3. PCA of the finger acoustic force measurement

In order to elucidate a possible relation between the fundamental acoustic force calculation and the friction coefficient between the finger and the plate (and how it changes due to vibration), two hypotheses are analyzed. Firstly, it is necessary to determine whether the acoustic force magnitude of a given participant ' $p$ ',  $F_{rp}$  can be expressed as a separable function of two distinct factors. The first factor is related to the motion of the plate, i.e. a function of the vibration amplitude, which will be denoted  $f(W)$ . The second factor is specific to the mechanical properties of the participant's finger i.e. a function of each subject, which will be denoted  $\sigma(p)$ . If the two effects are separable,  $F_{rp}(W)$  can be approximated to the addition of ' $n$ ' basic functions (similar to a Fourier series or a modal decomposition), to be expressed as in equation (81). A PCA (Principal Component Analysis) would therefore be useful for building such a model. In this case, function  $f_i(W)$  is called a "Principal Component  $i$ " (PC $i$ ). These components are orthogonal to each other and define a  $n$ -dimension space.

$$F_{rp}(W) \approx \sum_{i=1}^n f_i(W) \sigma_i(p) \quad (81)$$

The second hypothesis deals with a possible relation between the acoustic force and the friction between the finger and the plate and how this friction reduces when the plate vibrates. Indeed, if it is possible to find a model for the acoustic force response, where a few participant's parameters are differentiated from the influence of the vibration amplitude, it could then be possible to find a relation between these parameters and the friction measurements with and without vibration. This second hypothesis implies that the possible influence of an additional factor in this relation is negligible.

If these two hypotheses are validated, it would mean that the friction between the finger and the plate, with and without vibration, may be inferred with a certain precision by measuring the finger's acoustic force response. Moreover, if equation (81) is validated, this may help with identifying the influence of the human factor in the force response. Such a result may serve to calibrate the amplitude reference for friction simulation and to identify certain finger parameters in an improved finger model.

For analyzing the first hypothesis, one acoustic force matrix  $FR$  is constructed from the averaged data  $\overline{F}_{rp}(W)$ , as shown in

Figure 70. Each entry of  $FR$  corresponds to the mean acoustic force magnitude  $\overline{F}_r$  calculated from the measurements at each vibration amplitude (20 scanned amplitudes from 0.1 to 2  $\mu\text{m}_{p-p}$ ), for each participant (12 subjects).  $FR$  has, therefore, a dimension of 20x12 where the columns represent any given participant and the rows a vibration amplitude.

A PCA analysis is made for  $FR$ . The PCA helps represent the data as a series of projections on subsequent orthogonal normalized axes (the principal components) which will maximize the variance amongst data-points. The first component PC1 corresponds to the direction which explains the highest percentage of the variance while the succeeding ones explain the rest of the percentage of the variance in decreasing order.

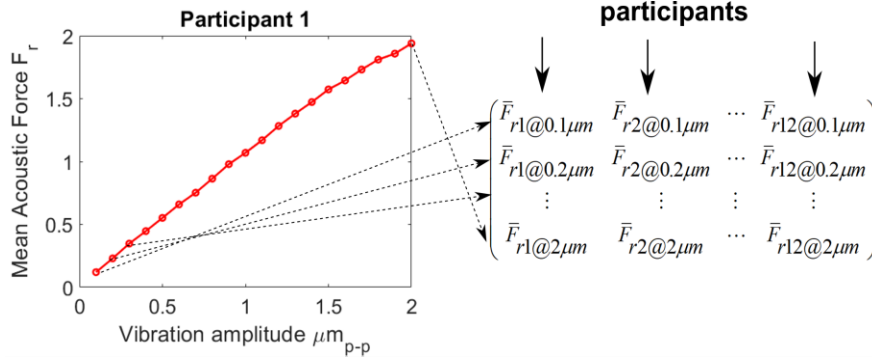


Figure 70. Construction of matrix  $FR$  from the participant's mean acoustic force calculation

As an example, we could say that for a given data set, the principal component 1 (PC1) could explain 95% of the variance, PC2 2%, PC3 0.5%, and so on). The PCA helps to re-write matrix  $FR$  in a 'reduced base', using only one or two components as described in (82).

$$\begin{aligned}
 FR &= \begin{pmatrix} \bar{F}_{r1@0.1\mu m} & \cdots & \bar{F}_{r12@0.1\mu m} \\ \vdots & \ddots & \vdots \\ \bar{F}_{r1@2\mu m} & \cdots & \bar{F}_{r12@2\mu m} \end{pmatrix} = \\
 & \begin{pmatrix} f_1(0.1\mu m) & f_2(0.1\mu m) & \cdots & f_{12}(0.1\mu m) \\ f_1(0.2\mu m) & f_2(0.2\mu m) & \cdots & \vdots \\ \vdots & \vdots & \ddots & \vdots \\ f_1(2\mu m) & f_2(2\mu m) & \cdots & f_{12}(2\mu m) \end{pmatrix} \begin{pmatrix} \sigma_1(p_1) & \sigma_1(p_2) & \cdots & \sigma_1(p_{12}) \\ \sigma_2(p_1) & \sigma_2(p_2) & \cdots & \vdots \\ \vdots & \vdots & \ddots & \vdots \\ \sigma_{12}(p_1) & \sigma_{12}(p_2) & \cdots & \sigma_{12}(p_{12}) \end{pmatrix} \approx \\
 & \begin{pmatrix} f_1(0.1\mu m) \\ f_1(0.2\mu m) \\ \vdots \\ f_1(2\mu m) \end{pmatrix} \begin{pmatrix} \sigma_1(p_1) & \sigma_1(p_2) & \cdots & \sigma_1(p_{12}) \end{pmatrix} + \begin{pmatrix} f_2(0.1\mu m) \\ f_2(0.2\mu m) \\ \vdots \\ f_2(2\mu m) \end{pmatrix} \begin{pmatrix} \sigma_2(p_1) & \sigma_2(p_2) & \cdots \end{pmatrix} \quad (82)
 \end{aligned}$$

A single significant PC in the analysis can be interpreted as a correlation between the measured data, explainable by a simple linear combination of the measurements. In other words, if in our previous example, PC1 explained over 95% of the data (i.e. the 'score' of component 1  $SC_1$  could be larger than 0.95), the mean acoustic force response for every participant  $p_i$  would be represented

by more or less the same ‘shape’:  $f_1(W)$  (first component), multiplied by a constant  $\sigma_1(p_i)$  which is a parameter specific only to the participant.

The PCA enables to extract ‘joint’ behaviors (or characteristics) of the participants if they exist. The reduction (82) is relevant only if the behavior of all participants can be explained (i.e. approximated) by a limited number  $m$  of principal components  $f_i(W)$  significantly lower than the number of participants. This means that, while the sum of all the scores  $SC_i$  is equal to 1, the addition of the  $m$  principal scores should be very close to 1 for the decomposition to yield useful information. If the terms  $SC_i$  are all of the same order of magnitude, one may conclude that there is no “joint” behavior of the participants and the decomposition (82) is not relevant.

#### 5.2.4. PCA results for matrix $FR$

After applying the PCA to the matrix  $FR$ , it was found that PC1 explains over 97% of the variance of the data in matrix  $FR$ . In other words, in the 12-dimensional space created by the measurements of each participant at each vibration amplitude, there exists a one-dimensional sub-space (a single axis: PC1), which serves to accurately represent most of the variance of the data.

Figure 71 represents the biplot of  $\bar{F}_{rp}(W)$  (red dots) in the PC1, PC2 plane. In blue, each axis represents the loadings, i.e., the projection of each participant on the principal component plane. If it was desired, for example, to find the value of the data for one of the 12 participants, it would suffice to project the force data points onto the axis corresponding to the desired subject. For this reason, axes which are projected close to each other are expected to produce similar  $\bar{F}_{rp}(W)$  responses.

This result confirms hypothesis 1, that the function describing  $F_{rp}$  at a given amplitude can be represented by separating the influence of the plate from the human. Hence, an estimation of the fundamental acoustic finger force  $\tilde{F}_{rp}$  may be

obtained by simplifying (82) to (83) if only one PC is considered, or to (84) if we consider PC1 and PC2.

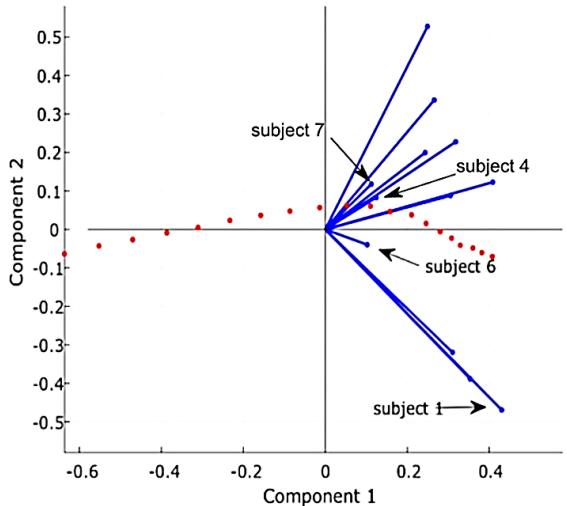


Figure 71. Biplot of scores and loadings for  $\bar{F}_{rp}(W)$  data from 0 to  $2\mu_{p-p}$  in PC1, PC2 plane. The loadings (in blue) represent the projections of the axes of each participant in the PC plane

$$\tilde{F}_{rp}(W) = f_1(W)\sigma_1(p) \tag{83}$$

$$\tilde{F}_{rp}(W) = f_1(W)\sigma_1(p) + f_2(W)\sigma_2(p) \tag{84}$$

Thanks to this result, the sought human characteristic becomes simpler to find. If (83) is considered, for a given participant  $p$ ,  $\sigma_1(p)$  can be estimated from the knowledge of  $f_1(W)$ , and the measurement of  $\bar{F}_{rp}(W)$ . Moreover, given that  $f_1(W)$  is already known,  $\sigma_1(p)$  can be estimated by measuring a single data point (predictor) of  $\bar{F}_{rp}(W)$  at a given amplitude for subject  $p$ . If two PC were considered, as in (84), two predictors would serve to find  $\sigma_1(p)$  and  $\sigma_2(p)$ , and so on. This is called a Principal Component Regression, or PCR.

Given these results, if we assume that the PCA of  $FR$  when an additional person is included is very similar to the original PCA result with 12 subjects, then the model is accurate, and force data extrapolation is feasible using a PCR. This means



that, if an additional person  $p_{13}$  is included, his/her complete acoustic force response can be reconstructed from the measurement of one or two predictors. This result is very interesting in the scenario of a possible calibration based on acoustic force: if the complete response, and eventually the person's coefficient can be inferred from a single (or two) point measurement, the calibration process can be substantially shorter and simpler.

### 5.2.5. Coefficient $\sigma_1$ and $\tilde{F}_{rp}$ estimation by PCR

A reconstruction of a person's force response using PCR with a single predictor is illustrated in an example.

Here, participant 12 ( $\sigma_1(p_{12}) = 0.305$ ) is removed from the calculation. A PCA is then performed with the data from the remaining 11 participants. One measurement of the 12<sup>th</sup> participant is then taken. For this example, the mean force magnitude at  $2 \mu\text{m}_{p-p}$  is used as predictor:  $\bar{F}_{r12@2\mu\text{m}} = 1.406 \text{ N}$ .

The estimated coefficient of the 12<sup>th</sup> participant can be calculated by dividing the measured data point by the value from the PCA model at the same amplitude of  $2 \mu\text{m}_{p-p}$ :  $\sigma_{1est}(p_{12}) = \bar{F}_{r12@2\mu\text{m}}/f_1(2 \mu\text{m}_{p-p})$ . This coefficient  $\sigma_{1est}(p_{12}) = 0.311$ , is then used to re-calculate the force response for subject 12 at each point, as can be seen in Figure 72. In this figure, the force estimation is compared to the measurement for subject 12. The results show a seemingly accurate estimation  $\tilde{F}_{r12}$  for participant 12 at each amplitude, with a mean relative error  $errF\% = 100 * \text{mean}\left(\frac{|F_{rp} - \tilde{F}_{rp}|}{F_{rp}}\right)$  of about 3.8% and a maximum relative error of less than 8% at each point. The relative error for  $\sigma_1(p_{12})$ , ( $err\sigma\% = 100 * \frac{|\sigma_1 - \sigma_{1est}|}{\sigma_1}$ ) is equal to 1.74%.

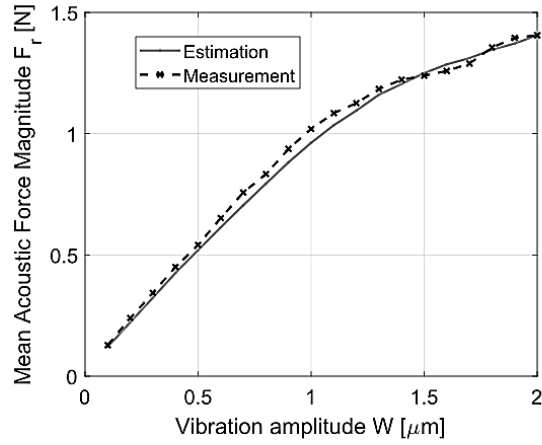


Figure 72. Fundamental acoustic force estimation  $\tilde{F}_{rp}(W)$  from one force measurement using the PCA model with only one principal component. Comparison with the mean fundamental acoustic force  $\bar{F}_{rp}(W)$

A similar approach would be used if two predictors were needed. However, since an additional measurement is required, we would obtain two data points from measurements at amplitudes  $W_1$  and  $W_2$ :  $P_1 = \bar{F}_{rp@W_1}$  and  $P_2 = \bar{F}_{rp@W_2}$ . Knowing these two points, the new  $\sigma_1(p)$  and  $\sigma_2(p)$  can be estimated using equations (85) and (86). The force estimation is then made by replacing  $\sigma_1(p)$  and  $\sigma_2(p)$  in (84).

$$P_1 = f_1(W_1)\sigma_1(p) + f_2(W_1)\sigma_2(p) \quad (85)$$

$$P_2 = f_1(W_2)\sigma_1(p) + f_2(W_2)\sigma_2(p) \quad (86)$$

### 5.2.6. PCR best predictor selection and results

#### 5.2.6.1. PREDICTOR SELECTION METHOD

Some predictors may produce better models than others. To select the best, it is possible to perform a cross validation of the PCR using the RMSEE (root mean squared error of estimation). The objective of this test is to find the predictors that minimize the average error between the estimation and the fit for the acoustic force

data. In order to find these points, the procedure described in 5.2.5 is performed for each participant, using every measurement point as a predictor and updating the PCA model from the other participants each time. For each participant, the RMSEE of the measured  $\bar{F}_{rp}$  vs. the estimated  $\tilde{F}_{rp}$  is calculated and averaged for every produced model. Finally, the predictor producing the model with the least average RMSEE amongst all participants is chosen.

Table 4. Mean Relative error *errF%* of the acoustic finger force estimation using one and two predictors

p	<i>errF%</i> 1 predictor	<i>errF%</i> 2 predictors
1	14.7	2.03
2	3.52	2.09
3	15.1	4.54
4	14.1	9.52
5	7.1	0.87
6	12.7	11.1
7	17.5	11.5
8	11.4	2.79
9	9.36	3.99
10	10.2	1.32
11	12.9	2.64
12	4.33	1.24

If the PCR uses only PC1,  $W = 1.5 \mu\text{m}_{p-p}$  is chosen, which produces an average RMSEE of 0.084, and an average relative error of the estimated coefficient of about 11%, which is relatively small, but could still mean significant differences for some subjects.

For two components, predictors at  $W_1 = 0.8 \mu\text{m}_{p-p}$  and  $W_2 = 1.8 \mu\text{m}_{p-p}$  are chosen, yielding an average RMSEE of 0.034, and an average relative error of the estimated acoustic force (*errF%* as calculated in section 5.2.5) of less than 4.5%, as can be deduced from Table 4.

### 5.2.6.2. RESULTS FOR $\tilde{F}_{rp}$ PCR USING SELECTED PREDICTORS

Figure 73 presents the resulting reconstruction for  $\tilde{F}_{rp}$  from the PCR models against  $\overline{F}_{rp}$  obtained from measurements, depicted in black. In red we can see the results if only one predictor is used, and in blue the effect of the inclusion of a second predictor. It can be observed that the blue curve produces a better description of the force behaviour than the red one.

The mean relative errors for the  $\tilde{F}_{rp}$  estimation reconstruction for all participants using the chosen predictors with one and with two components are listed in Table 4. From the obtained results, it may be concluded that, although PC1 explains over 97% of the variance of the data in matrix  $FR$ , the use of two predictors significantly improves the estimation of  $\tilde{F}_{rp}$ .

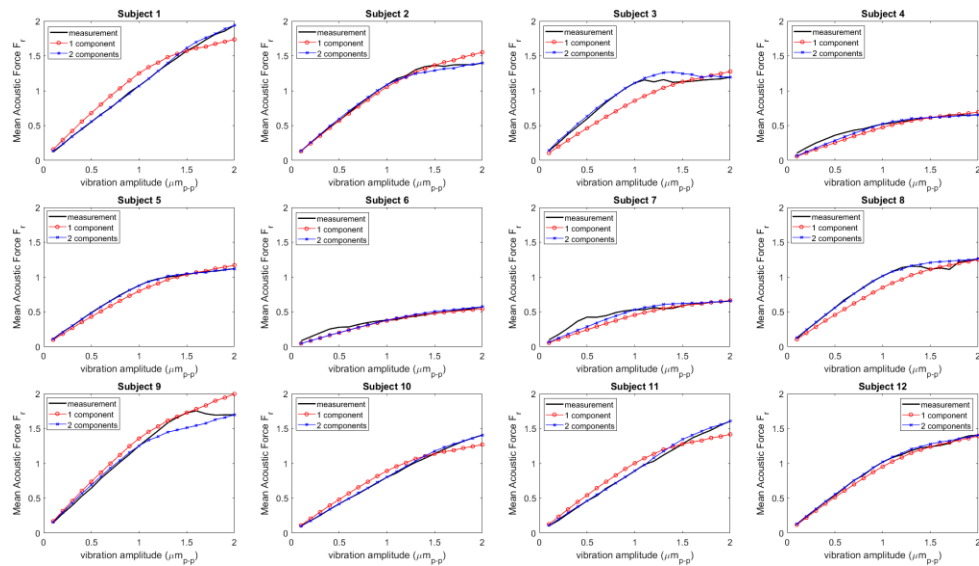


Figure 73. Mean Acoustic Force estimation comparison: using one PC (red), and using two PC (blue)

From Table 4 it can also be observed that, even though the inclusion of an additional component significantly improved the estimation error, the percentage

errors for subjects 4, 6 and 7 remained rather high in comparison to the other participants. This indicates that these subjects have a poorer fit in the PCA model; a result that could already be intuited from their PCA loadings being smaller in the principal component plane shown in Figure 71. It is interesting to note, as well, that these participants are the only ones displaying a maximum  $\overline{F}_{rp}$  lower than 1N, and a smaller breakpoint amplitude and force. Consequently, it may be deduced that these subjects have considerably different skin properties than the rest of the participants in the study.

### 5.2.7. PCR of $\sigma_n(\mathbf{p})$ and correlation with friction

In section 5.2.6, we were able to fairly estimate the acoustic finger force measurement for all participants at any tested amplitude with the use of two selected predictors. However, when the analysis explained is applied to the estimation of the PCA coefficients  $\sigma_n(\mathbf{p})$ , the predictors which yield the best acoustic force fit do not necessarily produce the best coefficient estimation.

Given that our final objective is to link these coefficients to the friction measurements, the analysis is applied to the PCA coefficients. It follows that new predictors are selected for the estimation.

#### 5.2.7.1. ESTIMATION OF $\sigma_n(\mathbf{p})$ USING A PCR WITH NEW SELECTED PREDICTORS

For obtaining  $\sigma_{1est}(\mathbf{p})$  with a single predictor, the acoustic force value at  $W = 2 \mu\text{m}_{p-p}$  is selected as the best predictor. The results of the coefficient estimations and errors for each participant are listed in

Table 5. Compared to the coefficients derived from the measurements, an average relative error  $error\% = 100 * \frac{|\sigma_1 - \sigma_{1est}|}{\sigma_1}$  equal to 8.1% is obtained.

Once again, it can be noticed that participants 4, 6 and 7 stand out from the rest. Aside from these ‘outliers’, the regression yields a maximum estimation error of

less than 10%. Finally, the impact of this error in the final friction estimation is analyzed in section 5.2.7.2.

Table 5. Mean coefficient derived from PCA vs. estimated coefficient from a single predictor

p	$\sigma_1$	$\sigma_{1est}$	err $\sigma$ 1%
1	0.431	0.428	0.72
2	0.318	0.308	3.23
3	0.250	0.265	6.01
4	0.124	0.145	16.39
5	0.244	0.247	1.45
6	0.102	0.127	23.99
7	0.113	0.145	29.24
8	0.266	0.280	5.23
9	0.409	0.368	9.93
10	0.311	0.311	0.01
11	0.354	0.355	0.29
12	0.305	0.311	1.75

When two components are used, it must be taken into account in advance that the second component PC2 only explained about 3% of the variance in the PCA. It is thus expected that the estimations of the second coefficient produce larger errors than the first. Predictors at  $W_1 = 0.8 \mu\text{m}_{p-p}$  and  $W_2 = 1.8 \mu\text{m}_{p-p}$  are selected, with their corresponding relative error:  $err\sigma 1\% = 100 * \frac{|\sigma_1 - \sigma_{1est}|}{\sigma_1}$  equal to 8.06% and  $err\sigma 2\% = 100 * \frac{|\sigma_2 - \sigma_{2est}|}{\sigma_2}$ , equal to 17.6%.

The results of the estimation of  $\sigma_1(p)$  and  $\sigma_2(p)$  for each participant and their corresponding errors are listed in

Table 6.

Comparing the results of

Table 6 and Table 5, it can be observed that the coefficient estimation has not been substantially improved by the inclusion of a second component, as was the case with the acoustic force. Moreover, very large error margins can be observed on the

estimation of the second component coefficient  $\sigma_2$ , especially for participants 4, 6 and 7. Because of these error margins, a single predictor was chosen for the coefficient vs. friction correlation analysis.

Table 6. Mean coefficients derived from PCA vs. estimated coefficient from two data points

p	$\sigma_1$	$\sigma_2$	$\sigma_{1est}$	$\sigma_{2est}$	err $\sigma$ 1%	err $\sigma$ 2%
1	0.431	-0.469	0.435	-0.497	1.1	6.0
2	0.318	0.228	0.303	0.219	4.8	3.6
3	0.250	0.527	0.262	0.535	5.0	1.4
4	0.124	0.083	0.143	0.133	14.9	60.8
5	0.244	0.199	0.244	0.197	0.1	1.5
6	0.102	-0.040	0.127	-0.024	23.9	40.8
7	0.113	0.118	0.144	0.143	27.8	21.6
8	0.266	0.336	0.277	0.255	4.1	24.2
9	0.409	0.123	0.364	0.162	11.0	32.2
10	0.311	-0.319	0.314	-0.296	1.1	7.3
11	0.354	-0.388	0.361	-0.392	2.0	0.8
12	0.305	0.088	0.309	0.097	1.0	10.6

#### 5.2.7.2. FRICTION CORRELATION WITH $\sigma_n(p)$ PCR RESULTS USING A SINGLE PREDICTOR

In Figure 74, the estimated coefficients  $\sigma_{1est}(p)$  are plotted (in red) against the friction coefficient  $\mu_{max}$  without vibration,  $\mu_{min}$  when there is a vibration at  $2 \mu m_{p-p}$ , and finally against the relative friction coefficient reduction  $\Delta\mu/\mu_{max}$  (friction contrast [197], a parameter associated with perception).

Linear regressions between  $\sigma_{1est}$  and  $\mu_{max}$ ,  $\mu_{min}$  and  $\Delta\mu/\mu_{max}$  are calculated. The resulting relations are written in (87) - (89).

When performing the approximation, we find that  $\mu_{max}$  has a correlation of about 75% with the estimated  $\sigma_1(p)$  and a standard mean squared error of 0.53. For  $\mu_{min}$  we get a correlation of about 71% and a standard mean squared error of 0.54. In the case of friction contrast, the relation between  $\sigma_{1est}(p)$  has a smaller correlation of about 65% and a standard mean squared error of 0.26.

$$\mu_{max} = 1.9\sigma_{1_{est}}(p) + 0.015 \quad (87)$$

$$\mu_{min} = 1.8\sigma_{1_{est}}(p) - 0.078 \quad (88)$$

$$\Delta\mu/\mu_{max} = -0.72\sigma_1(p) + 0.47 \quad (89)$$

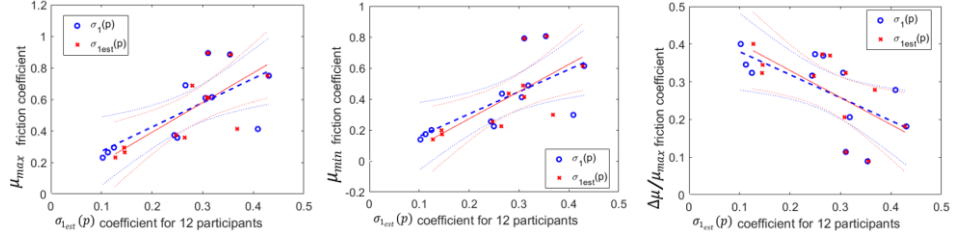


Figure 74. In red, continuous line, relation between the estimated PCA coefficients  $\sigma_{1_{est}}(p)$  and (left) friction coefficient without vibration, (center) friction coefficient with  $2\mu_{p-p}$  vibration, (right) friction contrast. In blue, dashed lines, the same relations, calculated with  $\sigma_1(p)$  are presented. The data-points at the origin of the linear regression model fits are plotted in red crosses and blue circles, respectively. Small dashed lines at both sides of each regression shows the 95% confidence bounds.

In order to find the effect of the estimation error of the PCA coefficients listed in Table 5 on the final friction estimation, a second regression is performed, using the actual  $\sigma_1(p)$ . The coefficients  $\sigma_1(p)$  and second regression are plotted in blue circles and blue dashed lines, respectively, over the regression performed for  $\sigma_{1_{est}}(p)$ . From the superposition of both lines, it is possible to see that the coefficient estimation from the PCA affects the friction coefficient estimation by less than 10% at worst, which is below the average JND (just noticeable difference) of friction of about 18% [198].

The friction coefficients are estimated with the linear regressions given by (87) - (89) for each participant. Table 7 details the estimation and relative error of the  $\mu_{max}$  and  $\mu_{min}$  estimations using  $\sigma_{1_{est}}$ , against the corresponding measurements.



The approximation produces average relative errors  $err\mu_{max}\% = 100 * \frac{|\mu_{max} - \mu_{max_{est}}|}{\mu_{max}}$  and  $err\mu_{min}\% = 100 * \frac{|\mu_{min} - \mu_{min_{est}}|}{\mu_{min}}$  of about 22% and 28% respectively, even though a group of outliers is identified.

From the results, it can be noted that most of the friction error estimation is due to the linear regression between the coefficients and the friction measurements. A more detailed tribology study may help shed light on this relationship.

Table 7. Friction Coefficient Measurement vs. Estimation from PCA Coefficients and Linear Regression

P	$\mu_{max}$	$\mu_{min}$	$\mu_{max_{est}}$	$\mu_{min_{est}}$	$err\mu_{max}\%$	$err\mu_{min}\%$
1	0.750	0.614	0.827	0.692	10.3	12.7
2	0.614	0.487	0.600	0.477	2.2	2.2
3	0.357	0.224	0.518	0.398	45.1	78.1
4	0.295	0.200	0.290	0.183	1.6	8.4
5	0.373	0.255	0.485	0.367	30.1	44.1
6	0.230	0.138	0.256	0.150	11.1	8.8
7	0.264	0.173	0.291	0.184	10.2	6.3
8	0.689	0.434	0.547	0.426	20.7	2.0
9	0.412	0.298	0.715	0.585	73.4	96.7
10	0.893	0.792	0.605	0.481	32.3	39.3
11	0.884	0.806	0.689	0.561	22.1	30.4
12	0.609	0.411	0.606	0.481	0.5	17.0

### 5.2.8. Discussion on the transverse mode study

The objective of this study was to propose a methodology to create and evaluate a model linking friction and the fundamental finger acoustic force for a single vibration amplitude in a USHD. From the measurements illustrated in Figure 67, it can be noted that for most participants, the force response in function of the vibration amplitude increases linearly up until a given amplitude (hereby named 'breakpoint'), when either the  $d$  or the  $q$  (or both) components of the acoustic force saturate, and from that point the response is non-linear. We believe that this change in force behavior corresponds to the onset of the intermittent contact.

This inflection point is different from one participant to another. This might be due to the different mechanical skin parameters.

Figure 69 shows that there may be a correlation between the friction coefficient and the measured acoustic force magnitude. This is explainable by taking into account that people with similar biomechanical finger properties may have similar friction responses. Those with a high friction coefficient  $\mu_{max}$  appear to have high acoustic finger forces, and vice versa. On the other hand, participants with high acoustic finger force have a lower friction contrast as can be seen in

Figure 74. This can be explained, for example, by the moisture level of the participant's finger. Indeed, [199] demonstrates that higher level of moisture leads to higher level of friction coefficient for all surfaces (without ultrasonic vibrations), while at the same time [149] shows that moist skin also has lower stiffness than dry skin and thus needs higher vibration amplitude to obtain the intermittent contact. As was observed in Figure 69, a high vibration amplitude 'breakpoint' is related to high acoustic finger force measurements.

A statistical model was derived from the PCA of the resulting acoustic finger force calculations. This model could help in the future for performing an 'offline' reference calibration, and eventually a more practical 'online' estimation of the friction in function of the vibration amplitude for a given user. More specifically, the offline calibration workflow for any new user would be divided in three steps. First, the fundamental acoustic finger force could be calculated for one or two selected amplitudes with a static finger measurement, as explained in section 5.2.5. Secondly, these measurements could be used to estimate the PCA coefficient specific to the tested subject. Finally, the estimated PCA coefficient could be fitted into the linear regression proposed in section 5.2.7, to estimate the maximum, minimum and eventually the friction contrast expected for a given vibration amplitude, which could be used to calibrate the controller reference. Indeed, the proposed calibration process, which would take place once before the user begins using the device, includes the acoustic force measurement, and

the adaption of the amplitude reference. The first step takes a fraction of a second to execute (about 0.4s for two points) while the second one could be executed at an even shorter time (in the order of microseconds) depending on the computational speed of the processing material available.

### **5.3 Acoustic Force measurement and friction correlation: Study for longitudinal modes at different vibration amplitudes**

Encouraged by the results obtained for the transverse mode in section 5.2, we use the same approach exposed in section 5.2, but for the longitudinal mode, and going further, i.e. extending the study to explore the relation between acoustic force and friction at more than one vibratory amplitude.

One advantage of using this approach with longitudinal modes, as compared to transverse modes, is that the mechanisms by which the lateral acoustic finger force is measured derive from the same type of interaction that originates the friction reduction, which are explained in Chapter 3. Also, since we assume that no (or very limited) intermittent contact occurs, the acoustic finger force measurement using longitudinal modes is less affected by factors such as the squeeze film [127] and/or shocks. For this reason, we expect there to obtain a clearer correlation between the lateral acoustic finger force and the friction reduction with longitudinal vibration. In order to do so, we propose building three models from experimental data. First, a linear regression of the lateral acoustic finger force against the friction reduction at the highest tested vibration amplitude is found. A second model consists of a PCA of the lateral acoustic finger force at every vibration amplitude. Finally, a third model consists of a second PCA of the friction reduction divided by the measured lateral acoustic finger force. The friction reduction at different amplitudes is then estimated for each participant, treating them as a 'new' subject and using the models described, derived from the data of all other participants.

### 5.3.1. Experimental procedure

#### 5.3.1.1. SETUP AND PROTOCOL

The setup for the experiments carried out in this study is shown in Figure 75. The longitudinal USHD tested is the one described in Chapter 2. The device is placed over a three-axial force sensor (GSV-4USB from ME-Meßsysteme). The USHD and force sensor are finally adapted over the moving section of a tribometer. A structure to support the hand and the finger is placed next to the device. A computer is connected to the DSP and force sensor, to provide the amplitude reference to the DSP and collect the force data.

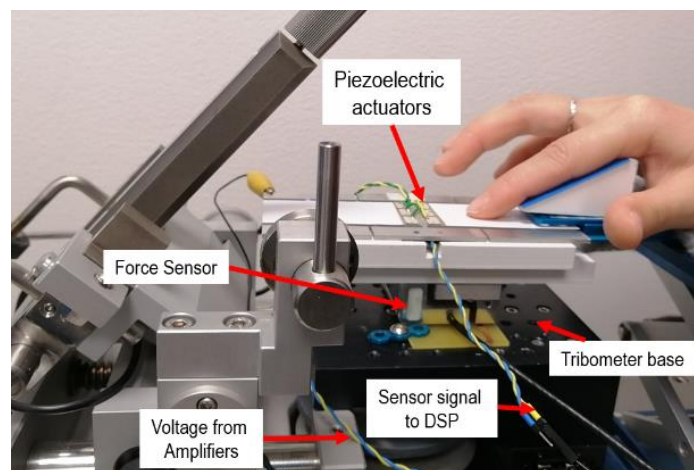


Figure 75. Setup for lateral acoustic finger force and friction measurements

Two experiments are performed with this set-up. The first one aims at measuring the finger lateral acoustic force (the user only presses his (her) finger on the plate). The second one is dedicated to the measurement of the finger-surface friction (the finger slides over the plate). In both experiments, data were collected from nine healthy volunteers aged between 18 and 50 (4 females). All participants gave informed consent. The investigation conformed to the principles of the Declaration of Helsinki and experiments were performed in accordance with relevant guidelines and regulations.

### 5.3.1.2. RESULTS

The results from the first experiment illustrate that the steady state voltages needed for the vibration amplitude control are mostly linear. When comparing them, we can see that the loaded curve describes a linear section which has a steeper slope than the curve with no load. For a few participants, a “saturation point” seems to be reached, where the linear section breaks into a second line with the same slope as the curve at no load. We believe this might be the passage from the sticking to the sliding regime.

An example for two participants is shown in Figure 76. According to the analysis on sub-section 5.1.2.2, the change in slope between the loaded and unloaded curve and the saturation point may be related to the elasticity and damping components of the finger. Based on the acquired measurements, the calculation of  $F_{rd}$ ,  $F_{rq}$  and  $F_r$  for the nine participants are shown in Figure 77. The relative friction coefficient  $\mu' = \mu/\mu_{max}$  measurements, such as the ones studied in chapters 3 and 4, are represented in Figure 78.

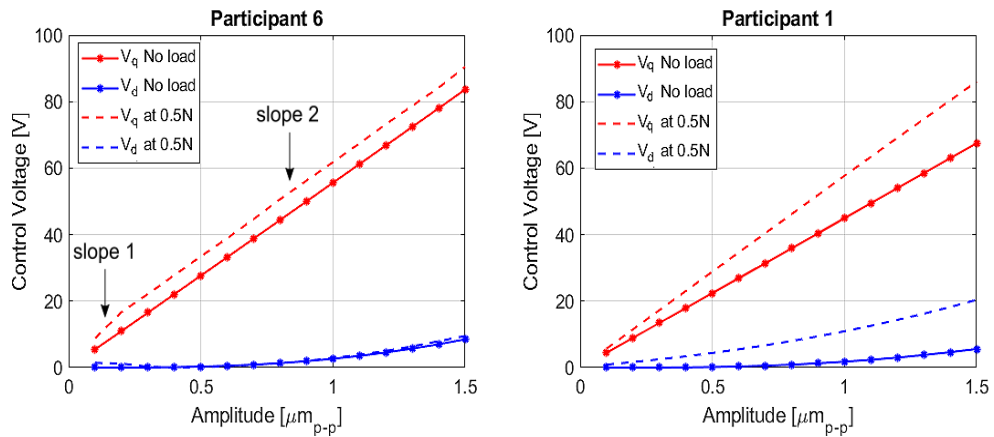


Figure 76. Examples of  $V_d$  and  $V_q$  measurements with and without a load for two participants

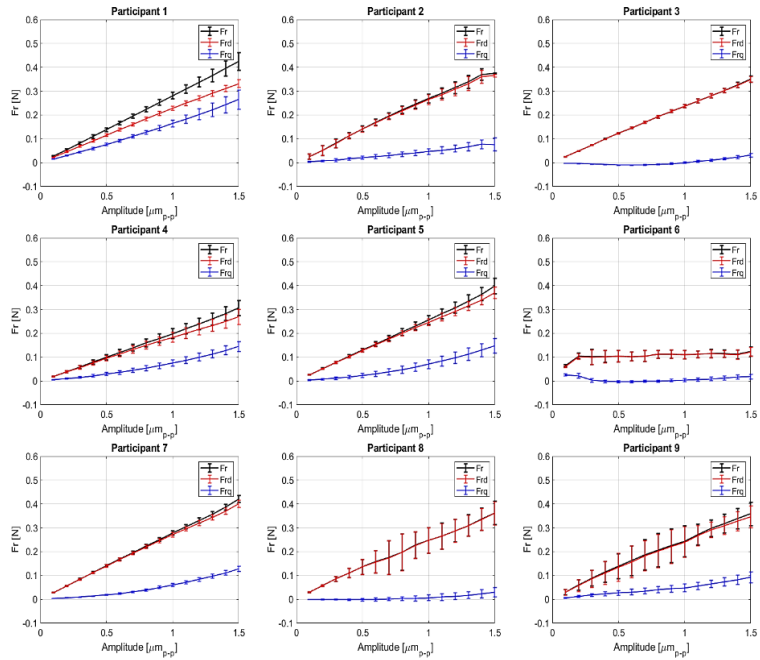


Figure 77. Mean and variance of  $F_d$ ,  $F_q$  and  $F_r$  for nine participants

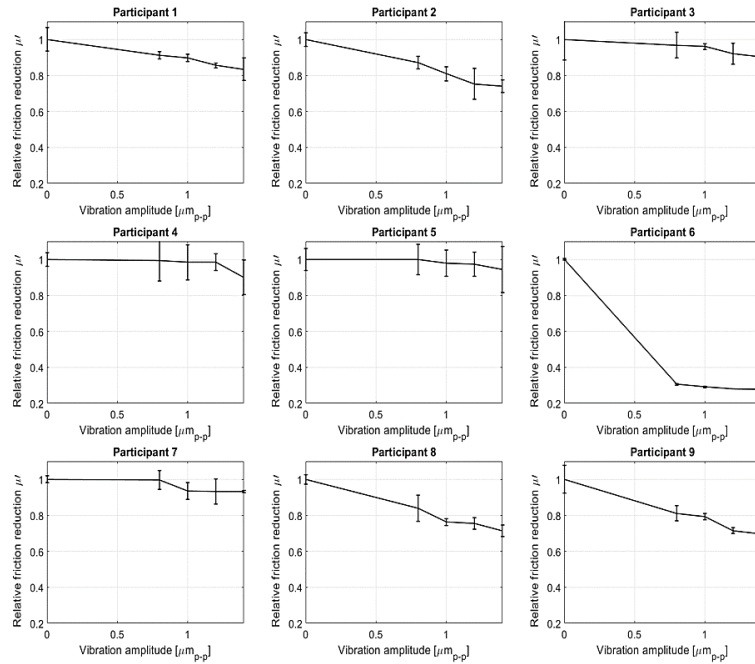


Figure 78. Mean and variance of  $\mu'$  for nine participants

### 5.3.2. Construction of predictive models

#### 5.3.2.1. LINEAR REGRESSION OF THE MEAN ACOUSTIC FORCE $\bar{F}_r$ VS. $\mu'$ FOR EACH PARTICIPANT AT $1.4 \mu m_{p-p}$

From the data collected in 5.3.1, it may be observed that for the participants concerned with a “saturation point” (p2 and p6), the lowest breakpoint vibration amplitude seems to be correlated to a higher friction reduction. A closer observation suggests that, for the tested amplitudes, most participants appear to remain in the first linear section. In this case, a steeper curve, leading to a higher  $\bar{F}_r$  is linked to less performant results in terms of friction attenuation for most participants. In other words, higher values of  $\bar{F}_r$  produce a larger  $\mu'$  at any vibrational amplitude. Consequently, a linear regression analysis is suggested for these measurements. The result of the linear regression which is shown in Figure 79 provides an R-squared value of over 0.78 and a Pearson correlation of over 88%. This result shows an improvement to the correlation found for transverse mode data [132], [176].

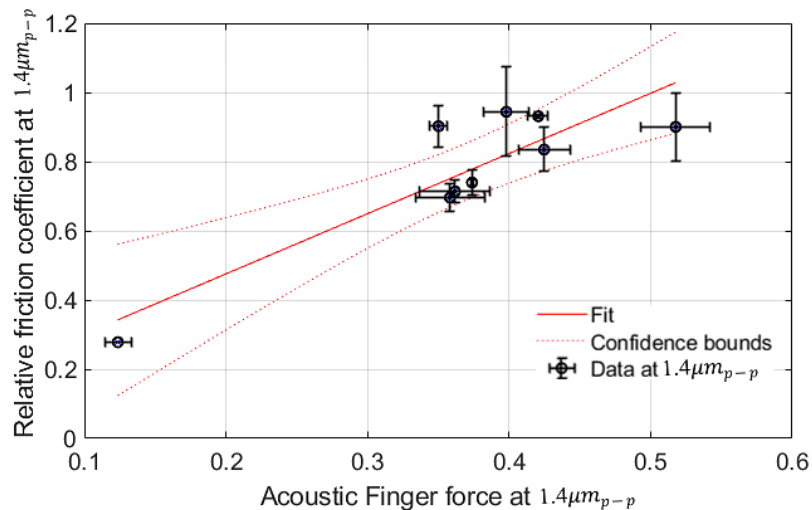


Figure 79. Linear regression for  $\bar{F}_r$  vs.  $\mu'$  for nine participants at  $1.4 \mu m_{p-p}$ , producing R-squared value of over 0.78 and a Pearson correlation 88%

#### 5.3.2.2. MEAN FORCE $\bar{F}_r$ PCA FOR LONGITUDINAL MODES

The methodology explained in 5.2.4 and 5.2.5 is applied to the acoustic force measurements obtained in 5.3.1. In order to produce the PCA for the longitudinal mode data, the value of  $\bar{F}_r$  for every participant is organized in a column, with every element corresponding to one vibrational amplitude. After performing the PCA on this matrix, we obtained a score of over 97% for PC1, meaning that, once again, only one or two components may suffice to describe the data. Therefore, the value of  $\bar{F}_r$  for any subject at any vibration amplitude up to  $1.4 \mu\text{m}_{\text{p-p}}$  could be rather accurately predicted using only two measurements at, for example  $0.8 \mu\text{m}_{\text{p-p}}$  and  $1.4 \mu\text{m}_{\text{p-p}}$ .

#### 5.3.2.3. PCA TO ESTIMATE THE RATIO $\mu'/\bar{F}_r$

From the regression shown in Figure 79, it is possible to conclude that there may exist a linear relation between the lateral force and the relative friction coefficient for every participant. However, this relation is far from being constant throughout an amplitude sweep. For this reason a PCA is produced to find the relation between  $\mu'/\bar{F}_r$  at every point, with the data for the participants at the points where the friction was measured. After performing the PCA on this matrix, we obtained a score of over 95% for PC1.

#### 5.3.3. *Tests of the methodology*

With the help of the three models constructed in section 5.3.2, the relative friction coefficient  $\mu'$  at different amplitudes could be estimated for any new subject following four steps. First, the lateral acoustic finger force is measured for a static finger pressing the surface of the device at two different vibration amplitudes. With this measurement, the complete acoustic finger force response for every amplitude can be calculated using a 2-point PCR (principal component regression) using the PCA model obtained in section 5.3.2.2



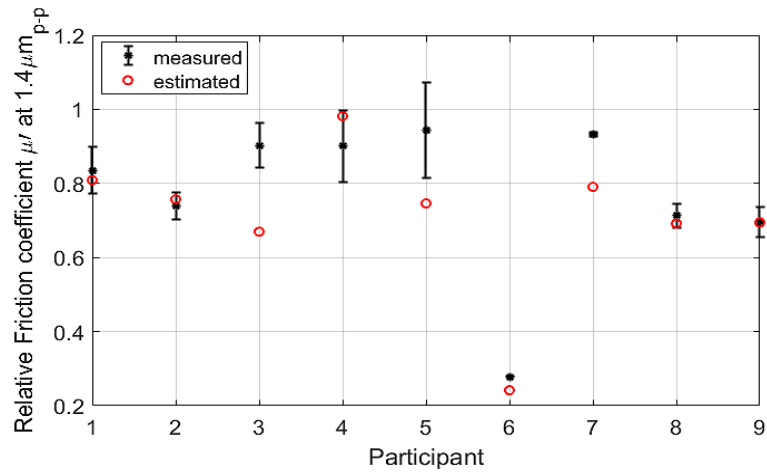


Figure 80. Estimation of  $\tilde{\mu}'$  vs. measured  $\mu'$  for nine participants at  $1.4 \mu\text{m}_{p-p}$

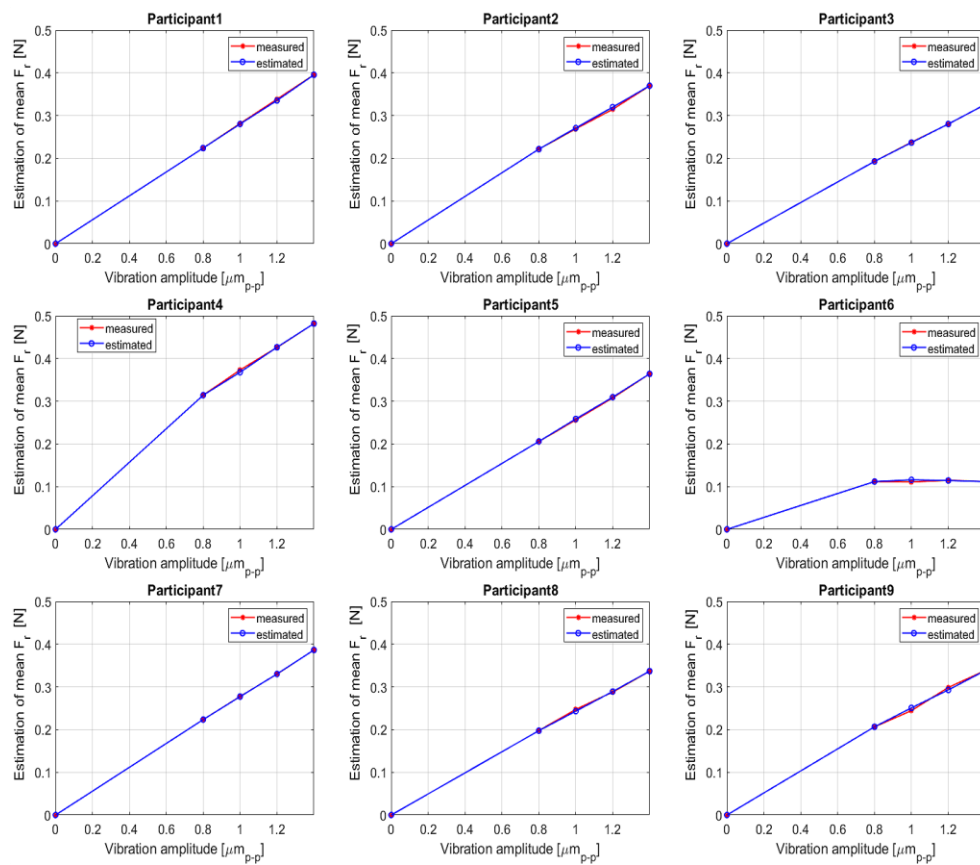


Figure 81. Estimation of  $\tilde{F}_r$  vs.  $\bar{F}_r$  for nine participants

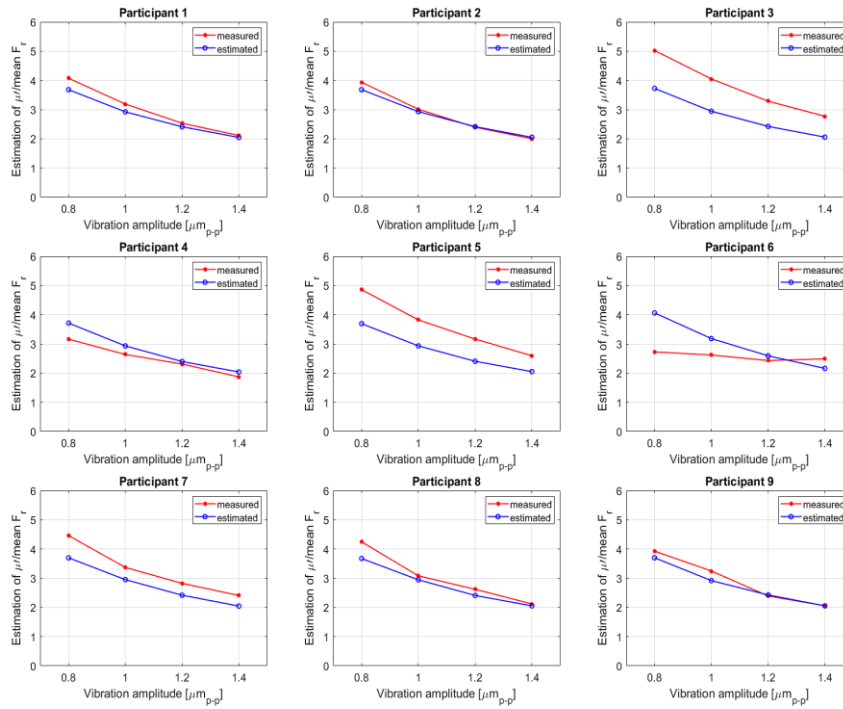


Figure 82. Estimation of  $\tilde{\mu}'/\tilde{F}_r$  vs. measured  $\mu'/\bar{F}_r$

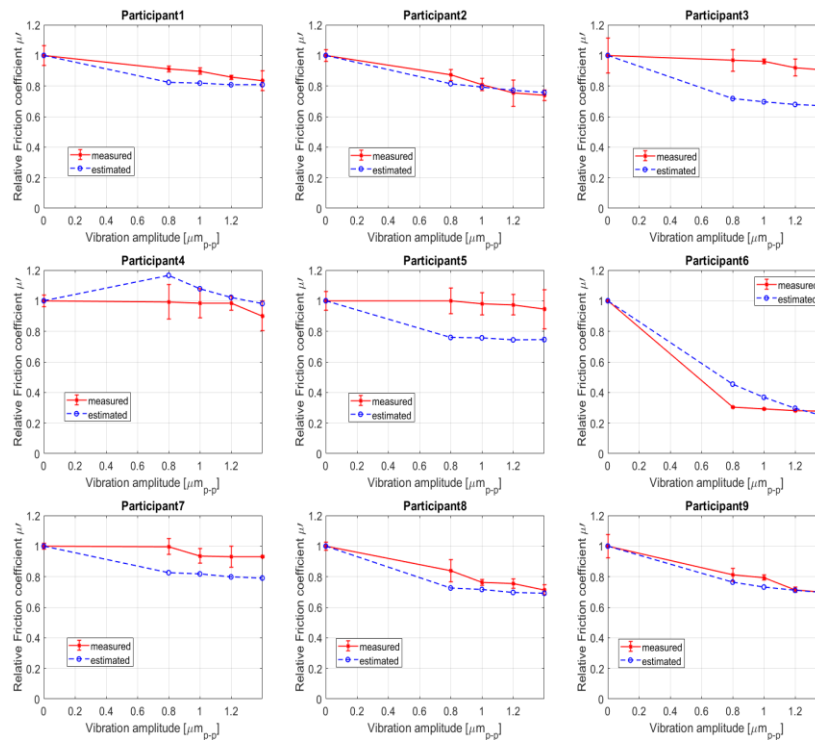


Figure 83. Estimation of  $\tilde{\mu}$  vs.  $\mu'$  for all measured amplitudes

In the second step, the friction reduction at the highest measurement point can be inferred using the linear regression of  $\overline{F}_r$  against  $\mu'$  described in section 5.3.2.1. The third step is to use the estimated  $\tilde{\mu}'$  and the  $\overline{F}_r$  measurement at  $1.4 \mu m_{p-p}$  to perform a 1-point PCR using the model obtained in section 5.3.2.3. Finally, the friction reduction at every point can be estimated multiplying the obtained PCR estimations  $\tilde{\mu}'/\overline{F}_r$  to the mean lateral acoustic finger force reconstruction  $\tilde{F}_r$  calculated in step one.

This process is tested for each participant, as if they were a ‘new’ user with models built from the data of the other 8. The estimations  $\tilde{\mu}'$  of  $\mu'$  at  $1.4 \mu m_{p-p}$  against the actual measurements are shown in Figure 80. The acoustic finger force reconstruction  $\tilde{F}_r$  against  $\overline{F}_r$  for the 5 points at which friction is measured are shown in Figure 81. Figure 82 shows the estimation of  $\tilde{\mu}'/\tilde{F}_r$  vs. measured  $\mu'/\overline{F}_r$  between  $0.8 \mu m_{p-p}$  and  $1.4 \mu m_{p-p}$ . Finally the complete  $\tilde{\mu}'$  against the measured relative friction coefficient  $\mu'$  at different amplitudes is depicted in Figure 83.

The average relative error for every estimation  $errX\% = 100 * \frac{|X - X_{est}|}{X}$  is presented in Table 8.

Table 8. Mean relative errors for estimated values in the longitudinal mode

P	Mean relative errors for the estimated values (err %)			
	$\mu'$ at $1.4 \mu m_{p-p}$	Mean $\tilde{F}_r$	$\mu'/\text{Mean } \tilde{F}_r$	Mean $\mu'$
1	3.1	0.2	5.1	5.4
2	2.3	0.4	2.5	2.6
3	25.8	0.05	21	21.1
4	8.9	0.3	8.2	7.9
5	20.9	0.3	18.4	18.2
6	13.1	0.9	18	19
7	15.1	0.03	11.8	11.7
8	3.1	0.4	5.8	6
9	0.2	0.9	3.5	2.8

The relative error from the PCR at the selected amplitudes help illustrate that correct estimations of the lateral force can be done with only two measurement points. However, concerning, the estimation of the relative friction coefficient based on the linear regression, a considerable margin of error of about 20% still exists for a few participants. We believe this error might be related to large amounts of variance in the friction data measurement, related also with the difficulty to provide exact measurements of friction in the human skin.

#### 5.3.4. *Conclusions on the longitudinal mode acoustic finger force study*

A method for predicting the friction reduction at different vibration amplitudes is presented in this chapter. The method uses three data-based models to estimate the relative friction coefficient  $\mu'$  achievable at a given vibration amplitude for any new subject, by making two static measurements of the control voltage in steady state when a finger is present. We were able to observe a good correlation between the measurement of the lateral acoustic finger force, and  $\mu'$ . The method has been validated for most participants, with a few outliers, which have a maximum relative prediction error of less than 22%. Moreover, from the results presented in this section, it is possible to observe that measurements from participant 6 are very different from the other participants. However, the correlation-based prediction when participant 6 is removed does not exceed the stated error, which testifies to a certain robustness of the proposed methodology and the fact that there may be a typological behaviour of the different skin types. Future studies will seek to validate the suggested method with a larger number of participants, higher range of vibration amplitudes and a smaller variance in the friction measurements.

Concerning the finger properties, we observe a relation between the slope of the linear part of the  $\overline{F}_r$  response and  $\mu'$ . Additionally, from equation (80) we observe that the slope of  $F_{rd}$  and  $F_{rq}$  are related to the properties of elasticity and damping of the sc. Extrapolating from the observed results and the scenario analysis in

section 5.1.2.1, it is possible to relate a high finger damping and elasticity to a high  $\mu'$ . The question still remains on how these properties may relate to the saturation point, where the slope changes value.

Finally, in Figure 82, we can observe how the estimation of  $\tilde{\mu}'/\tilde{F}_r$  using the second PCA provides about the same result for every participant.

As a general conclusion of this study, based on the results explained in sections 5.2 and 5.3, we can say that a ‘reference calibration method’ is validated, which uses two static acoustic force measurements of the closed loop control voltages at fixed amplitudes. In the case of both, longitudinal and transverse modes, we found that it is possible to achieve a relatively correct friction approximation using the suggested method.

#### **5.4. Look-ahead: Towards real time friction control using acoustic finger force observation with longitudinal modes**

Extrapolating from the ideas presented on sections 5.2 and 5.3, an ‘online’ operation can be imagined, similar to the one proposed in [132], [195], which would not require a calibration step.

This real time correction can be implemented using a real-time observation of the fundamental acoustic finger force on a static or a moving finger and a calculation of its corresponding friction coefficient reduction based on the estimation curves depicted in Figure 82.

In this section, the calculation, implementation and real time testing of the acoustic force observer are presented. The real time observation is then tested on a static finger. A discussion is then presented on the obtained results and the next steps.

#### 5.4.1. Acoustic finger force observation in the rotational reference frame

From the point of view of the decoupled single-axe amplitude plate controller in the rotating reference frame, depicted in section 2.4.1, it could be interpreted that the acoustic finger force enters the system as an input disturbance  $d$ . The real time values of  $F_{rd}$  and  $F_{rq}$  can therefore be found simultaneously using a disturbance observer on each decoupled axis. A simple calculation can thus provide  $F_r$ .

To explain the observer calculation, we begin from the decoupled  $dq$  axes equations calculated in section 2.4. Considering a simplified notation with a single axis, we designate, for example  $W_q = W$  and  $V_d = V$ . Given that both axes are symmetrical, the control diagram of a single axis in the rotational reference frame can be described as in Figure 84, where we define the system gain  $G = \frac{-N}{D\omega_n}$  and the time constant  $= \frac{2M}{D}$ .  $M, N$  and  $D$  are the modal parameters of the plate, identified in 2.4.2.

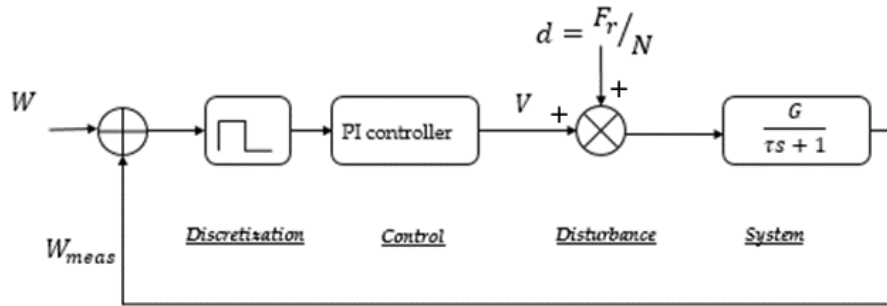


Figure 84. Representation of a single axis in the rotational reference frame, with  $F_r$  modelled as an input disturbance

##### 5.4.1.1. DISTURBANCE OBSERVER IN STATE SPACE

We calculate the disturbance observer using the state space representation, as described in [200]. For doing so we define the input  $u = V$ , the state  $x = W$ , and the output  $y = W$ . The state space representation of the first order system is therefore defined by (90), with  $A = \begin{bmatrix} -1 \\ \tau \end{bmatrix}$ ,  $B = \begin{bmatrix} G \\ \tau \end{bmatrix}$ ,  $C = [1]$  and  $D = [0]$ .

$$\begin{aligned} \dot{x} &= Ax + Bu \\ y &= Cx + Du \end{aligned} \quad (90)$$

The disturbance  $d = F_r/N$  represents the additional control voltage required to compensate for the load applied by the finger. We assume that  $d$  is constant, and so we write (91).

$$\begin{bmatrix} \dot{x} \\ \dot{d} \end{bmatrix} = \begin{bmatrix} -1 & G \\ \tau & \tau \\ 0 & 0 \end{bmatrix} \begin{bmatrix} x \\ d \end{bmatrix} + \begin{bmatrix} G \\ \tau \\ 0 \end{bmatrix} U \quad (91)$$

The disturbance observer is represented in Figure 85. The observer gains are listed in (92). The matrix  $Lobs$  is found by using pole placement on the observer, with an acceleration factor of 10.

$$\begin{aligned} Aobs &= \begin{bmatrix} -1 & G \\ \tau & \tau \\ 0 & 0 \end{bmatrix} \\ Bobs &= \begin{bmatrix} G \\ \tau \\ 0 \end{bmatrix} \\ Cobs &= [1 \quad 0] \end{aligned} \quad (92)$$

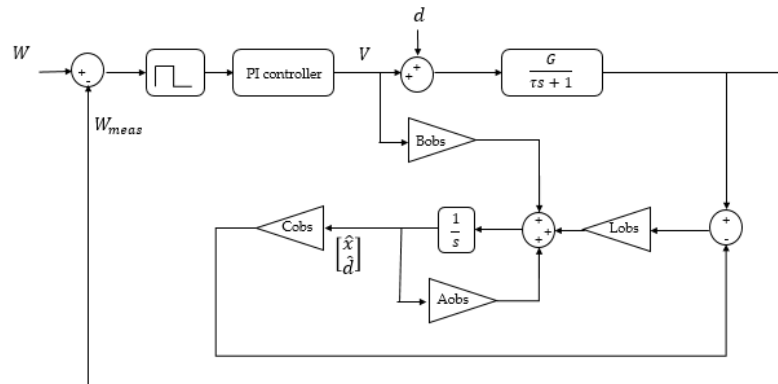


Figure 85. Disturbance observer representation

5.4.1.2. ACOUSTIC FORCE OBSERVATION FOR A STATIONARY FINGER IN THE ROTATIONAL REFERENCE FRAME

The disturbance observer was implemented in the DSP in the setup explained in 5.3.1. A procedure consisting of three different experiments is then made, to evaluate the results of the observation in static and dynamic exploration.

The first experiment intends to provide a comparison point, to evaluate the accuracy of the observation. For doing this, the values of  $F_{rd}$  and  $F_{rq}$  are measured using the procedure described in 5.3.1, for a stationary finger placed on the plate with a pressure force of about 0.5N. The result for a single participant is plotted in Figure 86.

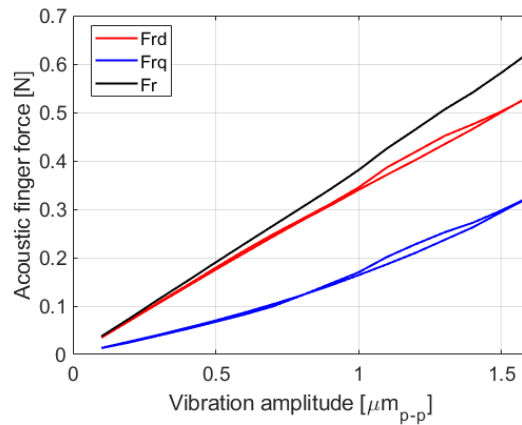


Figure 86.  $F_{rd}$ ,  $F_{rq}$  and  $\bar{F}_r$  measured “offline” from voltages  $V_d$  and  $V_q$

A second experiment was used to evaluate the accuracy of the real time observer values of  $F_{rd}$  and  $F_{rq}$  measured at two different amplitudes. In this experiment, the measurements are made on the same participant that was measured ‘offline’ in the first experiment. . At time  $t=0$ , a vibration amplitude step reference is imposed on the plate with no load. After 1-2 seconds, the participant places a finger on the plate, and holds a pressure of about 0.5N. The vibration amplitude control works so as to maintain the same wave amplitude. The observed values of the acoustic



finger force at vibration amplitudes  $0.5\mu m_{pp}$  and  $1\mu m_{pp}$  are plotted in Figure 87. If we compare the final values of the forces in Figure 87 with the corresponding values of  $F_{rd}$  and  $F_{rq}$  in Figure 86 at the same amplitudes, we are able to see a concordance between them. This result suggests that  $F_{rd}$  and  $F_{rq}$  can be accurately observed in real time.

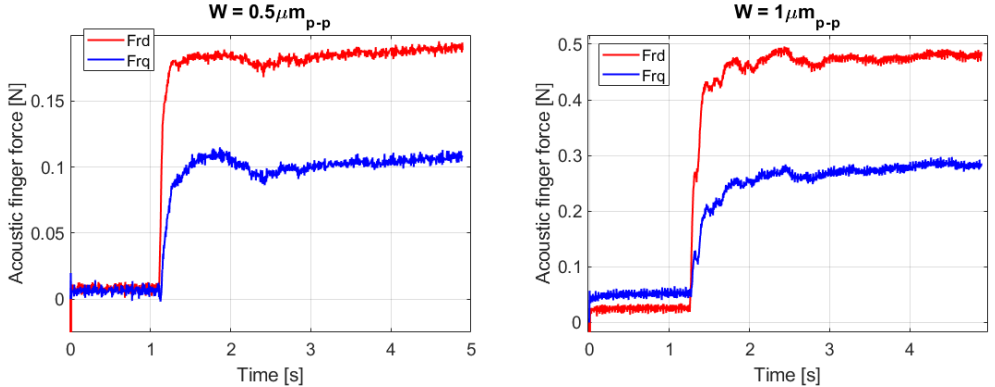


Figure 87.  $F_{rd}$  and  $F_{rq}$  using real time observer for 5 seconds. A finger is placed on the plate between 1-2 s after the vibration reference is imposed.

Finally, we evaluate whether it is possible to observe the dynamic acoustic force  $F_{rd}$  and  $F_{rq}$  on a finger actively exploring the plate, and how this would affect the acoustic force measurements, as compared to the stationary values.

For doing this, the tribometer base is set in motion at about 30 mm/s. Similarly to the previous experiment, a step reference is imposed on the plate’s amplitude at  $t=0$ . Once again, after 1-2s, the participant places a finger, this time on the moving plate, with a pressure of about 0.5N. The results at two different amplitudes are plotted in Figure 88.

Comparing the results of  $F_{rd}$  and  $F_{rq}$  during active exploration against those of a static finger, it is possible to see that the acoustic force measurements have been reduced to almost half their magnitude because of the sliding motion.

From sections 5.2 and 5.3, we know that there is a correlation between the acoustic finger force in the static condition and the friction measurement. Moreover, we

were able to deduce the relation  $\tilde{\mu}' / \tilde{F}_r$  for the longitudinal modes. However, we have not yet verified if such correlation exists with the dynamic observation of the acoustic finger force. This relation would be necessary to perform real-time friction control. Further research is needed to explore this method.

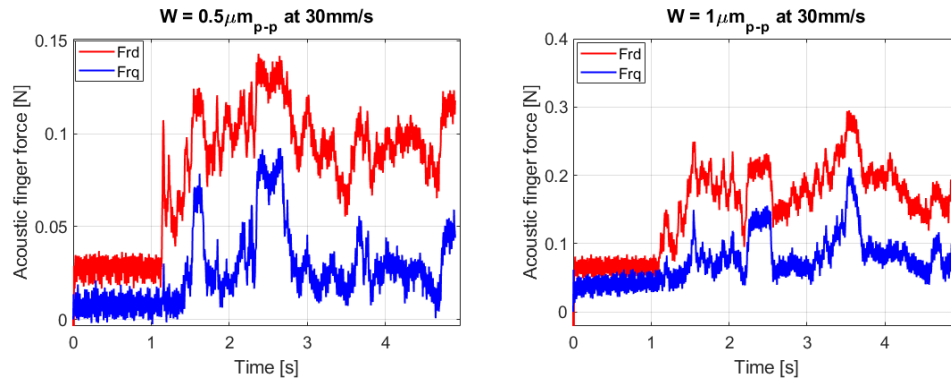


Figure 88.  $F_{rd}$  and  $F_{rq}$  using real time observer for 5 seconds on a plate sliding at 30mm/s. After 1-2 s a finger is placed on the plate with a pressing force of about 0.5N.

## 5.5. Conclusion

A method for predicting the friction reduction at different vibration amplitudes for longitudinal and transverse modes is presented in this chapter. This type of relation may help calibrating the USHD, to provide a more standardized response in terms of friction contrast and therefore sensation. The method uses three data-based models to estimate the relative friction coefficient  $\mu'$  achievable at a given vibration amplitude for any new subject, by making two static measurements of the control voltage in steady state when a finger is present. We were able to observe a good correlation between the measurement of the lateral acoustic finger force, and the friction reduction. The method has been validated for most participants, with a few outliers.

A larger range of amplitude measurements may also help correlating the saturation point with  $\mu'$ . This type of correlation may help simplifying the calibration process

for longitudinal mode USHD, and may yield interesting information regarding the finger's mechanical properties.

Extrapolating from this idea, we proposed that a real time friction correction could be achieved, using the observation of the acoustic finger force, which is possible with a disturbance observer, and the friction contrast correction during active exploration. From the results, it was possible to conclude that the acoustic finger force is significantly affected by the motion of the finger. For this reason, further research is recommended to evaluate the relationship between the observed acoustic finger force during active exploration, and the achievable friction contrast at a given vibration amplitude.

Further considerations on a systemic view of this methodology and preliminary results are explained in the upcoming chapter.

HUMAN-IN-THE-LOOP ANALYSIS FOR USHD INTERACTION

Research on haptic devices has repeatedly led to pose the question of human modelling [26], [116], [118], [149], interaction analysis [35], [38], [108], [112], [115], [127], perception [150], [151], and to consider the human behaviour into the system control [152]–[154]. In surface haptics, this may be interesting for several purposes, from the optimization of haptic device design to applications dealing directly with human cognitive and motor functions, and even health.

In this chapter, we seek to formalize the lessons learned in Chapter 5, to move towards a hiL (human-in-the-Loop) structured analysis and thus reflect upon the potential of this approach for future developments in haptic technology applications.

To perform this hiL analysis, we rely on a unified representation of the USHD and the human user, with the help of the simplified ‘lumped’ systemic approach, focusing mainly on the dynamics related to textural touch.

The causal model of the USHD and its closed-loop control are explained at length in Chapter 2. Starting from this model, and its representation thanks to the EMR formalism, the human elements are incorporated. To complete this functional view, we begin by recalling the physiology of human sensing mechanisms from Chapter 1 and explain the mechanisms by which texture illusions can be produced. Then, based on this knowledge, a systemic analysis of the USHD-human interaction is presented in more detail. We then introduce the human-in-the-Loop (hiL) representation, organized with the help of EMR [134].

## 6.1. Skin mechanics and the creation of texture illusions

A functional representation of the human as a part of a technological system requires firstly to identify which of the various complex human characteristics should be modelled, represented and analyzed for a given specific objective.

Chapter 5 dealt with skin identification and the enhancement of texture perception standardization techniques. Analyzing touch from a systemic level is a complex task, as it encompasses an enormous amount of physical, biological and neurologic phenomena occurring simultaneously.

From the mechanical point of view, two subsystems are of particular interest. Firstly, there is the analysis of the motion that the haptic device elicits on the sc. This motion is a function of the material, shape and velocity of the interface's surface; but also a function of the velocities and forces imposed by the user sliding the finger; and depends on the evolution of the contact between the skin and the interface. The second subsystem examines the transmission of mechanical strains and stresses along the finger's tissues until the sensing layer (the location where the mechanoreceptors associated to texture perception are found inside the skin). It is hypothesized that if a haptic device is able to elicit similar strains at the sensing layer as the ones produced by exploring a real texture, then a realistic illusion can be produced.

There are several significant challenges in the modelling and analysis of both subsystems, especially in the case of USHD. Regarding the first one, it is important to consider that, while it is relatively simple to model USHD surface and finger bone motion, we have determined in Chapter 3 that this is not so for the skin-device contact. As explained in the mentioned chapter, the contact between the skin and the surface of the USHD is not necessarily intimate all over the contact area. A 'gap', which evolves (non-linearly) through time and in function of the

exploration velocity, is formed between the two materials [31]. In this interstitial space, many different types of materials might be ‘trapped’, such as air, sweat, dust particles and others. We will see that the evolution of the mechanical parameters at the interstice (we denominate ‘air gap’) is a key component of our analysis.

The main challenge regarding the study of the second subsystem is the fact that measuring the transmission of strains and stresses throughout the different skin layers may be complex and invasive. For this reason, we rely on our previous knowledge of skin mechanics and experimentation to create analytical models. We observed in Chapter 1 that textural exploration induces stationary vibration on the finger that propagates up the hand. In [201], a dynamic relation was found between a finger vibration while sliding on a surface and the topology of this surface. However, the frequency spectrum of response is different each time the measurements are repeated, which makes the system hard to identify and suggests that it is not linear and sensitive to initial conditions.

From the perceptual point of view, despite these very different mechanical responses, the sense of touch is consistently efficient in material and texture identification. This means that the brain is capable of extracting specific information from this kind of system, apparently by identifying frequency and motion patterns [201]. Such patterns occur when the finger slides over a textured surface. As a consequence of the motion, the skin deforms locally, ‘copying’ the shape of the surface. This deformation travels over the surface of the skin as the finger slides. The deformation field can basically be defined as a motion gradient. Most of the neural equipment related to the hand is sensitive to these gradients or modifications in the mechanical state of the skin. The perception mechanism associated with sliding is especially sensitive to signals that are correlated in space and time, as such they appear as progressive waves [202]. The phase shift in the movement of the progressive wave will give the speed of the pattern (group speed).

We may conclude that the nervous system involved in touch is therefore sensitive to the speed of the group of determined patterns.

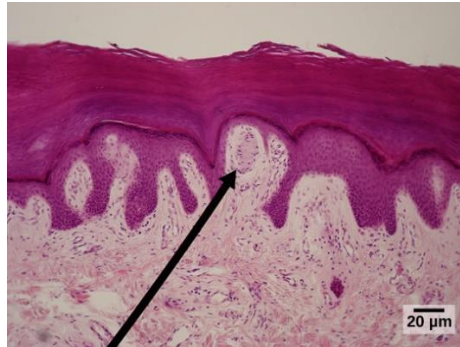


Figure 89. Meissner corpuscles in the fingertips, such as the one viewed here using bright field light microscopy, allow for touch discrimination of fine details [203].

As explained in Chapter 1, even if sliding a finger over a textured surface addresses almost all the mechanoreceptors, we consider here the main ones concerned are the ‘fast’ Meissner corpuscles (response time of a few milliseconds) and the (possibly) ‘slow’ Merkel cells [204]. These nervous system sensors are not directly located on the surface of the sc, but ‘far’ in the junction between the dermis and epidermis, as illustrated in Figure 89. The epidermis is about 1mm thick and the mechanoreceptors are placed at about 700  $\mu\text{m}$  behind the surface. We can therefore say that they respond to deformation fields that are the result of a ‘distant’ boundary conditions in space and time.

The problem behind the design of haptic stimulators becomes, therefore, to invert these boundary conditions from the data that have been transformed [202]: if we have a boundary condition that imposes a movement, such as the exploration on a wavy canvas, a second boundary condition where the skin is compressed and stretched in a similar pattern will, in theory, produce the same perception. By taking the right dynamic parameters of the deformation of the skin tissues from the sc. to the epidermis, we can reproduce the same field of deformation as the one created during tactile exploration [202].

There are two consequences to this observation:

1. Touch is somewhat ambiguous: Mathematically, there is an infinite number of boundary conditions that will produce the same motion at the sensing layer.
2. This gives us an idea of how to make devices that produce realistic tactile illusions.

It is known that friction is very important in discriminatory touch [4]. Indeed, as has been explained in Chapter 1, boundary conditions created by force modulation in the tangential plane are very efficient in the creation of texture illusions. The mechanisms concerned with this force modulation is further studied in the upcoming sections.

## **6.2. Dynamic model and representation of touch for real and virtual textures**

### *6.2.1. Dynamic model and representation of touch for real textures*

As explained in section 6.1, we could define the objective of haptic devices as a means to create a set of limit conditions to produce a specific motion at the perception level of the skin. In the case of texture exploration, the perception occurs when the interaction between the explored surface and the finger creates a specific deformation at the finger ridge level that induces a motion at the deep epidermis. The main forces and velocities taking place during sliding touch (see Chapter 1) are detailed in Figure 90. Since, ultimately, we are concerned with frictional quantities, the directions of the forces with respect to the surface are taken into account, by separating every force into their lateral and normal components.

Initially, a motor force  $f_{Lbone}$  is produced by the kinetic system of the human. This system is composed mainly of bones, muscles and tendons and is controlled by the brain. The force from the kinetic system is transmitted into the complete set of



tissues composing the hand and finger, creating a displacement velocity  $u_{bone}$  of the bone, which we consider as a rigid structure and the source of motion. When the finger is then placed on the surface with a pressure force  $f_{Nbone}$ , a contact is established between the sc and the surface. Energy is transmitted from the bone to the contact surface through soft tissues that are deformable only to a certain extent and then become rigid. As explained, the contact between the finger and the texture, however, is not intimate, so a ‘gap’ exists at several regions of the contact surface. This interstice contains materials such as air, moisture and dust particles.

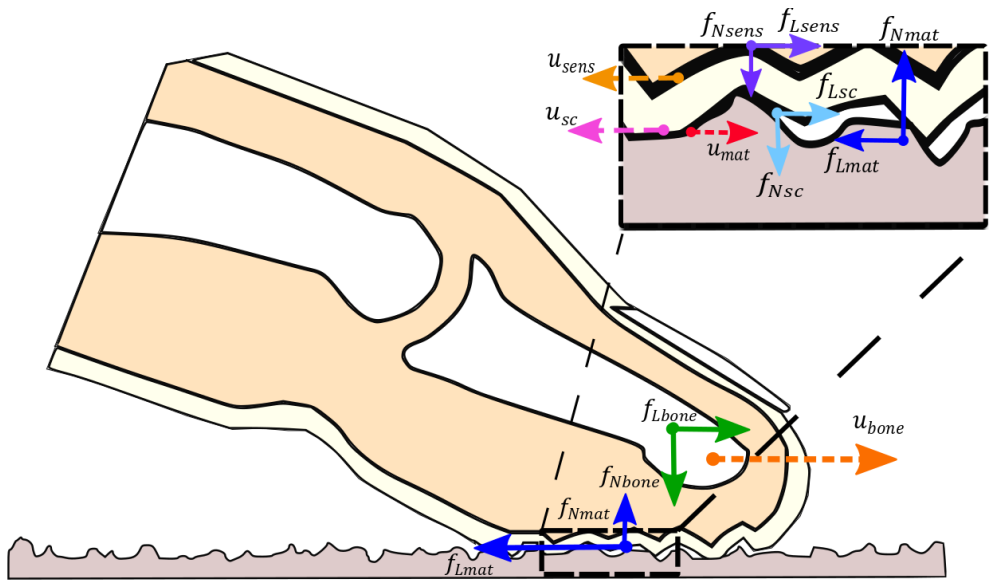


Figure 90. Forces and velocities during a real exploration and their consequences at the sensing level.

The force experienced by the touched object is therefore the addition of the force produced at the outmost layer of the skin  $f_{Nsc}$ ,  $f_{Lsc}$  at the contact points, and the effect of the material ‘trapped’ in the interstice or ‘gap’. The evolution of these forces is dynamic and non-linear and depends on  $u_{bone}$ , as explained in Chapter 3.

As a consequence of these transmitted forces, the surface of the touched object produces the reaction forces  $f_{Nmat}$  and  $f_{Lmat}$ . If the material is deformable, the force from the contact will induce a velocity  $u_{mat}$  at its surface.

At the skin level, the sc deforms and then slides with a velocity  $u_{sc}$ . This motion is transmitted throughout the epidermis, until the sensing point, where the velocity of deformation is noted  $u_{sens}$ , and the forces  $f_{Lsens}$  and  $f_{Nsens}$ .

We can thus distinguish three elements in the textural touch interaction. On the one hand, we have the explored surface. It has a shape, a surface topography and its own mechanical properties of hardness, elasticity, roughness, etc. An example of a surface topography and 2D roughness of different material surfaces at the microscopic level is shown in Figure 91.

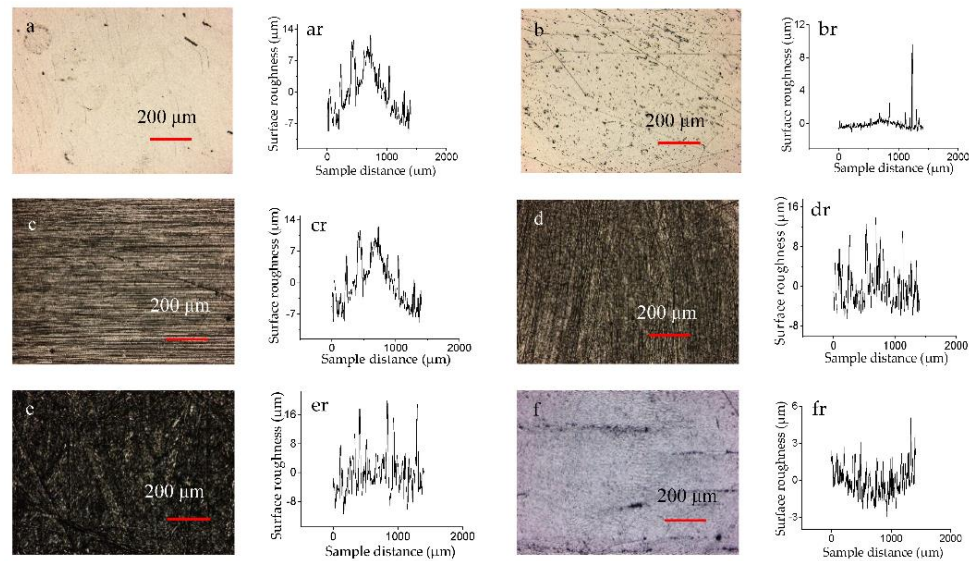


Figure 91. The 3D profiles and 2D roughness curves of the surface of different material samples [205]

On the other hand, we have a human being with their motor functions, temperature, sweat, mechanoreceptors and different skin layers. From [25], we get that each layer of the skin, up until the sensing point, can be modelled by a second

order dynamic mass-spring-damper system, as depicted in Figure 92. For this representation it is useful to isolate the sc. from the other layers of the epidermis, as it is the main layer concerned with ultrasonic vibration [30].

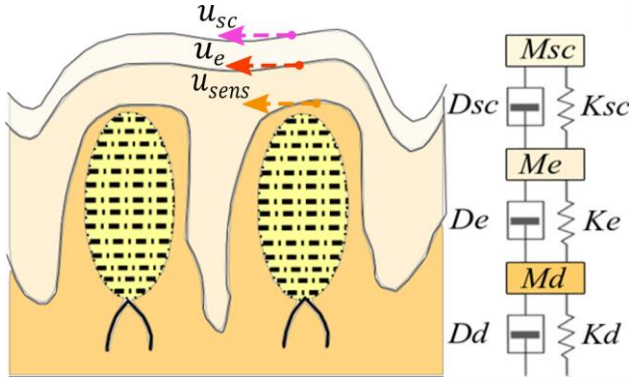


Figure 92. Modelling of the skin layers from the stratum-corneum up until the dermis as a series of interconnected mass-spring-slider systems. We assume that the perception occurs on the layer between the epidermis and the dermis, where the Meissner corpuscles are located.

The parameters  $M_{sc}$ ,  $K_{sc}$  and  $D_{sc}$  represent the inertia, elasticity and damping of the stratum corneum.  $M_e$ ,  $K_e$  and  $D_e$  are the mechanical parameters for the epidermis and  $M_d$ ,  $K_d$  and  $D_d$  the ones for the dermis. The velocities  $u_{sc}$ ,  $u_e$  (velocity at the epidermis level below the sc.) and  $u_{sens}$  are related to the deformation of the skin at each one of the mentioned layers. The yellow ovals represent the Meissner corpuscles located at the juncture between the epidermis and the dermis.

Finally, the gap between the surface of the touched object and the skin is considered to have a first order non-linear dynamic behaviour. This gap (or ‘third body’) is crucial in the systemic description of real texture interaction, as it serves as a physical interface between the textured surface and the human.

A representation of the complete dynamic system and its causality links are depicted in Figure 93. In this figure, it is detailed where the stimulation is created, and at which point it is perceived.

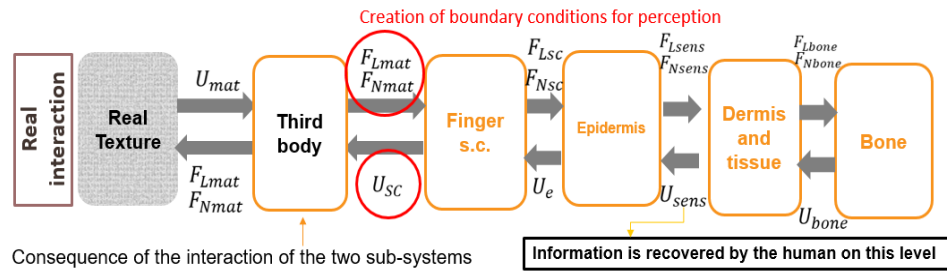


Figure 93. Dynamic system of the real texture interaction with links of causality

The ‘dermis and tissue’ block represents the ensemble of tissue, including hypodermis, collagen fibers, fat, blood vessels and tendons that might exist between the dermis and the bone. For the purpose of this study, the effect of the surface haptic stimulation on these underlying levels of human tissue are not relevant, so further detail of their dynamic behaviour will not be provided.

### 6.2.2. Dynamic model and representation of touch for virtual objects

As explained in section 6.1, the key for the creation of realistic haptic devices consists in being able to create an appropriate set of limit conditions at the outmost layer of the skin. In surface haptics this is done by friction modulation. The virtual object model is therefore represented as an arrangement of friction contrasts over the plane. Typically, a vibration velocity  $U(x, y)$  is assigned to each friction contrast, according to a texture model. The peak-to-peak value of this velocity at each position is noted  $U_{p\_ref}$ .

The haptic device used to render the model has its own dynamics, which are controlled in real time with the closed-loop velocity control explained in Chapter 2. The plate imposes a set of limit conditions to the gap and the finger, which are very different from the ones imposed by the real object. From the mechanical limit conditions imposed at the sc. to the ones perceived at the perception level, there is a transformation by the effect of the different layers of the skin. The reaction force

from the air gap and finger has been defined in Chapter 5 as the acoustic finger force  $f_r$ .

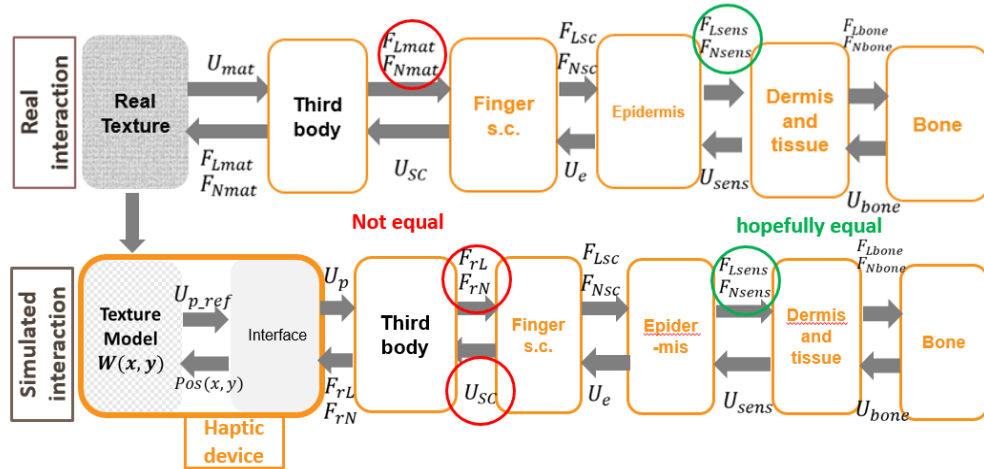


Figure 94. Dynamic system of the real texture interaction vs. the simulated texture interaction with links of causality

A diagram explaining the differences and similarities between the causal model for the real and the simulated texture interaction is depicted in Figure 94. The level at which the limit conditions are imposed on the finger are circled in red. The chosen variables at the perception level, which need to be mimicked by the haptic device are circled in green.

### 6.3. hiL approach for USHD-human interaction representation

Before moving on to the analysis of the hiL applications for USHD, it is useful to formalize the systemic interaction detailed in section 6.2. For doing so, it is possible to represent the system as a series of independent sub-systems participating in an energetic interaction described by links of causality. The idea defined by the ‘Hardware-in-the-Loop’ (HiL) [136], [137] analysis is therefore a useful departure point.

### 6.3.1. 'Human-in-the-Loop' system components

As explained in Chapter 1, in the 'Hardware-in-the-Loop' analysis, one part of the system is replaced by an equivalent hardware and then connected to a simulation software through an interface for real-time testing. As a result, the complete setup is represented as three interconnected components, each one with their very specific dynamic and nature: the hardware, the interface and the simulation software model. A series of requirements need to be taken into account for the successful interconnection of the three sub-systems. In [141], [144], [145], [206], it is explained how EMR [134] is used to organize this type of multi systemic interactions to successfully perform HiL testing in real time.

In an analogous manner, three interconnected components can also be assumed to take part in a hiL structure: the human, the interface and the software model.

Regarding the 'software model' component, in the case of haptics, it corresponds to the arrangement of mechanical characteristics of the sampled object that the modeler deems appropriate to reproduce. Generally, these are chosen based on psychophysical and biomechanical studies with the purpose of maximizing the similarities between the tactile perception of the real object and the virtual one. For this reason, the model may include aspects such as friction, temperature, skin indentation, vibrotaction and force-feedback, amongst others. In the case of USHDs, friction plays a major role in the tactile material discrimination [36], [199]. Finding and perfecting methods for frictional texture feature extraction is, in fact, an important subject of research in the textile industry [207]. We could therefore think of the software-model component as a two-dimensional spatial arrangement of friction coefficient variations. In Chapters 1, 3-5, we explain that the amount of friction modulation is a function of the vibration amplitude of the USHD. For this reason, USHD manufacturers often opt to translate the desired friction variations into vibration velocity, which will be varied in function of the finger position  $U_{p\_ref}(x, y)$ . The output velocity of the plate  $u_p$  is a high frequency

signal, which can be considered as an ultrasonic carrier, with the value  $U_{p\_ref}$  being the low-frequency envelope.

As for the interface, mandatory between the human and the virtual object model, it is here defined by our haptic device. Akin to the interface proposed in HiL systems, the fidelity of the simulation depends on both the quality of the model and the ability of the interface to reproduce it in real time. These considerations are summarized in Figure 95 where it is shown how the parts of the causal system for the simulated interaction described in section 6.2 can be divided in the three hiL components. In the figure, we can see the causality links taking part in the systemic analysis of the USHD-human interaction at the tactual level. Up to this point, the sub-components are represented in a simplified way, with a box representing each one of the main subsystems we are aiming to integrate in our analysis. A more detailed analysis will be presented further using EMR.

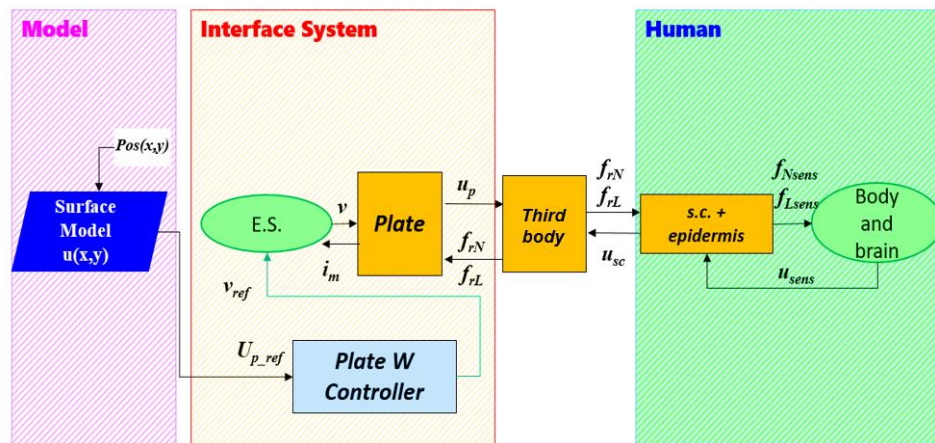


Figure 95. Human-in-the-Loop representation of a USHD in contact with a user. The causal model is separated in three sub-systems: the model, the interface and the human.

A particularity of the structure presented in Figure 95 is that an element has been placed between the interface and the human. This element represents the air gap, which, as explained in sections 6.1 and 6.2, is actually composed of many different

materials such as air, sweat and dust particles. This element has a complex dynamic behaviour, with non-linear parameters that vary depending on the type of vibration (normal/lateral), normal force, dwell time, temperature and atmosphere moisture level, amongst others. The behaviour of the air gap, nevertheless, is a fundamental factor in the evolution of the friction between the finger and the device [196], because it determines, amongst other things the true contact area between the two elements [8]. Since it is not a part of the interface or of the human, but a consequence of the interaction of the two, we decide to include it as a ‘physical’ interface between the two.

It is important to note that there is an averaging effect of the force and speed values at the human tissue level. This means that, while the velocities and forces at the level of the interaction between the plate and the stratum corneum are modulated by an ultrasonic carrier, the transmission into the tissue filters this signal. . At the sensing level, that is for  $f_{Nsens}$ ,  $f_{Lsens}$  and  $u_{sens}$ , it is the low frequency component that evolves with the variations of the envelope  $U_{p\_ref}$ , which is the most important.

### 6.3.2. EMR of the complete system

The detailed representation of the human-USHD interaction is performed using EMR, as illustrated in Figure 96. To build this representation we assume that each layer of the skin contains a damped-elastic element and an inertial element as explained in section 6.2.

According to studies [18], [116], it could be possible to simplify this approach, by stating that the bulk mechanical behaviour of the skin tissues at ultrasonic frequencies act mainly as a first-order damper. In this case, the inertial element at each layer of the skin would be neglected and, as the association rules of the EMR dictate, all damping elements of each layer of the finger would be regrouped into an equivalent first-order damper. This approach, however, does not allow us to retrace the links of causality from the plate motion to the sensing region. For this



reason, we deem relevant to include the detailed description of the human system up to the sensing level.

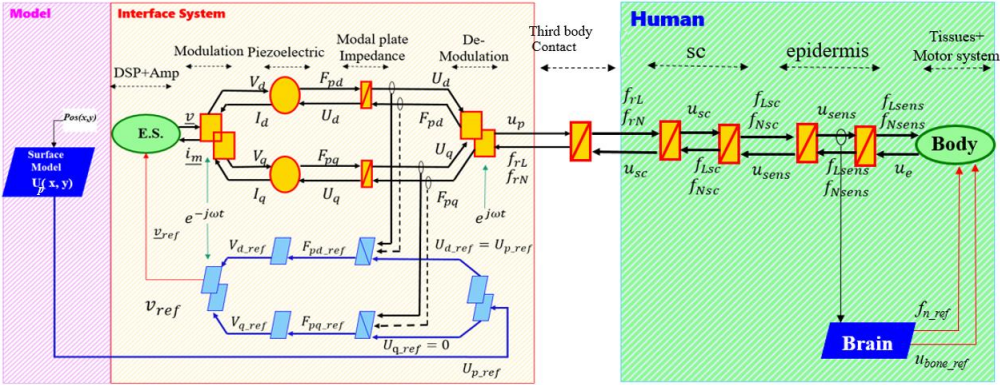


Figure 96. Human-in-the-Loop representation of a USHD in contact with a user. Complete systemic representation using EMR.

In this representation we input the brain as a strategy block, which will provide and receive all the necessary information for the control of the kinetic system. This control system arrives until the point of muscle and bone motion, but does not include the motion of the skin, as it is a consequence of the interaction, and not a voluntary action.

#### 6.4. hiL surface haptic applications

The systemic view put forward by the hiL analysis presented in section 6.3, allows us to illustrate the logic used for the design and implementation of haptic devices.

##### 6.4.1. hiL for introducing standardized perception

In the case of texture rendering, one recurring concern, as explained in Chapter 5, is the creation of a standardized tactile feedback throughout participants. This issue arises, because the existing technology does not consider the human factor neither in the virtual object model construction, nor the design and control of the haptic devices. As a result, the haptic return is not homogeneous between subjects.

As mentioned in section 6.3, the strategy block representing the texture model in Figure 96 intends to recreate an arrangement of friction variations that one could encounter exploring an actual texture. However, because in this strategy each friction variation corresponds to a single vibrational speed, and the relation between vibrational speed and friction modulation depends on each user, the model does not render friction accurately for all users.

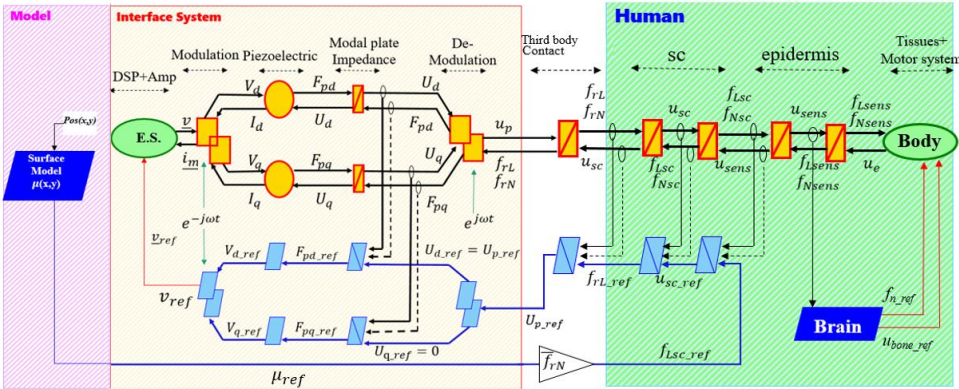


Figure 97. Human-in-the-Loop representation of a USHD in contact with a user. MCS derived from new strategy proposal to provide friction reference, instead of vibration amplitude.

A complete vision of the system (Figure 96) helps us understand that the objective of the interface is to act upon the variables at the epidermis level  $f_{Lsens}$  and  $u_{sens}$ , while producing specific limit conditions at the sc level by varying  $u_{p,ref}$ . We get from the literature [36] that these limit conditions can be determined by reproducing the frictional properties of a finger against a real object  $\mu = f_{Lsc}/f_{Nsc}$ . This simplifies the implementation of the controller, as it may act upon  $f_{Lsc}$  and  $u_{sc}$  instead of  $f_{Lsens}$  and  $u_{sens}$ . Our model could therefore be constructed as a spatial arrangement of friction variations instead of vibration velocity:  $\mu_{ref}(x, y) = f_{Lsc,ref}(x, y)/f_{Nsc}(x, y)$ , as illustrated in Figure 97. For simplicity, we assume that the mean value  $\bar{f}_{Nsc} \approx \bar{f}_{rN} \approx f_n$ , where  $f_n$  is the finger

pressure (it should be remembered that  $f_{Nsc}$  and  $f_{Lsc}$  are high frequency signals, so the mean  $\bar{f}_{Nsc}$  over a whole number of periods should be calculated to get  $f_n$ ). Taking into account these considerations, the tuning path to consider to provide a friction reference  $\mu_{ref}$  should go from the tuning variable ( $v_{ref}$ ) towards  $f_{Lsc}$ . Using the inversion-based control technique to deduce the MCS (Maximal Control structure), as explained in 2.4, yields to a control scheme that includes the inversion of the air gap and the inertial and elastic components of the sc, as shown in Figure 97.

Ideally, this control structure would allow us to reproduce the friction reference provided by the model. Unfortunately, the variables that need to be measured to construct such a control scheme are not measurable. Moreover, the non-linear, parametric nature of the blocks related to the air gap and the skin makes it impossible to produce a model to describe accurately their dynamic behaviour.

Chapter 5 has presented two different approaches for addressing this issue. The first one is a reference calibration. It is used to adapt the vibration speed reference to the user ‘offline’ (scaling  $U_{p\_ref}$ ), but does not adapt to eventual dynamical changes of the elements in real time. The second one introduces a strategy to correct friction in real time, using a disturbance observer. The upcoming subsections will recall these approaches, using the hiL representation, previously explained.

#### 6.4.1.1. USHD REFERENCE CALIBRATION WITH STATISTICAL MODELS

As explained in Chapter 5, it is possible to adapt the amplitude model to any user offline, by integrating a two-point measurement of selected values of  $f_{rN}$  or  $f_{rL}$  (depending on the mode), and input them into a pre-defined statistical model, which will provide the vibration velocity vs. friction relation for the complete range of vibration velocities achievable with the haptic device. This relation will then be

used to transform the  $U_{p\_ref}$  arrangement, by a linear transformation given by statistical-based models to estimate the desired friction modulation to the current user. In other words, the contact and sc sub-system inversions are simplified by linear regression models. This type of solution, represented as in Figure 98, can be defined as an ‘offline reference calibration’.

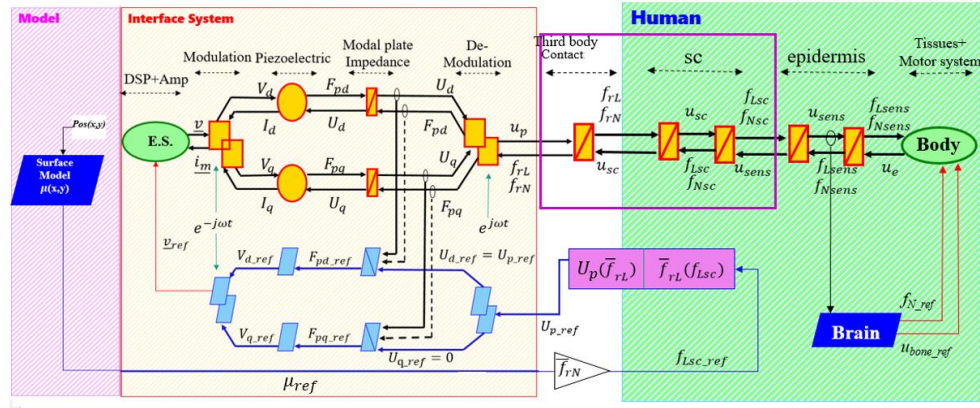


Figure 98. USHD reference calibration scheme. The dynamic evolution of the finger and the contact are simplified with a statistical model, which is used to calibrate the surface vibration amplitude to fit a given user

#### 6.4.1.2. REAL TIME FRICTION CORRECTION USING A DISTURBANCE OBSERVER

An alternative for integrating the same model simplification logic into a real-time correction scheme, can be achieved by dividing the model inversion in two parts, as represented in Figure 99. One part would serve as the inversion model for the air gap, providing the inversion  $U_{d\_ref}(\bar{f}_{rL\_ref})$ . The other part would serve to represent the inversion of the sc, to deduce  $\bar{f}_{rL\_ref}(\bar{f}_{Lsc\_ref})$ .

The external model inversion  $U_{d\_ref}(\bar{f}_{Lsc\_ref})$  can be achieved by implementing a real time disturbance observer such the one explained in chapter 5. However, through the observation in real time in Chapter 5, we have observed that the behaviour of the sc in the dynamic regime is different from the one measured at



the static regime. For this reason, future studies could focus on finding a statistical model providing the relation  $\bar{F}_{rL\_ref}(\bar{F}_{Lsc\_ref})$  in the dynamic regime.

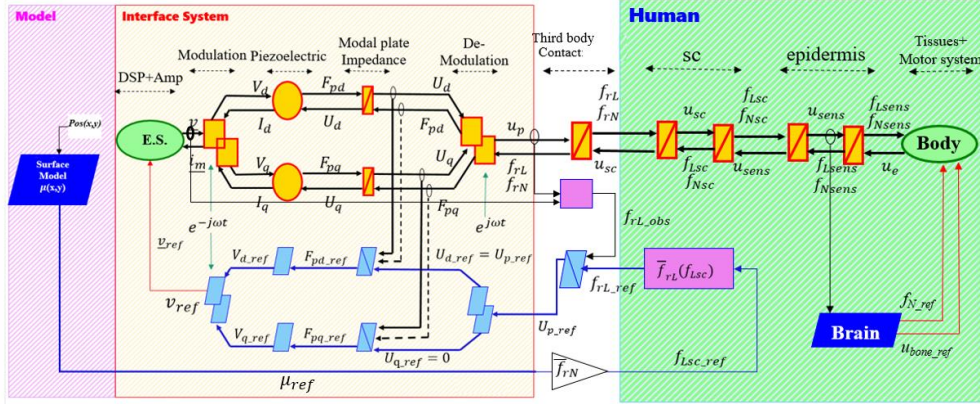


Figure 99. Model inversion with reaction force observation in the device design and control

### 6.5 Conclusions

This chapter summarizes the development and lessons learned from the previous chapters of this thesis, to present them from the perspective of a ‘human-in-the-Loop’ structured analysis, with the help of EMR. The advantage of this approach is that it helps in creating and standardizing techniques for integration of human physiological and behavioral aspects in the design and control of new haptic interfaces.

For the studied application, we focused mainly on the integration of the physiological properties of the skin-surface contact during active exploration of ultrasonic surface haptic devices, to explain the mechanism by which texture illusions are made. This development helped evidence potential design improvements, such as the inclusion of friction-based correction instead of vibration velocity-based correction in haptic devices. The main challenge to overcome for implementing this solution, is the difficulty of modelling, measuring and controlling the contact at ultrasonic frequencies. For that aim, two types of

solutions are explained in Chapter 5: one for the calibration of the device, and another one for the prospective real-time implementation. These two approaches are formalized in this chapter with hiL analysis. We hope this formalism may help understand and further optimize USHD.

'Human-in-the-Loop' analysis could help standardize and provide corporal integration of multimodal sensing in interactive technology. This possibility may have many advantages, not only from the point of view of texture rendering, but also to improve energy efficiency of devices and to imagine different interactive, training and diagnostic applications, where the human is directly involved. The analysis presented in this chapter may serve, therefore, as a starting point for addressing these questions and incorporating them in a structured manner in future research and developments.

## **1. Conclusions**

The present PhD. thesis focused on the generation, control and validation of longitudinal ultrasonic vibration for surface haptic devices. In the context of this work, we have strived to include the action and perception of the human in the system analysis, in order to address existing problematics in the design of ultrasonic surface haptic devices and explore future potential applications of this technology. Using the principles of piezoelectricity and vibrational mechanics, it was possible to illustrate a method for creating longitudinal and transverse ultrasonic vibration in the LFU spectrum (20 to 100 kHz) on a flat surface, to be used as a friction modulation surface haptic device.

Thanks to the use of a modal decomposition analysis and vector control, it was possible to impose a desired vibration amplitude and response time of a transverse and a longitudinal mode on a single device, independently. The implemented controller is able to perform robustly, even in the presence of external acoustic disturbances such as a finger posed on the device.

The human-machine interaction at the origin of the active lubrication phenomenon using longitudinal vibration was analyzed. A model was proposed and validated for two possible interaction cases. The first model considered the case when the finger moves in the axis of the stationary longitudinal wave propagation. It was theorized that, in this case, the ‘ratchet mechanism’ is mainly responsible for the friction reduction experienced with longitudinal ultrasonic vibration. The second model considered the more general case when the finger moves in any other direction over the surface. In this case, it was mainly the increase on the mean velocity of exploration and reduction of the finger dwell time that were at the origin of the active lubrication effect. The experimental validation of these models showed that

even though a margin of error still exists, the proposed interaction models are adequate to explain the friction reduction that occurs in longitudinal ultrasonic devices. These results also showed the dependence of the lubrication effect on parameters such as the relative velocity between the wave and the finger, and the mechanical impedance of the probing element. This parametric analysis is consistent with the results already observed in transverse modes.

The validation of longitudinal vibration as a technological alternative for the design and implementation of surface haptic devices was made through a series of experiments designed to compare the tribological and psychophysical performance of longitudinal modes against the transverse modes, which are currently applied in commercial technologies. The 'performance' of a haptic device was defined as the active power required to render a specific perceptual intensity. The results of these experiments showed that longitudinal modes have a tendency to provide a better performance than transverse modes, especially when using a high resonance frequency USHD. This is probably due to a better impedance coupling between the finger and the device, which allows minimizing the acoustic losses. It was however evidenced that the difference in finger impedance amongst different users caused an uneven perceptual intensity at a given vibration amplitude for both transverse and longitudinal modes. This issue had already been observed for transverse modes in previous studies.

Being able to propose a standardized perceptual response requires therefore the consideration of the mechanical impedance of the finger, to be able to provide an adequate stimulus for each individual. We explored one way of doing this, by implementing a calibration process based on the measurement of the acoustic finger force. The method uses data-based models to estimate the relative friction coefficient  $\mu'$  achievable at a given vibration amplitude for any new subject, by making two static measurements of the control voltage in steady state when a finger is present. We were able to observe a good correlation between the measurement



of the acoustic finger force, and the friction reduction, especially with longitudinal modes.

Finally, a new analysis perspective is presented with the ‘human-in-the-Loop’ system representation. This analysis helped in providing insightful clues for the integration of human physiological and behavioral aspects in the design and control of new haptic interfaces.

## **2. Perspectives**

In addition to the previous conclusions, many perspectives may be derived from these studies. The first one concerns the design of a longitudinal wave USHD. Even though we were able to create haptic return with longitudinal vibration, it was observed that the longitudinal modes achievable on the LFU frequency range on a planar structure have very large wavelengths, which may produce an uneven haptic return and possibly perceivable vibrational nodes along the explored surface. This particularity can be addressed through a proper design of longitudinal surface haptic devices, a subject that merits further research.

Another lead involves the prospective work that has been developed in Chapter 5, towards the adaptation of the friction provided by the controlled interface to each user. In particular, we were able to produce the acoustic force measurement in real time with the use of a disturbance observer. Using this method, it was possible to observe that the acoustic finger force is reduced when the finger is sliding. For this reason, it is interesting to look into the possible relation between the real time acoustic force and the friction modulation in real time, and whether this relation may provide the missing element for closed-loop real-time friction correction.

Finally, the ‘human-in-the-Loop’ representation for surface haptics that was introduced in this work is a technique that, we believe, has great potential, since advanced human-machine interfaces can help study and enhance human cognition, performance and health. This perspective helped envisaging and

proposing a new research perspective focused on possible 'human-in-the-Loop' applications, such as human task conditioning and training, and even the inclusion of additional interaction modes such as vision and audition.



PRINCIPLE OF SQUEEZE-FILM FOR FRICTION MODULATION IN  
ULTRASONIC SURFACE HAPTIC DEVICES

As explained in previous sections, submitting a volume to ultrasonic vibration causes a reduction of the friction of its surface. This ‘active lubrication’ effect has been widely studied for transverse vibration. Nonetheless, the actual interaction between the fingertip and the vibrating surface at ultrasonic frequencies is not yet completely clear. There is, therefore, not a definitive explanation for the friction reduction effect that occurs from this interaction. Two theories are offered in the literature as an explanation. These are the squeeze-film [38], [112], [125]–[127] and the intermittent contact [25], [114], [115] theories.

A.1. SQUEEZE-FILM

The principle behind this theory relies on the generation of a thin film of air in the contact region between the plate and the finger pad by the high speed compression-decompression cycle of the air. In [128]–[130], the authors characterize this phenomenon between a vibrating plate and a free one. With a finger pad, the film of air induced due to the ultrasonic vibration creates an acoustic levitation of the skin, thus reducing the friction between the finger and the plate. The solution proposed by [44] is recalled in this section.

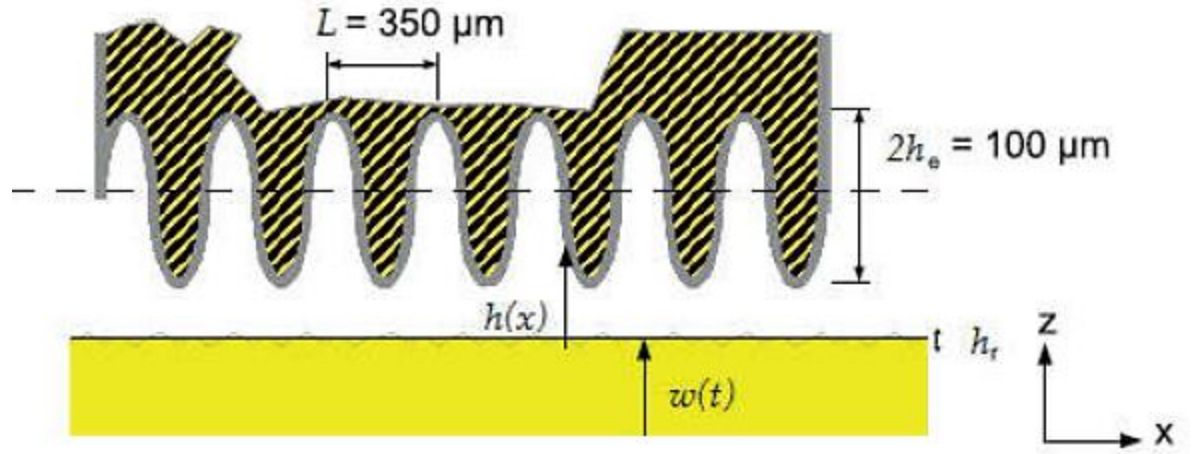


Figure 100. Approximation of the finger ridges for the analytical resolution of the Reynolds equations for ultrasonic surface haptic devices. Finger ridge structure is approximated to a sinusoid, with period  $L$  and peak amplitude  $h_e$ .  $h(x)$  is the distance between the vibrating surface and the finger. The surface vibrates with a, amplitude  $w(t) = h_{vib} \cos(\omega t)$ . The roughness of the surface is noted  $h_r$  [44].

To solve the complex fluid mechanics problem of the air pressure, the ridge structure is approximated to a sinusoid, with period  $L$  and peak amplitude  $h_e$ , as illustrated in

Figure 100. It is assumed that at ultrasonic frequencies, these ridges are stiff [30]. The vibrating surface has a vibration amplitude  $h_{vib}$  and angular frequency  $\omega$ . The thickness of the air gap can be expressed as (17).

$$h(x, t) = h_r + h_{vib} [1 + \cos(\omega t)] + h_e \left[ 1 + \cos\left(\frac{2\pi}{L} x\right) \right] \quad (93)$$

The relationship between the thickness of the air gap and the pressure between the two surfaces  $p$ , can be described by the Reynolds equations (94), where  $r_a$  and  $\eta$  represent the density and dynamic viscosity of the air.

$$\frac{\partial}{\partial x} \left( \frac{h^3 r_a}{\eta} \frac{\partial p}{\partial x} \right) + \frac{\partial}{\partial y} \left( \frac{h^3 r_a}{\eta} \frac{\partial p}{\partial y} \right) = 6v \frac{\partial}{\partial x} (hr_a) + 12 \frac{\partial}{\partial t} (hr_a) \quad (94)$$

When the finger moves laterally with a velocity  $v$ , a normalized version of (94) introduces the squeeze number  $\sigma$  and the bearing number  $\Lambda$ , as described by (95)

$$\frac{\partial}{\partial X} \left( H^3 P \frac{\partial P}{\partial X} \right) + \frac{\partial}{\partial Y} \left( H^3 P \frac{\partial P}{\partial Y} \right) = \Lambda \frac{\partial}{\partial X} (HP) + 12 \frac{\partial}{\partial T} (HP) \quad (95)$$

With  $l_0$  describing the contact length and  $p_0$  the atmospheric pressure, we can define:

$$\Lambda = \frac{6\eta v l_0}{h_0^2 p_0}, \quad \sigma = \frac{12\eta \omega_0 l_0^2}{h_0^2 p_0}, \quad X = \frac{x}{l_0}, \quad Y = \frac{y}{l_0}, \quad H = \frac{H}{l_0}, \quad P = \frac{P}{l_0}$$

This equation is solved assuming a very large squeeze number  $\sigma \rightarrow \infty$ . Solving the resulting differential equation leads to a solution for local pressure  $p_\infty$  of the thin film (96)

$$p_\infty = p_0 \frac{(1 + \delta \cos(kX)) \sqrt{(1 + \delta \cos(k/2))^2 + \frac{3}{2} \epsilon^2}}{(1 + \delta \cos(k/2))(1 + \epsilon \cos(T) + \delta \cos(kX))} \quad (96)$$

Where:

$$\epsilon = \frac{h_{vib}}{h_0 + h_e}, \quad \delta = \frac{h_e}{h_0 + h_e} \quad \text{and} \quad k = \frac{2\pi l_0}{L}$$

It is possible to calculate the force applied to the finger pad by the squeeze film, by integrating (96) in space and time. This force  $F_s$  can thus be defined as (97)

$$F_s = \frac{1}{2\pi} \int_0^{2\pi} \int_{-\frac{1}{2}}^{\frac{1}{2}} (1 - p_\infty) dX dT \quad (97)$$

The solution (96) assumed that  $\sigma \rightarrow \infty$ . However, it is generally admitted that restricting  $\sigma > 10$  is sufficient, and it is applicable for a vibrational frequency  $> 25$  kHz. It is then possible to calculate the relative friction coefficient at the vibration amplitude  $w$ ,  $\mu'(w)$  (defined by  $\mu(w)$ , the friction coefficient at an amplitude  $w$ , divide by  $\mu_0$ , which is the friction without vibration) in function of  $p_\infty$ , as expressed in (98).

$$\mu'(w) = \frac{\mu(w)}{\mu_0} = 1 - \frac{(p_\infty - 1)}{p_0} \quad (98)$$

## A.2. INTERMITTENT CONTACT

The squeeze film theory is one of the most widely accepted hypothesis to explain the active lubrication effect. However, as it has been observed in [113], the measured friction reduction between a finger pad and a flat surface subjected to ultrasonic vibration does not behave as predicted by the squeeze film effect only. For this reason, an alternative explanation is produced, which correlates with experimentally observed data. The ‘intermittent contact’ theory proposes an interaction mechanism in which, at certain vibration amplitudes, a regime is established where the finger loses and regains periodically contact with the vibrating plate, thus effectively reducing the amount of lateral force employed to slide over its surface. The proposed mechanism emphasizes the dependence of this effect on the vibration amplitude and frequency, and on certain finger parameters. Indeed, in addition to the vibration of the plate, the mechanical properties of the skin are a determinant factor when calculating the amount of friction modulation [116]–[118], [131]. It is possible to calculate the friction force based on this theory, by proposing a model for the lateral impedance of the finger.

At amplitudes at which the vibration is too small to produce loss of contact, the friction force is considered columbic and equal to the normal force  $F_n$  multiplied by the dynamic friction coefficient  $\mu_d$ . Once intermittent contact is established, the interaction may be represented as a state machine with three states: ‘stick’, ‘slip’ and ‘fly’, as described in [25]. The first two happen during contact and the third where there is loss of contact. To establish at which point there is loss of contact, the condition in (99) is verified. This is based on the fact that at equilibrium, the integral of the imposed force from the bed of springs must be equal to the total reaction force over a vibration cycle.

$$\int_{cycle} F_{reac} dt = F_n T \quad (99)$$

Where  $T$  denotes a period, and  $F_{reac}$  the normal reaction force of the plate in contact with the finger, modelled as the force of a spring elongation. During loss of contact, the state is called ‘fly’ and  $F_L$ , which is the lateral force felt by the finger is equal to zero. At first contact, the finger will be in ‘stick’ state, and the  $F_L$  will be dictated by  $F_{reac}$  and the elongation of the skin over the area of contact. Finally, when the force of the stretched skin is equal or larger than  $F_{reac}$  multiplied by the static friction coefficient  $\mu_s$ , the machine enters in ‘slip’ state, where it stays until loss of contact. The friction is then considered Columbic, and is dictated by  $F_{reac}$  multiplied by the constant dynamic friction coefficient  $\mu_d$ . The friction force is calculated as the average of  $F_L$  over a period.



## ENERGETIC MACROSCOPIC REPRESENTATION (EMR)

Energetic Macroscopic Representation (EMR) is a graphical formalism for modeling and control of energetic systems initiated in 2000s [208], [209]. EMR is a tool to organize the system model and to develop the control scheme based on three principles.

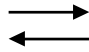
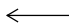
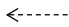

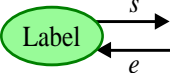
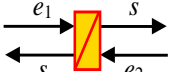
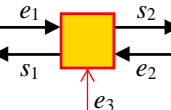
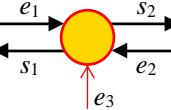
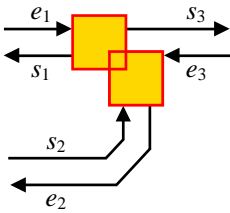
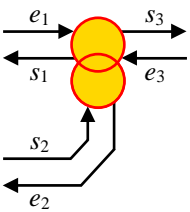
The system model is represented, i.e., organized, based on the two principles:

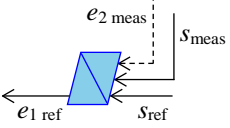
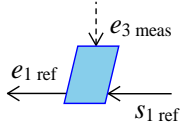
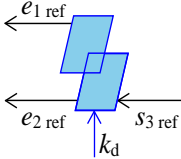
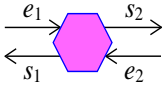

- *Principle of causality*: the inputs and the outputs of an energetic system must follow the integral causality; in which the outputs are functional integrals of the inputs. The outputs are delayed with respect to the inputs [210].
- *Principle of interaction*: the subsystems of an energetic system interact with each other via pairs of action and reaction variables; in which the product of these variables is the instantaneous power exchanged between these subsystems [208].

The control scheme is deduced from the model representation based on the principle of inversion. In which, the control is considered as a functional inversion of the model.

Table A2.1 gives EMR elements, their pictograms, and their descriptions. More information and the EMR library can be found in the EMR website [135].

Table A2.1: EMR elements (adapted from [134]).

Element	Pictogram	Description
Power variable		Pair of action and reaction variables of system model
Signal variable		Mandatory signal variable in the control scheme.
		Optional signal variable.
Measurement		Measurement of variables.
Source		Terminal of the system, which supplies or dissipates energy.
Accumulation		Accumulation of energy; introduce delay to the system; represent dynamics of the system.
Mono-physical conversion		Mono-domain conversion of energy; can be with or without tuning input.
Multi-physical conversion		Multi-domain conversion of energy; can be with or without tuning input.
Coupling		Mono-domain coupling or distribution of energy between more than two subsystems.
		Multi-domain coupling or distribution of energy between more than two subsystems.

Accumulation inversion		Indirect inversion of the accumulation elements to control its output; which is a closed-loop control
Conversion inversion		Direct inversion of energy conversion element.
Coupling inversion		Direct inversion of coupling element (both mono- and multi-domain)..
Estimation or model		Model copy of the system implemented in the control program; playing the role of estimation of reference model. (Hexagon means any possible block.)
Strategy		Strategy block to impose reference, distribution, and/or weighting factors to the control scheme.

MODAL MODELLING AND THE ORTHOGONALITY PRINCIPLE  
FOR TRANSVERSE MODE VIBRATION

A deformation at a point  $x$  of the structure in any direction  $\chi$  or  $\psi$  can be denominated  $d(x, t)$ . In modal theory, this spatio-temporal behaviour can be described with an infinite series of the products of spatial eigenvectors (mode shapes  $\varphi_k(x)$ , which describe the spatial deformation) multiplied by temporal coefficients ( $w_k(t)$ , that represent the temporal behaviour) as described by (23), with every  $k$  corresponding to each mode of the plate. Each one of these  $k$  modes is orthogonal to the others, and together, they form a  $k$ -dimensional sub-space.

$$d(x, t) = \sum_{k=1}^{\infty} \varphi_k(x) w_k(t) \quad (100)$$

In the case of forced vibration, the wave equation is modified, as the external force from the piezoelectric ceramics  $p(x, t)$  is included. This results in (24). When this equation is projected into the modal base, we obtain (25).

$$p(x, t) = \rho S \frac{d^2 \psi(x, t)}{dt^2} + E_e I \frac{\partial^4 \psi(x, t)}{\partial x^4} \quad (101)$$

$$p(x, t) = \sum_{k=1}^{\infty} \rho S \varphi_k(x) \frac{d^2 w_k(t)}{dt^2} + \sum_{k=1}^{\infty} E_e I \frac{\partial^4 \varphi_k(x)}{\partial x^4} w_k(t) \quad (102)$$

Because the modes are orthogonal in the  $k$ -dimensional base, by the orthogonality principle, the integrals of the projections  $\int_{-L/2}^{L/2} \varphi_i(x) \cdot \varphi_j(x) dx = 0$  for every  $i \neq j$  and 1 for  $i = j$ . If we project the  $n^{th}$  mode on the modal base, we get (26).

$$\begin{aligned} \int_{-L/2}^{L/2} p(x, t) \varphi_n(x) dx \\ = \sum_{k=1}^{\infty} \int_{-L/2}^{L/2} \rho S \varphi_k(x) \frac{d^2 w_k(t)}{dt^2} \varphi_n(x) dx \\ + \sum_{k=1}^{\infty} \int_{-L/2}^{L/2} E_e I \frac{\partial^4 \varphi_k(x)}{\partial x^4} w_k(t) \varphi_n(x) dx \end{aligned} \quad (103)$$

Using the orthogonality principle, we can deduce (27) from the first term on the right of the equation. Moreover, applying the boundary conditions explained in section 2.2.2.2, it is also possible to obtain (28) from the second factor.

$$\sum_{k=1}^{\infty} \int_{-L/2}^{L/2} \rho S \varphi_k(x) \frac{d^2 w_k(t)}{dt^2} \varphi_n(x) dx = \frac{d^2 w_n(t)}{dt^2} \int_{-L/2}^{L/2} \rho S \varphi_n^2(x) dx \quad (104)$$

$$\begin{aligned} \sum_{k=1}^{\infty} \int_{-L/2}^{L/2} E_e I \frac{\partial^4 \varphi_k(x)}{\partial x^4} w_k(t) \varphi_n(x) dx \\ = w_n(t) \int_{-L/2}^{L/2} E_e I \frac{\partial^4 \varphi_n(x)}{\partial x^4} \varphi_n(x) dx \end{aligned} \quad (105)$$

As explained in [166], the modal values of mass  $M_n$  and elasticity  $K_n$  may be introduced as per equations (29) and (30).

$$M_n = \int_{-L/2}^{L/2} \rho S \varphi_n^2(x) dx \quad (106)$$

$$K_n = \int_{-L/2}^{L/2} E_e I \frac{\partial^4 \varphi_n(x)}{\partial x^4} \varphi_n(x) dx \quad (107)$$

Replacing (29) and (30) in (27) and (28) respectively, (26) can be written as (31), with  $F_p = \int_{-L/2}^{L/2} p(x, t) \varphi_n(x) dx$  being the piezoelectric force associated to the  $n^{th}$  mode. For simplicity, we use  $\dot{w}_n(t)$  to denote the first time derivative of  $w_n(t)$  and  $\ddot{w}_n(t)$  for the second time derivative. For this reason (31) is applicable to all modes of the plate, independently of the direction of the deformation.

$$F_n(t) = M_n \ddot{w}_n(t) + K_n w_n(t) \quad (108)$$

In reality, all systems lose energy, so  $\int_{-L/2}^{L/2} p(x, t) \varphi_n(x) dx + [F(L)\varphi_n(L)] - [F(0)\varphi_n(0)] = F_p(t) - D_n \dot{w}_n(t)$ . Moreover, the force of the piezoelectrics can be represented as a simple linear electro-mechanical transformation factor, such that  $F_p(t) = N_n v(t)$ , with  $N_n$  equal to the electromechanical transformation constant for the piezoelectrics for the  $n^{th}$  mode, and  $v(t)$  equal to the input voltage [167], [168]. The final result is the modal dynamic model of the piezoelectric-plate system (32), which is used for the closed-loop control purpose

$$N_n v(t) = M_n \ddot{w}_n(t) + D_n \dot{w}_n(t) + K_n w_n(t) \quad (109)$$

## *Appendix 4*

### DESIGN OF 30 KHZ SURFACE HAPTIC DEVICES FOR TRANSVERSE AND LONGITUDINAL MODE COMPARISON

In this chapter, we present the design and implementation of two surface haptic devices around 30 kHz. One transverse and one longitudinal device. The objective of these devices is to perform a psychophysical and tribological comparison of the two vibration modes, in terms of perceived friction contrast for a range of vibration amplitudes, with the help of a group of participants. These results are compared to the results produced at 60 kHz in chapter 4

#### *A4.1. Design specifications*

For the design, a few constraints are taken into account. Firstly, it is desired for each device, that a single compressional mode is excited at a resonance frequency around 30 kHz, without interference from other vibrational modes in the usable bandwidth. Additionally, the device must allow an exploration surface of minimum about 3cm, in order to perform the desired tests.

Taking into account these constraints, a beam-type resonator is designed for the longitudinal mode. In order to move this mass, a Langevin piezoelectric transducer is considered to be a simple solution for a motion source (attention must be made to avoid mechanical interference at the intersection between the source of motion and the resonator.). The same Langevin transducer is placed vertically to produce the transverse mode.

This Langevin transducer consists of a stack of piezoelectric ceramics. To avoid disturbances when the compressional wave moves from one medium to the other

in the longitudinal mode device, aluminum is chosen as material for the resonator beam. The section  $S$  of the beam should allow a contact area large enough so the glue sustains the weight of the beam. A Langevin transducer is able to produce a small displacement (of a few micrometers), but works well at heavy loads. Different sizes of Langevin transducer are available. The model *Fujicera* ref. *FBL28502HA* is chosen. It has a resonance frequency of 28500Hz, and a diameter of 45 mm. The aluminum beam is designed to have a section of dimensions 42mm x 20mm to facilitate the attachment of the two parts.

In order to verify the last constraint, the beam should have two vibrational nodes at the sides and one maximum along the middle. The resonance frequency of the beam is calculated as explained in 2.2.2.1.

With  $L=165\text{mm}$ , the resonance frequency of the device is of about 30 kHz. This design allows a reasonable exploration area for the finger, through a length of about 6cm between two nodes. The design is tested with a FE simulation, and implemented.

#### *A4.2. Finite element simulation*

A FE simulation with Salome-Meca<sup>R</sup> [164] is performed, in order to evaluate the design, and find the resonant frequency and modal deformation of the complete structure.

For simplicity, the structure of the Langevin transducer is simplified to an aluminum cylinder, with the beam in close contact, neglecting possible glue effects.

The final design dimensions of the beam, which helped move the possible interfering modes away from the device's operational bandwidth, are 168 mm x 42 mm x 20 mm. Simulation results, illustrated in Figure 101, show that the resonance frequency of the desired mode 3 (one node at the center of the Langevin) is present at a resonance frequency of 27.6 kHz. Three different vibration modes proper to



the structure are found in the vicinity of this mode, but far enough to minimize interference in the bandwidth.

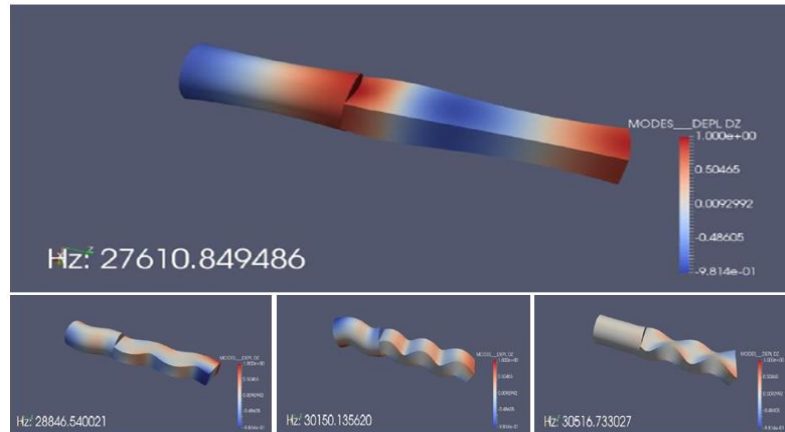


Figure 101. Top Finite Element simulation of the vibration modes of the designed longitudinal device consisting of a Langevin transducer and an aluminium beam.

#### *A4.3. Implementation*

The implemented device is shown in Figure 102. A damp-proof polymeric material is glued to the top face of the aluminum beam. This design allows a reasonable exploration area for the finger, through a length of about 6cm between two nodes. The resonator is situated on top of two support points placed at the vibration nodes.



Figure 102. Longitudinal wave haptic device created with a Langevin transducer attached to an aluminum beam

The resonance frequency of the actual system is about 29240Hz (with variations due to temperature). An almost purely longitudinal vibration mode is confirmed with laser cartography, performed as explained in 2.2.4. The results of the measurements are depicted in Figure 103. The surface represented in the cartography maps, corresponds to the vibration amplitudes measured on top face of the beam. The colors of the figure (ranging from blue to red) represent the vibration amplitude at resonance.

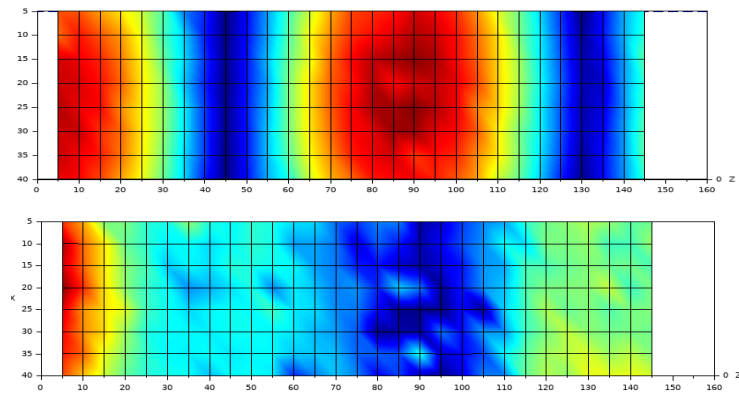


Figure 103. Top Cartography of the beam at resonance. Exploration area between 60 and 120 mm. Up: Longitudinal mode vibration amplitude (red corresponding to a maximum of  $1.5\mu\text{m}$ , dark blue  $0\mu\text{m}$ ). Down: Transverse mode vibration Amplitude. (red corresponding to a maximum of  $0.5\mu\text{m}$ )



## References

- [1] V. Hayward, “A Brief Overview of the Human Somatosensory System,” in *Musical Haptics*, S. Papetti and C. Saitis, Eds. Cham: Springer International Publishing, 2018, pp. 29–48. doi: 10.1007/978-3-319-58316-7\_3.
- [2] H. Watanabe, H. Hashizume, H. Inoue, and T. Ogura, “Collagen framework of the volar plate of human proximal interphalangeal joint,” *Acta Med Okayama*, vol. 48, no. 2, pp. 101–108, Apr. 1994, doi: 10.18926/AMO/31103.
- [3] Y. C. Fung, *Biomechanics: Mechanical Properties of Living Tissues*. 1993.
- [4] G. Robles-De-La-Torre and V. Hayward, “Force can overcome object geometry in the perception of shape through active touch,” *Nature*, vol. 412, no. 6845, pp. 445–448, Jul. 2001, doi: 10.1038/35086588.
- [5] R. P. Smith, F. H. Netter, C. A. G. Machado, and F. H. Netter, Eds., *The Netter collection of medical illustrations*, 2nd ed. Philadelphia, PA: Elsevier, 2011.
- [6] T. Quilliam, *The structure of finger print skin*. Pergamon Press Oxford, 1978.
- [7] J. A. McGrath and J. Uitto, “Anatomy and Organization of Human Skin,” in *Rook’s Textbook of Dermatology*, T. Burns, S. Breathnach, N. Cox, and C. Griffiths, Eds. Oxford, UK: Wiley-Blackwell, 2010, pp. 1–53. doi: 10.1002/9781444317633.ch3.
- [8] B. M. Dzidek, M. J. Adams, J. W. Andrews, Z. Zhang, and S. A. Johnson, “Contact mechanics of the human finger pad under compressive loads,” *J. R. Soc. Interface.*, vol. 14, no. 127, p. 20160935, Feb. 2017, doi: 10.1098/rsif.2016.0935.
- [9] A. Méliissopoulos, C. Levacher, L. Robert, and R. Ballotti, *La peau structure et physiologie*. Paris: Lavoisier, 2012.
- [10] P. H. Warman and A. R. Ennos, “Fingerprints are unlikely to increase the friction of primate fingerpads,” *Journal of Experimental Biology*, vol. 212, no. 13, pp. 2016–2022, Jul. 2009, doi: 10.1242/jeb.028977.
- [11] Seoung-Mok Yum, In-Keun Baek, Dongpyo Hong, Juhan Kim, Kyunghoon Jung, Seontae Kim, Kihoon Eom, Jeongmin Jang, Seonmyeong Kim, Matlabjon Sattorov, Min-Geol Lee, Sungwan Kim, Michael J. Adams, Gun-Sik Park, “Fingerprint ridges allow primates to regulate grip,” *Proc Natl Acad Sci USA*, vol. 117, no. 50, pp. 31665–31673, Dec. 2020, doi: 10.1073/pnas.2001055117.
- [12] A. Prevost, J. Scheibert, and G. Debrégeas, “Effect of fingerprints orientation on skin vibrations during tactile exploration of textured surfaces,” *arXiv:0911.3226 [physics]*, Nov. 2009, Accessed: Jul. 20, 2021. [Online]. Available: <http://arxiv.org/abs/0911.3226>
- [13] M. J. Adams, S.A. Johnson, P. Lefevre, V. Levesque, V. Hayward, T. Andre, J.L. Thonnard, “Finger pad friction and its role in grip and touch,” *Journal of The Royal Society Interface*, vol. 10, no. 80, pp. 20120467– 20120467, Dec. 2012, doi: 10.1098/rsif.2012.0467.

- [14] S. E. Tomlinson, R. Lewis, X. Liu, C. Texier, and M. J. Carré, “Understanding the Friction Mechanisms Between the Human Finger and Flat Contacting Surfaces in Moist Conditions,” *Tribology Letters*, vol. 41, no. 1, pp. 283–294, Jan. 2011, doi: 10.1007/s11249-010-9709-y.
- [15] L. Norlén, “Stratum corneum keratin structure, function and formation - a comprehensive review: A review of stratum corneum keratin,” *International Journal of Cosmetic Science*, vol. 28, no. 6, pp. 397–425, Nov. 2006, doi: 10.1111/j.1467-2494.2006.00345.x.
- [16] W. Maurel, Ed., *Biomechanical models for soft tissue simulation*. Berlin Heidelberg: Springer, 1998.
- [17] N. Huloux, “Etude de la réflexion et de l’absorption des ondes ultrasonores par le doigt: application aux surfaces haptiques,” Thèse, Aix-Marseille Université, 2021.
- [18] T. C. Pataky, M. L. Latash, and V. M. Zatsiorsky, “Viscoelastic response of the finger pad to incremental tangential displacements,” *Journal of Biomechanics*, vol. 38, no. 7, pp. 1441–1449, Jul. 2005, doi: 10.1016/j.jbiomech.2004.07.004.
- [19] D. T. V. Pawluk and R. D. Howe, “Dynamic Contact of the Human Fingerpad Against a Flat Surface,” *Journal of Biomechanical Engineering*, vol. 121, no. 6, pp. 605–611, Dec. 1999, doi: 10.1115/1.2800860.
- [20] E. R. Serina, E. Mockensturm, C. D. Mote, and D. Rempel, “A structural model of the forced compression of the fingertip pulp,” *Journal of Biomechanics*, vol. 31, no. 7, pp. 639–646, Jul. 1998, doi: 10.1016/S0021-9290(98)00067-0.
- [21] E. R. Serina, C. D. Mote, and D. Rempel, “Force response of the fingertip pulp to repeated compression—Effects of loading rate, loading angle and anthropometry,” *Journal of Biomechanics*, vol. 30, no. 10, pp. 1035–1040, Oct. 1997, doi: 10.1016/S0021-9290(97)00065-1.
- [22] Q. Wang and V. Hayward, “In vivo biomechanics of the fingerpad skin under local tangential traction,” *Journal of Biomechanics*, vol. 40, no. 4, pp. 851–860, Jan. 2007, doi: 10.1016/j.jbiomech.2006.03.004.
- [23] C. E. Jamison, R. D. Marangoni, and A. A. Glaser, “Viscoelastic properties of soft tissue by discrete model characterization,” *Journal of Biomechanics*, vol. 1, no. 1, pp. 33–46, Jan. 1968, doi: 10.1016/0021-9290(68)90036-5.
- [24] M. Wiertelowski and V. Hayward, “Mechanical behavior of the fingertip in the range of frequencies and displacements relevant to touch,” *Journal of Biomechanics*, vol. 45, no. 11, pp. 1869–1874, Jul. 2012, doi: 10.1016/j.jbiomech.2012.05.045.
- [25] F. Giraud, T. Hara, C. Giraud-Audine, M. Amberg, B. Lemaire-Semail, and M. Takasaki, “Evaluation of a friction reduction based haptic surface at high frequency,” in *2018 IEEE Haptics Symposium (HAPTICS)*, San Francisco, CA, Mar. 2018, pp. 210–215. doi: 10.1109/HAPTICS.2018.8357178.
- [26] A. Z. Hajian and R. D. Howe, “Identification of the Mechanical Impedance at the Human Finger Tip,” *Journal of Biomechanical Engineering*, vol. 119, no. 1, pp. 109–114, Feb. 1997, doi: 10.1115/1.2796052.

- [27] R. G. Dong, J. Z. Wu, T. W. McDowell, D. E. Welcome, and A. W. Schopper, "Distribution of mechanical impedance at the fingers and the palm of the human hand," *Journal of Biomechanics*, vol. 38, no. 5, pp. 1165–1175, May 2005, doi: 10.1016/j.jbiomech.2004.05.021.
- [28] R. Lundström, "Local vibrations—Mechanical impedance of the human hand's glabrous skin," *Journal of Biomechanics*, vol. 17, no. 2, pp. 137–144, Jan. 1984, doi: 10.1016/0021-9290(84)90131-3.
- [29] M. Jocelyn, "Perception d'un transitoire tactile en phase d'appui par la réduction rapide d'adhérence," Thèse, Aix-Marseille Université, 2021.
- [30] E. Vezzoli, "Tactile feedback devices: friction control and texture generation," thesis, Lille 1, 2016. Accessed: Aug. 03, 2019.
- [31] B. Dzidek, S. Bochereau, S. A. Johnson, V. Hayward, and M. J. Adams, "Why pens have rubbery grips," *Proc Natl Acad Sci USA*, vol. 114, no. 41, pp. 10864–10869, Oct. 2017, doi: 10.1073/pnas.1706233114.
- [32] S. Bochereau, B. Dzidek, M. Adams, and V. Hayward, "Characterizing and Imaging Gross and Real Finger Contacts under Dynamic Loading," *IEEE Trans. Haptics*, vol. 10, no. 4, pp. 456–465, Oct. 2017, doi: 10.1109/TOH.2017.2686849.
- [33] V. Levesque and V. Hayward, "Experimental Evidence of Lateral Skin Strain During Tactile Exploration," in *EuroHaptics*, Dublin, Ireland, 2003, p. 15.
- [34] V. Hayward, A. V. Terekhov, S.-C. Wong, P. Geborek, F. Bengtsson, and H. Jörntell, "Spatio-temporal skin strain distributions evoke low variability spike responses in cuneate neurons," *J. R. Soc. Interface.*, vol. 11, no. 93, p. 20131015, Apr. 2014, doi: 10.1098/rsif.2013.1015.
- [35] E. Vezzoli, B. Dzidek, T. Sednaoui, F. Giraud, M. Adams, and B. Lemaire-Semail, "Role of fingerprint mechanics and non-Coulombic friction in ultrasonic devices," in *2015 IEEE World Haptics Conference (WHC)*, Evanston, IL, Jun. 2015, pp. 43–48. doi: 10.1109/WHC.2015.7177689.
- [36] D. Gueorguiev, S. Bochereau, A. Mouraux, V. Hayward, and J.-L. Thonnard, "Touch uses frictional cues to discriminate flat materials," *Sci Rep*, vol. 6, no. 1, p. 25553, Jul. 2016, doi: 10.1038/srep25553.
- [37] S. J. Lederman and R. L. Klatzky, "Hand movements: A window into haptic object recognition," *Cognitive Psychology*, vol. 19, no. 3, pp. 342–368, Jul. 1987, doi: 10.1016/0010-0285(87)90008-9.
- [38] M. Biet, F. Giraud, and B. Lemaire-Semail, "Squeeze film effect for the design of an ultrasonic tactile plate," *IEEE Transactions on Ultrasonics, Ferroelectrics and Frequency Control*, vol. 54, no. 12, pp. 2678–2688, Dec. 2007, doi: 10.1109/TUFFC.2007.596.
- [39] B. Dandu, Y. Shao, and Y. Visell, "Rendering Spatiotemporal Haptic Effects Via the Physics of Waves in the Skin," *IEEE Trans. Haptics*, vol. 14, no. 2, pp. 347–358, Apr. 2021, doi: 10.1109/TOH.2020.3029768.

- [40] B. Delhaye, V. Hayward, P. Lefèvre, and J.-L. Thonnard, “Texture-induced vibrations in the forearm during tactile exploration,” *Front. Behav. Neurosci.*, vol. 6, 2012, doi: 10.3389/fnbeh.2012.00037.
- [41] L. R. Manfredi, A. T. Baker, D. O. Elias, J. F. Dammann, M. C. Zelinski, V. S. Polashock, S. J. Bensmaia, M. Maravall, “The Effect of Surface Wave Propagation on Neural Responses to Vibration in Primate Glabrous Skin,” *PLoS ONE*, vol. 7, no. 2, p. e31203, Feb. 2012, doi: 10.1371/journal.pone.0031203.
- [42] T. Callier, H. P. Saal, E. C. Davis-Berg, and S. J. Bensmaia, “Kinematics of unconstrained tactile texture exploration,” *Journal of Neurophysiology*, vol. 113, no. 7, pp. 3013–3020, Apr. 2015, doi: 10.1152/jn.00703.2014.
- [43] J. C. Cohen, J. C. Makous, and S. J. Bolanowski, “Under which conditions do the skin and probe decouple during sinusoidal vibrations?,” *Experimental Brain Research*, vol. 129, no. 2, pp. 211–217, Nov. 1999, doi: 10.1007/s002210050891.
- [44] M. Biet, “Conception et contrôle d’actionneurs électro-actifs dédiés à la stimulation tactile,” Thesis, Lille 1, 2007.
- [45] B. G. Green, “Temperature perception and nociception,” *Journal of Neurobiology*, vol. 61, no. 1, pp. 13–29, Oct. 2004, doi: 10.1002/neu.20081.
- [46] P. Grigg, “Properties of Sensory Neurons Innervating Synovial Joints,” *Cells Tissues Organs*, vol. 169, no. 3, pp. 218–225, 2001, doi: 10.1159/000047885.
- [47] Y. K. Dillon, J. Haynes, and M. Henneberg, “The relationship of the number of Meissner’s corpuscles to dermatoglyphic characters and finger size,” *Journal of Anatomy*, vol. 199, no. 5, pp. 577–584, Nov. 2001, doi: 10.1046/j.1469-7580.2001.19950577.x.
- [48] K. O. Johnson and S. S. Hsiao, “Neural mechanisms of tactual form and texture perception,” *Annual review of neuroscience*, vol. 15, pp. 227–250, 1992.
- [49] K. Johnson, “The roles and functions of cutaneous mechanoreceptors,” *Current Opinion in Neurobiology*, vol. 11, no. 4, pp. 455–461, Aug. 2001, doi: 10.1016/S0959-4388(00)00234-8.
- [50] Z. Yi, Y. Zhang, and J. Peters, “Biomimetic tactile sensors and signal processing with spike trains: A review,” *Sensors and Actuators A: Physical*, vol. 269, pp. 41–52, Jan. 2018, doi: 10.1016/j.sna.2017.09.035.
- [51] H. Takahashi-Iwanaga and H. Shimoda, “The three-dimensional microanatomy of Meissner corpuscles in monkey palmar skin,” *J Neurocytol*, vol. 32, no. 4, pp. 363–371, May 2003, doi: 10.1023/B:NEUR.0000011330.57530.2f.
- [52] K. Gottschaldt and C. Vahle-Hinz, “Merkel cell receptors: structure and transducer function,” *Science*, vol. 214, no. 4517, pp. 183–186, Oct. 1981, doi: 10.1126/science.7280690.
- [53] J. M. Loomis, “An investigation of tactile hyperacuity,” *Sensory Processes*, pp. 289–302, 1979.

- [54] R. H. LaMotte and M. A. Srinivasan, "Surface Microgeometry: Tactile Perception and Neural Encoding," in *Information Processing in the Somatosensory System: Proceedings of an International Symposium at the Wenner-Gren Center, Stockholm, 3–5 July, 1989*, O. Franzén and J. Westman, Eds. London: Macmillan Education UK, 1991, pp. 49–58. doi: 10.1007/978-1-349-11597-6\_4.
- [55] L. Skedung, M. Arvidsson, J. Y. Chung, C. M. Stafford, B. Berglund, and M. W. Rutland, "Feeling Small: Exploring the Tactile Perception Limits," *Sci Rep*, vol. 3, no. 1, p. 2617, Dec. 2013, doi: 10.1038/srep02617.
- [56] F. McGlone, J. Wessberg, and H. Olausson, "Discriminative and Affective Touch: Sensing and Feeling," *Neuron*, vol. 82, no. 4, pp. 737–755, May 2014, doi: 10.1016/j.neuron.2014.05.001.
- [57] V. Hayward, "A brief taxonomy of tactile illusions and demonstrations that can be done in a hardware store," *Brain Research Bulletin*, vol. 75, no. 6, pp. 742–752, Apr. 2008, doi: 10.1016/j.brainresbull.2008.01.008.
- [58] D. Wang, Y. Guo, S. Liu, Y. Zhang, W. Xu, and J. Xiao, "Haptic display for virtual reality: progress and challenges," *Virtual Reality & Intelligent Hardware*, vol. 1, no. 2, pp. 136–162, Apr. 2019, doi: 10.3724/SP.J.2096-5796.2019.0008.
- [59] A. Kaci, "Méthodologie de commande de vibrations multimodales par modulation-démodulation synchrone: application au retour tactile 'multitouch,'" Thèse, Université de Lille, 2020.
- [60] C. Basdogan, F. Giraud, V. Levesque, and S. Choi, "A Review of Surface Haptics: Enabling Tactile Effects on Touch Surfaces," *IEEE Trans. Haptics*, vol. 13, no. 3, pp. 450–470, Jul. 2020, doi: 10.1109/TOH.2020.2990712.
- [61] "Force Dimension Inc." <https://www.forcedimension.com>
- [62] M. C. Lin and M. A. Otaduy, Eds., *Haptic rendering: foundations, algorithms, and applications*. Wellesley, Mass: A.K. Peters, 2008.
- [63] T. H. Massie and J. K. Salisbury, "The PHANToM haptic interface: A device for probing virtual objects," in *Proceedings of the ASME Dynamic Systems and Control Division*, 1994, pp. 295–301.
- [64] D. Chamaret, M. Naud, L. Hamon, S. Ullah, E. Richard, and P. Richard, "Human-Scale Haptic Interaction Using the SPIDAR," Dec. 2009, p. 7. doi: hal-00957369.
- [65] "Haption Inc." <https://www.haption.com>
- [66] "Butterfly Haptics, LLC." <https://butterflyhaptics.com>
- [67] "Quanser." <https://www.quanser.com>
- [68] Y. Kurita, "Wearable Haptics," in *Wearable Sensors*, Elsevier, 2014, pp. 45–63. doi: 10.1016/B978-0-12-418662-0.00025-8.
- [69] "GotouchVR." <https://www.gotouchvr.com>
- [70] "CyberGlove Systems LLC." <http://www.cyberglovesystems.com/>
- [71] "HGlove-HAPTIONSA." <https://www.haption.com/en/products-en/hglove-en.html>



- [72] “Dextarobotics.” <https://www.dextarobotics.com>
- [73] “HaptX Inc.” <https://haptx.com>
- [74] “Plexus/High-performanceVR/AR Gloves.” <http://plexus.im/>
- [75] “Sense Glove.” <https://www.senseglove.com/>
- [76] “Contact CI.” <https://contactci.co/>
- [77] “Senso Glove.” <https://senso.me/>
- [78] “VR Electronics Ltd. - Teslasuit.” <https://teslasuit.io/blog/vr-glove-by-teslasuit/>
- [79] “VRgluv.” <https://vrgluv.com>
- [80] G. Burdea, *Force and touch feedback for Virtual Reality*. New York: Wiley, 1996.
- [81] T. A. Kern, Ed., *Engineering Haptic Devices*. Berlin, Heidelberg: Springer Berlin Heidelberg, 2009. doi: 10.1007/978-3-540-88248-0.
- [82] A. El Saddik, M. Orozco, M. Eid, and J. Cha, *Haptics Technologies*. Berlin, Heidelberg: Springer Berlin Heidelberg, 2011. doi: 10.1007/978-3-642-22658-8.
- [83] S. Choi and K. J. Kuchenbecker, “Vibrotactile Display: Perception, Technology, and Applications,” *Proc. IEEE*, vol. 101, no. 9, pp. 2093–2104, Sep. 2013, doi: 10.1109/JPROC.2012.2221071.
- [84] I. Rakkolainen, A. Sand, and R. Raisamo, “A Survey of Mid-Air Ultrasonic Tactile Feedback,” in *2019 IEEE International Symposium on Multimedia (ISM)*, San Diego, CA, USA, Dec. 2019, pp. 94–944. doi: 10.1109/ISM46123.2019.00022.
- [85] T. Iwamoto, M. Tatzono, and H. Shinoda, “Non-contact Method for Producing Tactile Sensation Using Airborne Ultrasound,” in *Haptics: Perception, Devices and Scenarios*, vol. 5024, M. Ferre, Ed. Berlin, Heidelberg: Springer Berlin Heidelberg, 2008, pp. 504–513. doi: 10.1007/978-3-540-69057-3\_64.
- [86] “Ultraleap Ltd.” <https://www.ultraleap.com>
- [87] “Bristol Interaction Group.” <http://www.biglab.co.uk>
- [88] D. Hajas, D. Ablart, O. Schneider, and M. Obrist, “I can feel it moving: Science Communicators Talking About the Potential of Mid-Air Haptics,” *Front. Comput. Sci.*, vol. 2, p. 534974, Nov. 2020, doi: 10.3389/fcomp.2020.534974.
- [89] Y. Ujitoko, T. Taniguchi, S. Sakurai, and K. Hirota, “Development of Finger-Mounted High-Density Pin-Array Haptic Display,” *IEEE Access*, vol. 8, pp. 145107–145114, 2020, doi: 10.1109/ACCESS.2020.3015058.
- [90] C. Simonelli, A. Musolino, R. Rizzo, and A. Jones, “Development of an Innovative Magnetorheological Fluids-Based Haptic Device Excited by Permanent Magnets,” *2021 IEEE World Haptics Conference*, 2021.
- [91] E. Enferad, “Dynamic Spatial Vibration Form Generation Using Modal Decomposition,” Thesis, Université de Lille, France, 2018.

- [92] J.-H. Woo and J.-G. Ih, "Vibration rendering on a thin plate with actuator array at the periphery," *Journal of Sound and Vibration*, vol. 349, pp. 150–162, Aug. 2015, doi: 10.1016/j.jsv.2015.03.031.
- [93] C. Hudin, J. Lozada, and V. Hayward, "Localized tactile stimulation by time-reversal of flexural waves: Case study with a thin sheet of glass," *2013 IEEE World Haptics Conference*, Apr. 2013, pp. 67–72. doi: 10.1109/WHC.2013.6548386.
- [94] D. J. Meyer, M. A. Peshkin, and J. E. Colgate, "Fingertip friction modulation due to electrostatic attraction," in *2013 World Haptics Conference (WHC)*, Apr. 2013, pp. 43–48. doi: 10.1109/WHC.2013.6548382.
- [95] E. Vezzoli, M. Amberg, F. Giraud, and B. Lemaire-Semail, "Electrovibration Modeling Analysis," in *Haptics: Neuroscience, Devices, Modeling, and Applications*, 2014, pp. 369–376.
- [96] D. J. Meyer, M. Wiertelowski, M. A. Peshkin, and J. E. Colgate, "Dynamics of ultrasonic and electrostatic friction modulation for rendering texture on haptic surfaces," in *2014 IEEE Haptics Symposium (HAPTICS)*, Houston, TX, USA, Feb. 2014, pp. 63–67. doi: 10.1109/HAPTICS.2014.6775434.
- [97] E. Vezzoli, W. Ben Massoud, C. Nadal, F. Giraud, M. Amberg, B. Lemaire-Semail, M-A. Bueno "Coupling of ultrasonic vibration and electrovibration for tactile stimulation," *European Journal of Electrical Engineering*, vol. 17, no. 5–6, pp. 377–395, Dec. 2014, doi: 10.3166/ejee.17.377-395.
- [98] J. Mullenbach, M. Peshkin, and J. E. Colgate, "eShiver: Lateral Force Feedback on Fingertips through Oscillatory Motion of an Electroadhesive Surface," *IEEE Transactions on Haptics*, vol. 10, no. 3, pp. 358–370, Jul. 2017, doi: 10.1109/TOH.2016.2630057.
- [99] E. Mallinckrodt, A. L. Hughes, and W. Sleator, "Perception by the Skin of Electrically Induced Vibrations," *Science*, vol. 118, no. 3062, pp. 277–278, Sep. 1953, doi: 10.1126/science.118.3062.277.
- [100] O. Bau, I. Poupyrev, A. Israr, and C. Harrison, "TeslaTouch: electrovibration for touch surfaces," in *Proceedings of the 23rd annual ACM symposium on User interface software and technology - UIST '10*, New York, New York, USA, 2010, p. 283. doi: 10.1145/1866029.1866074.
- [101] S.-C. Kim, A. Israr, and I. Poupyrev, "Tactile rendering of 3D features on touch surfaces," in *Proceedings of the 26th annual ACM symposium on User interface software and technology - UIST '13*, St. Andrews, Scotland, United Kingdom, 2013, pp. 531–538. doi: 10.1145/2501988.2502020.
- [102] "Tanvas," *Tanvas*. <https://tanvas.co/> (accessed Aug. 24, 2019).
- [103] D. Wijekoon, M. E. Cecchinato, E. Hoggan, and J. Linjama, "Electrostatic Modulated Friction As Tactile Feedback: Intensity Perception," in *Proceedings of the 2012 International Conference on Haptics: Perception, Devices, Mobility, and Communication - Volume Part I*, Berlin, Heidelberg, 2012, pp. 613–624. doi: 10.1007/978-3-642-31401-8\_54.

- [104] T. Watanabe and S. Fukui, “A method for controlling tactile sensation of surface roughness using ultrasonic vibration,” in *Proceedings of 1995 IEEE International Conference on Robotics and Automation*, May 1995, vol. 1, pp. 1134–1139 vol.1. doi: 10.1109/ROBOT.1995.525433.
- [105] M. Amberg, F. Giraud, B. Semail, P. Olivo, G. Casiez, and N. Roussel, “STIMTAC: a tactile input device with programmable friction,” in *Proceedings of the 24th annual ACM symposium adjunct on User interface software and technology - UIST '11 Adjunct*, Santa Barbara, California, USA, 2011, p. 7. doi: 10.1145/2046396.2046401.
- [106] L. Winfield, J. Glassmire, J. E. Colgate, and M. Peshkin, “T-PaD: Tactile Pattern Display through Variable Friction Reduction,” in *Second Joint EuroHaptics Conference and Symposium on Haptic Interfaces for Virtual Environment and Teleoperator Systems (WHC'07)*, Tsukuba, Japan, Mar. 2007, pp. 421–426. doi: 10.1109/WHC.2007.105.
- [107] M. Wiertlewski, D. Leonardis, D. J. Meyer, M. A. Peshkin, and J. E. Colgate, “A High-Fidelity Surface-Haptic Device for Texture Rendering on Bare Finger,” in *Haptics: Neuroscience, Devices, Modeling, and Applications*, vol. 8619, M. Auvray and C. Duriez, Eds. Berlin, Heidelberg: Springer Berlin Heidelberg, 2014, pp. 241–248. doi: 10.1007/978-3-662-44196-1\_30.
- [108] C. Winter, Y. Civet, and Y. Perriard, “Optimal design of a squeeze film actuator for friction feedback,” *Proceedings of the 2013 IEEE International Electric Machines and Drives Conference (IEMDC 2013)*, 2013. <https://infoscience.epfl.ch/record/191333>.
- [109] F. Giraud, M. Amberg, and B. Lemaire-Semail, “Design and control of a haptic knob,” *Sensors and Actuators A: Physical*, vol. 196, pp. 78–85, Jul. 2013, doi: 10.1016/j.sna.2013.03.012.
- [110] S. Ghenna, F. Giraud, C. Giraud-Audine, and M. Amberg, “Vector Control of Piezoelectric Transducers and Ultrasonic Actuators,” *IEEE Transactions on Industrial Electronics*, vol. 65, no. 6, pp. 4880–4888, Jun. 2018, doi: 10.1109/TIE.2017.2784350.
- [111] F. Giraud, M. Amberg, B. Lemaire-Semail, and G. Casiez, “Design of a transparent tactile stimulator,” in *2012 IEEE Haptics Symposium (HAPTICS)*, Vancouver, BC, Canada, Mar. 2012, pp. 485–489. doi: 10.1109/HAPTIC.2012.6183835.
- [112] M. Wiertlewski, R. F. Friesen, and J. E. Colgate, “REPLY TO JACKSON ET AL.: Precision on the squeeze film levitation of human fingertip,” *Proceedings of the National Academy of Sciences of the United States of America*, vol. 113, no. 45, p. E6907, Nov. 2016, doi: 10.1073/pnas.1614426113.
- [113] T. Sednaoui, E. Vezzoli, B. Dzidek, B. Lemaire-Semail, C. Chappaz, and M. Adams, “Experimental evaluation of friction reduction in ultrasonic devices,” in *2015 IEEE World Haptics Conference (WHC)*, Evanston, IL, Jun. 2015, pp. 37–42. doi: 10.1109/WHC.2015.7177688.

- [114] T. Sednaoui, E. Vezzoli, B. Dzidek, B. Lemaire-Semail, C. Chappaz, and M. Adams, “Friction Reduction through Ultrasonic Vibration Part 2: Experimental Evaluation of Intermittent Contact and Squeeze Film Levitation,” *IEEE Transactions on Haptics*, vol. 10, no. 2, pp. 208–216, Apr. 2017, doi: 10.1109/TOH.2017.2671376.
- [115] E. Vezzoli, V. Zlatko, G. Vincenzo, B. Lemaire-Semail, F. Giraud, R. Tomaz, P. Djordje, M. Adams, “Friction Reduction through Ultrasonic Vibration Part 1: Modelling Intermittent Contact,” *IEEE Transactions on 32 Haptics (ToH)*, vol. 10, no. 2, pp. 196–207, 2017, doi: 10.1109/TOH.2017.2671432.
- [116] R. F. Friesen, M. Wiertlewski, and J. E. Colgate, “The role of damping in ultrasonic friction reduction,” in *2016 IEEE Haptics Symposium (HAPTICS)*, Philadelphia, PA, Apr. 2016, pp. 167–172, doi: 10.1109/HAPTICS.2016.7463172.
- [117] J. Monnoyer, E. Diaz, C. Bourdin, and M. Wiertlewski, “Optimal skin impedance promotes perception of ultrasonic switches,” in *2017 IEEE World Haptics Conference (WHC)*, Munich, Germany, Jun. 2017, pp. 130–135. doi: 10.1109/WHC.2017.7989889.
- [118] J. Monnoyer, E. Diaz, C. Bourdin, and M. Wiertlewski, “Perception of Ultrasonic Switches Involves Large Discontinuity of the Mechanical Impedance,” *IEEE Transactions on Haptics*, vol. 11, no. 4, pp. 579–589, Oct. 2018, doi: 10.1109/TOH.2018.2844186.
- [119] S. Ghenna, E. Vezzoli, C. Giraud-Audine, F. Giraud, M. Amberg, and B. Lemaire-Semail, “Enhancing Variable Friction Tactile Display Using an Ultrasonic Travelling Wave,” *IEEE Transactions on Haptics*, vol. 10, no. 2, pp. 296–301, Apr. 2017, doi: 10.1109/TOH.2016.2607200.
- [120] H. Kotani, M. Takasaki, T. Mizuno, and T. Nara, “Glass Substrate Surface Acoustic Wave Tactile Display With Visual Information,” in *2006 International Conference on Mechatronics and Automation*, Luoyang, Jun. 2006, pp. 1–6. doi: 10.1109/ICMA.2006.257425.
- [121] M. Takasaki, Ji HongXu, Hiroyuki Kotani, and T. Mizuno, “Application of surface acoustic wave tactile display for pen tablet interface with visual information,” in *2007 IEEE International Conference on Robotics and Biomimetics (ROBIO)*, Sanya, China, Dec. 2007, pp. 1024–1028. doi: 10.1109/ROBIO.2007.4522304.
- [122] X. Dai, J. E. Colgate, and M. A. Peshkin, “LateralPaD: A surface-haptic device that produces lateral forces on a bare finger,” in *2012 IEEE Haptics Symposium (HAPTICS)*, Mar. 2012, pp. 7–14. doi: 10.1109/HAPTIC.2012.6183753.
- [123] E. C. Chubb, J. E. Colgate, and M. A. Peshkin, “ShiverPaD: A Glass Haptic Surface That Produces Shear Force on a Bare Finger,” *IEEE Transactions on Haptics*, vol. 3, no. 3, pp. 189–198, Jul. 2010, doi: 10.1109/TOH.2010.7.
- [124] H. Xu, M. A. Peshkin, and J. E. Colgate, “UltraShiver: Lateral force feedback on a bare fingertip via ultrasonic oscillation and electroadhesion,” in *2018*

- IEEE Haptics Symposium (HAPTICS)*, Mar. 2018, pp. 198–203. doi: 10.1109/HAPTICS.2018.8357176.
- [125] W. B. Messaoud, E. Vezzoli, Marie-Ange Bueno, and B. Lemaire-Semail, “Analyse Des Modulations De Frottement Par Effet Squeeze Film Et Electrovibration: Validité De La Complémentarité,” *Journées Internationales Francophones de Tribologie (JIFT 2014)*, Mulhouse, France, 2014, doi: 10.13140/RG.2.1.4394.7686.
- [126] R. F. Friesen, M. Wiertelwski, M. A. Peshkin, and J. E. E. Colgate, “The contribution of air to ultrasonic friction reduction,” Munich, France, 2017 *IEEE World Haptics Conference (WHC)*, Jun. 2017. doi: 10.1109/WHC.2017.7989955.
- [127] M. Wiertelwski, R. F. Friesen, and J. E. Colgate, “Partial squeeze film levitation modulates fingertip friction,” *Proceedings of the National Academy of Sciences of the United States of America*, vol. 113, no. 33, pp. 9210–9215, Aug. 2016, doi: 10.1073/pnas.1603908113.
- [128] A. Minikes and I. Bucher, “Comparing numerical and analytical solutions for squeeze-film levitation force,” *Journal of Fluids and Structures*, vol. 22, no. 5, pp. 713–719, Jul. 2006, doi: 10.1016/j.jfluidstructs.2006.02.004.
- [129] A. Minikes and I. Bucher, “Coupled dynamics of a squeeze-film levitated mass and a vibrating piezoelectric disc: numerical analysis and experimental study,” *Journal of Sound and Vibration*, vol. 263, no. 2, pp. 241–268, May 2003, doi: 10.1016/S0022-460X(02)01121-5.
- [130] A. Minikes, I. Bucher, and S. Haber, “Levitation force induced by pressure radiation in gas squeeze films,” *The Journal of the Acoustical Society of America*, vol. 116, no. 1, pp. 217–226, Jul. 2004, doi: 10.1121/1.1760110.
- [131] M. Janko, M. Wiertelwski, and Y. Visell, “Contact geometry and mechanics predict friction forces during tactile surface exploration,” *Scientific Reports*, vol. 8, no. 1, Dec. 2018, doi: 10.1038/s41598-018-23150-7.
- [132] N. Huloux, C. Bernard, and M. Wiertelwski, “Estimation of the Modulation of Friction from the Mechanical Impedance Variations,” *IEEE Trans. Haptics*, pp. 1–1, 2020, doi: 10.1109/TOH.2020.3038937.
- [133] R. F. Friesen, M. Wiertelwski, and J. E. Colgate, “The role of damping in ultrasonic friction reduction,” in *2016 IEEE Haptics Symposium (HAPTICS)*, Philadelphia, PA, Apr. 2016, pp. 167–172. doi: 10.1109/HAPTICS.2016.7463172.
- [134] A. Bouscayrol, B. Lemaire-Semail, and J. P. Hautier, *Systemic design methodologies for electrical energy systems: analysis, synthesis and management*. London : Hoboken, NJ: ISTE ; Wiley, 2012.
- [135] “EMRwebsite - Home.” <http://www.emrwebsite.org/> (accessed Aug. 07, 2019).
- [136] H. Hanselmann, “Hardware-in-the-loop simulation testing and its integration into a CACSD toolset,” in *Proceedings of Joint Conference on Control Applications*

*Intelligent Control and Computer Aided Control System Design*, Dearborn, MI, USA, 1996, pp. 152–156. doi: 10.1109/CACSD.1996.555253.

- [137] “Hardware-in-the-Loop Simulations,” in *An Introduction to Network Modeling and Simulation for the Practicing Engineer*, Hoboken, NJ, USA: John Wiley & Sons, Inc., 2011, pp. 114–142. doi: 10.1002/9781118063651.ch6.
- [138] A.-L. Allegre, A. Bouscayrol, J.-N. Verhille, P. Delarue, E. Chattot, and S. El-Fassi, “Reduced-Scale-Power Hardware-in-the-Loop Simulation of an Innovative Subway,” *IEEE Trans. Ind. Electron.*, vol. 57, no. 4, pp. 1175–1185, Apr. 2010, doi: 10.1109/TIE.2009.2029519.
- [139] A. Bouscayrol, *Control and Mechatronics: The Industrial Electronics Handbook*, 2nd ed. CRC Press, 2018. doi: 10.1201/9781315218403.
- [140] D. Maclay, “Simulation gets into the loop,” *IEE Review*, vol. 43, no. 3, pp. 109–112, May 1997, doi: 10.1049/ir:19970312.
- [141] A. S. Abdelrahman, K. S. Algarny, and M. Z. Youssef, “A Novel Platform for Powertrain Modeling of Electric Cars With Experimental Validation Using Real-Time Hardware in the Loop (HIL): A Case Study of GM Second Generation Chevrolet Volt,” *IEEE Trans. Power Electron.*, vol. 33, no. 11, pp. 9762–9771, Nov. 2018, doi: 10.1109/TPEL.2018.2793818.
- [142] C. Mayet, H. Ludivic, A. Bouscayrol, P. Delarue, J.-N. Verhille, E. Chattot, B. Lemaire-Semail, “Comparison of Different Models and Simulation Approaches for the Energetic Study of a Subway,” *IEEE Trans. Veh. Technol.*, vol. 63, no. 2, pp. 556–565, Feb. 2014, doi: 10.1109/TVT.2013.2280727.
- [143] P. Terwiesch, T. Keller, and E. Scheiben, “Rail vehicle control system integration testing using digital hardware-in-the-loop simulation,” *IEEE Trans. Contr. Syst. Technol.*, vol. 7, no. 3, pp. 352–362, May 1999, doi: 10.1109/87.761055.
- [144] C. Mayet, P. Delarue, A. Bouscayrol, and E. Chattot, “Hardware-In-the-Loop Simulation of Traction Power Supply for Power Flows Analysis of Multitrain Subway Lines,” *IEEE Trans. Veh. Technol.*, vol. 66, no. 7, pp. 5564–5571, Jul. 2017, doi: 10.1109/TVT.2016.2622245.
- [145] A. Bouscayrol, W. Lhomme, P. Delarue, B. Lemaire-Semail, and S. Aksas, “Hardware-in-the-loop simulation of electric vehicle traction systems using Energetic Macroscopic Representation,” in *IECON 2006 - 32nd Annual Conference on IEEE Industrial Electronics*, Paris, France, Nov. 2006, pp. 5319–5324. doi: 10.1109/IECON.2006.347679.
- [146] A. Bouscayrol, X. Guillaud, R. Teodorescu, and Ph. Delarue, “Validation of MPPT strategy for a wind energy conversion system using a hardware-in-the-loop simulation,” in *Proceedings of the 10th International Conference on Optimization of Electrical and Electronic Equipment*, Brasov, Romania, May 2006, p. 7.
- [147] H. R. Booher, Ed., *Handbook of Human Systems Integration: Booher/Human Systems Integration*. Hoboken, NJ, USA: John Wiley & Sons, Inc., 2003. doi: 10.1002/0471721174.

- [148] D. Fass and R. Lieber, "Rationale for human modelling in human in the loop systems design," in *2009 3rd Annual IEEE Systems Conference*, Vancouver, BC, Canada, Mar. 2009, pp. 27–30. doi: 10.1109/SYSTEMS.2009.4815766.
- [149] J. van Kuilenburg, M. A. Masen, and E. van der Heide, "Contact modelling of human skin: What value to use for the modulus of elasticity?," *Proceedings of the Institution of Mechanical Engineers, Part J: Journal of Engineering Tribology*, vol. 227, no. 4, pp. 349–361, Apr. 2013, doi: 10.1177/1350650112463307.
- [150] W. B. Messaoud, M.-A. Bueno, and B. Lemaire-Semail, "Relation between human perceived friction and finger friction characteristics," *Tribology International*, vol. 98, pp. 261–269, Jun. 2016, doi: 10.1016/j.triboint.2016.02.031.
- [151] Y. Tanaka, Y. Horita, A. Sano, and H. Fujimoto, "Tactile sensing utilizing human tactile perception," in *2011 IEEE World Haptics Conference*, Istanbul, Jun. 2011, pp. 621–626. doi: 10.1109/WHC.2011.5945557.
- [152] B. Yu, R. B. Gillespie, J. S. Freudenberg, and J. A. Cook, "Identification of human feedforward control in grasp and twist tasks," in *2014 American Control Conference*, Portland, OR, USA, Jun. 2014, pp. 2833–2838. doi: 10.1109/ACC.2014.6858847.
- [153] R. B. Gillespie, A. H. Ghasemi, and J. Freudenberg, "Human Motor Control and the Internal Model Principle," *IFAC-PapersOnLine*, vol. 49, no. 19, pp. 114–119, 2016, doi: 10.1016/j.ifacol.2016.10.471.
- [154] J. Nishizawa, Y. Sonoi, Y. Tanaka, M. Fukasawa, N. Usuda, Y. Otake, M. Fukumoto, A. Sano, "A Study on FEM Analysis of a Flexible Tactile Sensor Using Structure of Subcutaneous Tissue," *Robomech*, vol. 2018, no. 0, pp. 1P1-K17, 2018, doi: 10.1299/jsmermd.2018.1P1-K17.
- [155] K. Tanaka, Y. Tanaka, and A. Sano, "A Study toward equalization of tactile sensitivity using simple tactile nail chip," *Robomech*, vol. 2018, no. 0, pp. 1A1-J18, 2018, doi: 10.1299/jsmermd.2018.1A1-J18.
- [156] T. Zeng, "Conception et Contrôle d'un périphérique dédié à la simulation couplée kinesthésique et tactile," Thesis, University of Lille, Lille, France, 2012.
- [157] D. J. Inman, "Active Modal Control for Smart Structures.," *JSTOR*, vol. 359, no. 1778, pp. 205–219, 2001.
- [158] D. A. Torres Guzman, B. Lemaire-Semail, A. Kaci, F. Giraud, and M. Amberg, "Comparison Between Normal and Lateral Vibration on Surface Haptic Devices," in *2019 IEEE World Haptics Conference (WHC)*, Tokyo, Japan, Jul. 2019, pp. 199–204. doi: 10.1109/WHC.2019.8816124.
- [159] F. Giraud, M. Amberg, B. Lemaire-Semail, and C. Giraud-Audine, "Using an ultrasonic transducer to produce tactile rendering on a touchscreen," in *2014 Joint IEEE International Symposium on the Applications of Ferroelectric, International Workshop on Acoustic Transduction Materials and Devices & Workshop on Piezoresponse Force Microscopy*, State College, PA, USA, Aug. 2014, pp. 1–4. doi: 10.1109/ISAF.2014.6922972.

- [160] M. Doelle, D. Mager, P. Ruther, and O. Paul, “Geometry optimization for planar piezoresistive stress sensors based on the pseudo-Hall effect,” *Sensors and Actuators A: Physical*, vol. 127, no. 2, pp. 261–269, Mar. 2006, doi: 10.1016/j.sna.2005.08.014.
- [161] M. Géradin and D. Rixen, *Mechanical vibrations: theory and application to structural dynamics*, Third edition. Chichester, West Sussex, United Kingdom: Wiley, 2015.
- [162] L. Meirovitch, *Fundamentals of vibrations*. Long Grove, Illinois: Waveland Press, 2010.
- [163] C. Lanczos, *The variational principles of mechanics*, 4th ed. New York: Dover Publications, 1986.
- [164] *Code\_Aster*. EDF R&D. [Online]. Available: <http://www.code-aster.org>
- [165] W. Heylen, S. Lammens, and P. Sas, *Modal analysis theory and testing*, 2. ed. Leuven: Katholieke Univ. Leuven, Departement Werktuigkunde, 2007.
- [166] S. Ghenna, “Approche multimodale pour la conception d’interfaces à retour tactile à plusieurs doigts,” Thesis, University of Lille, Lille, France, 2016.
- [167] W. P. Mason, *Electromechanical Transducers and Wave Filters*, 2nd ed. Princeton, New Jersey: D. Van Nostrand Company, 1948.
- [168] S. Ghenna, F. Giraud, C. Giraud-Audine, M. Amberg, and B. Lemaire-Semail, “Modelling, identification and control of a Langevin transducer,” in *2015 IEEE International Workshop of Electronics, Control, Measurement, Signals and their Application to Mechatronics (ECMSM)*, Liberec, Czech Republic, Jun. 2015, pp. 1–6. doi: 10.1109/ECMSM.2015.7208676.
- [169] F. Giraud, *Piezoelectric actuators: vector control method*, 1st edition. Cambridge, CA: Elsevier, 2019.
- [170] D. A. Torres Guzman, A. Kaci, F. Giraud, C. Giraud-Audine, M. Amberg, S. Clénet, B. Lemaire-Semail, “PCA Model of Fundamental Acoustic Finger Force for Out-of-Plane Ultrasonic Vibration and its Correlation with Friction Reduction,” *IEEE Trans. Haptics*, pp. 1–1, 2021, doi: 10.1109/TOH.2021.3060108.
- [171] F. Giraud, C. Giraud-Audine, M. Amberg, and B. Lemaire-Semail, “Vector control method applied to a traveling wave in a finite beam,” *IEEE Trans. Ultrason., Ferroelect., Freq. Contr.*, vol. 61, no. 1, pp. 147–158, Jan. 2014, doi: 10.1109/TUFFC.2014.6689782.
- [172] F. Giraud and C. Giraud-Audine, *Piezoelectric actuators: vector control method*, 1st edition. Cambridge, CA: Elsevier, 2019.
- [173] A. Kaci, C. Giraud-Audine, F. Giraud, M. Amberg, and B. Lemaire-Semail, “LQR based MIMO-PID controller for the vector control of an underdamped harmonic oscillator,” *Mechanical Systems and Signal Processing*, vol. 134, p. 106314, Dec. 2019, doi: 10.1016/j.ymsp.2019.106314.
- [174] D. A. Torres Guzman, B. Lemaire-Semail, F. Giraud, C. Giraud-Audine, and M. Amberg, “Energy Analysis of Lateral vs. Normal Vibration Modes for Ultrasonic Surface Haptic Devices,” in *Haptics: Science, Technology, Applications*,



- vol. 12272, Springer International Publishing, 2020, pp. 416–424. doi: 10.1007/978-3-030-58147-3\_46.
- [175] R. F. Friesen, M. Wiertlewski, and J. E. Colgate, “The role of damping in ultrasonic friction reduction,” in *2016 IEEE Haptics Symposium (HAPTICS)*, Philadelphia, PA, Apr. 2016, pp. 167–172. doi: 10.1109/HAPTICS.2016.7463172.
- [176] A. Kaci, A. Torres, F. Giraud, C. Giraud-Audine, M. Amberg, and B. Lemaire-Semail, “Fundamental Acoustical Finger Force Calculation for Out-of-Plane Ultrasonic Vibration and its Correlation with Friction Reduction,” Tokyo, Japan, 2019, p. 6.
- [177] S. M. Pasumarty, S. A. Johnson, S. A. Watson, and M. J. Adams, “Friction of the Human Finger Pad: Influence of Moisture, Occlusion and Velocity,” *Tribol Lett*, vol. 44, no. 2, pp. 117–137, Nov. 2011, doi: 10.1007/s11249-011-9828-0.
- [178] A. Tiwari, T. Tolpekina, H. van Benthem, M. K. Gunnewiek, and B. N. J. Persson, “Rubber Adhesion and Friction: Role of Surface Energy and Contamination Films,” *Front. Mech. Eng.*, vol. 6, p. 620233, Mar. 2021, doi: 10.3389/fmech.2020.620233.
- [179] A. Genovese, F. Carputo, M. Ciavarella, F. Farroni, A. Papangelo, and A. Sakhnevych, “Analysis of Multiscale Theories for Viscoelastic Rubber Friction,” in *Proceedings of XXIV AIMETA Conference 2019*, A. Carcaterra, A. Paolone, and G. Graziani, Eds. Cham: Springer International Publishing, 2020, pp. 1125–1135. doi: 10.1007/978-3-030-41057-5\_91.
- [180] Y. B. Chernyak and A. I. Leonov, “On the theory of the adhesive friction of elastomers,” *Wear*, 108 (1986) 105 - 138.
- [181] A. N. Gent, G. R. Hamed, and W. J. Hung, “Adhesion of elastomers: Dwell time effects,” *The Journal of Adhesion*, vol. 79, no. 4, pp. 315–325, Apr. 2003, doi: 10.1080/00218460309584.
- [182] B. Delhayé, P. Lefèvre, and J.-L. Thonnard, “Dynamics of fingertip contact during the onset of tangential slip,” *J. R. Soc. Interface.*, vol. 11, no. 100, p. 20140698, Nov. 2014, doi: 10.1098/rsif.2014.0698.
- [183] A. J. Tuononen, “Onset of frictional sliding of rubber–glass contact under dry and lubricated conditions,” *Sci Rep*, vol. 6, no. 1, p. 27951, Sep. 2016, doi: 10.1038/srep27951.
- [184] A. Schallamach, “A theory of dynamic rubber friction,” *Wear*, vol. 6, no. 5, pp. 375–382, Sep. 1963, doi: 10.1016/0043-1648(63)90206-0.
- [185] S. Mathôt, D. Schreij, and J. Theeuwes, “OpenSesame: An open-source, graphical experiment builder for the social sciences,” *Behav Res*, vol. 44, no. 2, pp. 314–324, Jun. 2012, doi: 10.3758/s13428-011-0168-7.
- [186] P. Garcia, F. Giraud, B. Lemaire-Semail, M. Rupin, and M. Amberg, “2MoTac: Simulation of Button Click by Superposition of Two Ultrasonic Plate Waves,” in *Haptics: Science, Technology, Applications*, Springer International Publishing, 2020, pp. 343–352, .

- [187] R. Holland, "Representation of Dielectric, Elastic, and Piezoelectric Losses by Complex Coefficients," *IEEE Trans. Son. Ultrason.*, vol. 14, no. 1, pp. 18–20, Jan. 1967, doi: 10.1109/T-SU.1967.29405.
- [188] K. Uchino and S. Hirose, "Loss mechanisms in piezoelectrics: how to measure different losses separately," *IEEE Trans. Ultrason., Ferroelect., Freq. Contr.*, vol. 48, no. 1, pp. 307–321, Jan. 2001, doi: 10.1109/58.896144.
- [189] Y. Yang, B. Lemaire-Semail, F. Giraud, M. Amberg, Y. Zhang, and C. Giraud-Audine, "Power analysis for the design of a large area ultrasonic tactile touch panel," *Eur. Phys. J. Appl. Phys.*, vol. 72, no. 1, p. 11101, Oct. 2015, doi: 10.1051/epjap/2015150051.
- [190] K. Uchino, J. H. Zheng, Y. H. Chen, X. H. Du, J. Ryu, Y. Gao, S. Ural, S. Prys, S. Hyrose, "Loss mechanisms and high power piezoelectrics," *J Mater Sci*, vol. 41, no. 1, pp. 217–228, Jan. 2006, doi: 10.1007/s10853-005-7201-0.
- [191] F. Giraud, M. Amberg, R. Vanbelleghem, and B. Lemaire-Semail, "Power Consumption Reduction of a Controlled Friction Tactile Plate," in *Haptics: Generating and Perceiving Tangible Sensations*, vol. 6192, A. M. L. Kappers, J. B. F. van Erp, W. M. Bergmann Tiest, and F. C. T. van der Helm, Eds. Berlin, Heidelberg: Springer Berlin Heidelberg, 2010, pp. 44–49. doi: 10.1007/978-3-642-14075-4\_7.
- [192] M. Wiertelwski and J. E. Colgate, "Power Optimization of Ultrasonic Friction-Modulation Tactile Interfaces," *IEEE Transactions on Haptics*, vol. 8, no. 1, pp. 43–53, Jan. 2015, doi: 10.1109/TOH.2014.2362518.
- [193] P. Sergeant, F. Giraud, B. Lemaire-Semail. "Geometrical optimization of an ultrasonic tactile plate for surface texture rendering". *Sensors and Actuators A: Physical*, Elsevier, 2010, pp.91- 100. doi:10.1016/j.sna.2010.05.001ff.
- [194] M. K. Saleem, C. Yilmaz, and C. Basdogan, "Psychophysical Evaluation of Change in Friction on an Ultrasonically-Actuated Touchscreen," *IEEE Transactions on Haptics*, vol. 11, no. 4, pp. 599–610, Oct. 2018, doi: 10.1109/TOH.2018.2830790.
- [195] W. Ben Messaoud, M. Amberg, B. Lemaire-Semail, F. Giraud, and M.-A. Bueno, "High fidelity closed loop controlled friction in SMARTTAC tactile stimulator," in *2015 17th European Conference on Power Electronics and Applications (EPE'15 ECCE-Europe)*, Geneva, Sep. 2015, pp. 1–9. doi: 10.1109/EPE.2015.7309191.
- [196] N. Huloux, J. Monnoyer, M. Boyron, and M. Wiertelwski, "Overcoming the Variability of Fingertip Friction with Surface-Haptic Force-Feedback," in *Haptics: Science, Technology, and Applications*, vol. 10894, D. Prattichizzo, H. Shinoda, H. Z. Tan, E. Ruffaldi, and A. Frisoli, Eds. Cham: Springer International Publishing, 2018, pp. 326–337. doi: 10.1007/978-3-319-93399-3\_29.
- [197] W. B. Messaoud, M.-A. Bueno, and B. Lemaire-Semail, "Relation between human perceived friction and finger friction characteristics," *Tribology*

*International*, vol. 98, pp. 261–269, Jun. 2016, doi: 10.1016/j.triboint.2016.02.031.

- [198] E. Samur, J. E. Colgate, and M. A. Peshkin, “Psychophysical evaluation of a variable friction tactile interface,” *IS&T/SPIE Electronic Imaging*, San Jose, CA, Feb. 2009, p. 72400J. doi: 10.1117/12.817170.
- [199] D. Gueorguiev, E. Vezzoli, A. Mouraux, B. Lemaire-Semail, and J.-L. Thonnard, “The tactile perception of transient changes in friction,” *Journal of The Royal Society Interface*, vol. 14, no. 137, p. 20170641, Dec. 2017, doi: 10.1098/rsif.2017.0641.
- [200] S. Beale and B. Shafai, “Robust control system design with a proportional integral observer,” *International Journal of Control*, vol. 50, no. 1, pp. 97–111, Jul. 1989, doi: 10.1080/00207178908953350.
- [201] M. Wiertlewski, C. Hudin, and V. Hayward, “On the 1/f noise and non-integer harmonic decay of the interaction of a finger sliding on flat and sinusoidal surfaces,” in *2011 IEEE World Haptics Conference*, Istanbul, Jun. 2011, pp. 25–30. doi: 10.1109/WHC.2011.5945456.
- [202] Q. Wang and V. Hayward, “Tactile synthesis and perceptual inverse problems seen from the viewpoint of contact mechanics,” *ACM Trans. Appl. Percept.*, vol. 5, no. 2, pp. 1–19, May 2008, doi: 10.1145/1279920.1279921.
- [203] C. Molnar and J. Gair, *Concepts of Biology - 1st Canadian Edition*. 2015.
- [204] Neubarth NL, Emanuel AJ, Liu Y, Springel MW, Handler A, Zhang Q, Lehnert BP, Guo C, Orefice LL, Abdelaziz A, DeLisle MM, Iskols M, Rhyins J, Kim SJ, Cattel SJ, Regehr W, Harvey CD, Drugowitsch J, Ginty DD., “Meissner corpuscles and their spatially intermingled afferents underlie gentle touch perception,” *Science*, vol. 368, no. 6497, p. eabb2751, Jun. 2020, doi: 10.1126/science.abb2751.
- [205] R. Shi, B. Wang, Z. Yan, Z. Wang, and L. Dong, “Effect of Surface Topography Parameters on Friction and Wear of Random Rough Surface,” *Materials*, vol. 12, no. 17, p. 2762, Aug. 2019, doi: 10.3390/ma12172762.
- [206] A. Bouscayrol, P. Delarue, and B. Lemaire-Semail, “Graphical description for Hardware-in-the-loop simulation,” in *2008 IEEE International Symposium on Industrial Electronics*, Cambridge, Jun. 2008, pp. 2140–2145. doi: 10.1109/ISIE.2008.4677307.
- [207] W. Ben Messaoud, “Design and control of a tactile stimulator for real texture simulation : application to textile fabrics,” Thesis, University of Lille, Lille, France, 2016. Accessed: Aug. 03, 2019.
- [208] A. Bouscayrol, B. Davat, B. de Fornel, B. François, J. P. Hautier, F. Meibody-Tabar and M. Pietrzak-David, “Multi-converter multi-machine systems: application for electromechanical drives,” *The European Physical Journal - Applied Physics*, vol. 10, no. 2, pp. 131–147, 2000, doi: 10.1051/epjap:2000124.
- [209] A. Bouscayrol, J. P. Hautier, and B. Lemaire-Semail, “Graphic Formalisms for the Control of Multi-Physical Energetic Systems: COG and EMR,” in *Systemic Design Methodologies for Electrical Energy Systems: Analysis, Synthesis and*

*Management*, X. Roboam, Ed. ISTE Ltd, 2013, pp. 89–124. doi: 10.1002/9781118569863.ch3.

- [210] R. Béarée, J. Gomand, P. J. Barre, and J. P. Hautier, “On the causality integration in the design of axis drive control,” *16th IFAC World Congress*, Pragues (Praha), 2005.